University of Southampton

Faculty of Engineering and Physical Sciences

Maritime and Environmental Engineering

A combined volume of fluid and immersed boundary method for simulations of ship bow breaking waves

by

Qiu Jin

Thesis for the degree of

Doctor of Philosophy

11.01.2021

University of Southampton

Abstract

Faculty of Engineering and Physical Sciences

Maritime and Environmental Engineering

Thesis for the degree of Doctor of Philosophy

A combined volume of fluid and immersed boundary method for simulations of ship bow breaking waves

by

Qiu Jin

The study of breaking bow waves has significant benefits due to its influence in many aspects. The consequences caused by breaking bow waves include, but are not limited to, the increase of resistance, increased detectability and damage to port facilities. Analytic studies are not suitable for this problem because of over-simplified model. Present experimental studies are costly and not robust. This thesis presents a new two-phase flow solver for the analysis and prediction of complex ship flows through an investigation of bow breaking waves and builds an air-water boundary layer model to overcome the discontinuity over the two-phase interface.

A combined volume of fluid and immersed boundary method is developed to simulate two-phase flows with high density ratio. The problems of discontinuity of density and momentum flux are known to be challenging to handle in simulations. In order to overcome the numerical instabilities encountered near the interface, an extra velocity field is designed to extend the velocity of the heavier phase into the lighter phase and to enforce a new boundary condition near the interface, which is similar to non-slip boundary conditions in Fluid-Structure Interaction (FSI) problems. The interface is captured using a Volume of Fluid (VOF) method, and a new boundary layer is built on the lighter phase side by an immersed boundary method.

The accuracy of the new method is validated by a wide range of test cases relevant to ship wave flows. The results of the new solver are compared with the original VOF solver, analytical solutions and single-phase flow solver results. The designed boundary layer helps to reduce the spurious velocity caused by the imbalance of dynamic pressure gradient and density gradient and to prevent the tearing of the interface due to the tangential velocity between the two phases across the interface. It is shown to improve the robustness and stability of two-phase flow simulations, and higher accuracy can be obtained on a relatively coarse grid compared to the original VOF method.

The new solver is used to study bow breaking waves generated by a wedge-shape bow and KRISO Container Ship (KCS). The numerical results of velocity components and axial vorticity at different locations in the vicinity of the bow show that the new solver can predict well the vortical cross flow associated with the overturning bow wave.

Table of Contents

Table of Tables

Table of Figures

Declaration of Authorship

Print name:	Qiu Jin

Title of thesis:	A combined volume of fluid and immersed boundary method for simulations of ship bow breaking waves

I declare that this thesis and the work presented in it are my own and has been generated by me as the result of my own original research.

I confirm that:

1. This work was done wholly or mainly while in candidature for a research degree at this University;
2. Where any part of this thesis has previously been submitted for a degree or any other qualification at this University or any other institution, this has been clearly stated;
3. Where I have consulted the published work of others, this is always clearly attributed;
4. Where I have quoted from the work of others, the source is always given. With the exception of such quotations, this thesis is entirely my own work;
5. I have acknowledged all main sources of help;
6. Where the thesis is based on work done by myself jointly with others, I have made clear exactly what was done by others and what I have contributed myself;
7. Delete as appropriate None of this work has been published before submission or Parts of this work have been published as:

Signature:	Qiu Jin	Date:	11/01/2022

Nomenclature

Abbreviations and acronyms

1D	One Dimensional
2D	Two Dimensional
3D	Three Dimensional
CFD	Computational Fluid Dynamics
CLSVOF	Coupled Level Set and Volume of Fluid
CSF	Continuum Surface Force
CSS	Continuous Surface Stress
DNS	Direct Numerical Simulation
DW	Density-weight Smoothing
EV	Extrapolated Velocity
EFD	Experimental Fluid Dynamics
FVM	Finite Volume Method
GFM	Ghost Fluid Method
HPC	High Performance Computing
IB	Immersed Boundary
KCS	KRISO Container Ship
LS	Level Set
MULES	Multidimensional Universal Limiter of Explicit Solution
OpenFOAM	Open source Field Operation and Manipulation
PISO	Pressure Implicit Splitting Operator
RANS	Reynolds average Naiver-Stokes
SIMPLE	Semi-Implicit Method for pressure-Linked Equations
SPH	Smoothed Particle Hydrodynamics
SST	Shear Stress Transport
VOF	Volume of Fluid

Symbols

Symbol	Description	SI unit
a	Vector variable	[various]
b	distance	[m]

B	Bond number	[-]
c	Wave celerity	[m/s]
C_γ	Interface compression coefficient	[-]
Co	Courant number	[-]
D	Diameter	[m]
	Water depth	[m]
$\mathbf{g}$	Gravitational acceleration g= s9.81	[m/s^2]
F	Face mass fluxes	[kg/s]
Fr	Froude number	[-]
h	Wave height	[m]
L	Length	[m]
$\mathbf{n}$	Unit normal vector	[-]
p	Pressure	[N/m^2]
t	Time	[s]
$\mathbf{u}$	Velocity	[m/s]
V_p	Volume of cell	[m^3]
Re	Reynolds number	[-]
$\mathbf{S}$	Outward-pointing face area vector	[m^2]
We	Weber number	[-]
$\mathbf{x}$	Position vector	[m]
α	Volume fraction in VOF method	[-]
ϵ	Relative error	[-]
	Wave steepness	[-]
η	Wave profile	[m]
θ	Angle	[°]
κ	local curvature	[-]
μ	Dynamic viscosity	[kg/(s m)]
ρ	Density	[kg/m^3]
σ	Surface tension coefficient	[N/m]
τ	Pseudo time step	[-]
ϕ	Scaler property	[various]

Acknowledgements

During the four years I spent at the University of Southampton, I have had many opportunities to be grateful for the help and support of others.

Firstly, I would like to thank my supervisors Dominic Hudson, Pandeli Temarel and W. Geraint Price for allowing me the opportunity to embark on this once in a lifetime adventure in the U.K. I also owe them great thanks for all of their guidance, encouragement and support along the way. Thanks also go to the University of Southampton and China Scholarship Council for providing the funding.

Furthermore, I would like to thank all my colleagues at the Maritime Engineering Group and others who worked around me in Building 176 for creating such a socially vibrant and friendly atmosphere. The list of people to thank can be long but I would like to mention Artur Lidtke, Mehmet Cihan and Andhini Zurman Nasution for helping me survive all the ups and downs during my Ph. D.

Finally, a very special gratitude goes out to my parents for supporting me spiritually throughout writing this thesis and my life in general. They kept me going on and this work would not have been possible without their input.

Chapter 1 Introduction

1.1 Background

Breaking bow waves are important to engineers for many reasons. (1) For ship designers, bow waves are a source of resistance. For a ship to move forward, it must push tons of water out of its way to the sides and thus generate surface waves. (2) The breaking induces splashing and entrains air bubbles, resulting in a white-water wake. This wake can be a substantial source of radar signature of naval craft. The air bubbles also create noise in the water which is detectable using underwater acoustics. Current ships are designed to have such low radar, infra-red and acoustic signatures that the breaking waves are often more detectable than the ship itself. (3) Ship waves are also a persistent problem for harbours and near-shore ferries as significant damage can be produced by large, steep waves. (4) Accurate predictions of the detailed flow field are useful for improving the ship's hull form design and local information on the flow enable the analysis and improvement of appendages and propulsive systems.

Accurate and applicable prediction tools are required to better predict the behaviours of bow breaking waves. Analytical studies are over-simplified by simple ship geometry and flow conditions and their application is limited to very initial stages of design and primary description for ship wave system[1]. Experimental studies are over-specific to ship type. The results can be accurate but the time and expense for each observation is large and is not applicable for most general ships. From this perspective, reliable numerical simulations are required for developing mathematical models to understand and simulate the features of bow waves.

Ship bow waves exhibit both large and small-scale features. The most notable large-scale characteristic is the Kelvin bow wave pattern. Wave systems are often described by potential flow theories without taking in to account the influence of viscosity. However, for sufficiently large ship speed and depending on the shape of a bow, spilling and/or plunging breaking occurs and induces vortices and scars additionally (see Figure 1-1). The most prominent small-scale feature is the thin overturning sheets generated from the bow wave crest and the plunging breaking waves. Nonlinear potential flow methods are suitable for modelling steep waves up to the point of breaking but have a limited ability to capture the spray and bubbles along with the breaking wave processes. Therefore, efficient Computational Fluid Dynamics (CFD) methods with turbulence models and sharp free surface capturing methods are required to investigate the mechanics of the bow wave breaking process.

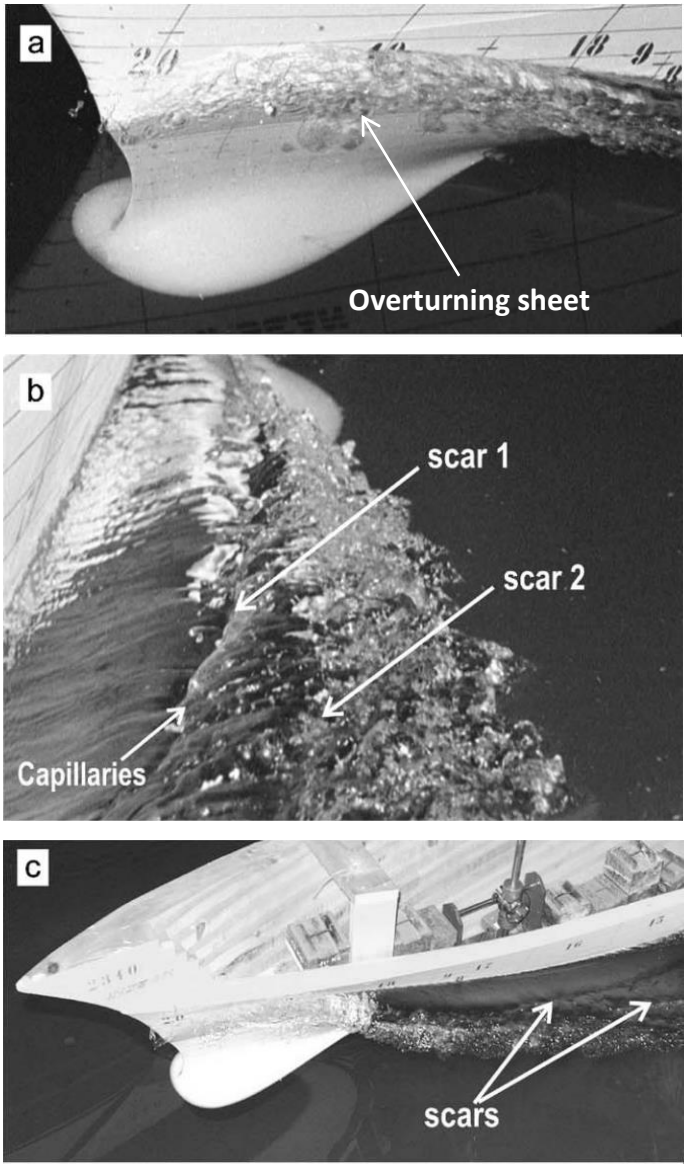

Figure 1-1 Bow breaking waves[2]

1.2 Problem definition

A challenge of the simulation of bow breaking waves is the need to resolve the flow of two phases, i.e., air and water, and the evolution of the interface between them. Various free surface simulation methods are available, but these tools have their own limitations. In surface fitting methods, the grid must be deformed to match the shape of the free surface[3]. As a result, topology changes, such as in overturning water sheets, cannot be properly handled and the simulation of steep waves could be challenging. Although Level set methods can always maintain a sharp interface and can capture plunging breakers and flow topology, they suffer a known defect of mass conservation [4]. While none of the approaches provide a physically correct model for the wave breaking, the Volume of Fluid (VOF) comes closest as it approximates the formation of foam and bubbly regions by zones where the volume fraction is dissipation[3]. Numerical dissipation of foam and bubbly regions by

zones, while not related to the actual physical dissipation in breaking waves, takes on the same role of dissipation energy, as well as keeping the solution stable. Thus, the method is robust and reasonably accurate even in presence of strong plunging breakers[1].

VOF methods allow topologically complex free surfaces to be treated generally by defining a volume-based colour-function over a background grid instead of tracking the interface location explicitly. However, the volume function and the fields based on it, such as density and viscosity, are discontinuous across the interface. This discontinuous form of transport results in the addition of jump conditions across the interface which are difficult to implement numerically and unphysical characteristics like spurious bubbles or spray may occur.

The free-surface boundary layer is not resolved in VOF simulations at high Reynolds numbers with large density jumps between air and water[5]. A numerical breakdown is associated with the jump that occurs in the tangential velocity across the free surface. As a result, unphysical tearing tends to occur even with high-order VOF advection schemes. In reality, there is a viscous boundary layer that makes the transition from the water velocity slightly beneath the free surface to the air velocity slightly above the free surface. Smoothing and/or filtering are required to reduce the jump in the tangential velocity that occurs at the free-surface interface. Fu et al.[6] used a density-weighted velocity smoother to simply push the water particle velocity into the air. The resulting fields do not capture the true jump at the free boundary but show a better comparison with the experimental results. A more robust and physics-based solution is required to resemble the viscous boundary layer near the air-water interface.

1.3 Aim and objectives

The overall purpose of this work is to contribute to the improvement of the modelling and analysis of complex ship flow through an investigation of bow breaking waves. A physics-based air-water boundary layer model is developed and applied to VOF methods to deal with the discontinuity in the fluid properties over the two-phase interface and to offer a better resolution of the free-surface. This aim is met through the following objectives:

(a) Carry out a literature review on the research of air-water interface boundary conditions which mainly include the physical mechanics of two-phase boundary and numerical treatments for jumps over the interface.

(b) Summarise the challenges for two-phase flow solvers, define the sources of the spurious velocities near the interface.

(c) Build a new boundary layer model to transit the water velocity to the air velocity physically smoothly and propose a new two-phase flow solver with the new boundary condition.

(d) Validate the proposed two-phase flow solver with a series of test cases.

(e) Investigate the detailed process of bow breaking waves for a realistic ship geometry.

1.4 Novel contributions

A general contribution of this thesis is the development of novel techniques to solve problems for breaking wave with high-density ratio free surface. The techniques were implemented in OpenFoam platform using High Performance Computing (HPC).

In addition, the following original contributions are made:

(1) The free-surface boundary layer is not resolved in VOF simulations at high Reynolds' numbers with large density jumps between air and water. This thesis provides a new two-phase solver (IBVOF solver) based on VOF to prevent tearing due to a discontinuity in the tangential velocity between the air and the water across the free surface. An air-water boundary layer model is built with the new solver. The way the air velocity at the interface is driven by the water velocity is studied and discussed. The model is also applicable for other two-phase flow solvers with Level set methods or Coupled Level Set and Volume of Fluid (CLSVOF) methods.

(2) The characteristic of the breaking waves, especially for plunging breaking waves, is something which, although often mentioned is not widely studied or discussed. The detailed development of breaking waves, i.e., deformation, initiation, overturning, merging, air entrainment and change of trailing wave form, is given and discussed.

Several papers have been published, presenting the findings of this thesis to a broader audience. Papers authored by Jin et al. relate directly to the methodology presented in this thesis. Other papers have also been contributed to as a direct result of the studies presented here.

1.4.1 Journal papers

Jin, Q., Hudson, D. A., Temarel, P., & Price, W. G. (2021a). Turbulence and energy dissipation mechanisms in steady spilling breaking waves induced by a shallowly submerged hydrofoil, Ocean Engineering 229. http://doi.org/10.1016/j.oceaneng.2021.108976

Jin, Q., Hudson, D. A. & Price, W. G. (2021b). A combined volume of fluid and immersed boundary method for modelling of two-phase flows with high density ratio, Journal of Fluids Engineering (Accepted).

Jin, Q., Hudson, D. A., Temarel, P. (2021c). A combined volume of fluid and immersed boundary method for free surface simulations induced by solitary waves, Ocean Engineering (Under review).

1.4.2 Peer reviewed conference papers

Jin, Q., Hudson, D. A., Temarel, P., & Price, W. G. (2019). Performance of a two-phase flow solver for the simulation of breaking waves, in 'Proceedings of 38th international conference on ocean, offshore and arctic engineering, 9th -14th June, Glasgow, UK'.

Jin, Q., Hudson, D. A., Temarel, P., & Price, W. G. (2020). Numerical simulation of plunging breaking waves on a ship bow by a two-phase flow solver, in 'Proceedings of 30th International Ocean and Polar Engineering Conference, 11th -16th June, Shanghai, China'.

1.4.3 Other conference papers

Jin, Q., Hudson, D., & Temarel, P. (2018). Simulation of non-breaking and breaking waves with OpenFOAM, in 'Proceedings of the 21st Numerical Towing Tank Symposium, 30th September-2nd October, Cortona, Italy'.

Jin, Q., Hudson, D., & Temarel, P. (2019). Simulation of plunging breaking waves induced by a submerged bump, in 'Proceedings of the 22nd Numerical Towing Tank Symposium, 29th September-1st October, Tomar, Portugal'.

1.5 Structure of the report

This thesis presents a new two-phase flow solver to improve the accuracy and stability of bow breaking wave simulation using a velocity extrapolation approach. This method is motivated by the realization that the free surface boundary layer has not been resolved in existing two-phase flow simulations with large density jumps between air and water. The new solver is presented to reduce the unphysical tearing of the free surface. An outline of this Thesis is given below.

Chapter 2 reviews exiting literature and background information on the bow breaking waves and air-water interface modelling and analyses the trends and limitation of existing research results.

The ship hydrodynamic tools are required to be improved with more accurate prescription and prediction of air-water interface behaviour.

Chapter 3 gives a description to the fundamental basis and algorithm for the proposed two-phase flow solver. The sources of the spurious velocities and shear are analysed based on governing equations. In order to achieve stable numerical solution at high density ratios, a boundary layer is built on the air phase side by an immersed boundary (IB) method and an extrapolated velocity (EV) approach is used to reconstruct the velocity inside the boundary layer. The velocity extrapolation from liquid to gas is designed and validated with simple test cases.

Chapter 4 examines the accuracy and stability of the new solver with two sets of test cases, steady stratified flow and convection of a high-density droplet. In the former case, the effects of mesh size, time step and density ratio to the spurious velocity generated near the interface are further examined. In the latter case, the effect of the spurious velocities to the captured interface is investigated. The results of both test cases with the new solver are compared with the original VOF solver, analytical solutions or one-phase flow solver.

Chapter 5 extends the applications of the IBVOF solver to general flow simulations. Another velocity extrapolated method, density-weight smoothing method, is proposed and applied into the new solver. The DW method extends the applications of the new solver from 2D simulations with uniform mesh to 3D simulations with unstructured mesh. Several test cases are carried out and the effects of fluid viscosity and surface tension are investigated.

In Chapter 6, the performance of the proposed two-phase flow solver is further evaluated through two sets of numerical benchmark tests with solitary waves and Stokes waves. In both sets of benchmark tests, the fluids are first modelled as inviscid for wave propagation simulations. This assumption allows comparisons with the well-controlled potential theory. In the latter cases of wave breaking, the influence of fluid viscosity and surface tension are considered, and the numerical results are compared with published experimental data.

In Chapter 7, an assessment of the capability of the IBVOF solver is first performed on a test case specifically conceived, plunging breaking waves generated by a sharp wedge-shaped bow. The numerical results of the bow wave profile at different locations in the vicinity of the bow are compared to experiments to validate the proposed two-phase flow solver. Then, the IBVOF solver is used to simulation the wave pattern generated by the KRISO Container Ship (KCS) in forward motion. The focuses are put on the hydrodynamic simulation of the whole process of plunging breaking waves and the velocity and vorticity field in the region of the bow and in breaking waves.

Chapter 8 presents the major research findings and suggestions for the future work.

Chapter 2 Research on bow breaking waves

2.1 Introduction

As with most scientific problems, the development of this bow breaking waves investigation goes hand in hand with discovering which phenomena are involved. This chapter will review, by means of experimental observations and numerical simulations, how this process has played in the past several decades.

The review is started with a brief introduction to the types of bow breaking waves, the existing literature on experimental and numerical studies of the bow wave, and the reasons why the simulation of breaking waves is challenging. An in-depth discussion on free surface viscous flow solvers is presented by comparison between one-phase flow solvers and two-phase flow solvers. Because of their ability to deal with air-water interaction problems, two-phase flow solvers are the best choice for bow breaking wave simulation. This chapter serves both to highlight the hydrodynamic phenomena involved in bow breaking waves and the problems that the two-phase flow solvers face.

2.2 Literature review of bow breaking wave investigations

2.2.1 Classification of bow breaking waves

The bow wave is a feature of the flow generated around the bow of a ship hull. It is worth studying for several reasons. An important basic property of a bow wave is that it mainly depends on the shape of the ship bow instead of the length of the ship or the hull geometry aft of the bow region [7]. This fundamental characteristic allows the bow waves generated by a typical family of ship bows to be calculated by defining a set of geometric parameters.

Another important feature is that the waterline entrance angle and ship speed are thought to have a considerable impact on the breaking type of bow waves. Depending on the appearance of stability at the crest, the breaking waves can be classified as plunging breaking waves or spilling breaking waves, as shown in Figure 2-1 [8]. Fast ships with fine bows tend to produce plunging bow waves which are made up of detached thin sheets of water. The water sheets are relatively steady until they reach the main free surface and break up and undergo turbulent diffusion. Slow ships with blunt bows, on the other hand, tend to produce highly unsteady and turbulent breaking bow waves. Noblesse et al. [9] tried to divide the two types of bow breaking waves with a boundary by

approximating a simple analytical solution for a wedge-shaped ship without a bulbous bow in clam water. This analytical expression was used in Bernoulli's equation for the bow wave and compared with the experimental approximation method. According to Noblesse's research, the depth-based Froude number and the waterline entrance angle are the two major characteristics that impact the stability of the bow-wave crest. As a result of this finding, it may be determined that the features of the bow wave created by a certain ship may be dynamically modified by the ship's speed or depth.

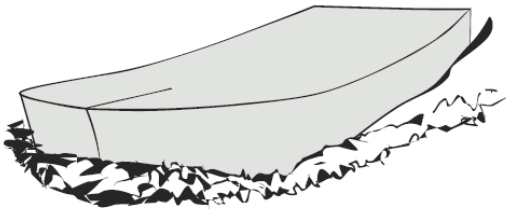

(a) Spilling breaking

(b) Plunging breaking

Figure 2-1 Classification of the bow wave breaking [8].

For both types of breaking waves, the numerical treatment of these highly nonlinear free-surface behaviours is usually very difficult and challenging due to the complexity of fully nonlinear free-surface and body boundary conditions. The free surface eruptions in spilling wave breaking indicate that the broken free surface is a result of the strong turbulence generated underneath the free surface meeting the free surface[10]. Spilling wave breaking is a vast area of study, which is not yet fully understood. The physics of primary interest in spilling breaking is the initiation of breaking, change of trailing wave form and the mean and turbulent flow structure in the trailing wake[11]. The broken free surface makes the investigation of waves more complex caused by the waves and their interaction with boundary layers and vortices, free surface turbulence, and air-water interfacial effects such as bubble entrainment and surface tension. Gaining a better understanding of the fluid mechanics of the free surface would be of both fundamental and practical interest, especially for ship and ocean engineering.

Plunging wave breaking is one of the most violent phenomena of air–water interface interactions, producing strong turbulence with large amounts of air bubbles, water droplets, jets and sprays. These phenomena commonly occur in ship flows and are one of the main sources of the underwater sounds and white-water wakes, which are of great importance for signature of ships. The physics of primary interest in plunging breaking waves is unsteady development of plunging jets, i.e., deformation, initiation, overturning, merging, air entrainment and splash-up. However, the process of plunging wave breaking is not well understood and there are few studies that provide a detailed quantitative description of breaking waves. It is therefore important to investigate the conditions under which breaking appears and the interactions of air and water[12].

2.2.2 Experimental observation

Experimental observations on bow waves mainly focus on the wave height or the velocity fields. The University of Tokyo Towing Tank has done many experimental studies on bow waves [13]. Inui et al. [14] measure the flow structure of bow waves using surface visualization techniques (aluminium powder and tracking particles). Toda et al. [15] measured the wave height and average velocity using a capacitance wire and a 5-hole pitot tube for Series 60 and characterized the presence of a bow-wave-induced vortex.

Duncan[16] investigated the surface height profile and vertical distributions of velocity behind an constant-speed underwater hydrofoil in a towing tank. According to wake observation, the drag associated with wave breaking at a free surface is triple the theoretical maximum drag of a nonbreaking wave. Dong et al. [17] and Roth et al. [18] investigated the early stages of bow-wave development in flow generated by the DTMB 4817 model with PIV measurements and free-surface visualization. The results showed that viscosity and surface tension play a role in inhibiting the bow breaking waves formation and evolution.

Waniewski et al. [19] studied the dynamics and air entrainment mechanisms of ship waves with a wedge-shaped bow and demonstrated that the bow wave is a nonlinear phenomenon. The structure of bow waves (thin water sheet formation, overturning sheet with surface disturbance, fingering and breaking up into spray, plunging and splashing, and air entrainment) are displayed and documented with valuable experimental data provided such as wave elevation, extent of wave breaking, spray droplets size and number. The experiments are carried out in both a water flume and a towing tank with a fixed deflecting plate and a towing wedge model. A thin liquid sheet is generated at the leading edge of the wedge, and it continues to ride up on the side wall according to the bow wave profile obtained in the towing tank experiment. A large area of splash is crested at the wake of the wedge due to wave plunge and air entrainment. Noblesse et al. [9] established

a set of simple mathematical relations for a wedge-shaped bow wave based on the experimental data and elementary fundamental concepts that characterise the key properties of a ship bow (wave height, wave crest location and profile, and flow steadiness or unsteadiness) in terms of ship speed, draught and waterline entrance angle.

Olivieri et al. [20] [2] investigated the velocity field of bow wave breaking generated by a naval combatant, INSEAN model 2340 using a 5-hole pitot tube downstream of the bow wave and observed a bow and shoulder wake of a model ship in a subsequent study. As shown in mean velocity measurements, the breaking waves create a complex vortex structure beneath the free surface.

Karion et al. [21] investigated the size and velocity distribution of the bow breaking waves generated by a wedge-shaped bow through high-speed video analysis. Measurements were characterized by Froude, Reynolds, and Weber numbers. According to their findings, wave breaks occur when the Froude and Reynolds numbers pass a certain level and there is a key Weber number for bow wave spraying. The findings are used to examine scaling issues related to bow-wave breaking.

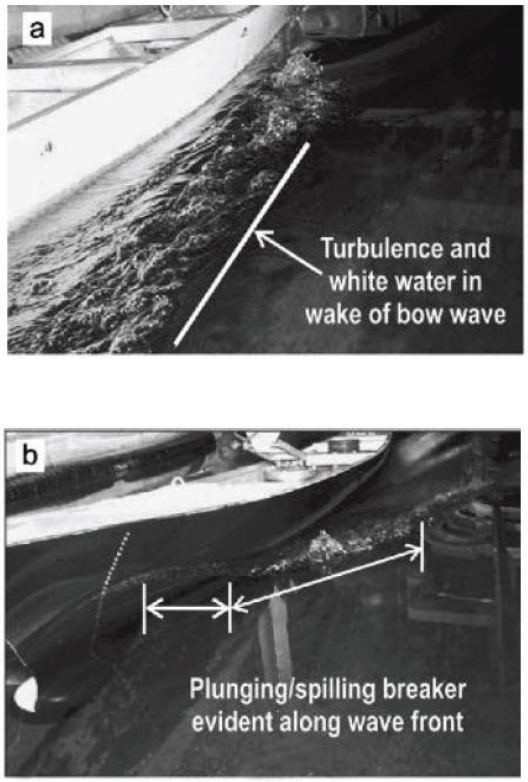

Figure 2-2 Experimental observation of bow waves by Olivieri et al. [2]

Maxeiner et al. [22] investigated the characteristics of a bow wave by using a two-dimensional plus time (2D+T) approximation method using a flexible wave board designed to simulate one side of

bow waves for an advancing ship with a simple bow shape. The height of the bow wave and shape of the crest are considered when investigating the characteristics of the bow wave. It is found that the wave parameters such as wave velocity and the maximum wave height closely correlate with the motion of a wave generator.

Experimental measurements are the most reliable methods to evaluate the bow wave breaking. The hydrodynamical phenomena involved in ship flow are usually discovered from experimental observation and then validated and investigated with numerical simulations. However, as analysed above, there are lots of limitation with the experimental measurements. The experimental measurements highly depend on experimental conditions and involve time consuming procedures for test preparation. Due to the high money and time cost, the observation is usually limited to benchmarks ships or simple geometries.

What's more, it is possible to measure data such as the position of free surface and velocity fields near the free surface at pre-breaking stages via experimental observation, but hard to measure when wave breaking occurs. The measurement of small-scale phenomena, such as water droplets and air bubbles, is a huge challenge in the experiments. Though techniques develop, it is presently impossible to obtain velocity information of the air phase.

2.2.3 Numerical simulations

A review of numerical research on bow waves is presented. Good solvers are required to investigate the complex interaction between bow waves and incident waves. Many technologies have been applied to analyse bow waves statistically, and satisfactory progress has been achieved recently. For example, many investigation has been conducted on the diffraction of bow waves when the ship has a constant advancing speed [23][24][25].

Dommermuth et al. [26] simulated the flow with spilling breaking around a ship model by using an immersive body and volumetric methods. A high-resolution direct numerical simulation (DNS) of the Navier-Stokes equation is applied to capture unsteady breaking waves. The findings reveal that vorticity and surface tension have a significant effect in wave breaking strength.

Carrica et al. [27] used the RANS approach to numerically analyse the forward diffraction problem using the RANS approach. A mixed turbulence model is used to simulate the turbulent viscosity and the level set method is used to describe the free surface. According to the flow analysis, the wave force can cause nonlinear behaviour of the free surface. The RANS approach was used by Olivieri et al. [2] to analyse the vortices formed by wave breaking.

Colagrossi and Landrini [28] and Marrone et al. [29] investigated the wave pattern generated by a fast ship with a fine bow by a 2D+t SPH mode. The smoothed particle hydrodynamics (SPH) model is used to model the free surface. The 2D+t method simulates the shape of the bow waves by approximating the ship motion by a mathematically equivalent set of equations and governing the abnormal 2D free-surface flow generated by the deformable body on a vertical plane across the ship. RANS or DNS model can be used to realistically model complex processes. Each computation, however, takes time.

In[30], the wave breaking mechanism and small scale features of ship bow waves are numerically investigated through the flows around a wedge-shaped bow. Broglia et al.[20] carried out simultiaons on breaking wave at the bow of a fast displacement ship model and compared their results with the experimental data [19]. However, the small-scale interface structures were not captured, since a single-phase level set method was used for the free surface tracking. The mechanism of the liquid sheet disturbance, fingering, pinching off droplets and spray production has yet to be fully investigated. The study [19] was selected as test cases to validate the capability of the code of CFD Ship-Iowa Version 6 [31][32] for small scale features of ship bow waves. A Cartesian grid solver is first used for the two-phase flow simulation with coupled level set and volume-of-fluid (CLSVOF) to track the free surface and immersed boundaries methods for fluid-structure interface. An orthogonal curvilinear grid solver [33] is also proposed in order to increase the grid resolutions near the wall.

2.3 Trends and limitations

No matter what kind of breaking wave it is, the key point and the challenge of the simulation of bow breaking waves is the need to resolve the flow of two phases, i.e. air and water, and the evolution of the interface between them. The focus of recent research has been to improve hydrodynamic tools. Various free surface simulation methods are available, but these tools have their own limitations. The research trends and limitations are analyzed below.

(a) Interface conditions

Air-water interface modelling must satisfy kinematic and dynamic constraints[1]. The kinematic constraint requires that the particles on the interface to stay on the interface, and the dynamic conditions require stress to be applied continuously across the interface. The stress on the interface is mainly composed of viscous stresses and surface tension. The latter is usually neglected for many ship hydrodynamics applications.

(b) Interface representation

One fundamental question for interface modelling is the indication and description of the interface. The SPH [28]method identifies phase information by particles of specified physical properties and there is no need to track the interface explicitly. The particle density is therefore used as an indicator function to determine the position of interface while specifying surface tension. Compared to the SPH method, Lagrangian interface tracking methods such as front tracking method or marker point tracking method can give an accurate interface position. However, a field function is still required within the flow field to identify the phase information at each location[34]. Eulerian methods such as Volume of Fluid (VOF), level set (LS) and phase field methods only provide the indicator functions at each point or each cell, while the interface location is implicitly embedded in the flow field.

The treatment of the air-water interface is another key point in air-water interface modelling. The interface should be treated as a transition zone with a finite thickness or a sharp interface with zero thickness. Different choice leads to different mathematical formulations and the numerical strategies for solving the two-phase flow. This choice refers to the variation of physical properties such as density and viscosity of the fluids across the interface. The surface tension, on the other hand, can also be treated in both sharp and diffusive interface manners, despite the fact that the specific treatments are not directly related to the mathematical approximation of jumps in the fluid physical properties. Detailed discussion of interface capturing methods is given in the section 2.4.

(c) Requirements of Free-surface flow solution

The modelling of viscous free surface flow is a subject that has reached a certain maturity and has been used in engineering applications. Many of these methods are being used with success. However, for the simulation of bow breaking waves, there are some important requirements for numerical solvers.

Some of the earlier results[18] [20] [11] of free surface flow around ships contained different wave profiles from the experimental observations in the predicted wave pattern that exceeded the viscous effects on that pattern or dominated the computed scale effects. Even now, several methods exist that are unable to reliably forecast these aspects. In particular, the need to function properly at full scale, for Reynolds numbers (depending on ship length and speed) up to 5e9, is particularly difficult to meet.

In addition, the solution must be robust with respect to breaking waves. The method should not break down when wave breaking occurs, either as plunging breakers appearing at sharp bows or as

spilling breakers at blunt bow flow. The importance of these aspects increases for high-speed ships with a sharp bow where stronger breaking occurs.

2.4 Air-water interface modelling

During the last thirty years, much progress has been made in the development of robust and accurate computational algorithms capable to predict two-phase flows with both viscous and turbulent effects. While this development continues unabated, the application of these strategies to full-complexity real-life problems is entering industrial practice. In ship and ocean engineering, the accurate prediction of highly nonlinear free-surface flows and the related impact loads by the fluids is very important in various applications including high waves, liquid sloshing, bow/deck slamming, or green water. Due to the complexity of fully nonlinear free-surface and body boundary conditions, numerical treatment of this type of highly nonlinear free-surface behaviour is usually very difficult and challenging. The most challenging task is capturing the free surface in case of extremely violent motions, such as overturning, plunging, and splashing.

The fluids involved in ship hydrodynamic are water and air. In general, they can be treated as Newtonian fluids. The bow wave breaking phenomena can also be considered as incompressible due to usually very low Mach numbers. Therefore, the governing equations for ship flow are the incompressible Navier-Stokes equations. Solvers for ship flows are categorized based on the solution methods for the two different fluids involved in as: (1) One-phase flow solvers and (2) Two-phase flow solvers. In one-phase flow solvers, only the water phase is solved using atmosphere pressure boundary condition at the free-surface while in the two-phase flow solvers, both air and water phases are solved using one-fluid formulation.

2.4.1 One-phase flow solvers

In free-surface flow solvers or one-phase flow solvers, only the water phase is solved while the effect of air to water is simplified as atmospheric pressure boundary condition at the free surface. Many ship hydrodynamics solvers have adopted this mathematical models, for example, CFDShip-Iowa version 3[35] and 4 [36] from IIHR, xship [37] from INSEAN, SURF [3] from NMRI, PARNASSO [38] from MARIN, ICARE [39] from ECN/HOE, WISDAM [23] from the University of Tokyo, among others. These solvers are applicable in a wide range of applications, since the water phase accounts for most resistance. However, most of these solvers are not capable of solving problems with wave breaking and air entrainment. When a one-phase method is applied to flows with bow wave breaking of a blunt ship, it is observed that numerical solutions fail to predict wave breaking accurately in some case[40].

In one-phase solvers, surface tracking method are often used cause only the water is considered in the computational domain. The position of free surface is defined by massless particles. Marker-and-Cell method proposed by Harlow and Welch[41] is one of the earliest attempts to employ massless particles. In this method, massless particles are distributed all over the computational domain, move with the underlying flow and are used to identify each phase as a single fluid. The interface is reconstructed based on the position of these particles. More recently, Unverdi and Tryggvason[42] have proposed a front-tracking method. Massless particles that are distributed over the interface is used to explicitly track the surface. Front tracking methods is proved to be accurate in their cases. However, re-gridding algorithm must be employed in order to prevent the clustering or the rarefaction of marker particles. Moreover, special care is required when dealing with an interface that changes in topology, for instance, in the case of a free surface that breaks and/or merges[34].

Besides surface tracking methods, one of surface capturing method, i.e., single-phase Level Set methods is also used in one-phase flow solvers. Foster and Fedkiw [43] simulated the 3D free surface flow around simple geometries. Carrica et al. [27][36] applied unsteady single-phase Level Set to the study of the forward speed diffraction problem and unsteady viscous free surface flow around a combatant ship. In the single Level Set approach, the solution is computed only in the liquid phase. The gas phase being computed only for numerical reasons. The single-phase Level Set is not suitable neither for problems with air entrainment or bubbles, nor for problems where stresses on the free surface due to air play an important role[37].

Even though the one-phase solvers fail to describe the evolution of free surface, Rhee and Stern [11] proposed a RANS model for spilling breaking waves, modelling the breaking effects on the underlying flow as a whole, therefore renouncing the description of flow details within the foamy turbulent mass of fluid. The dynamic free surface condition is then modified with the C&T models. Similar models can also be found in [44][45] for breakers in surf zone. It is was worth to mark that these models can only simulate the evolution of waves and the effects on flow beneath the free surface to some extent. The investigation for the mechanism of breaking wave is still not clear especially for plunging breaking waves.

The breaking wave phenomenon is a challenging problem for mathematical modelling. It is strongly unsteady, is a two-phase flow and air entrainment cannot be neglected. Although larger computer resource is required, an accurate description of air-water interface is essential with both air and water considered.

2.4.2 Two-phase flow solvers

In the two-phase solvers, both the air and water phase are solved in a coupled manner, which requires treatment of density and viscosity jump at the interface[33]. The two-phase flow solvers are more common in commercial codes such as FLUENT [46], CFX [47], STAR-CCM+[48] and open-source CFD platform OpenFOAM [49], as they are more general tools for a wide range of application. Compare to one-phase solvers, they are less computational efficient due to high total grid resolution requirement for resolving the air flow besides the water flow. Two-phase flow simulations are of interest in many applications, in particular, wind generated waves, breaking waves, and bubbly wakes, among others[1].

Theoretically, it is possible to solve each phase separately and couple the solutions at the interface. However, mentioned above, this approach is only practicable for cases with mild, non-breaking free surface or a very limited number of non-breaking air bubbles or water droplets. Most two-phase flow solvers for practical applications apply a one-field formulation and a single set of governing equations is used to describe the fluid motion of both phases. In a one-field formulation, each phase needs to be identified using a marker or indicator function. Surface tension at the interface becomes a singular field force in the flow field rather than a boundary condition in the phase-separated solvers. Several numerical methods have been developed over the past decades for the air-water interface modelling. Among them, the level set (LS), volume of fluid (VOF) and the coupled level set and volume of fluid (CLSVOF) methods have been widely employed for interface capturing in ship and ocean engineering. Large distortions and geometrical changes are allowed in the simulations with these three methods.

(a) Level set methods.

Level set methods is first induced by Osher and Sethian[50]. In LS methods, the interface is implicitly represented by the LS function which is defined as a signed distance function. The level set function can be considered as a general scalar and its advection equation can be solved using similar temporal and spatial discretization schemes to those of the single-phase flow. Geometrical information such as interface normal and curvature is easily derived from the continuous and smooth distance function[33]. These advantages have boosted its applications in many CFD fields including ship and ocean engineering. However, the level set advection equation does not impose a volume constraint in course of level set evolution and makes the mass conservation a serious concern in level set methods.

Many schemes have been developed for possible improvements, such as the particle level set methods[51] [4], coupled level set and volume of fluid methods[31][52]. Some studies chose

different definitions of the level set function, for instance in[53] a smoothed Heaviside function was used with value 0–1 across the interface at iso-level 0.5, instead of a signed distance function. Although they were named level set techniques since a reinitialization step was still required, they are similar to other methods that establish a smoothed transition band between different phases such as phase field, constrained interpolated propagation [54], and colour function methods.

Level set methods represent the surface as the zero contour of a level set function ϕ： $R^N \to R$. In the domain enclosed by the surface, one has $\phi < 0$, while outside $\phi > 0$. Geometric quantities, such as normal vectors and curvature, can be obtained from the level set function: $\vec{n} = \nabla\phi/|\nabla\phi|$ and $\kappa = \nabla\vec{n}$. In order to move the surface with a velocity field, the level set function is advected according to the partial differential equation:

$$\phi_t + \vec{u} \cdot \nabla\phi = 0 \tag{2-1}$$

The level set function can be defined on a regular grid. High order ENO[55] or WENO[56] schemes are commonly used to approximate the equation.

Gradients and curvatures can be approximated by finite differences. For an accurate and stable approximation, it is beneficial if ϕ is a signed distance function.

$$|\nabla\phi(x)| = 1 \tag{2-2}$$

Even if ϕ is a distance function initially, it typically ceases to be so due to deformations induced by the velocity field. One remedy to this problem is to recover the sign distance function by solving the re-initialization equation

$$\phi_\tau = \text{sign}(\phi_0)(1 - \nabla\phi) \tag{2-3}$$

(b) Volume of fluid methods.

The Volume of fluid method was first proposed by Hirt and Nichols [57]. The flow equations are volume averaged directly to obtain single set of equations and the interface is tracked using a phase indicator function (or colour function or volume fraction).

In the volume of fluid method, the interface is tracked using a phase indicator function F (F ∈ [0,1]), if F=1, control volume is filled with phase 1, if F=0, control volume is filled with phase 2, if 0<F<1, interface present). At each time step, the free surface is constructed by geometric solution using by the volume ratio and then the volume functions F are obtained by solving the transport equation of the volume ratio according to the reconstructed free surface.

The control differential equation for F is:

$$\frac{\partial F}{\partial t} + \nabla \cdot (F\vec{u}) = 0 \tag{2-4}$$

The above equation is the transport process of the fluid volume function, and its calculation accuracy directly affects the fineness of the free surface. Since F is a step function, the control equation is purely a convection equation. If the solution method is not correct, it directly results in a larger error or even divergence. Two critical issues with the VOF method are (i) interface reconstruction and (ii) Calculation of the volume function and solution of advection transport equations.

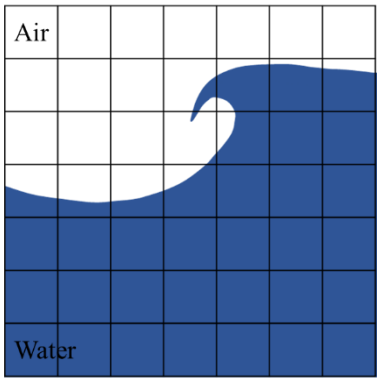

Figure 2-3 Real free surface of a typical plunging breaking wave

0	0	0	0	0	0	0
0	0	0	0.1	0.8	0.9	0.8
0	0	0	0	0.7	1	1
0.5	0.4	0.4	0.6	1	1	1
1	1	1	1	1	1	1
1	1	1	1	1	1	1
1	1	1	1	1	1	1

Figure 2-4 Volume fraction α distribution with the VOF methods

In VOF methods, the interface is indirectly represented by a numerical field that describes the volume fraction of water within each computational cell. The basic idea of VOF methods is to calculate how much water is floating over the faces between adjacent cells within each time step[1]. According to the way of reconstruction of interface, the VOF methods can be divided into two parts: 1) geometric VOF methods, using geometric operations to reconstruct the fluid interface inside a cell and to approximate the water fluxes across faces, and 2) algebraic VOF methods, relying on the limiter concept to blend first and higher order schemes in order to retain sharpness and boundedness of the time advanced VOF field[58]. Geometric VOF schemes are typically much more

accurate, but also computationally more expensive, more difficult to implement, and limited to particular types of computational meshes, such as hexahedral meshes. Algebraic VOF methods, on the other hand, are less precise, but they are usually quicker, simpler to implement, and designed for a wider range of mesh types[59].

In the geometrical VOF methods, the volume function is directly advected, but a special interface reconstruction process is required because of the sharp jump in the marker function across the interface. Due to the discontinuous volume function, it is difficult to obtain accurate geometric information such as interface normal and curvature. Therefore, VOF methods combined with a level set function can be quite useful to solve this problem. Wang et al.[33] proposed a new VOF method with a distance function constructed from the VOF function, and greatly expands the applications of the VOF method. Further improvements on VOF methods have been investigated through tracking additional information such as the material centroids in the moment of fluid method[60]. Recently Sussman's group coupled the level set method with the moment of fluid method[61]. It is also possible to couple front tracking methods with the VOF methods such as in [62]. Of course, these approaches are more complicated compared with the level set and algebraic VOF methods, but they reduce interface position errors than the algebraic VOF methods and improve mass conservation properties than the level set methods.

Compare to the geometric VOF methods, the algebraic VOF methods have a wider application for both structured and unstructured mesh. The algebraic VOF schemes implemented in OpenFOAM are representative examples. A major problem of these schemes is the blurred interface. Very high resolution is required when capturing small-scale air-water interaction phenomena such as water droplets and air bubbles. Convection term discrete format is the key to solve the volume fraction convection equation. Since the liquid surface separates the gas-liquid two-phase medium, the volume fraction flux function is a discontinuous function, and the numerical dissipation will quickly mix the two-phase medium which may form a certain thickness of the transition layer around the interface, make it difficult to keep the interface sharp and even lead to loss of mass. Higher order schemes are unstable and result in numerical oscillations while lower order schemes like the first order upwind method tend to smear the interface owing to numerical diffusion. It is necessary to derive advection schemes that can maintain the sharpness of interface and provide monotonic profiles of the volume function.

(c) Coupled level set and volume of fluid methods.

A Coupled Level Set and Volume of Fluid (CLSVOF) method was proposed by Sussman and Puckett [52] and explored in [31][63][52]. It applies VOF to calculate the transport-diffusion equation to ensure mass conservation and uses a set method to calculate the normal direction, curvature and

physical quantities relating to the curvature. The interface is reconstructed via a geometric VOF scheme and the interface normal vector which is computed from the LS function. Based on the reconstructed interface, the LS functions are re-distanced via a geometric procedure for achieving mass conservation.

Mass is conserved while still maintaining a sharp representation of the interface by representing the free surface as volume fractions. However, it is difficult to compute accurate local curvatures from volume fractions. Too much smoothing has the effect of making the curvature constant along the free surface. In the CLSVOF method, no smoothing of the curvature is done, instead the curvature is obtained via finite differences of the level set function which in turn is derived from the level set function and volume-of-fluid function at the previous time step.

2.5 Challenges for two-phase flow solvers

Bow wave breaking has been a difficult phenomenon to model theoretically because the bow wave changes continuously through the interaction of air and water with significant differences in properties. It requires accurate simulations owing to ship resistance estimation, wake elimination and ship safety. According to the literature review, on the three interface capturing methods mentioned above, at least the four factors listed below are critical to the accuracy of two-phase flow solvers.

2.5.1 Accurate interface representation and advection

The interface location, its normal and curvature are known only implicitly in the framework of implicit interface capturing methods, as they are derived from the underlying colour function. In the VOF methods, for example, the interface is defined by a discontinuous change in the volume fractions. The difficulties related to its advection have been analysed in the literature above. Excessive diffusion of the interface is known to occur with VOF methods, which is highly undesirable in numerical simulations. Such a diffusion is a result of naïve advection of the underlying, discontinuous VOF function for either geometrical or algebraic VOF methods.

Aside from precise advection of the VOF function, difficulties arise in the estimation of interface normal and curvature, due to the discontinuous nature of the volume fraction field, and in this regard, several alternatives, including smoothing of the volume fraction field [64] and construction of height function [65]. While these methods appear to perform well in mildly behaved test cases, several authors [66][67] have indicated that these methods also become error-prone in high-curvature or poorly resolved regions.

2.5.2 Mass conservation

It is difficult to maintain a sharp and accurate interface with VOF methods. Accurate representation of the interfacial quantities can be obtained by the level set methods. This is especially advantageous in two-phase flows with surface tension effects. However, a well-known disadvantages of this approach has been that mass conservation is not embedded in the level set formulation[68]. As a result, high-curvature or poorly resolved regions of the flow are typically prone to lose or gain mass during the simulations. Significant improvements have been made in this regard through the development of techniques mentioned in section 2.4.2. Another pending issue that has yet to be resolved is the loss of signed distance property owing to advection issues. An extra re-initialization operation is required[68][69] to restore property of signed distance function. This not only increased the computational cost, but also causing an artificial displacement of the interface which results in mass loss/gain[4].

2.5.3 Spurious currents

Almost all the implicit interface capturing methods are known to be generate unphysical flow at the interface solely due to numerical inadequacies. The inaccurate interface curvature, and the discontinuities in material properties, especially in high-density ratio are the two main sources of spurious velocities. The first one is related to surface-tension-dominated flow, while the latter related to momentum transport equations which is a major issue in inertia-dominated flows. For the first source of spurious currents, five kinds of strategies have been employed to mitigate this shortcoming.

(1) Improvements to curvature estimation[70][71];

(2) Ensuring a discrete balance between pressure gradient and surface tension[70][72][73];

(3) Sharp representation of the interface using ghost fluid approach in conjunction with accurate curvature estimation[74][75];

(4) Time resolution of capillary flow generated at the stair-stepped interface in an explicit implementation of the surface tension[76];

(5) Temporally semi-implicit treatment of surface tension[77].

The generation of spurious velocity is one of the major issues for surface-tension-dominated flows. It poses serious concerns in the computation of capillary flows, which generally affect the small liquid structures in hydrodynamic flows involving wave breaking.

2.5.4 Handling large density ratios

Several strategies have been employed to mitigate the errors caused by the surface tension force [70][76][78], while less solutions are proposed to handle the discontinuities in the flow with high-density ratios. Rudman [79] tried to solve this problem by using a VOF density-based flux correction scheme to calculate the momentum convection term, and Raessi [80] adopted this strategy for level set methods. It is shown to slightly improve the result of numerical simulations, but spurious interface deformations still exist [81]. Another potential solution to this density-jump problem is to use a Ghost Fluid Method (GFM) [75][82][83][84]. Artificial fluid cells are introduced to implicitly capture the jump condition across the interface without any transition thickness between the two phases. Two additional distinct velocity fields are defined across the whole domain for the two phases separately and reconnected though a pressure jump condition. It is proved that a GFM helps to eliminate the spurious oscillation and minimize numerical smearing near the interface. However, these additional velocity fields give rise to further problems. Having an interfacial velocity separate from the fluid velocity with a velocity jump condition has its own stability problems, and more computational resources are required as the complexity of the two-phase flow solver increases [85].

Apart from the problem of solving continuity and momentum equations, the free-surface boundary layer is not resolved in all implicit interface capturing methods at high Reynolds numbers with large density jumps between air and water[5]. A numerical breakdown is associated with the jump that occurs in the tangential velocity across the free surface. As a result, unphysical tearing tends to occur even with high-order advection schemes. In reality, there is a viscous boundary layer that makes the transition from the water velocity slightly beneath the free surface to the air velocity slightly above the free surface. Smoothing and/or filtering are required to reduce the jump in the tangential velocity that occurs at the free-surface interface. Fu et al. [86]used a density weighted velocity smoother to simply push the water particle velocity into the air. A more robust and physics-based solution is required to resemble the viscous boundary layer near the air-water interface.

2.6 Conclusion

The existing literature on experimental and numerical studies of the bow wave breaking has been reviewed. Bow wave breaking has been a difficult phenomenon to model theoretically because the bow wave changes continuously through the interaction of air and water with significant differences in properties. It requires accurate simulations owing to ship resistance estimation, wake elimination and ship safety.

Experimental measurements are the most reliable method to evaluate bow wave breaking. However, it is difficult to measure the bow flow for all ships experimentally. Experiments to measure bow breaking waves depend on experimental conditions and involve time-consuming procedures for test preparation. What's more, due to the techniques, the experimental measurements can be only be done in the water region and the detailed description of the flow in the energetic wave breaking region is not available.

Numerical studies are suitable as alternatives to experimental measurements. With the development of computer performance, detailed wave breaking processes and velocity profile can be obtained in both water and air phases in CFD simulations, however, the results can be uncertain and artificial. The trend of recent research is to improve hydrodynamic tools with accurate prescription and prediction of air-water interface behaviour.

The review also focused on the air-water interface modelling. Various air-water interface tracking/capturing methods have been compared and discussed. One-phase flow solvers are more efficient since only the water phase is considered in computation. However, the effect of air is neglected, and the numerical solution usually fails to predict wave breaking accurately. Two-phase solvers solve both the air and water phase in a coupled manner and are more suitable for breaking wave simulations. The three most common-used interface capturing methods Level Set, VOF and CLSVOF have different ways to represent the interface but share same challenges when dealing with the air-water interface conditions as two-phase flow solvers. The free-surface boundary layer is not resolved in all implicit interface capturing methods at high Reynolds numbers with large density jumps between air and water. As a result, spurious currents and unphysical tearing tends to appear near the interface.

A physics-based viscous air-water boundary layer model is required to be developed and applied to VOF methods to deal with the discontinuity in the fluid properties over the two-phase interface and to offer a better resolution of the free-surface. The thickness of air-water boundary and how the air velocity at the interface driven by the water velocity needs to be studied and discussed. The developed the free-surface capturing method helps to improve the accuracy of simulations of breaking waves.

Chapter 3 Free-surface boundary conditions

3.1 Introduction

Despite the popularity of two-phase flow solvers, the three most commonly used interface capturing methods have different ways to represent the interface and share similar challenges when dealing with two-phase interface conditions. The boundary layer thickness on both phases is much smaller than the mesh size that is usually generated near the moving interface. The interface boundary layer is not well resolved in all implicit interface capturing methods, and unphysical flow tends to be generated at the interface due to the numerical inadequacies. The inaccurate interface curvature, and the discontinuities in material properties, especially in high-density ratio are the two main sources of spurious velocities. The first one is related to surface-tension-dominated flow, while the latter related to momentum transport equations which is a major issue in inertia-dominated flows. Conventional linear momentum flux interpolation practices can lead to significant errors, which cause 'fake' momentum and numerical instability when the density ratio increases and ultimately results in spurious velocities and spurious shear near the interface [81]. For the two-phase flow problems with strong gas-liquid interface interactions, such as rain, atomization, ink-jet printing and breaking waves in ship and ocean engineering, better strategies are required to deal with accurate liquid-gas interface tracking and the discontinuous fluid properties across the interface.

Several strategies have been employed to mitigate the errors caused by the surface tension force [70][76][78], while less solutions are proposed to handle the discontinuities in the flow with high-density ratios. Rudman [79] tried to solve this problem by using a VOF density-based flux correction scheme to calculate the momentum convection term and Raessi [80] adopted this strategy for level set methods. It is shown to slightly improve the result of numerical simulations, but spurious interface deformations still exist [81].

Another potential solution to this density-jump problem is to use a Ghost Fluid Method (GFM) [75][82][83]. Artificial fluid cells are introduced to implicitly capture the jump condition across the interface without any transition thickness between the two phases. Two additional distinct velocity fields are defined across the whole domain for the two phases separately and reconnected though a pressure jump condition. It is proved that a GFM helps to eliminate the spurious oscillation and minimize numerical smearing near the interface. However, these additional velocity fields give rise to further problems. Having an interfacial velocity separate from the fluid velocity with a velocity

jump condition has its own stability problems and more computational resources are required as the complexity of the two-phase flow solver increases [85].

In this chapter, a combined volume of fluid and immersed boundary method is proposed to deal with high-density ratio flows. This method is developed from the Immersed Boundary (IB) Method which is initially introduced to enforce jump/boundary conditions at solid-fluid interfaces when simulating flows around moving solid bodies on fixed Cartesian grids [32]. The solid boundary may cut through the grids, so the boundary conditions are imposed by modifying the governing equations near the interface. A similar strategy is here adopted for a two-phase flow solver and combined with a VOF method to improve the robustness and accuracy of high-density ratio two-phase flow simulations.

3.2 Navier-Stokes equations

The governing equations for the two-dimensional (2D) incompressible viscous flow are the Navier-Stokes equations:

$$\nabla \cdot \mathbf{u} = 0, \tag{3-1}$$

$$\frac{\partial \rho \mathbf{u}}{\partial t} + \nabla \cdot (\rho \mathbf{u}\mathbf{u}) = -\nabla p + \nabla \cdot (\mu \rho \nabla \mathbf{u}) + \mathbf{g}\rho, \tag{3-2}$$

where **u** is the velocity vector with components of the velocity (u, v) in the x-, y-direction, respectively, and t, p, ρ, μ and **g** are the time, the pressure, the density, the dynamic viscosity coefficient and gravitational acceleration, respectively.

A finite volume method (FVM) is used to discretize the Navier-Stokes equations on a fixed Cartesian coordinate system on a mesh. All dependent variables are defined at cell centres and a collocated variable arrangement is used.

For spatial discretization, the generalized form of Gauss's theorem [87] is used throughout the discretization procedure:

$$(\nabla \cdot \mathbf{a})V_p = \sum_f \mathbf{S} \cdot \mathbf{a}_f, \tag{3-3}$$

where V_p is the volume of the cell, **a** is a vector variable, the subscript f implies the value of the variable in the middle of the face, and **S** is the outward-pointing face area vector. The discretization of a convection term of any scalar property ϕ is obtained by:

$$\int_{V_p} \nabla \cdot (\rho \mathbf{u}\phi)\, dV = \sum_f \mathbf{S} \cdot (\rho \mathbf{u}\phi)_f = \sum_f \mathbf{S} \cdot (\rho \mathbf{u})_f \phi_f. \tag{3-4}$$

The spatial discretization is defined by specifying the interpolation of face values from averaged values stored in the central volumes [88]. The discretization becomes more and more challenging as the density ratio increases. These face mass fluxes ($F = \mathbf{S} \cdot (\rho \mathbf{u})_f$) are calculated from the interpolated values of ρ and $\mathbf{u}$, which is not straightforward because of the discontinuous gradients of both density and velocity. The numerical instabilities could be one of the sources of spurious velocities seen near the surface.

Another cause of the spurious velocity coming from the momentum equation is the imbalance between pressure gradient and density gradient [83]. Consider a hydrostatic case and neglect the viscous term, the momentum equation can be written as:

$$\frac{\partial \mathbf{u}}{\partial t} = -\frac{1}{\rho}\nabla p + \mathbf{g}. \tag{3-5}$$

This equation becomes ill-conditioned because of the density which changes discontinuously from one phase to another with the volume fraction on the right-hand side of the equation [81]. The errors causing from the imbalance between pressure gradient and density gradient result in spurious velocities near the interface. The spurious velocity is larger in the lighter phase as the spurious pressure is the same across the interface. Furthermore, the resulting spurious velocity acts as a source of disturbance in velocity fields, and, accumulated over time, generates vorticity, especially in the lighter phase and ultimately affect the velocity field in the heavier phase as well.

3.3 Free surface modelling

3.3.1 Volume of Fluid method

Two-phase flows are considered as two incompressible, isothermal and immiscible fluids [49]. An algebraic VOF method is used to capture and represent the dynamic behaviours of the interface between the two phases. Defining a volume fraction α as the relative proportion of water in each cell, the position of the interface can be tracked by solving the VOF evolution equation:

$$\frac{\partial \alpha}{\partial t} + \nabla \cdot (\mathbf{u}\alpha) = 0. \tag{3-6}$$

If $\alpha = 1$, the cell is full of phase 1 and if $\alpha = 0$, the cell is full of phase 2, and in any other case the cell contains the interface between the two phases. The unit normal vector, $\mathbf{n}$, and the local curvature, κ, are defined as

$$\mathbf{n} = \frac{\nabla \alpha}{|\nabla \alpha|}, \tag{3-7}$$

and

$$\kappa = \nabla \cdot \mathbf{n} = \nabla \cdot \frac{\nabla \alpha}{|\nabla \alpha|}. \tag{3-8}$$

In a VOF method, the two immiscible fluids are considered as one effective fluid throughout the domain. The physical properties, density and viscosity, are defined by the volume fraction α:

$$\rho = \rho_1 \alpha + \rho_2 (1 - \alpha), \tag{3-9}$$

$$\mu = \mu_1 \alpha + \mu_2 (1 - \alpha). \tag{3-10}$$

One of the critical issues in numerical simulations of two-phase flows using VOF models is the discontinuity of the volume fraction α [89]. This discontinuity not only gives rise to the difficulties in sharp interfacial shape and geometrical properties such as curvatures, but also results in sharp jumps of fluid properties, such as momentum flux and density gradient. Small errors in calculation of the volume fraction and related gradient or divergency terms can cause significant errors near the interface in simulations, especially for cases with high-density ratios. Special treatment is required to resolve the boundary layer near the interface and to eliminate the errors caused by the discontinuous volume fraction.

A Multidimensional universal Limiter of Explicit Solution (MULES) method [49] is used to resolve the VOF equation. An artificial term $\mathbf{u}_r$ is added into the VOF evolution equation to limit the amount of interface smearing:

$$\frac{\partial \alpha}{\partial t} + \nabla \cdot (\mathbf{u}\alpha) - \nabla \cdot \left(\mathbf{u}_r \alpha (1 - \alpha)\right) = 0, \tag{3-11}$$

$$\mathbf{u}_r = \mathbf{n}_f \min\left[C_\gamma \frac{|F|}{|\mathbf{s}_f|}, \max\left(\frac{|F|}{|\mathbf{s}_f|}\right)\right], \tag{3-12}$$

where $\mathbf{u}_r$ is the artificial compressible velocity that applies only near the interface, $\mathbf{n}_f$ is the normal vector of the cell surface, F is the mass flux, and C_γ is a constant scalar parameter controlling the intensity of the interface compression. In general, this artificial compressibility has no physical meaning and is designed to limit the numerical diffusion near the interface and hence sharpen the interface. The extent of the artificial compression velocity depends on the value of C_γ. If $C_\gamma = 0$, there is no compression, if C_γ=1, there is a conservative compression and if $C_\gamma > 1$, there is an enhanced compression [59].

3.3.2 Surface tension

The momentum equation is modified to account for the effects of surface tension. The surface tension at the liquid-gas interface generates an additional pressure gradient resulting in a force, which is evaluated per unit volume using the continuum surface force (CSF) model[71].

$$\mathbf{f}_b = \sigma \kappa \nabla \gamma \tag{3-13}$$

This equation is only valid for the cases with constant surface tension, as considered here. In the case of variable surface tension, e.g., due to nonuniformly distributed temperature, surface tension gradients are encountered, generating an additional shear stress at the interface, which should be considered.

Both fluids are considered to be Newtonian and incompressible $\nabla \cdot \mathbf{U}$=0, and the rate of strain tensor is linearly related to the stress tensor, which is decomposed into a more convenient form for discretization,

$$\nabla \cdot \mathbf{T} = [\mu \nabla \mathbf{U} + (\nabla \mathbf{U})^{\mathrm{T}}] = \nabla \cdot (\mu \nabla \mathbf{U}) + (\nabla \mathbf{U}) \cdot \nabla \mu \tag{3-14}$$

In a single pressure system as considered for the present VOF method, the normal component of the pressure gradient at a stationary nonvertical solid wall, with no-slip condition on velocity, must be different for each phase due to the hydrostatic component *ρg* when the phases are separated at the wall, i.e., if a contact line exists. In order to simplify the definition of boundary conditions, it is common to define a modified pressure as

$$p_d = p - \rho \mathbf{g} \cdot \mathbf{x} \tag{3-15}$$

where $\mathbf{x}$ is the position vector. It can be easily show that the gradient of modified pressure p_d of the static pressure gradient, the body force due to gravity and an additional contribution originating from the density gradient. In order to satisfy the momentum equation, the pressure gradient is expressed whereas the momentum equation is rearranged:

$$\frac{\partial(\rho \mathbf{U})}{\partial t} + \nabla \cdot (\rho \mathbf{U}\mathbf{U}) - \nabla \cdot (\mu \nabla \mathbf{U}) - (\nabla \mathbf{U}) \cdot \nabla \mu = -\nabla p_d - \mathbf{g} \cdot \mathbf{x} \nabla \rho + \sigma \kappa \nabla \gamma \tag{3-16}$$

Body forces due to pressure gradient and gravity are implicitly accounted for by the first two terms on the right-hand side.

3.4 A combined volume of fluid and immersed boundary method

An IBVOF method is developed in the present study to deal with the spurious velocity near the interface caused by the high-density ratio between the two phases. An extra velocity field is designed to extend the velocity of the heavier phase onto the lighter phase and to enforce a new boundary condition near the interface which is similar to non-slip boundary conditions in Fluid-Structure interactions problems [90]. In the developed IBVOF method, there are three steps, i) identify the position of the interface and the phase state of the grid cells, ii) calculate the velocity on the lighter phase side by an extrapolated velocity approach, iii) update the velocity of both sides to satisfy the new boundary conditions on the interface. These steps are each described in detail. The present two-phase flow solver is developed using a Cartesian mesh. For convenience, the

governing equations, the methodology and discretisation scheme are illustrated here in 2D for simplicity though it can be extended to 3D simulations.

3.4.1 Identify the position of the interface

Accurately locating the position of the interface is a challenge in the algebraic VOF method since there is a narrow band of cells containing both two phases with $0 < \alpha < 1$. This band becomes wider when it comes to complex interface behaviours, such as breaking waves with white water. A cleaner definition needs to be set to distinguish the two phases. In this study, $\alpha = 0.5$ is used to identify the interface and to separate the two phases (see Figure 3-1). If α is not fixed, the further analysis is needed to identify the certain value for α in context of interface identification.

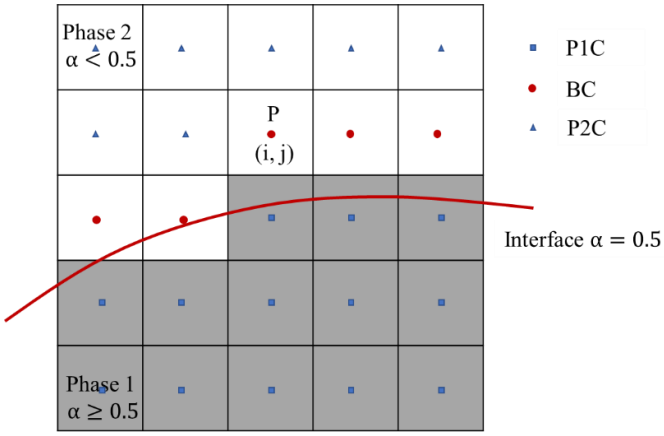

Figure 3-1 Phase state re-identification near the free surface.

(P1C: Phase 1 cells, BC: Boundary cells, P2C: Phase 2 cells)

In the present work, the boundary layer is designed only in the low density of the free surface phase side to ensure the accurate calculation of the heavier phase, since the lighter phase is more sensitive to the numerical instability and larger spurious velocities tend to be observed. Thus, for a uniform Cartesian grid system, the phase 1 cells, boundary layer cells and phase 2 cells are identified as:

(1) P1C: if $\alpha(i,j) \geq 0.5$;

(2) BC: if $\alpha(i,j) < 0.5$ and $(\alpha(i-1,j) \geq 0.5$ or $\alpha(i+1,j) \geq 0.5$ or $\alpha(i,j-1) \geq 0.5$ or $\alpha(i,j+1) \geq 0.5)$;

(3) P2C: if $\alpha(i,j) < 0.5$ and $(\alpha(i-1,j) < 0.5$ and $\alpha(i+1,j) < 0.5$ and $\alpha(i,j-1) < 0.5$ and $\alpha(i,j+1) < 0.5)$;

where (i, j) is the grid node represent the x- and y-direction position of the cell.

3.4.2 Extrapolated velocity approach

Once the boundary cells are identified, the next step is to build an extra velocity field for this boundary layer through an extrapolated velocity approach. The concept is first proposed by Sussan et al. [91] and used in [6] with a Level set method on a staggered grid. An extended version is adapted in the present work.

To initialize the process, the new velocity field $\mathbf{u}^{\boldsymbol{N}}(u_x^{\boldsymbol{N}}, u_y^{\boldsymbol{N}})$ is set equal to the momentum-equation-deduced velocity **u**.

$$\mathbf{u}^N = \mathbf{u} \tag{3-17}$$

For the boundary layer cells identified in section 3.4.1, the $\mathbf{u}^N$ is calculated by outwards extrapolation along the interface normal from phase 1 to phase 2. For example, the velocity $\mathbf{u}^N(i,j)$ at cell P(i,j) in Figure 3-1 is calculated by the following equation [6]:

$$\frac{\partial \mathbf{u}_{i,j}^N}{\partial \tau} + n_i \frac{\partial \mathbf{u}_{i,j}^N}{\partial x_i} = 0 \tag{3-18}$$

A forward Euler scheme is used for time discretization for this extrapolation in pseudo-time τ:

$$\frac{\mathbf{u}_{i,j}^{N\,n+1} - \mathbf{u}_{i,j}^{N\,n}}{\Delta\tau} = -\left(n_x \frac{\partial \mathbf{u}^N}{\partial x}\right)_{i,j}^n - \left(n_y \frac{\partial \mathbf{u}^N}{\partial y}\right)_{i,j}^n \tag{3-19}$$

where τ is pseudo time step and is set equal to $0.3\min(\Delta x, \Delta y)_{i,j}$, n_x and n_y are x- and y-components of interface normal vector. According to research in Xiao et al. [6], this requires 8 time-steps to reach steady state. A first order upwind scheme is adapted for spatial discretization:

$$\left(\frac{\partial \mathbf{u}^N}{\partial x}\right)_{i,j} = \begin{cases} \frac{\mathbf{u}_{i,j}^N - \mathbf{u}_{i-1,j}^N}{\Delta x} & if\ (n_x)_{i,j} > 0 \\ \frac{\mathbf{u}_{i+1,j}^N - \mathbf{u}_{i,j}^N}{\Delta x} & if\ (n_x)_{i,j} < 0 \end{cases} \tag{3-20}$$

$$\left(\frac{\partial \mathbf{u}^N}{\partial y}\right)_{i,j} = \begin{cases} \frac{\mathbf{u}_{i,j}^N - \mathbf{u}_{i,j-1}^N}{\Delta y} & if\ (n_y)_{i,j} > 0 \\ \frac{\mathbf{u}_{i,j+1}^N - \mathbf{u}_{i,j}^N}{\Delta y} & if\ (n_y)_{i,j} < 0 \end{cases} \tag{3-21}$$

3.4.3 Simple tests of the extrapolated liquids velocity approach

Three test cases are used here to check the velocity extrapolation approach. The initial velocity is given and is the only parameter that is modified. The volume function is not updated, and the momentum equations are not solved in this section. In case one and case two, shear flow is designed to check 1D and 2D performance. The velocity of gas is 10 times as liquid and parallel to the interface. In case three, a more general situation is set with a liquid droplet moving in a static gas field.

The initial velocity field are set as Figure 3-2, Figure 3-4 and Figure 3-6. Figure 3-3, Figure 3-5 and Figure 3-7 are the resulted velocity fields accordingly in which (a) are original velocity; (b) are modified velocity with just one pseudo-time step; (c) are modified velocity with 8 pseudo-time steps. As shown in the results, the velocity of one-cell thick layer on the gas side of the interface is modified and getting close to the velocity of liquid with the increase of pseudo-time step.

Case one

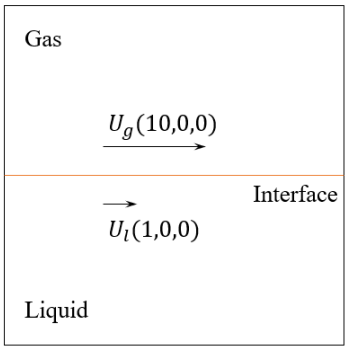

Figure 3-2 Initial velocity field for case one.

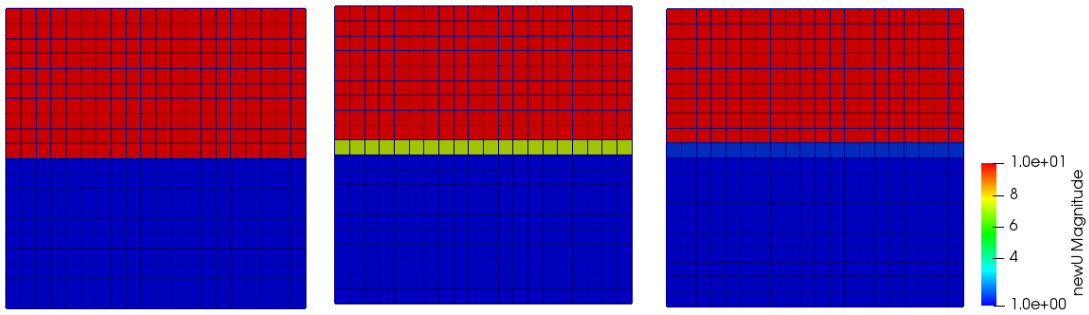

(a) U=(10, 0, 0) (b) NewU=(7.3, 0, 0) (c) NewU=(1.519, 0, 0)

Figure 3-3 Velocity field of case one. (a) Without modified; (b) Updated once; (c) Updated 8 times.

Case two

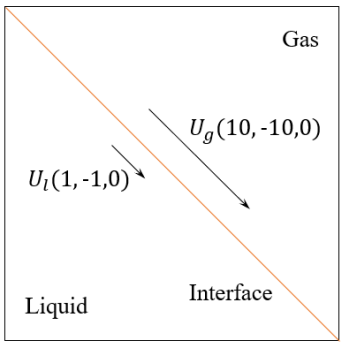

Figure 3-4 Initial velocity field for case two.

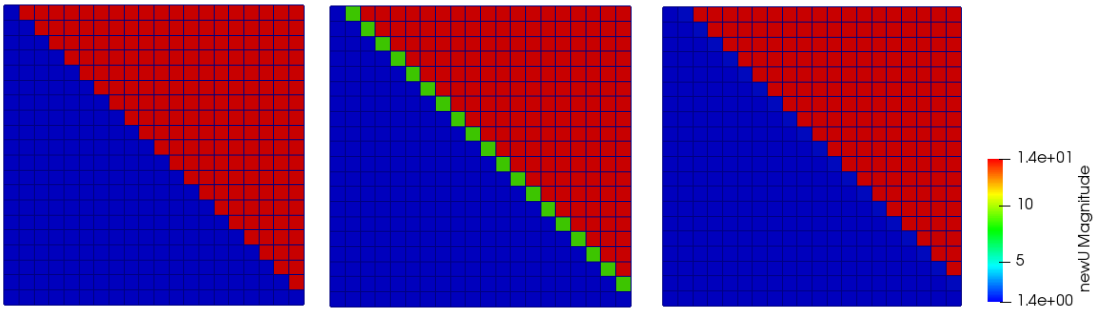

(a) U=(10, 0, 0) (b) NewU=(3.983, -3.983,0) (c) NewU=(1.109, -1.109, 0)

Figure 3-5 Velocity field of case two.

(a) Without modified; (b) Updated once; (c) Updated 8 times

Case three

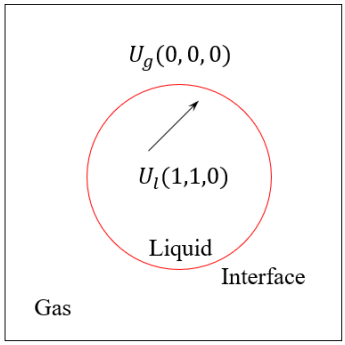

Figure 3-6 Initial velocity field for case three.

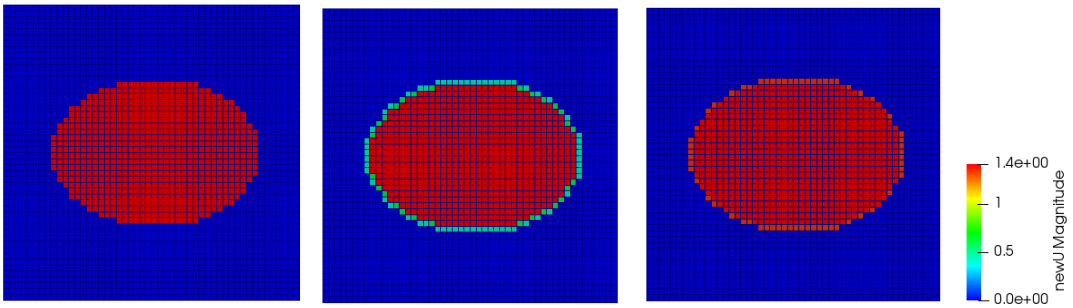

(a) U=(0, 0, 0) (b) NewU≈(0.4, 0.4, 0) (c) NewU≈(0.96, 0.96, 0)

Figure 3-7 Velocity field of case three.

(a) Without modified; (b) Updated once; (c) Updated 8 times

3.4.4 Direct forcing approach

A discrete forcing function, f_i, is added into the momentum equation to mimic the effect of the modified boundary on the phase 2 field.

$$\frac{\partial \rho \mathbf{u}}{\partial t} + \nabla \cdot (\rho \mathbf{u}\mathbf{u}) + \nabla p - \nabla \cdot (\mu \rho \nabla \mathbf{u}) - \mathbf{g}\rho = f_i \tag{3-22}$$

f_i is a body source in an IB method when imposing the boundary condition in fluid-structure interaction problems and now acts as a velocity corrector for the grids inside the identified boundary layer. When $f_i = 0$, Eq.3-22. is a normal momentum equation and a momentum-equation-deduced velocity $\mathbf{u}^*$ field is obtained. This velocity does not satisfy the boundary condition. For a time-stepping scheme, Eq.3-22 can be re-written with $\mathbf{u}^*$.

$$\frac{\mathbf{u}^* - \mathbf{u}_n}{\Delta t} = RHS_i(\mathbf{u}_n) + f_i, \tag{3-23}$$

where $\mathbf{u}_n$ is velocity from the previous time step t=n, and $f_i = 0$ at this step, $RHS_i(\mathbf{u}_n)$ is the sum of all the terms in the right hand of the momentum equation.

Then, the velocity field for the boundary layer cells is reconstructed according to the extrapolated velocity approach in section 3.4.2. The velocity corrector f_i^* is computed from Eq. 19 by replacing the momentum-equation-deduced velocity $\mathbf{u}^*$ with the extrapolated velocity $\mathbf{u}^N$:

$$\frac{\mathbf{u}^N - \mathbf{u}_n}{\Delta t} = RHS_i(\mathbf{u}_n) + f_i^*, \tag{3-24}$$

$$f_i^* = \frac{\mathbf{u}^N - \mathbf{u}_n}{\Delta t} - \frac{\mathbf{u}^* - \mathbf{u}_n}{\Delta t} = \frac{\mathbf{u}^N - \mathbf{u}^*}{\Delta t}, \tag{3-25}$$

and then applied back to the discretized momentum equations

$$\frac{\mathbf{u}_{new}-\mathbf{u}_n}{\Delta t} = RHS_i(\mathbf{u}_n) + f_i{}^*. \quad (3\text{-}26)$$

The resulting velocity $\mathbf{u}_{new}$ will satisfy the desired boundary conditions on the interface. The new velocity field is then used to solve the pressure Poisson equation and the final velocity $\mathbf{u}_{n+1}$ and pressure fields p_{n+1} for the next time step t=n+1 are obtained.

3.5 Velocity and pressure decoupling algorithm

The solution of the momentum equations shows strong coupling of the velocity and pressure. The PIMPLE algorithm that is widely used in the OpenFOAM platform is applied in present solver[49]. It is a hybrid of a Pressure Implicit Splitting Operator (PISO) algorithm and a Semi-Implicit Method for pressure-Linked Equations (SIMPLE) algorithm [92] and takes benefits from both of them.. The momentum equations are generally solved by two iteration loops. The SIMPLE algorithm acts as the outer corrector while the PISO algorithm acts as the inner correction loop. Better stability is obtained compared to the PISO and SIMPLE algorithms to ensure the convergence of all the equations at each time step until the solution is completes. There are three convergence criteria within each timestep: the residual falls below the solver tolerance, the ratio of current to initial residuals falls below the solver relative tolerance and the number of iterations exceeds a maximum number of iterations[49]. Normally, for the cases in this paper, the number of iterations ranges from 1 to 400.

3.6 Solution procedure

The basic computational process at one time step for the combined volume of fluid and immersed boundary method for two-phase flows is as follows.

(1) Obtain the VOF volume fraction (α), fluid variables (velocity $\mathbf{u}_n$, pressure P_n) and the interface property (normal vector $\mathbf{n}$,) at the time step t=n.

(2) Represent the interface using the iso-surface $\alpha = 0.5$ and identify the phase state of the grid cells, phase 1 cells, phase 2 cells and boundary cells. A thin boundary layer is identified, with one- or two-cell thickness.

(3) Compute the momentum-equation-deduced velocity $\mathbf{u}^*$ by solving the momentum equation directly. Spurious velocity exists near the interface in this velocity field.

(4) Reconstruct the velocity field $\mathbf{u}^N$ by an extrapolated velocity approach. In the new velocity field $\mathbf{u}^N$, velocity is the extended from one phase slightly beneath the interface to the other slightly above the interface.

(5) Calculate the velocity corrector f_i^*.

(6) Compute $\mathbf{u}_{new}$ from the discretized momentum equations with the velocity corrector. The resulting velocity will satisfy the desired boundary conditions on the interface.

(7) Compute the pressure using the velocity and pressure coupling algorithm. The velocity $\mathbf{u}_{n+1}$ and the pressure P_{n+1} are updated for the next step t=n+1.

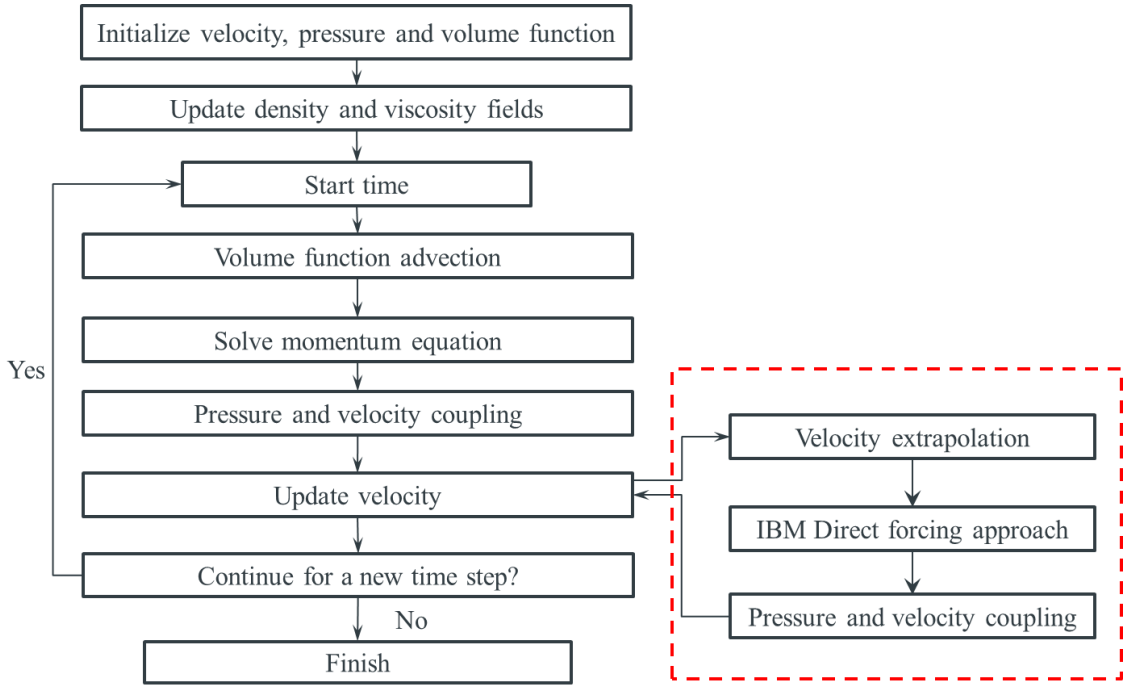

Figure 3-8 Flow chart of the IBVOF solver

3.7 Conclusion

A two-phase flow solver, IBVOF solver has been developed to simulate multiphase flows with high density ratios. The numerical method is presented in detail with the emphasis on the treatment of the free surface boundary. The sources of the spurious velocity generated near the interface are identified to lie in the interpolation of the momentum flux and the imbalance of the dynamic pressure gradient and density gradient because of the density jump across the interface.

An extrapolated velocity approach is developed to extend the velocity from the denser phase to the lighter phase and an immersed boundary method is used to build a thin boundary layer above the interface. The designed boundary layer smoothing of the velocity helps to prevent the tearing

of the interface due to the tangential velocity between the two phases across the interface. Such treatment reduces the spurious velocity caused by the momentum interpolation errors across the interface and improve the accuracy and stability of high-density ratio two-phase flow simulations.

Chapter 4 Two-phase flow IBVOF solver verification

4.1 Introduction

As the mathematical model is exact for two-phase flow simulations having a large density ratio, viscous effects and surface tension are not considered in this chapter. Two sets of test cases are designed to analyse the causes of spurious velocity and to validate the proposed IBVOF method. The first case is a stratified flow composed of two liquids of different densities. Theoretically, the interface between the two phases would remain flat unless numerical instability exists. Simulations are carried out using fixed uniform Cartesian grids. The effect of mesh size and density ratio on the velocity field are investigated to identify the sources of the spurious velocities. The second set of test cases considers the effect of the numerical instability on advection of the interface. The new IBVOF method is evaluated on a 2D test case of high-density droplet transport [93]. The results of both sets of cases are compared with analytical solutions and the original two-phase flow solver in OpenFoam 5.0.

It is important to note that these two causes of spurious velocity do not include surface tension effects using Continuous Surface Stress (CSS) model [64]. The surface tension effects are not considered in all cases and analysis in this chapter. These simplifications are adopted to estimate the influence of numerical viscosity and other spurious effects and enable direct comparison with potential theory, which helps to identify the source of problems, highlights the effects of the spurious velocities to the interface, and allows quantitative investigation of the effect of mesh size, time step and density ratio on the final results.

4.2 Steady stratified flow

A set of extreme simplified steady stratified flow cases are designed to check the velocity evolution near the interface during numerical simulation. The simulations are conducted in a numerical flume on a 2D computation domain of x= [-0.5L, 0.5L] and y= [0, L] where L= 10m is the length of the domain. The entire computational domain and the different boundaries applied at inlet, outlet, bottom and upper are shown in Figure 4-1. The front and back boundary conditions are set as empty since it is a 2D simulation. The empty boundary condition means no solution is required for the front and back boundaries. A symmetry boundary condition is assigned to the upper and bottom boundaries to avoid generation of vorticity as required by the underlying potential flow theory. Cyclic boundary conditions are applied on the left and right boundaries to avoid numerical errors generated by inlet or outlet boundaries.

The initial velocities and physical parameters of the two phases are listed in Table 4-1. The initial interface is set in the middle of the domain with a height of 0.5L. Theoretically, without any viscous shear force or surface tension effect, the velocity field in both phases and the interface between the two phases should remain the same as for the initial condition.

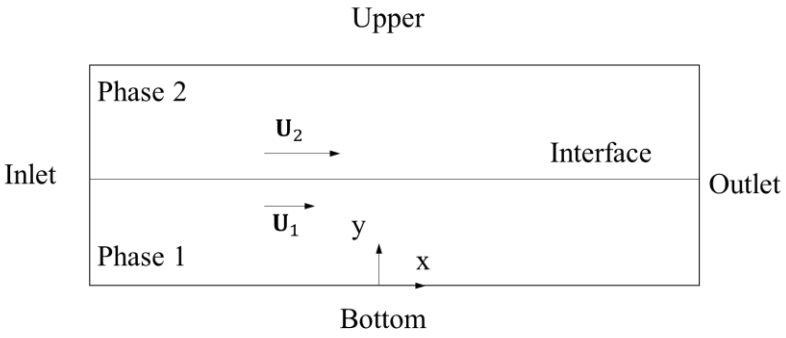

Figure 4-1 Computation domain for the steady stratified flow case.

Table 4-1 Physical parameters and initial velocities for the steady stratified flow case.

Test case	$\mathbf{U}_1$ (m/s)	$\mathbf{U}_2$ (m/s)	ρ_1 (kg/m^3)	ρ_2 (kg/m^3)
Case A1	(10,0,0)	(1,0,0)	1	1
Case A2	(10,0,0)	(1,0,0)	10	1
Case A3	(10,0,0)	(1,0,0)	100	1
Case A4	(10,0,0)	(1,0,0)	1000	1
Case B1	(1,0,0)	(10,0,0)	1	1
Case B2	(1,0,0)	(10,0,0)	10	1
Case B3	(1,0,0)	(10,0,0)	100	1
Case B4	(1,0,0)	(10,0,0)	1000	1

4.2.1 The effect of mesh size

Before investigating the effect of density ratio on spurious velocities, numerical settings are investigated through a mesh and time refinement study. For all simulations in the following, fixed uniform square cells are applied cover the whole computational domain. Four grids are applied in

this case, which consecutively increased sizes from grid one 8,193 cells to grid four 131,072 cells. The numbers of cells in x direction are 64, 128, 256 and 512, respectively. Adaptive time steps are used based on a maximum allowed Courant number, Co= 0.2. The influence of time step is investigated in section 4.2.2.

To investigate the effect of spatial resolution, a density ratio of 1,000:1 is chosen in this section since air and water interaction problems are the typical cases in the nature and engineering. Both case A4 and case B4 are investigated, with different initial velocities in lighter and denser phases. The maximum Co number equals 0.2 in each case. Figure 4-2 illustrates the instantaneous velocity magnitude fields at t= 10s of case A4 with both the original two-phase flow solver, interFoam, in OpenFoam and the proposed solver, IBVOF. The position of the initial interface is added as a reference with a dashed white line. Theoretically, the velocities in both lighter and denser phases would remain the same as the initial condition. However, in the simulation results of case A4 with interFoam, the velocity of the main part of the lighter phase remains at 10m/s but is decreased closer to the interface. A shear flow layer is generated near the interface, which is not reasonable in the numerical setup in this case. Compared with the original VOF method in original solver interFoam, the present solver with IBVOF have better results in the velocity prediction. The velocity fields for both lighter and denser phase remain uniform, as for the initial condition.

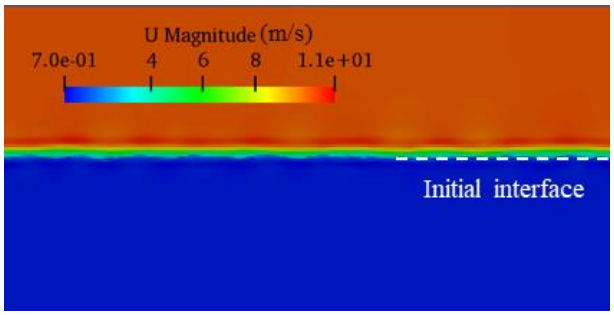

(a) InterFoam solver

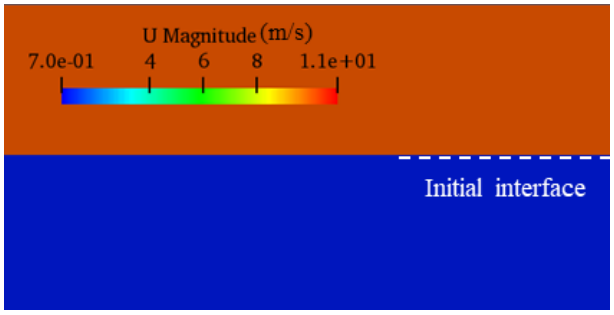

(b) IBVOF solver

Figure 4-2 Instantaneous velocity field of case A4 with 256×128 cells at t=10s for the steady stratified flow case.

The horizontal velocity profiles at the middle section of the computational domain x= 5m are compared for different mesh sizes with the two solvers and shown in Figure 4-3 and Figure 4-4, respectively. In each of these figures, the coordinate x shows the velocity magnitude (nominalized by the initial relative velocity of the two phases, $U_r = |U_1 - U_2|$), the coordinate y shows the distance of the cell centre to the bottom boundary and the numbers in legend are the mesh numbers in x-direction in each case. The theoretical solution is shown with a dashed black line.

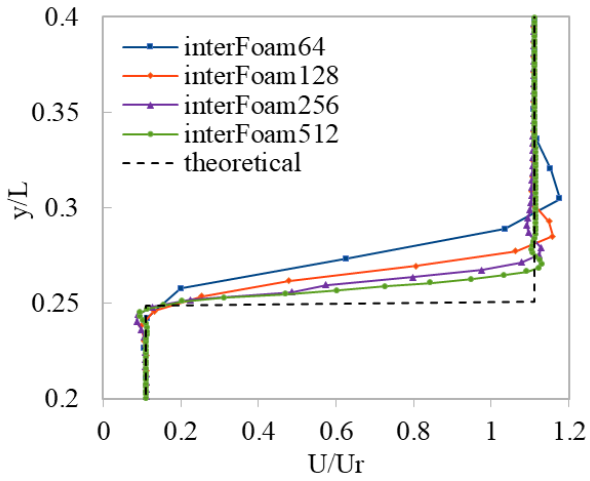

(a) Case A4

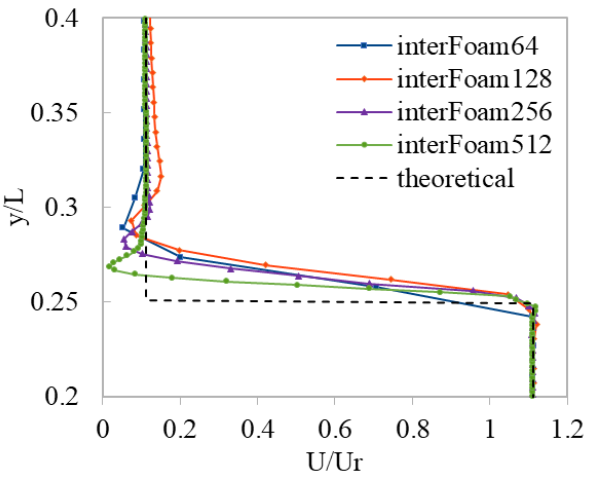

(b) Case B4

Figure 4-3 Horizontal velocity profiles on section x= 0m for different mesh sizes with Co=0.2 using interFoam solver at t= 10s.

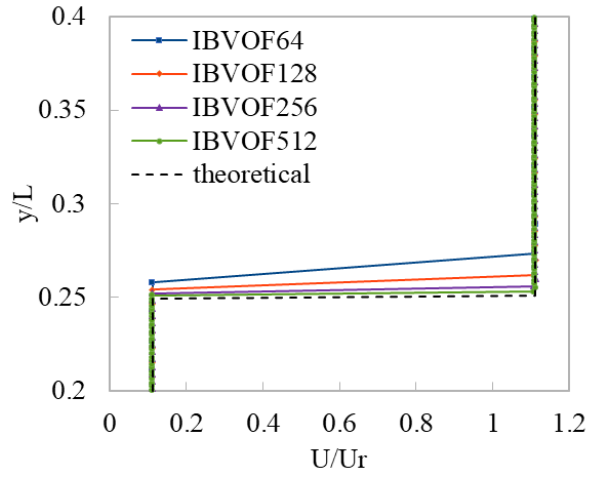

(a) Case A4

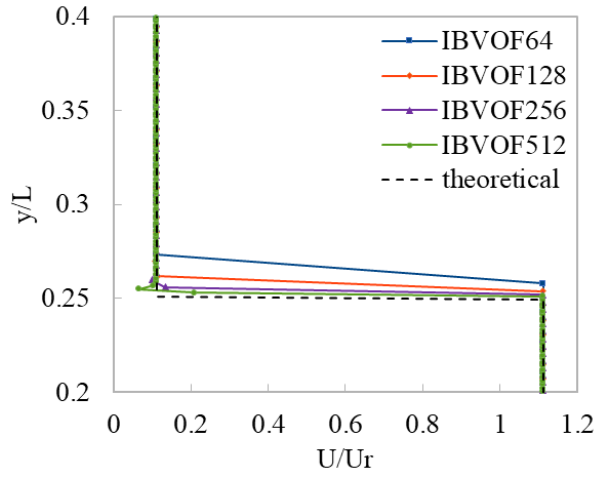

(b) Case B4

Figure 4-4 Horizontal velocity profiles on section x= 0m for different mesh sizes with Co=0.2 using IBVOF solver at t= 10s.

Without any treatment on the interface boundary, the numerical instability caused by the large jump in the material properties across the interface accumulates over time and eventually leads to spurious dynamics characteristics. As shown in Figure 4-3, a large amount of spurious velocity is generated near the interface, especially on the lighter phase side. The cells containing less density mass are more sensitive to the numerical errors in the pressure. The relative error measure is used to quantify the solution quality:

$$\epsilon_U = \frac{|U_t - U_{ini}|}{U_r} \times 100\% \tag{4-1}$$

where U is the horizontal velocity, U_t is the instantaneous horizontal velocity at time t, U_{ini} is the initial velocity in each cell and U_r is the relative velocity between the two initial velocities, $U_r = |U_1 - U_2|$.

Figure 4-5 and Figure 4-6 show the relative errors ϵ_U on section x=5m for different mesh sizes with Co=0.2 using the two solvers. The comparison of the relative errors shows that the present IBVOF solver is superior at preserving the velocity on all investigated meshes. The relative errors only exist on the nearest cell above the interface because of the designed interface boundary condition. The original interFoam solver tends to generate a band of layer that transmit the velocity from the denser phase to the lighter phase. The thickness of the band seems to decrease with the finer mesh but never vanishes. In both case A and case B, the corresponding thickness of the band, where the relative errors ϵ_U are larger than 2%, is approximately 6-8 grids cells on all mesh sizes.

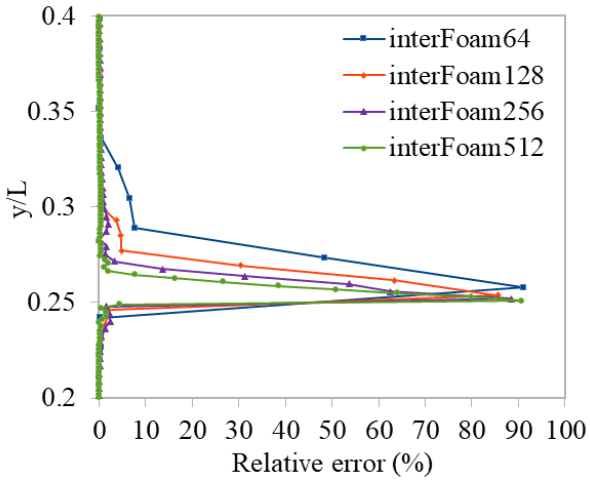

(a) Case A4

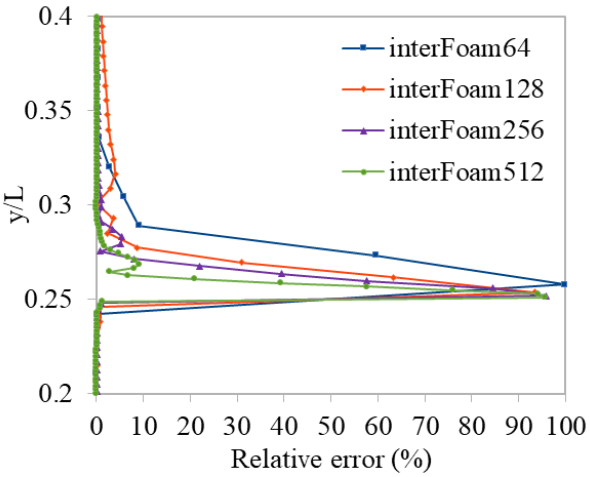

(b) Case B4

Figure 4-5 Relative error ϵ_U on section x= 0 m for different mesh sizes with Co=0.2 using interFoam solver at t= 10s.

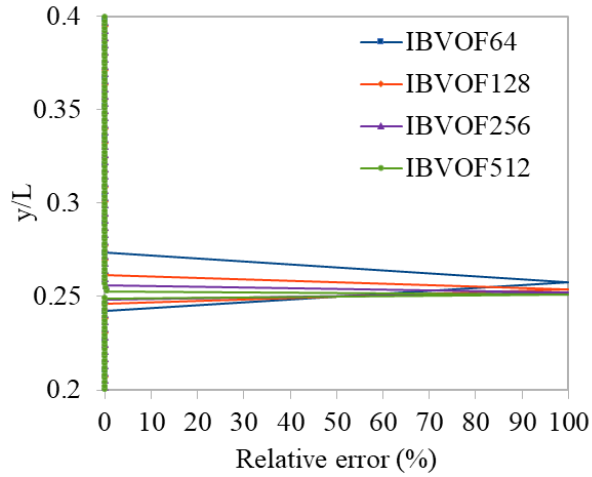

(a) Case A4

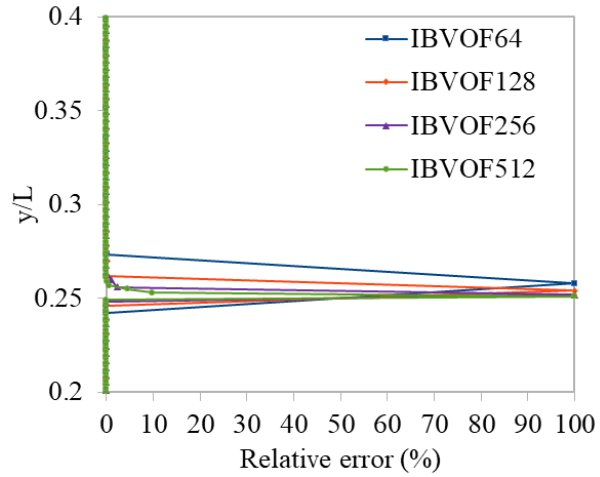

(b) Case B4

Figure 4-6 Relative error ϵ_U on section x= 0 m for different mesh sizes with Co=0.2 using IBVOF solver at t= 10s.

Beside the width of the band, the maximum ϵ_U keeps increasing with the refinement of mesh, except the coarsest mesh. This means that refining the mesh is not a solution for the spurious velocities. Too refined a mesh may cause other numerical instability problems. The smaller the cell is, the less mass the cell contains, making it more sensitive to numerical errors. It is also proved by the phenomena that the spurious velocities are mainly generated in the lighter phase and are much larger than in the denser phase.

The spurious velocity eventually results in spurious dynamics of the interface. The errors ϵ_α of the volume fraction α are defined by:

$$\epsilon_\alpha = \frac{|\alpha_t - \alpha_{ini}|}{\alpha_r} \times 100\%, \tag{4-2}$$

where α_t is the instantaneous value and α_{ini} is the initial setup value, α_r is the relative initial volume fraction between the two phases, $\alpha_r = |\alpha_1 - \alpha_2| = 1$.

In Table 4-2, the relative error ϵ_α in nearest cells just above and beneath the interface at x=0m are compared with the two solvers. The IBVOF solver is significantly better than interFoam for all the meshes in terms of surface shape preservation. The maximum value of the ϵ_α using the IBVOF solver is smaller than the minimum value using interFoam solver. The results for ϵ_α also shows that the error does not decrease monotonically with the mesh refinement. Simply refining the mesh cannot reduce or eliminate the numerical errors caused by the large density ratio. Based on the analysis of the velocity and volume fraction, the Mesh 256×128 is chosen as an appropriate resolution for the following studies in this work.

Table 4-2 Relative error ϵ_α at x=0m for different mesh sizes with Co=0.2.

Case	Solver	Above the interface				Beneath the interface			
		64	128	256	512	64	128	256	512
A4	interFoam	4.7	10.7	9.5	0.9	4.0	12.5	32.4	8.7
	IBVOF	3e-3	6e-10	1e-24	0	5e-3	1e-3	1e-3	0
B4	interFoam	0.2	5.6	17.1	8.80	0.2	8.5	6.7	8.7
	IBVOF	8e-3	0.02	0.02	0.04	8e-3	0.02	0.02	0.04

4.2.2 The effect of time steps

In order to evaluate the influence of the time step, three Co numbers are tested, Co= 0.1, 0.2and 0.4 based on the selected Mesh 256×128. Again, the relative errors ϵ_U for different Co numbers are calculated and compared. Figure 4-7 shows relative errors ϵ_U of the interFoam solver. Similar results are obtained with interFoam solver with all three Co numbers. For case A4, the three lines almost overlap each other and for case B4, the results demonstrate that the region of the spurious velocities is decreased slightly through refinement of the time step. A Co=0.2 is thus adopted to achieve a necessary condition for time convergence for the interFoam solver. As shown in Figure 4-8, IBVOF solver has a better performance in time step convergency. The errors remain in a very low level (except for the nearest cell above the interface) for the Co number up to 0.4. This means that IBVOF solvers would allow accurate simulation with larger time steps.

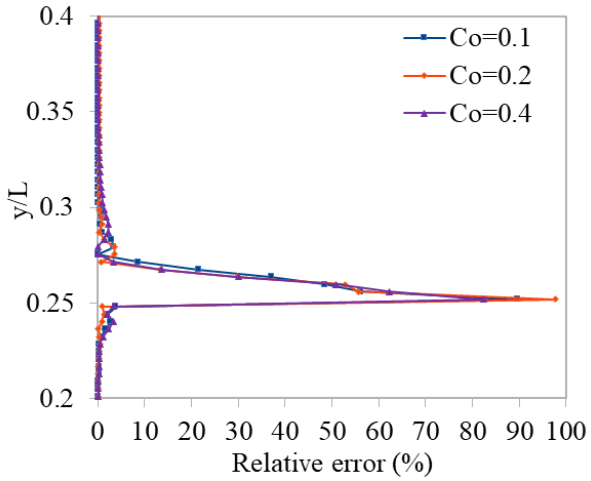

(a) Case A4

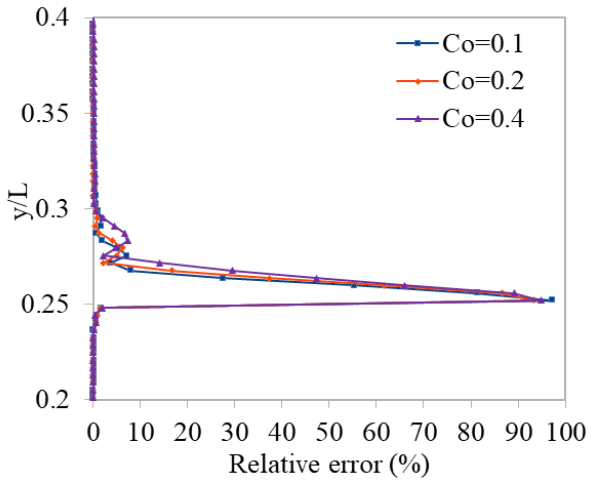

(b) Case B4

Figure 4-7 Relative error ϵ_U on section x=0m for different Co numbers with Mesh 256×128 using interFoam solver at t= 10s.

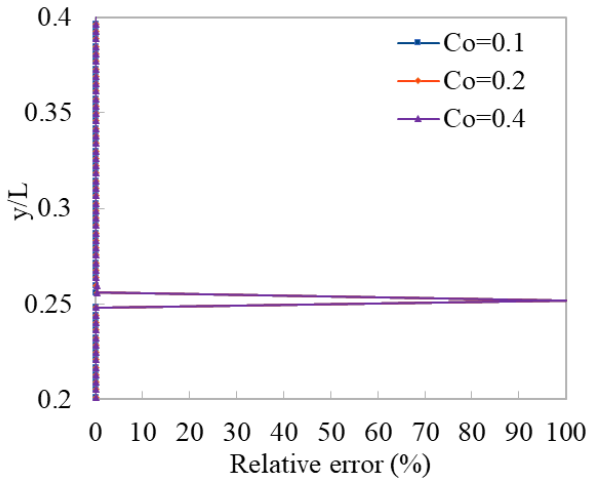

(a) Case A4

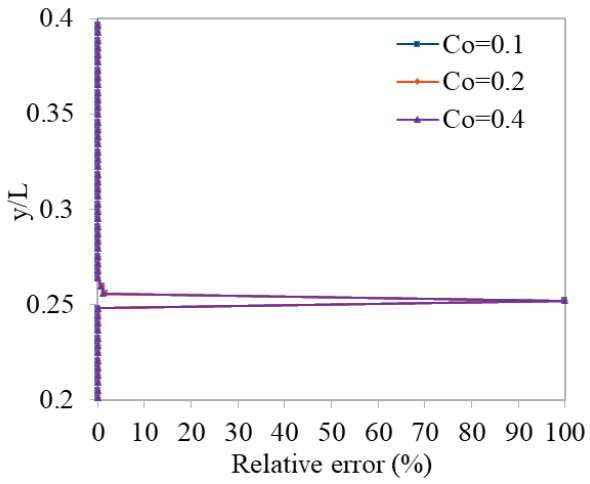

(b) Case B4

Figure 4-8 Relative error ϵ_U on section x= 0m for different Co numbers with Mesh 256×128 using IBVOF solver at t= 10s.

4.2.3 The effect of density ratio

In this section, the influence of changes in density ratio on the generation of the spurious velocity near the interface is investigated. The density and velocity are initialized as Table 4-1. Four different density ratios are designed ranging from 1 to 1000. The cases are divided into two parts, case A and case B, with different initial velocities in the two phases. The Mesh 256×128 is used with the maximum Co number 0.2 according to the analysis in section 4.2.1 and 4.2.2. Figure 4-9 shows the relative error ϵ_U with different density ratios using interFoam at t = 1 s.

It is obvious to see that the spurious velocity increases with the density ratio. When the density of each phase is equal, the velocity field of each phase remains the same as the initial conditions. The spurious velocities start to appear for the cases with density differences across the interface. As analysed in section 3.2, it comes from the imbalance between pressure gradient and density gradient in the momentum equation. The effect of the numerical error on the lighter phase is much greater than on the denser phase since the same stress is generated from the momentum equations. If IBVOF solver is used, much better accuracy can be obtained in the calculation of velocity fields even for the large density ratio 1000:1 (see Figure 4-10).

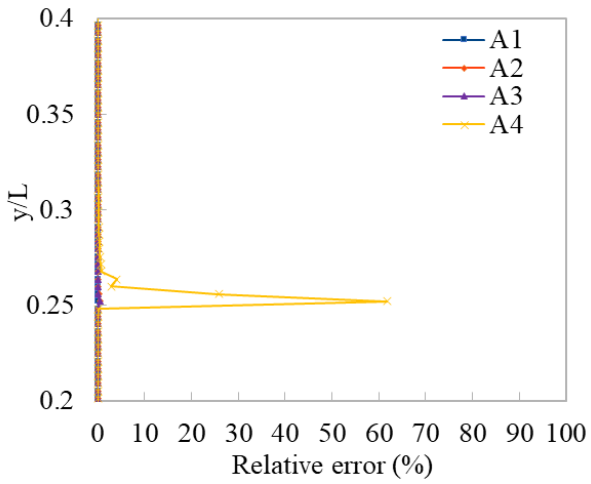

(a) Case A

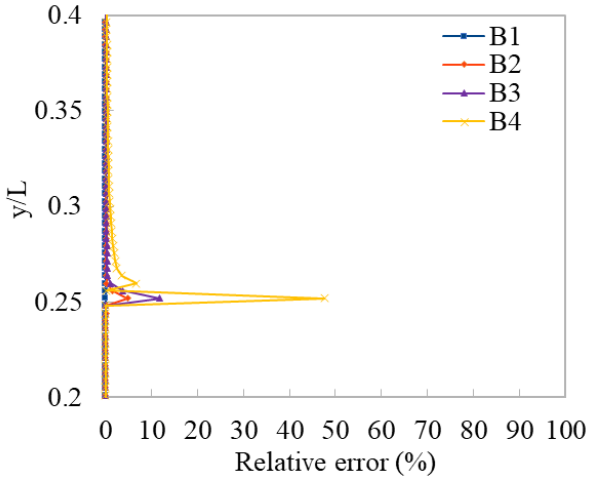

(b) Case B

Figure 4-9 Relative error ϵ_U on section x= 0m for different density ratios with Mesh 256×128 and Co=0.2 using interFoam solver.

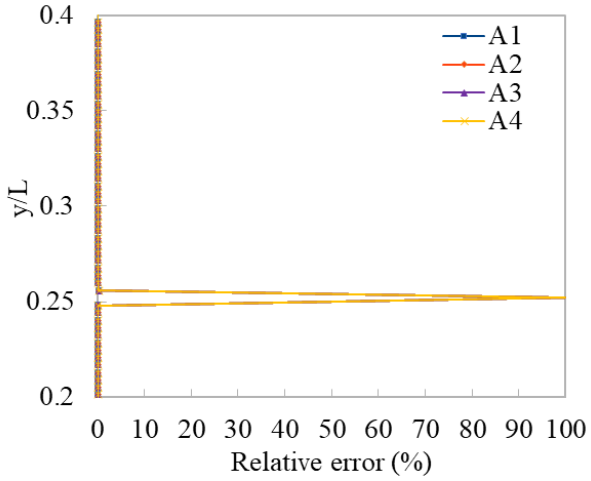

(a) Case A

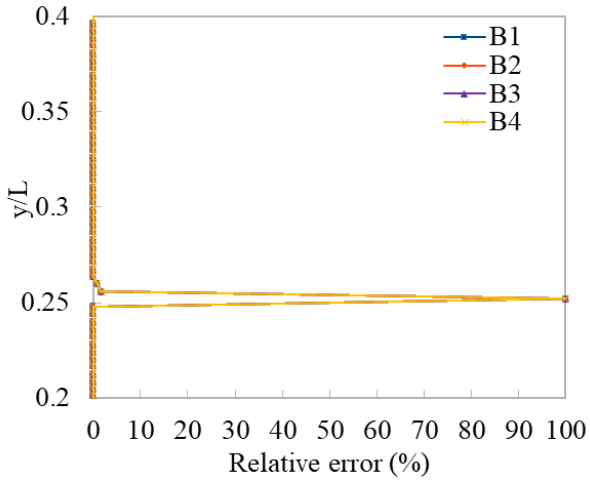

(b) Case B

Figure 4-10 Relative error ϵ_U on section x= 0 m for different density ratios with Mesh 256×128 and Co=0.5 using IBVOF solver at t= 1 s.

The momentum-equation-deduced velocity is then used in the convection of the volume fraction. Numerical errors caused by the jump of density across the interface accumulate over time and finally affect the distribution of volume fraction near the interface. The numerical errors act as a source of a small disturbance in fluids of different densities moving at different speeds and Kelvin-Helmholtz instability can occur near the interface. Figure 4-11(a) shows the distribution of volume fraction of case A2 at t=2 s with interFoam solver. Typical Kelvin–Helmholtz instability is observed, which, however, is not supposed to be generated in this case. In the same numerical setup and initial conditions, a much better result is obtained with the IBVOF solver. The spurious velocities and interface instabilities are suppressed with the present approach.

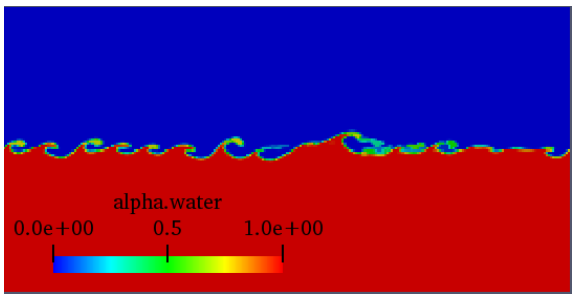

(a) InterFoam solver

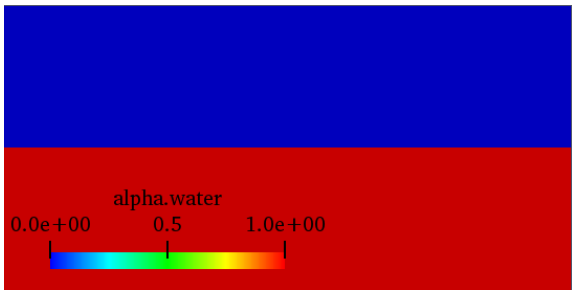

(b) IBVOF solver

Figure 4-11 Distribution of volume fraction of case A2 with 256×128 cells and Co=0.2 at t=2 s

4.3 Convection of a high-density droplet

The droplet test cases have been numerically studied in [81] [93] [94], among others, to check numerical stability and robustness of two-phase flow solvers. The computation is conducted for a domain of [0 m, 10 m]×[0 m, 5 m] with a uniform grid. A droplet with diameter D=1 m is initially placed in the air with its center at (2.5m, 2.5m). The droplet is given a constant horizonal velocity $\mathbf{U}_l = (1,0)$ m/s whilst the gas is initially at rest. The density of the air is set as 1 kg/m^3 while the density of the droplet is set as 1,000,000 kg/m^3.

Both viscous effects and surface tension are neglected in this case. Theoretically, the high-density droplet is therefore expected to remain perfectly circular when passing through the air, as dashed line shown in Figure 4-12. Various meshes are considered, ranging from 128×64, 256×128 to 512×256, while the maximum Courant number, Co, equals 0.1 for limiting the growth if spurious velocities in all these cases.

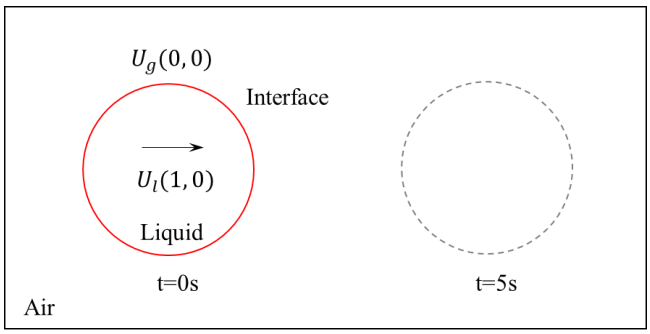

Figure 4-12 Convection of droplet case setup.

4.3.1 Velocity profiles

The velocity field in the early stages of the simulation, t=0.1s, is first analyzed. At this stage, the high-density droplet remains circular with its center moves to x=2.6m. The velocity field of the air region, in these conditions, should be similar to the field produced by an air flow around a solid cylinder whilst the velocity in the liquid should remain exactly equal to its initial value. Figure 4-13(a) shows the results of a one-phase flow solver in OpenFOAM, pimpleFoam. In the one-phase flow solver, the cylinder is fixed in a uniform air flow. A slip wall boundary condition is used on the surface of the cylinder. Other numerical setup and mesh distribution are set up as similar as the two-phase flow solver with 256×128 cells.

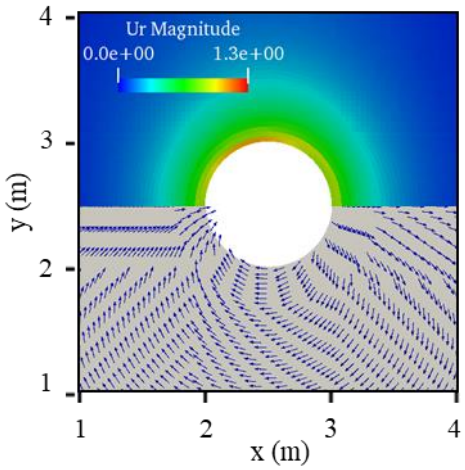

(a) One-phase flow solver

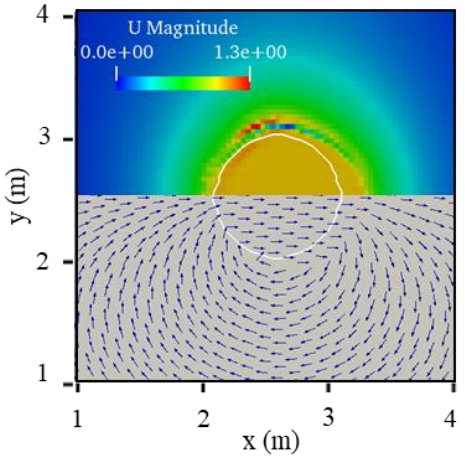

(b) InterFoam solver

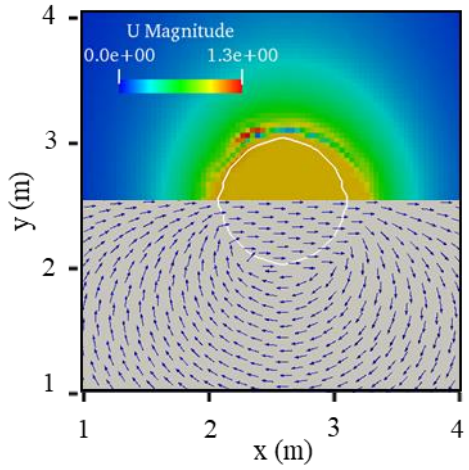

(c) IBVOF solver

Figure 4-13 Velocity field with 256×128 cells at t=0.1s. The top half shows the colored velocity magnitude and the bottom half shows the velocity direction with arrows.

The velocity field showed in Figure 4-13(a) is the relative velocity to the initial droplet velocity, $\mathbf{U}_r = \mathbf{U}_l - \mathbf{U}$, where $\mathbf{U}$ is the air flow velocity obtained from the one-phase flow solver. Even though the Reynolds number is infinite, no wake region has yet formed at this early stage. The fields are nearly symmetric. For visualization purpose, the figures are divided into two parts. The top half shows the colored velocity magnitude and the bottom half shows the velocity directions with arrows.

However, some deviations from these assumed values are found in two-phase flow solvers near the interface especially on the top and bottom sides of the droplet, which we interpret as spurious velocities. The shape of the droplet and the velocity field with the two solvers on Mesh 256×128 at t=0.1s are shown in Figure 4-13(b) and (c). The shape of the droplet is shown with the iso-surface α=0.5 in a white line. The velocity inside the droplet keeps its initial value while a large spurious velocity is observed in the air region. The maximum value of velocity $\mathbf{U}_r$ in the one-phase flow solver simulations is 1.04 m/s while the maximum value in the interFoam solution reaches 1.27 m/s. A non-viscous vortex is generated on the upper left region of the droplet since the air velocity adapts to the droplet movement to preserve continuity and momentum. The vortex is enlarged by the large velocity gradients in the air region as a result of the discontinuous velocity near the interface.

As analyzed in section 4.2.1, since the pressure is the same across the interface, the velocity gradient in the air is much higher than in the liquid. Therefore, larger velocity gradients in the air tend to be generated when solving the momentum equations. Furthermore, though the value is relatively small compared to the air side, the spurious velocity exists on the liquid side as well, especially on the upper left part of the droplet. This velocity is then used for volume fraction

function convection and hence ultimately distorts the interface. Compared to the interFoam solver, the velocity field in the air obtained from the IBVOF solver is closer to the one-phase solver. The deviations of the maximum and minimum velocity magnitude near the interface are smaller which means the velocity gradient in the air is more reasonable with the IBVOF solver.

To better understand the issues behind the generation of the spurious velocity, the velocity profiles along the vertical cross-section going through the center of the droplet are investigated to compare the three solvers. It is an important feature to show the accuracy of the two-phase flow solvers in wave propagation [95] [58], and is suitable in the droplet convection problem. The velocity field in the air $\mathbf{U}_r$ obtained with the one-phase flow solver and the initial velocity field in the liquid are used as a reference to compare the two different two-phase flow solvers (see Figure 4-14). The time is chosen again as t = 0.1 s before large interface deformation is generated.

Differences between the one-phase solver and the two two-phase flow solvers are most visible in the air region, while in the main bulk of the liquid the velocities follow the initial value reasonably well. In both two-phase solvers, a spurious boundary layer is generated to smooth out the jump of the velocity at the interface and acts as a source of the no-viscous vortex on the upper left side of the droplet. The width of the layer decreases with the grid refinement, but always exists. For both solvers, the magnitude of spurious velocities decreases with the grid refinement and the velocity profile converges to the reference resolution. For the coarsest mesh 128×64, the cells are too large and fails to capture the steep transition of velocity between the two phases since the values stored in the cell centre are averaged by the control volume. However, an increase of velocity is visible in the liquid right beneath the interface in the interFoam solver even for the lowest resolution. The increase is not a unique result of the coarse mesh since similar phenomena are observed in finer mesh 256×128 and 512×256.

The presence of spurious currents around an interface was also reported in [95] and [58]. As analysed in section 4.2.3, the reason for such behaviour lies in the discontinuity of the density of the fluids. For IBVOF solver, the profiles below the interface are better than the interFoam solver. The boundary layer designed by the extrapolated velocity approach and immersed boundary method improves the accuracy in calculation of the velocity of the denser fluid on the one hand and reduces the velocity gradient in the lighter fluid near the interface. Though the difference between the two solvers might be small as shown in Figure 4-14 at the early stage, the small errors in the velocity fields will accumulate with time and affect the volume fraction fields, which will be discussed in section 4.3.2.

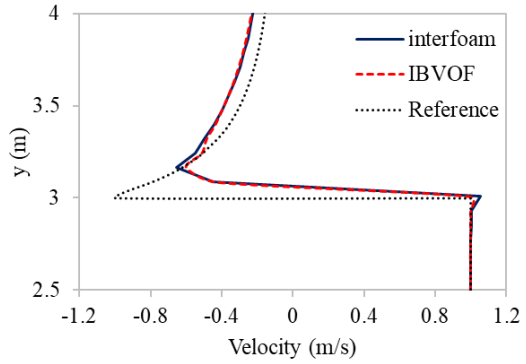

(a) 128×64

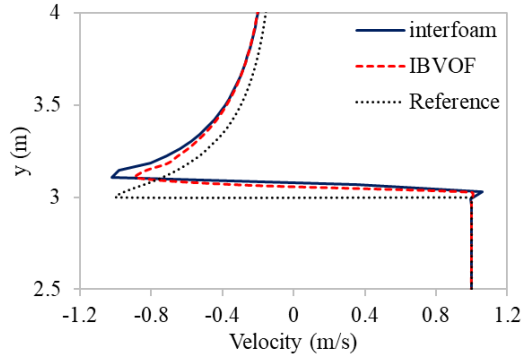

(b) 256×128

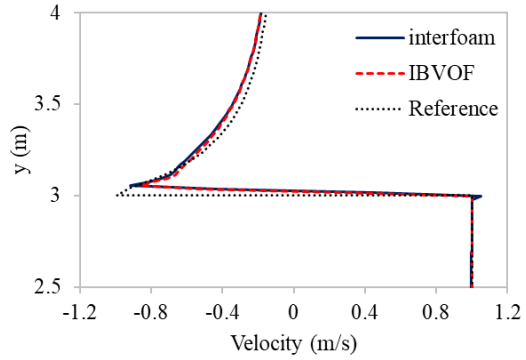

(c) 512×256

Figure 4-14 The horizontal velocity profiles along a vertical cross-section going through the centre of the droplet at t=0.1s.

4.3.2 Shape of the interface

As analysed in section 4.2.3, the momentum-equation-deduced velocity used in the convection of the volume fraction ultimately distorts the shape of the interface. Figure 4-15 presents the volume fraction α fields for different meshes using the interFoam solver, which are the final shapes and positions of the droplet at t = 5 s. The theoretical solution is also given in the figures with dashed

black lines. Most part of the droplets are located inside the exact circle, whilst large deformations are observed in all three meshes. Erroneous transfer of momentum from the liquid to the gas results in an unphysical shattering of the drop. The liquid inside of the droplet tends to spread to gas cells on the top and bottom sides. The maximum volume fraction α for the coarsest mesh is only 0.886, which should be 1. The droplet shape monotonically converges towards the exact solution. However, large scale interface deformations are still visible.

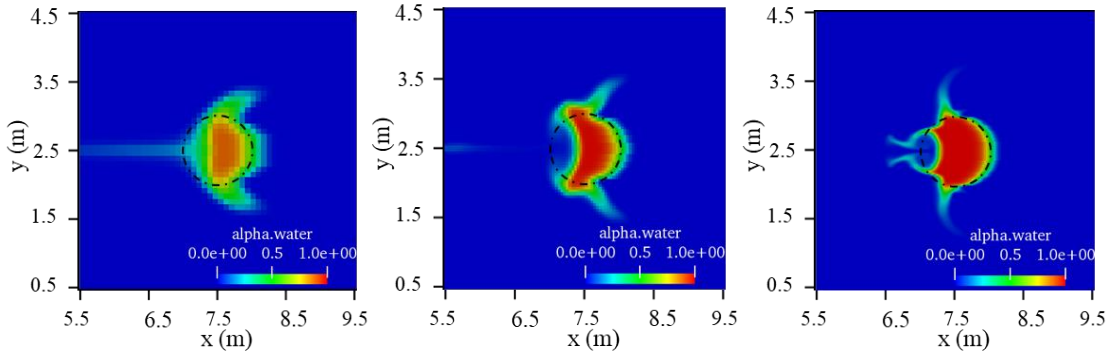

(a) 128×64 (b) 256×128 (c) 512×256

Figure 4-15 Volume fraction α distribution of high-density droplet with the interFoam solver at t = 5s.

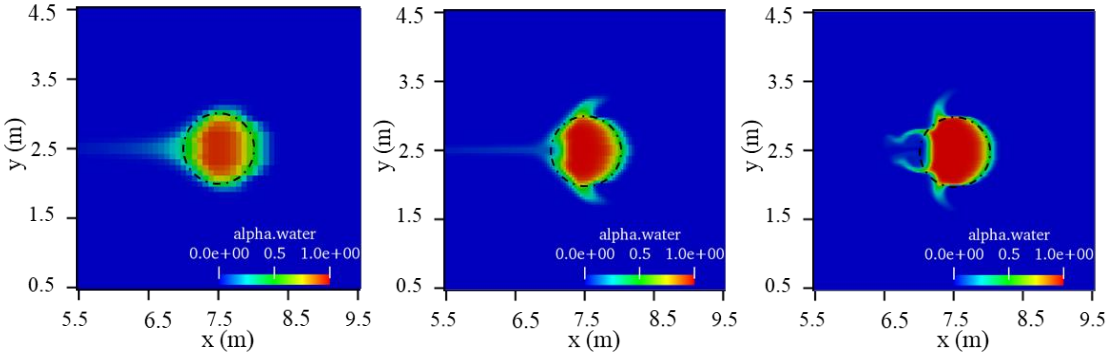

(a) 128×64 (b) 256×128 (c) 512×256

Figure 4-16 Volume fraction α distribution of high-density droplet with the IBVOF solver at t = 5s.

The results of the IBVOF solver are presented in Figure 4-16. Compared to the interFoam solver, better performance is obtained with the IBVOF solver in terms of both droplet position and shape. In order to get a quantitative analysis for this case, several error measures [96] are used as follows:

(1) Volume conservation, ϵ_{VC}, is the change in the total volume of liquid at time t in the whole domain relative to the initial value at t = 0.

$$\epsilon_{VC} = \frac{\left|\sum_i^N \alpha_i(t)V_i - \sum_i^N \alpha_i(0)V_i\right|}{\sum_i^N \alpha_i(0)V_i}, \tag{4-3}$$

where *i* is serial number of the cell, *i* = 1,2,3…*N*, *N* is the total grid number, *V* is the volume of the cell. ϵ_{VC} also represents mass conservation of the simulations.

(2) Shape preservation, ϵ_{SP}, is the difference of volume fraction distribution between the numerical results and the exact solution.

$$\epsilon_{SP} = \frac{\sum_i^N V_i\left|\alpha_i(t) - \alpha_i^{exact}(t)\right|}{\sum_i^N V_i \alpha_i^{exact}(t)}, \tag{4-4}$$

where α^{exact} is the volume fraction of the exact interface.

(3) Sharpness, ϵ_S, represents the thickness of the interface. For a sharp interface, the width of the region where the cell contains both liquid and gas should be similar to, or smaller than the cell size.

$$\epsilon_S = \frac{\sum_{is}^N \alpha_{is}(t)V_{is}}{\sum_i^n V_i \alpha_i^{exact}(t)}\ , \tag{4-5}$$

where *is* = 1,2,3…*n*, *n* is the total number of the cells with $0.1 < \alpha_{is} < 0.9$.

Figure 4-17 shows the comparison of the three error measurements between the interFoam and the IBVOF solvers with three different meshes at t = 5 s. Compared to the interFoam solver, the IBVOF solver is superior in all the mesh cases for all three error measures. For the volume conservation, the VOF method is known to inherently conserve the liquid volume [6] which is also proved with the present work. Though fluctuating a little with mesh size, the maximum value of the error ϵ_{VC} with the interFoam solver is around 0.01%. The IBVOF solver shows an even better performance in terms of conservation.

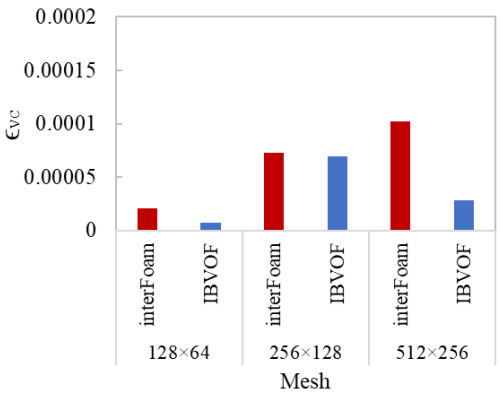

(a) Volume conservation, ϵ_{VC}.

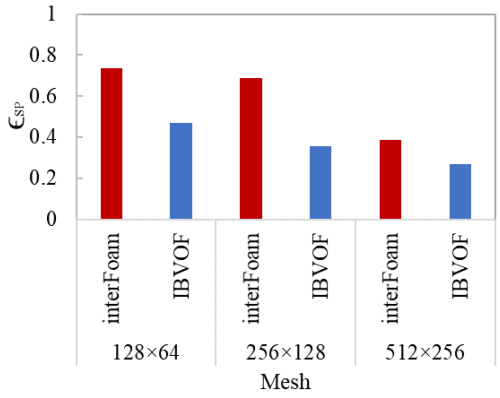

(b) Shape preservation, ϵ_{SP}.

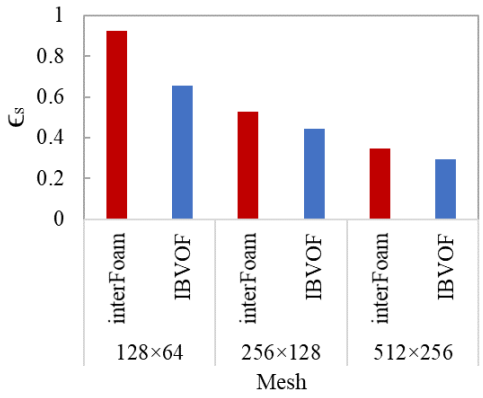

(c) Sharpness, ϵ_S.

Figure 4-17 Performance for convection of a high-density droplet with the interFoam and IBVOF solvers at t = 5s.

In terms of shape preservation, the visual impression from Figure 4-16 is that the IBVOF shows a better performance, and Figure 4-2(b) quantifies the large difference between them. The shape preservation error ϵ_{SP} reaches 0.735 for the interFoam solver over 35% of the liquid drifts from the droplet over the interface into the gas cells. Even though the shape of the liquid is similar to a circle, the high-density droplet has become a mass of 'white water', where the grids contains both liquid and air, and would turn into a mist of fog after that. The momentum-equation-deduced velocity is used for volume fraction advection and the spurious velocity ultimately leads to the deformation of the interface. Better shape preservation is obtained with the IBVOF solver. The value of shape preservation error ϵ_{SP} with the IBVOF for the coarsest mesh 128×64 is smaller than the interFoam with a finer mesh 256×128, and the volume fraction α remains close to 1 in most cells near the center of the droplet. For both solvers, monotonic convergence is achieved with the uniform grids.

The comparison of sharpness with the two solvers are similar to the shape preservation. The error measurement ϵ_S is designed to check the width of the interface. It is obvious from the data in Figure 4-17(c) that the IBVOF solver is better performing in this respect.

It is interesting to see that the gap between the two solvers also decreases monotonously with the mesh. The simulation results of the IBVOF solver are slightly better than the interFoam with the finest mesh. This is partly because the accuracy of the interFoam is improved with a finer mesh. Another reason could be the width of the designed boundary decreases at the same time. In the present work, the width of the interface boundary is set equal to one cell, so the effect of the extrapolated velocity approach and the immersed boundary method on the original solver is reduced when the grid size is reduced. A more robust and physically based boundary is desired in the future. The present work could be extended to viscous two-phase flow simulations, where the width and the velocity distribution of the interface boundary layer need to be treated more carefully.

4.4 Influence of the IBVOF boundary condition

In section 4.2 and 4.3, the proposed IBVOF solver is proved to reduce the physical instabilities in the air-water interface. As the air and water interactions are sensitive to the boundary conditions, the influence of the designed boundary condition is investigated. In this section, two other solvers, IBVOF10 and IBVOFW, are proposed based on the IBVOF solver to quantify this effect.

In the solver IBVOF10, the main process keeps the same as the basic IBVOF solver in section 3.6, while the momentum-equation-deduced velocity $\mathbf{u}^*$ is replaced by the $\mathbf{u}_{new}$ obtained from the IB

condition every 10 timesteps. This operation weakens the effect of the IBVOF boundary condition but saves some calculation.

In the basic solver IBVOF, the extrapolation velocity approach is used to extrapolate the velocity of one phase slightly beneath the interface to the other slightly above the interface. The velocities of only one or two cells in the air and water phases is modified by the IBVOF boundary condition. In the solver IBVOFW, the boundary layer is widened into three to four cells as shown in Figure 4-18. Thus, for a uniform Cartesian grid system, the phase 1 cells, boundary layer cells and phase 2 cells are identified as:

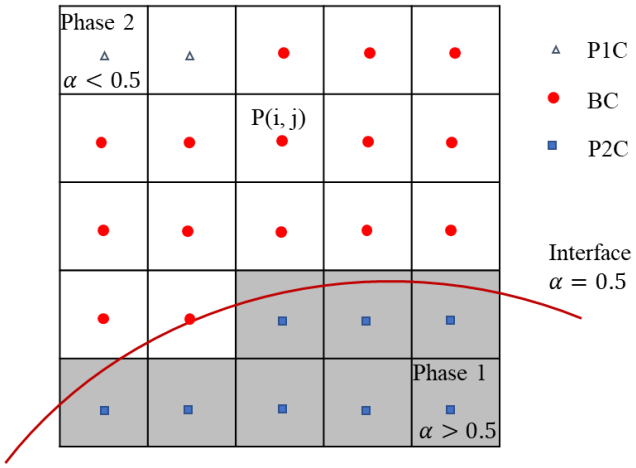

Figure 4-18 Phase state re-identification for IBVOFW solver.

(P1C: Phase 1 cells, BC: Boundary cells, P2C: Phase 2 cells)

(1) P1C: if $\alpha(i,j) \geq 0.5$;

(2) BC: if $\alpha(i,j) < 0.5$ and $(\alpha(i-b,j) \geq 0.5$ or $\alpha(i+b,j) \geq 0.5$ or $\alpha(i,j-b) \geq 0.5$ or $\alpha(i,j+b) \geq 0.5)$, b=1, 2, 3;

(3) P2C: if $\alpha(i,j) < 0.5$ and $(\alpha(i-b,j) < 0.5$ and $\alpha(i+b,j) < 0.5$ and $\alpha(i,j-b) < 0.5$ and $\alpha(i,j+b) < 0.5)$, b= 1, 2, 3;

where (i, j) is the grid node represent the x- and y-direction position of the cell.

The case, convection of a high-density droplet, is continually used in this section to quantify the effect of the IBVOF boundary condition. Figure 4-19 shows the velocity profiles of the three solvers, IBVOF10, IBVOF and IBVOFW together with the original interFoam and reference results. In order to highlight the differences among the solvers, the vertical slice of velocity field is selected as where the maximum velocity occurs in the results of interFoam solver. The position of the slice is slightly different with mesh density.

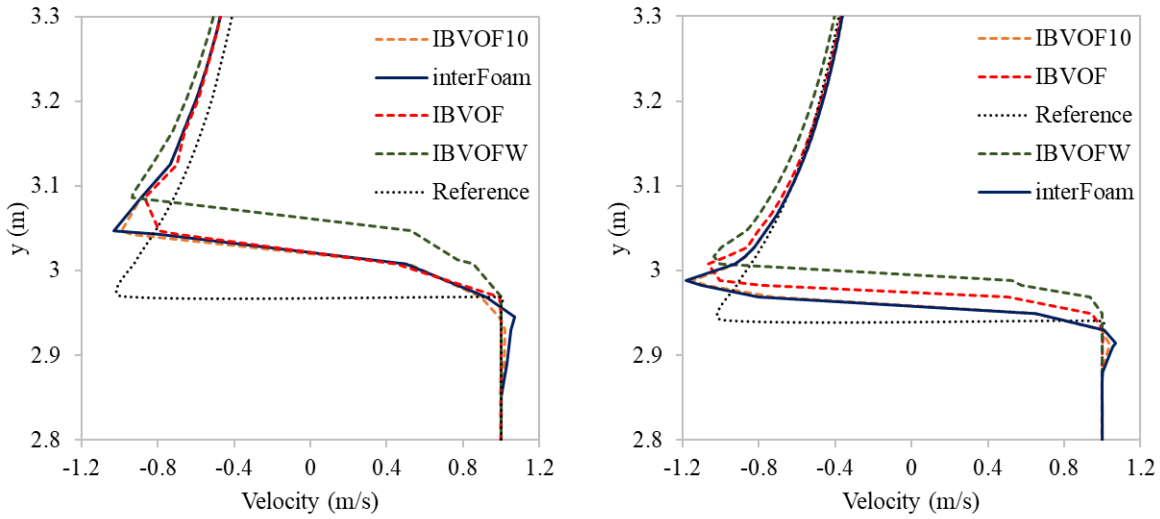

(a)Mesh 256×128 at slice x=2.35m (b) Mesh 512×256 at slice x= 2.4m

Figure 4-19 The velocity profiles of high-density droplet with three different solvers at t=0.1s.

As analysed in section 4.3.1, a spurious boundary layer is generated to smooth out the jump of the velocity at the interface and acts as a source of the no-viscous vortex in lighter phase. In Figure 4-19, for both mesh densities, the interFoam solver shows the largest velocity gradients across the interface and spurious velocities are observed in the water phase closed to the interface. The IBVOF10 solver reduces the spurious velocities a bit but not as well as the IBVOF solver. Though less than the interFoam solver, the spurious velocity and velocity gradients in the denser phase would eventually distort the shape of droplet.

The IBVOFW solver maintains the velocity of the denser phase as the IBVOF solver does. It extends the velocity of water phase two- to three- cell layer further away into the lighter phase as shown in Figure 4-19 and Figure 4-20. Adding the thickness of the IBVOF boundary improves the stability of the simulation of the denser phase. However, it further ignores the interactions between the two phases. The smoothing process, on the one hand, ignores the effect of the lighter phase by enforcing the lighter phase with the velocity of denser phase, and on the other hand, weakens the effect of the denser phase to the light phase by reducing the velocity gradient in the lighter phase closed to the interphase.

Figure 4-21 shows the velocity fields of high-density droplet with three different solvers with mesh 256×128 at t = 5s. The white lines are the position of the interface. Compare to the interFoam solver in Figure 4-15, all the three solvers obtain quite good shape of the high-density droplet. However, large differences are observed in the lighter phase. The larger the thickness of the boundary, the weaker the vortex is generated in the lighter phase behind the droplet. Compared to the IBVOF10 solver and IBVOFW solver, the IBVOF solver reduces the influence of the lighter

phase on the denser enough to gain stability but keeps as much as influence between the two phases above one or two cell length.

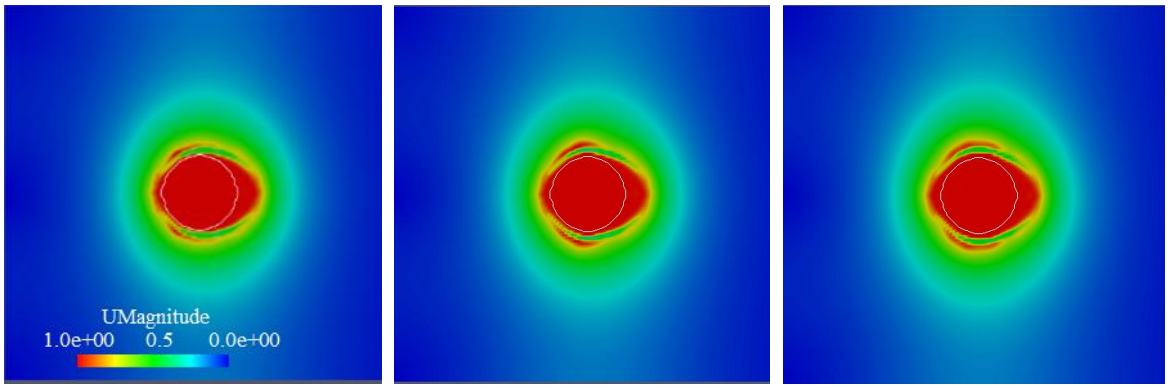

(a) IBVOF10 (b) IBVOF (c) IBVOFW

Figure 4-20 Velocity fields of high-density droplet with three different solvers with mesh 256×128 at t = 0.1s.

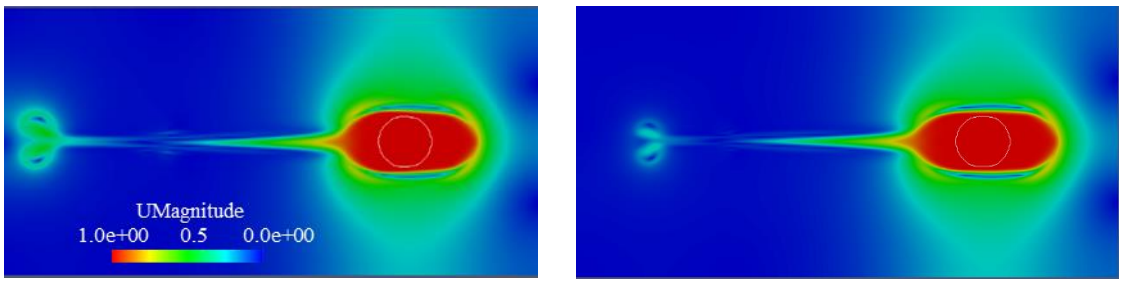

(a) IBVOF10 (b) IBVOF

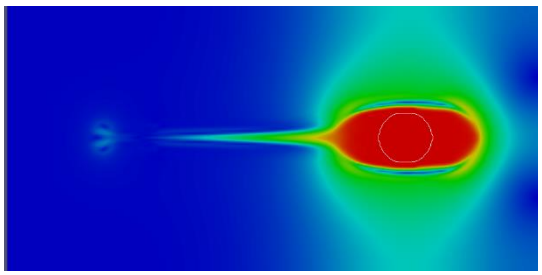

(c) IBVOFW

Figure 4-21 Velocity fields of high-density droplet with three different solvers with mesh 256×128 at t = 5s.

The overall purpose of this work is to develop a physics-based air-water boundary layer model applied it to VOF methods to deal with the discontinuity in the fluid properties over the two-phase interface and to offer a better resolution of the free-surface. The designed IBVOF boundary layer model helps to transit the water velocity to the air velocity physically smoothly. With the IBVOF solver, we are including the influence of the lighter phase on denser phase above one or two cell

length, which allows us to better simulate the behaviour of the denser phase. In contrast, a standard 2-phase simulation will become unstable, and a single phase fails to simulate complex free surface flow when the interface merges or breaks up.

4.5 Conclusion

Two sets of test cases are designed to analyse the source of the spurious velocity observed in the normal VOF solver and to validate the proposed IBVOF method, steady stratified flow, and convection of a high-density droplet. The results of the two solvers are compared with analytical solutions or one-phase flow solver results. The source of the problem in the original solver is believed to lie in the interpolation of the momentum flux and the imbalance of the dynamic pressure gradient and density gradient because of the density jump across the interface. The spurious errors in momentum cannot be eliminated with mesh or time refinement and finally distort the interface.

The IBVOF solver presented in this study provides a solution to this problem. The designed boundary layer smoothing of the velocity field helps to prevent the tearing of the interface due to the tangential velocity between the two phases across the interface. It is shown to improve the robustness and stability of two-phase flow simulations and higher accuracy can be obtained on a relatively coarse grid compared to the original solver.

Chapter 5 Applications of the IBVOF solver to general flows

5.1 Introduction

With the IBVOF solver well verified by the two sets of test cases, it is now extended to prediction of breaking waves in general simulations with unstructured mesh. First, in order to extend the application of the proposed IBVOF method, another density-weight smoothing (DW) approach is developed in this chapter. The extrapolated velocity (EV) approach extends the velocity of the denser phase beneath the interface to the lighter phase above the interface. This approach improves the accuracy of the two-phase solver. However, the application is limited on uniform Cartesian coordinate system since x- and y- coordinates are used. The DW approach is tested for compatibility against the IBVOF solver of Chapter 3 and test cases in Chapter 4 with uniform and unstructured mesh.

Next, the performance of the proposed IBVOF solvers is evaluated through a variety of numerical benchmark tests. In section 5.4, the case of a high-density droplet convection is extended to 3-dimensional (3D) simulation. The effects of fluid viscosity and surface tension are analysed in section 5.5 and section 5.6. Finally, a real-life problem of a droplet impact on a thin liquid file at short time is investigated to further validate the new two-phase flow solver.

5.2 Density-weight smoothing method

After the boundary cell are identified, the next step is to build an extra velocity field for this boundary layer. The extrapolated liquid velocity (EV) approach used in Chapter 3 and Chapter 4 is proposed by Xiao et al. [6] by extending the velocity of the denser phase beneath the interface to the lighter phase above the interface. This approach improves the accuracy of the two-phase solver. However, the application is limited on uniform Cartesian coordinate system. In order to extend the application of the proposed IBVOF method, another density-weight smoothing (DW) method is developed in this section.

The idea of density-weight smoothing comes from Fu's research [97]. The complete formulation for this smoother is as follows:

$$\widetilde{u_i} = \frac{\langle \rho u_i \rangle}{\langle \rho \rangle} \quad \text{for } \alpha \geq 0.5, \tag{5-1}$$

where $\widetilde{u_i}$ is the smoothed velocity field, u_i is the unfiltered velocity field, ρ is the density, α is the volume fraction. Brackets denote smoothing.

In present work, a smoother proposed by Lafaurie et al. [98], namely a Laplacian filter that transforms the function into a smoother one:

$$\langle F(x)\rangle_P = \frac{\sum_{f=1}^{n}(F(x))_f S_f}{\sum_{f=1}^{n} S_f}, \tag{5-2}$$

where the subscript P denotes the cell index and f denotes the face index. The interpolated value $(F(x))_f$ at the face centre is calculated using linear interpolation.

Namely:

$$\langle \rho\rangle_P = \frac{\sum_{f=1}^{n}(\rho)_f S_f}{\sum_{f=1}^{n} S_f}, \tag{5-3}$$

$$\langle \rho u_i\rangle_P = \frac{\sum_{f=1}^{n}(\rho u_i)_f S_f}{\sum_{f=1}^{n} S_f}. \tag{5-4}$$

The formulation of the smoothed velocity keeps the same:

$$(\widetilde{u_i})_p = \frac{\langle \rho u_i\rangle_P}{\langle \rho\rangle_P} \quad \text{for } \alpha \geq 0.5. \tag{5-5}$$

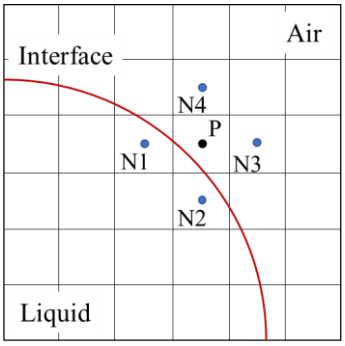

Figure 5-1 Air cell (P) and neighbour cells (N) used in density-weighted smoother.

Compared to the EV approach, the DW approach has advantages in two aspects. Numerically, the DW is relatively easy to apply to two-phase flow solvers. No coordinate information is required in the smoothing process, which means irregular or unstructured mesh is allowed. It is also easier for the DW approach to extend to 3D dimension as well. The DW approach is more reasonable in term of physical property. The two phases are considered when smoothing the velocity across the interface, while the denser phase has larger effect on the boundary layer. To distinguish the two solvers, the IBVOF solver combined with the EV approach is called EV-IBVOF solver, and the one with the DW approach is called DW-IBVOF solver.

5.3 2D simulations on unstructured mesh

In this section, the two cases, the steady stratified flow and the convection of a high-density droplet, investigated in Chapter 4 are used again to compare the two different approaches. The numerical setup for both cases keeps the same as Chapter 4. The differences are the meshes that the solvers use. For the EW-IBVOF solver, only uniform structured mesh is allowed while unstructured mesh is applied in the simulations of DW-IBVOF solver. In both section 5.3.1 and section 5.3.2, uniform structures mesh is firstly used to check the accuracy of the DW-IBVOF solver with comparison of the DW-IBVOF solver and the original interFoam solver. Locally refined unstructured mesh is then used to validate its robustness.

5.3.1 Steady stratified flow with DW-IBVOF solver

In order to check the DW-IBVOF in dealing with the spurious velocities, the case A4 and case B4 in Chapter 4 with high density ratios are selected in this section. As shown in Figure 5-2 and Figure 5-3, two set of meshes are used in the simulations. In the first mesh, uniform square cells are applied cover the whole computational domain with the mesh size $\Delta x = \Delta y = \frac{5}{128} m$. In the unstructured mesh, a refinement zone covering the interface is added based on a coarser background mesh. The mesh size in the refined interface zone is the same with the first uniform mesh.

Horizontal velocity profiles on section x= 5 m using the three different solvers are compared with each other in Figure 5-4. In these very simple test cases, the profiles with the DW-IBVOF solver on both meshes are almost the same as the EV-IBVOF solver on the uniform structured mesh.

As shown in Figure 5-5, the difference between the values of Relative error ϵ_U obtained from the two IBVOF solvers is very small. This means that the DW approach also successfully extrapolate the velocity of the denser phase slightly below the interface to the velocity of the lighter phase slightly above the interface through the high-density ratio. The spurious velocities are suppressed in the DW-IBVOF solver.

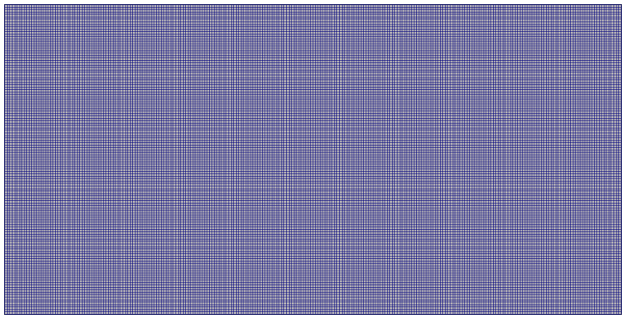

Figure 5-2 Uniform structured mesh for steady stratified flow

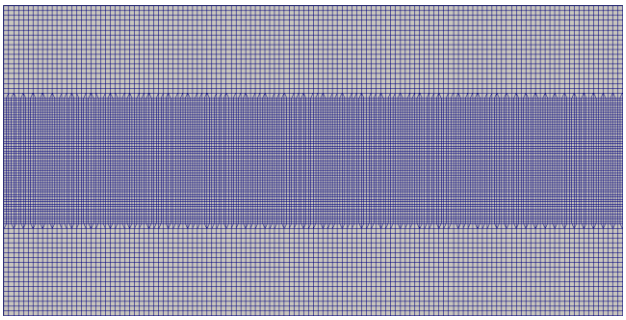

Figure 5-3 Local refined unstructured mesh for steady stratified flow.

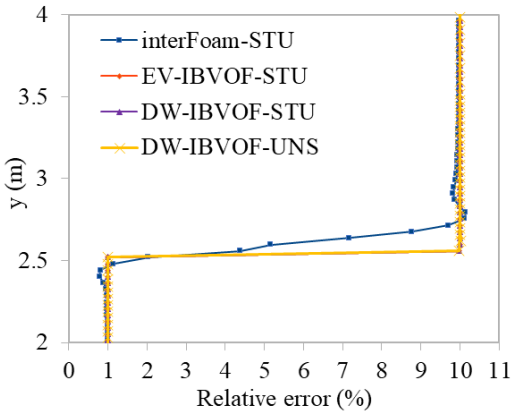

(a) Case A4

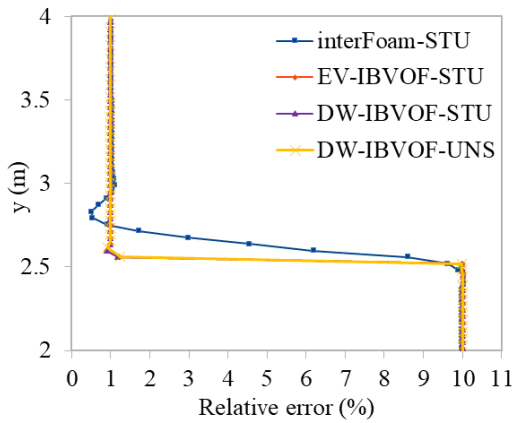

(b) Case B4

Figure 5-4 Horizontal velocity profiles on section x= 5 m using different solvers.

What's more, the DW-IBVOF shows its ability on the unstructured mesh. Compared to the uniform mesh with 32, 768 cells, the locally refined unstructured mesh contains 18,176 cells, which is much less. But the accuracy of the DW-IBVOF solver does not affect by the reduced meshes. In this stratified flow problem, the mesh size in the interface zone is the most important parameter in numerical simulations. In ship and ocean engineering problems, it is usually impossible to generated uniform mesh around complex ships or other offshore structures and refinements are usually required in the free surface area in breaking wave problems. It is therefore important for the two-phase solver to be robust with respect to general mesh systems.

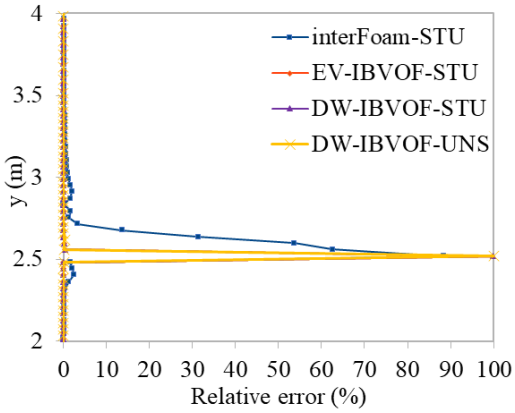

(a) Case A4

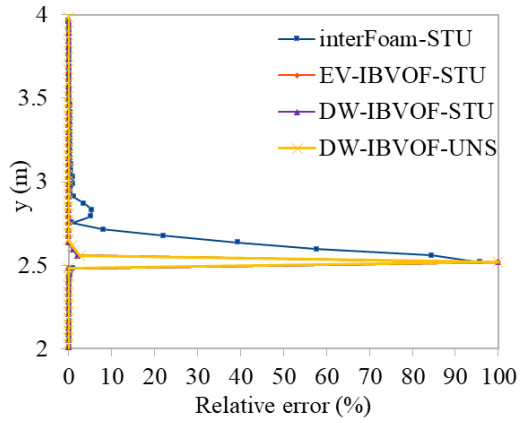

(b) Case B4

Figure 5-5 Relative error ϵ_U on section x=5m using different solvers.

5.3.2 2D simulations of a high-density droplet convection

Similar to the steady stratified flow cases, the high-density droplet convection case is used in this section to further validate the proposed DW-IBVOF solver. The numerical setup keeps the same as section 4.3 and the results obtained with the interFoam and the EV-IBVOF solver with uniform structured mesh with 128×64, 256×128 to 512×256 square cells are used directly in this section. In the simulations with the DW-IBVOF, however, unstructured meshes are used accordingly. The mesh type is shown in Figure 5-6. For the coarsest mesh, shown in Figure 5-6 (a),the mesh sizes in both x- and y- direction are $\Delta x = \Delta y = \frac{5}{64}m$. The mesh is the same as the coarsest uniform mesh 128×64. A finer mesh is generated by adding a refinement zone covering the interface region. The mesh sizes near the interface are $\Delta x = \Delta y = \frac{5}{128}m$. In the finest mesh, another refinement zone is added on the second mesh and the finest mesh sizes are $\Delta x = \Delta y = \frac{5}{256}m$. In this case, it is the mesh sizes near the interface that really matters in the simulations. The usage of unstructured mesh maintains the accuracy of the simulation on the one hand and reduces the calculation amount on the other hand.

Similar to section 4.3, the velocity profiles at early stage and the final shape of the interface obtained with the three two-phase flow solvers are compared with each other. As shown in Figure 5-7, the velocity profile using the DW-IBVOF solver is very closed to the EV-IBVOF solver at the early stage. This is reasonable since the only difference between the two solver is the different operation when drive the lighter phase above the interface by the velocity of the denser phase. In the EV approach, this aim is achieved through pure mathematical operations while the DW approach is

through density weighting. When it comes to the problems with density ratios equals to 10e6, the resulting value of the lighter phase with DW approach almost equals to the denser phase next to it.

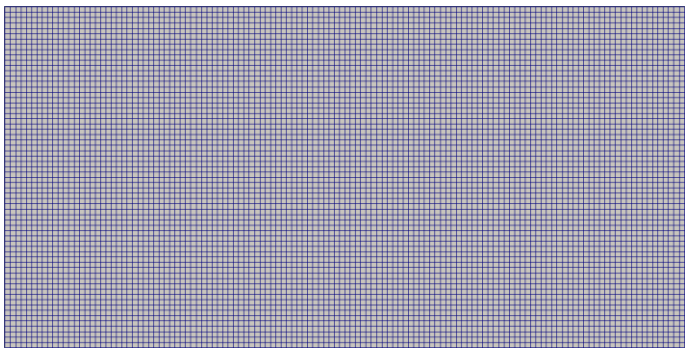

(a) Square cells

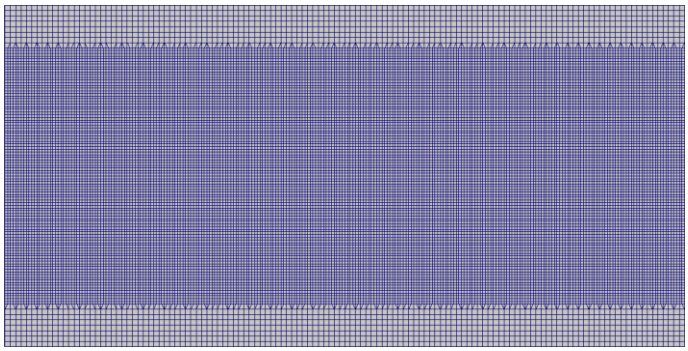

(b) Square cells and one refinement zone

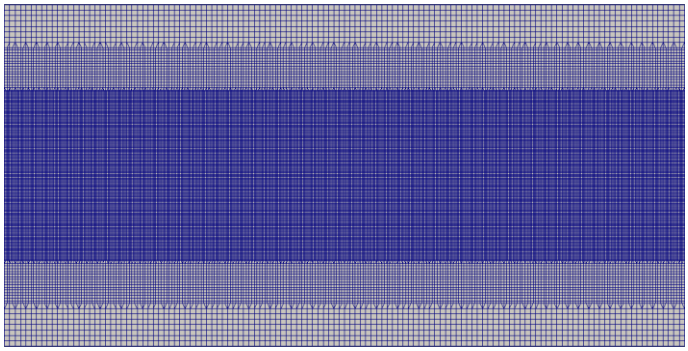

(c) Square cells and two refinement zones

Figure 5-6 Unstructured mesh used in the simulation with the DW-IBVOF solver

Though the velocity field obtained with the two IBVOF solvers are very simlar at the early stage, the discrepancies between the two solvers grows with time. Figure 5-8, Figure 5-9 and Figure 5-10 show the final shape of the interface with different mesh sizes. In the simulations of the interFoam solver and the EV-IBVOF, the uniform structured meshes are used while the unstructured mesh with the corresponding minimum mesh sizes are used in the simulations of the DW-IBVOF solver. In terms of interface shape conservation, the DW-IBVOF solver provides a best performance.

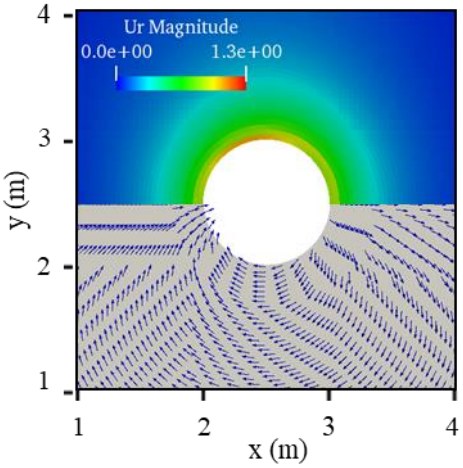

(a) One phase solver

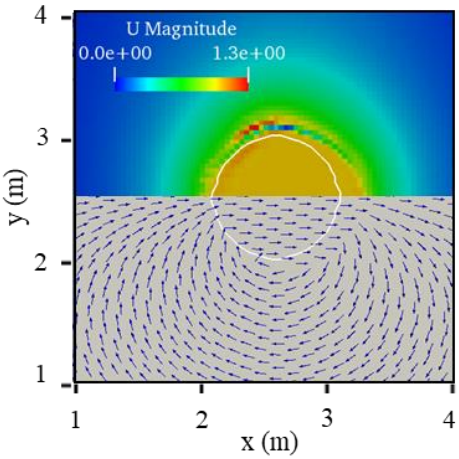

(b) InterFoam solver

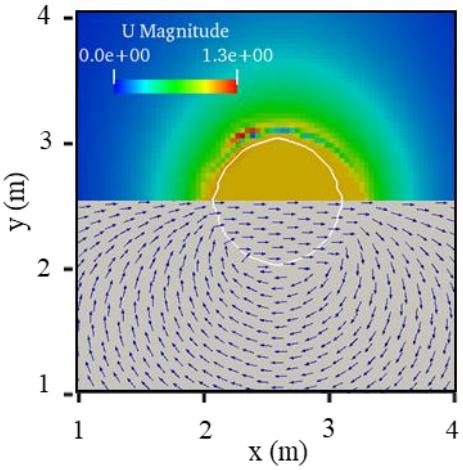

(c) EV-IBVOF solver

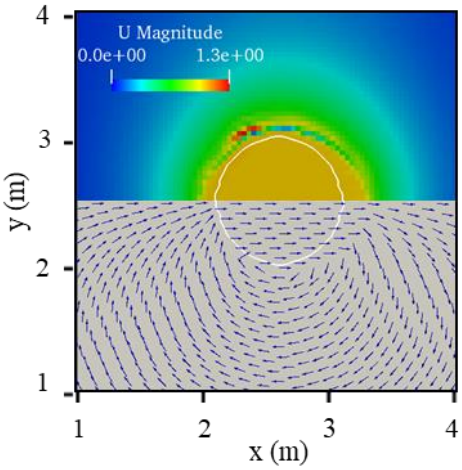

(d) DW-IBVOF solver

Figure 5-7 Velocity field at t=0.1s with mesh size $\Delta x = \Delta y = \frac{5}{128} m$ near the interface. The top half shows the coloured velocity magnitude, and the bottom half shows the velocity direction with arrows.

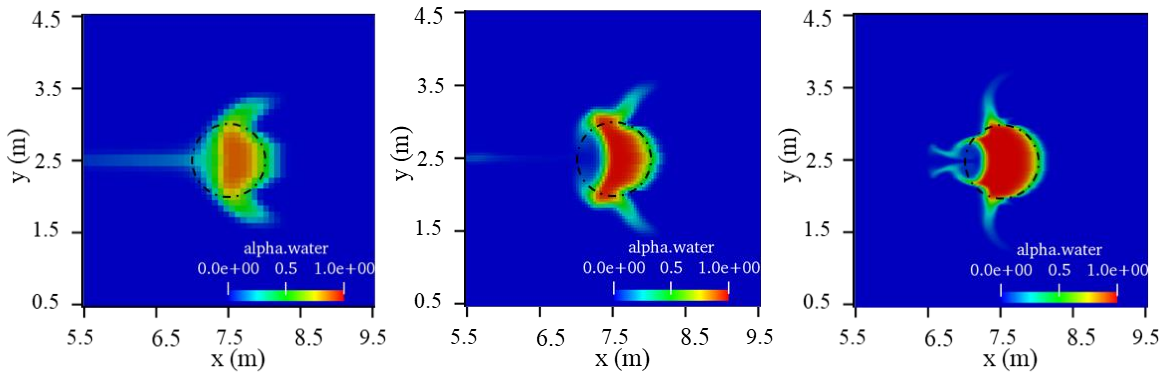

(a) $\Delta x = 5/64$ (b) $\Delta x = 5/128$ (c) $\Delta x = 5/256$

Figure 5-8 Volume fraction α distribution with the interFoam solver on structured mesh at t = 5s.

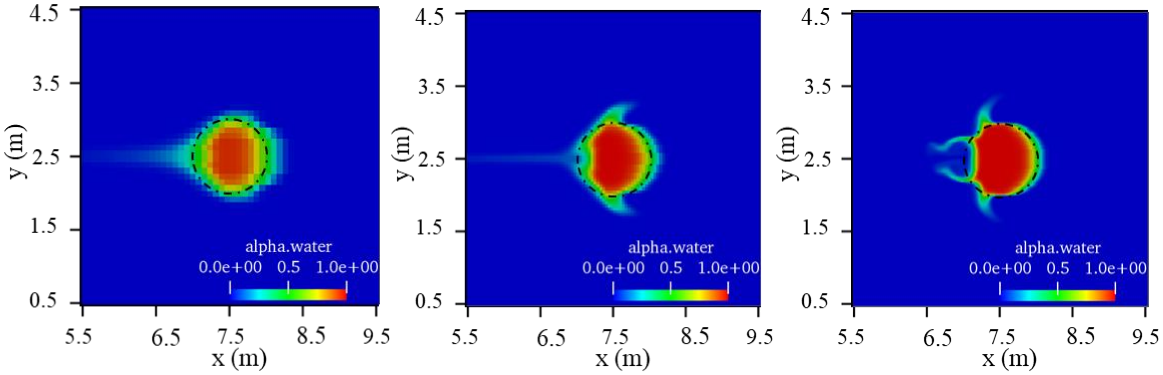

(a) $\Delta x = 5/64$ (b) $\Delta x = 5/128$ (c) $\Delta x = 5/256$

Figure 5-9 Volume fraction α distribution with the EV-IBVOF solver on structured mesh at t = 5s.

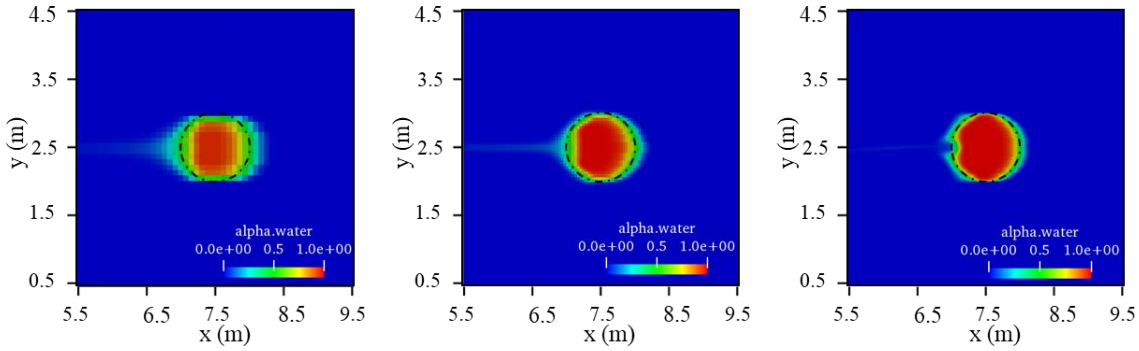

(a) $\min \Delta x = 5/64$ (b) $\min \Delta x = 5/128$ (c) $\min \Delta x = 5/256$

Figure 5-10 Volume fraction α distribution with the DW-IBVOF solver on unstructured mesh at t = 5s.

Compared to the results with the interFoam solver, the EV-IBVOF solver indeed suppress sightly the unphysical tearing of the interface. However, the discrepancies between numerical results and exact solution still exist. The position and shape of the wiggly surface obtained with the EV-IBVOF solver are very similar to that with the interFoam solver especially with the finer mesh (see Figure 5-9). The ability of the proposed EV-IBVOF solver is therefore doubted when it comes to ship hydrodynamic problems with long-term simulations. The extrapolated velocity from the denser phase to the lighter phase via pure mathematic operation may be not good enough.

As shown in Figure 5-10, the final shapes of the droplet obtained with the DW-IBVOF solver are smoothed and closer to the perfect circle on all the mesh sizes. Major part of the deformation generated in the results of the interFoam and EV-IBVOF solvers are eliminated, though a small notch is observed on the left side of the droplet on the finest mesh. Even though the effects of the EV-IBVOF and the DW-IBVOF solvers to the simulation results don't show big differences in the case of steady stratified flow analysed in section 5.3.1, the DW-IBVOF solver shows its advantages in dealing with problems with a band of layers that the value of α transmit from 0 to 1.

To demonstrate the differences between the two approaches in velocity reconstruction, a simplified test is designed. As shown in Figure 5-12, the value of the volume fraction α distribution and the momentum equation deduced velocity field for each cell is given the same number. The position of the interface is shown with the iso-surface α=0.5 in a red line. The red line is added to divide the two phases for visualization, but in the calculation, a band of layers with α=0.2 and α=0.8 are used. According to the definition of boundary layer cells in section 3.4.1, the velocities of the cells with α=0.2 are required to reconstructed. Take the cell P for example, the reconstructed velocity with the two different approach is shown in Figure 5-13. The value of the momentum equation deduced velocity of cell P is 0.2.

In the EV approach, the reconstructed velocity $\mathbf{u}^N$ of cell P should be similar to the closest denser phase cell, which is 0.8 in this test, so that the velocity of denser phase extends to the lighter phase. It is true that the gradient of velocity across the interface has been reduced in this process. However, this operation enlarges gradient of velocity on the lighter phase side. Though not as strong as the discontinuous velocity across the interface, the effect of this sudden increase in velocity on the lighter phase side on the final velocity field still exist, especially for the cases with a wide band of transition layers. As analysed in section 4.3.1and section 5.3.2, the non-viscous vortex is generated due to the large velocity gradients in the lighter phase region and eventually results in spurious velocity in the denser phase and distort the interface.

In the DW approach, even though the velocity of boundary cells with α=0.2 is required to be reconstructed, the denser phase that contains in the cell is considered during the velocity

smoothing process. The value of the smoothed velocity for the boundary cell P is 0.34, which is between the original momentum equation deduced velocity 0.2 and the straightforward extrapolated velocity 0.8. As shown in Figure 5-12, the gradients of velocity on both phase side are smoothed by the density weights. Compared to the EV approach, it is more reasonable for the DW-IBVOF approach since the effect of the denser phase should not be neglected. The denser phase may domain the cell behaviour of the cell due to inertia if the density ratio is large.

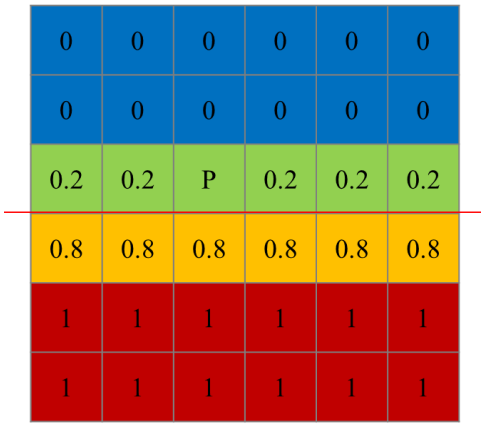

Figure 5-11 Volume fraction α distribution and velocity field.

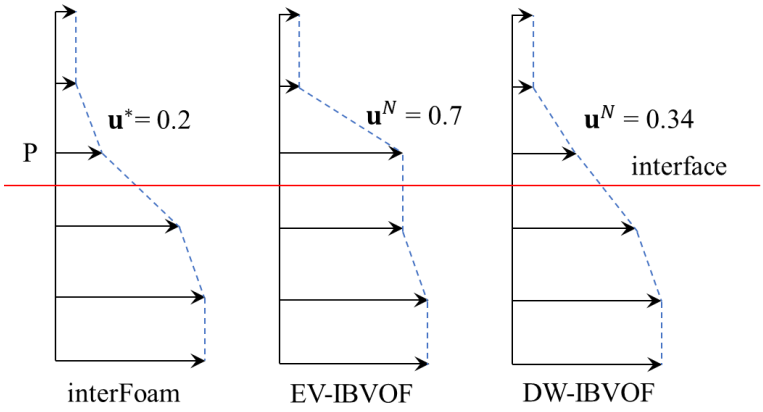

Figure 5-12 Momentum equation deduced velocity and constructed velocity with two approaches.

Similar to the analysis in section 4.3.2, the three error measures, volume conservation, shape preservation and sharpness, are calculated to compare the two IBVOF solvers. For volume conservation (mass conservation), both solvers perform very well. Though small differences are observed in Figure 5-13 (a), the maximum value of the error is less than 8e-05 which is smaller than the original interFoam solver.

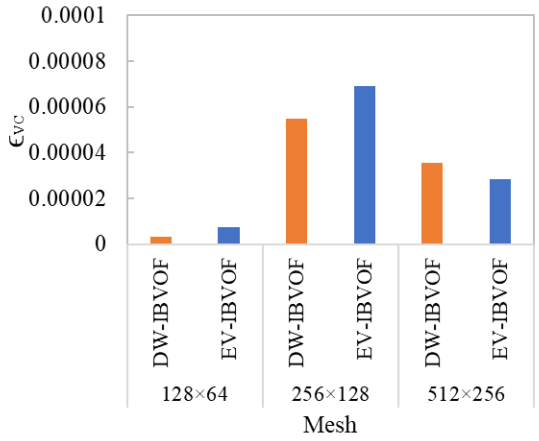

(a) Volume conservation, ϵ_{VC}.

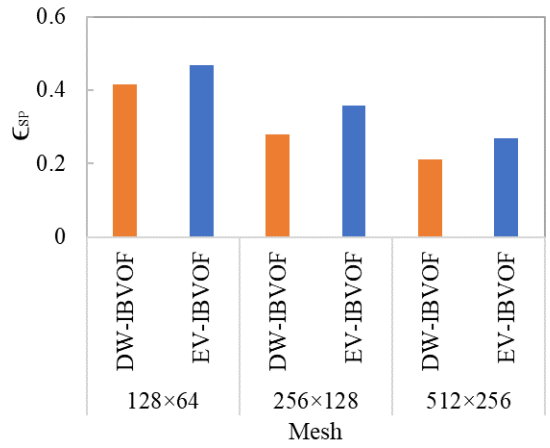

(b) Shape preservation, ϵ_{SP}.

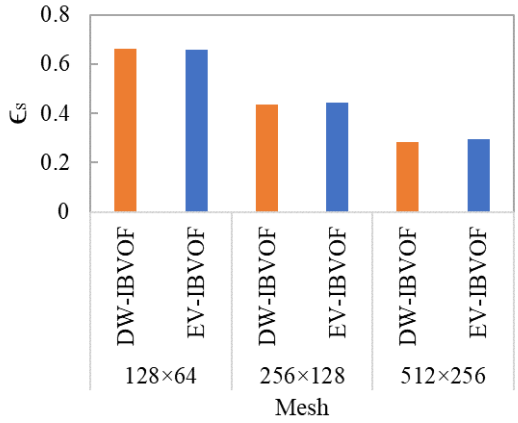

(c) Sharpness, ϵ_S.

Figure 5-13 Performance for high-density droplet with DW- and EV-IBVOF solvers at t = 5s.

In terms of shape preservation, the DW-IBVOF solver gives a better performance than the EV-IBVOF solver. The error ϵ_{SP} of DW-IBVOF solver is 15%-20% smaller than EV-IBVOF. It is therefore evident that the density-weight smoothing method is more reasonable than the extrapolated velocity approach for the cases with a band of layers with $0<\alpha<1$.

As for the sharpness errors ϵ_S, slightly smaller value is obtained with DW-IBVOF. The sharpness of the interface is mainly determined by the mesh size. Both solvers show monotonic space convergence.

It is therefore proved that the DW-IBVOF solver performs better than the EV-IBVOF solver. For the same uniform mesh, the DW-IBVOF solver shows higher accuracy in prediction of both velocity fields and volume fraction α distribution fields. What's more, unstructured mesh is allowed with the DW-IBVOF solver. The local refined mesh reduces the amount of calculation while maintaining the accuracy. It is also easier for the DW approach to extend to 3D simulations. In order to provide better predictions of two-phase flow simulations, the DW-IBVOF solver is selected as an appropriate resolution for all of the future studies in this work.

5.4 3D high-density droplet simulation

With the DW-IBVOF solver well verified by the 2D test problems, it is now extended to prediction of 3D fluid flows. The simple test case, transport of a very-high density fluid sphere, is extended to 3D simulations to further validate the new solver.

The computation is conducted for a domain of [0 m, 10 m]×[0 m, 5 m] ×[0 m, 5 m]. A sphere of fluid droplet with diameter D=1 m is initially placed in the air with its center at (2.5m, 2.5m, 2.5m). The droplet is given a constant horizonal velocity $\mathbf{U}_l = (1,0,0)$ m/s whilst the gas is initially at rest. Other numerical setups keep the same as the 2D case investigated in section 4.3 and section 5.3.2. Both viscous effects and surface tension are neglected in this case. Theoretically, the high-density droplet is expected to remain perfectly circular when passing through the air.

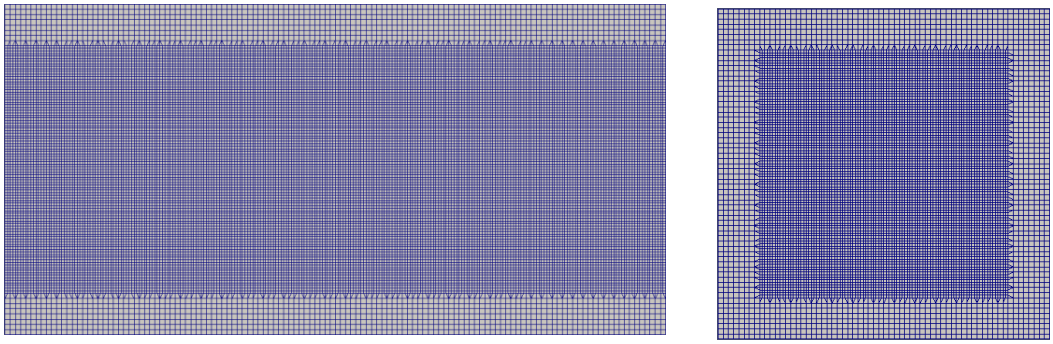

(a) Cross section at z= 2.5m (b) Cross section at x= 5m

Figure 5-14 Computational mesh including a local refined zone.

Two sets of mesh are used in this section. The first one is a uniform grid with $\Delta x = \Delta y = \Delta z = \frac{5}{64}m$. The number of cells in the whole domain is 524,288. The second set mesh is unstructured mesh as shown in Figure 5-14. A refinement zone covering the sphere region is added based on the uniform mesh. The minimum mesh size near the interface is $\Delta x = \Delta y = \Delta z = \frac{5}{128}m$. The number of cells for the finer mesh reaches 2,887,168. For both meshes, adaptive time steps are used based on a maximum allowed Courant number, Co=0.2.

Again, the velocity field in the early stages of the simulation, t=0.1s, is first analysed. Figure 5-15 and Figure 5-16 show the velocity field at section z= 2.5m with the interFoam and the DW-IBVOF solvers respectively. In order to highlight the difference of velocity values between the two solvers, the velocity range in both figures is set from 0.5 m/s to 1.05 m/s, which is the maximum value of velocity obtained from the interFoam solver with the coarse mesh.

In order to highlight the difference of velocity fields between the interFoam and DW-IBVOF solvers, the velocity ranges in Figure 5-15 and Figure 5-16 are set from 0.5 m/s to 1.08m/s. Spurious velocities are smaller than that in the 2D simulations but still presents on the left side of the droplet. The maximum value of velocity in the interFoam simulations is 1.08 m/s with mesh $\Delta x = \Delta y = \Delta z = \frac{5}{64}m$ and 1.03 m/s with mesh $\Delta x = \Delta y = \Delta z = \frac{5}{128}m$, while 1.02 m/s and 1.01m/s in the DV-IBVOF solver simulations accordingly. The spurious velocities accumulate with time and eventually affect the shape of the interface.

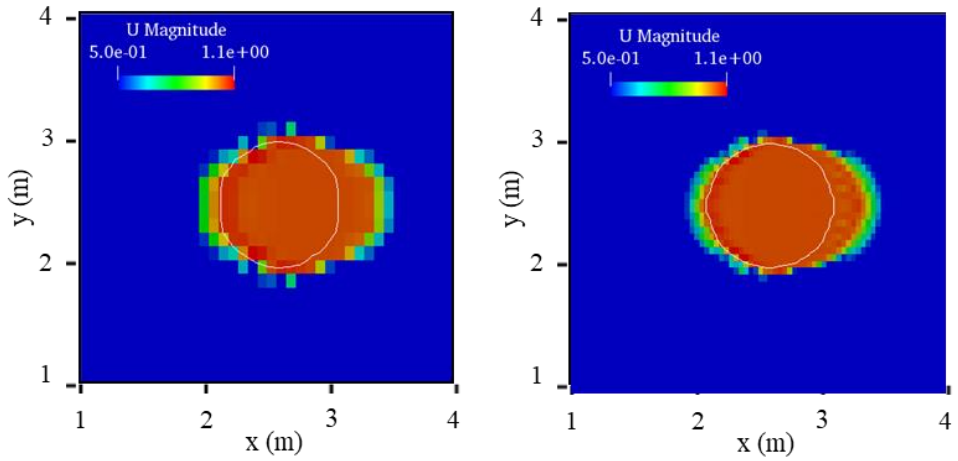

(a) $\Delta x = \Delta y = \Delta z = \frac{5}{64} m$ (b)$\Delta x = \Delta y = \Delta z = \frac{5}{128} m$

Figure 5-15 Velocity field at t= 0.1 s with interFoam solver at cross section *z*=2.5m near the interface.

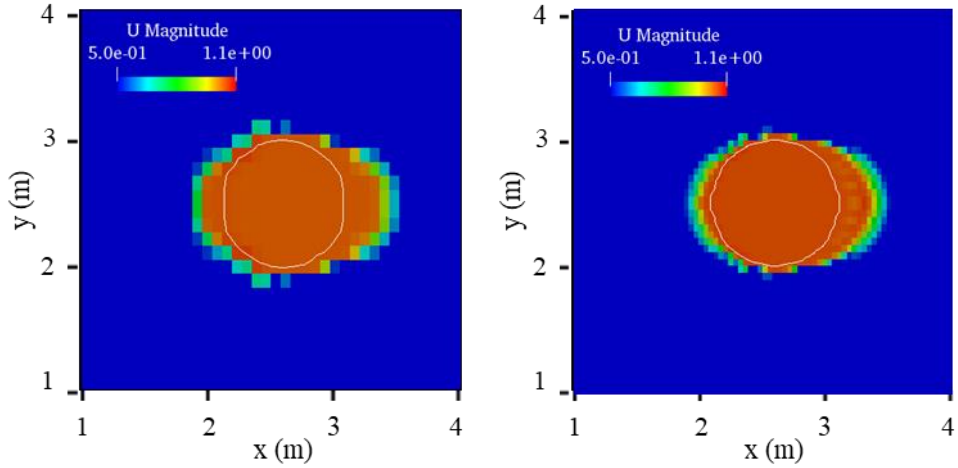

(a) $\Delta x = \Delta y = \Delta z = \frac{5}{64} m$ (b) $\Delta x = \Delta y = \Delta z = \frac{5}{128} m$

Figure 5-16 Velocity field at t= 0.1 s with DW-IBVOF solver at cross section *z*=2.5m near the interface.

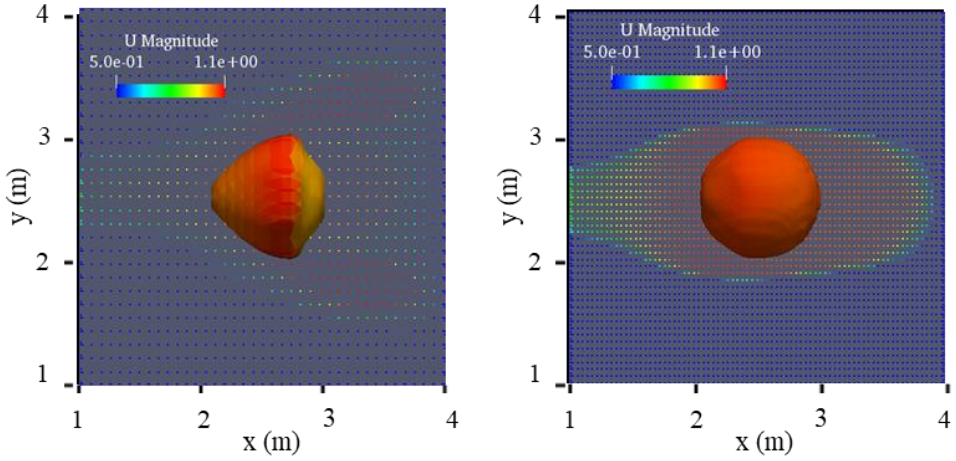

(a) $\Delta x = \Delta y = \Delta z = \frac{5}{64} m$ (b) $\Delta x = \Delta y = \Delta z = \frac{5}{128} m$

Figure 5-17 3D iso-surface at t=5 s with interFoam solver and velocity field at cross section *z*=2.5m coloured by velocity.

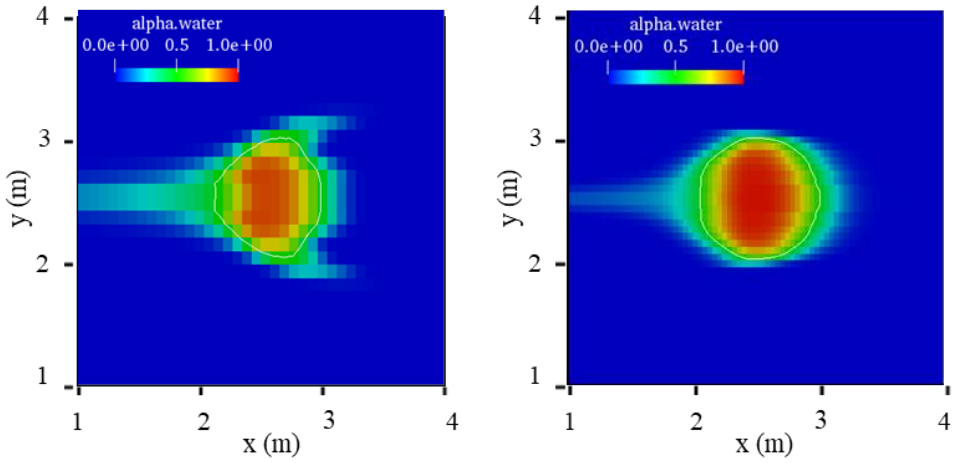

(a) $\Delta x = \Delta y = \Delta z = \frac{5}{64} m$ (b) $\Delta x = \Delta y = \Delta z = \frac{5}{128} m$

Figure 5-18 Volume fraction α distribution at t=5 s with interFoam solver at cross section *z*=2.5m coloured by velocity.

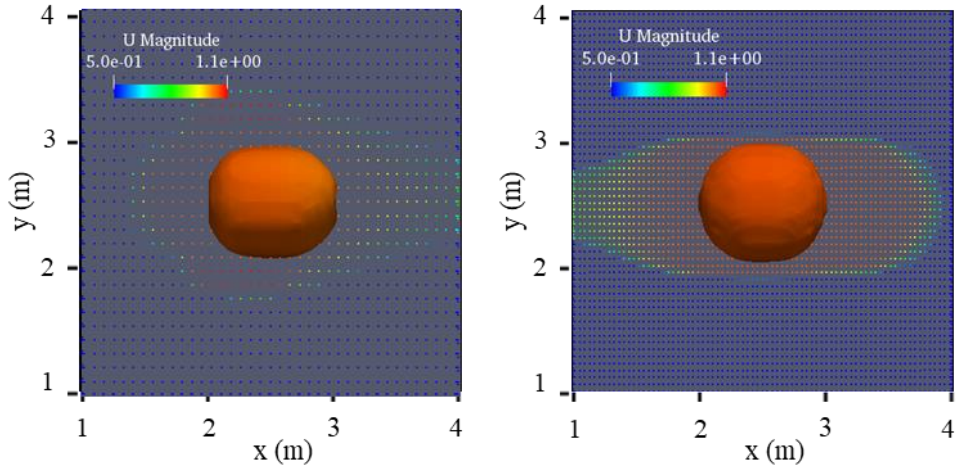

(a) $\Delta x = \Delta y = \Delta z = \frac{5}{64} m$ (b) $\Delta x = \Delta y = \Delta z = \frac{5}{128} m$

Figure 5-19 3D iso-surface at t=5 s with DW-IBVOF solver and velocity field at cross section *z*=2.5m coloured by velocity.

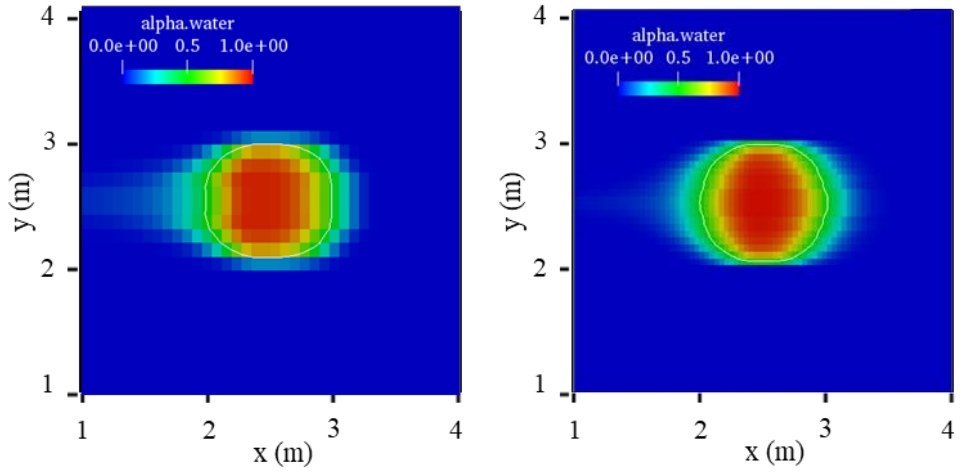

(a) $\Delta x = \Delta y = \Delta z = \frac{5}{64} m$ (b) $\Delta x = \Delta y = \Delta z = \frac{5}{128} m$

Figure 5-20 Volume fraction α distribution at t=5 s with DW-IBVOF solver at cross section *z*=2.5m coloured by velocity.

Figure 5-17 and Figure 5-19 show the final shape and position of the interface at t= 5s with the two solvers and the volume fraction α distributions at the mid-cross section at z- direction are shown in Figure 5-18 and Figure 5-20. The volume fraction distribution at the mid-cross sections obtained with interFoam with the coarse mesh is very similar to the 2D results with the same mese size but much closer to the theoretical solution. Though the minimum mesh size in each direction in the fine mesh is half of the coarse mesh, one cell in the coarse mesh is split into 8 cells. In the 3D simulations,

mesh refinement leads to a substantial increase in the amount of calculation. It is therefore more important to improve the accuracy of the two-phase flow solvers.

5.5 Viscous two-phase Poiseuille Flows

Besides the density, viscosity is another important parameter in general two-phase flow simulations. The basic idea of the DW-IBVOF method in section 3.4 is designed velocity boundary layer similar to non-slip boundary conditions in Fluid-Structure interactions problems. In this section, the influence of the viscosity to the generation of spurious velocity is investigated.

The layered Poiseuille flow is classical and simple two-phase benchmark problems. Owing to the shear phenomena in the layered flows, the simulations are sensitive to numerical errors and it is therefore a good test case for validating the two-phase flow solvers. The configuration of the problem is illustrated in Figure 5-21. Two incompressible, immiscible flows flow in the z- direction through the horizontal channel with dimensions of [0, 5]$\times$[-1, 1]. Initially, the phase 1 fluid is placed in the lower region of $-1 \leq y < 0$ and the region of $0 \leq y \leq 1$ is filled with phase 2. Gravity and the surface tension forces are neglected. The flow is driven by a horizontal pressure gradient.

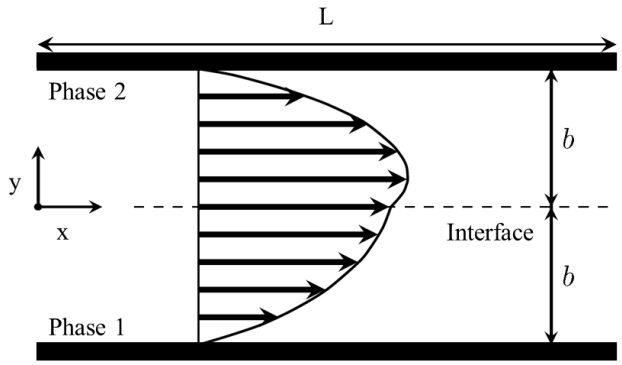

Figure 5-21 Configuration of the viscous two-phase Poiseuille Flow.

In this case, the focus is kept on the viscosity so the densities of the two phases are considered equally as $\rho_1 = \rho_2 = 10\ kg/m^3$. Three different sets of viscosity are carried out (as shown in Table 5-1) to investigate the effect of viscosity ratio on the velocity profile. The pressure difference between the left and the right boundary is set as $\Delta p = 2\ Pa$. No-slip boundary conditions are imposed on the upper and the bottom walls and Neumann conditions are assumed on the velocity on the left and the right boundaries while the pressures are fixed. The whole domain is discretised using a uniform Cartesian mesh with $\Delta x = \Delta y = 0.02\ m$.

For long times, a steady solution is obtained for the two-phase Poiseuille flow and the analytical solution for the horizontal velocity field[99]:

$$u_{x,1}(y) = \frac{\Delta p b^2}{2\rho L \mu_2}\left[-\left(\frac{y}{b}\right)^2 - \frac{y}{b}\left(\frac{\mu_1-\mu_2}{\mu_1+\mu_2}\right) + \frac{2\mu_2}{\mu_1+\mu_2}\right], \quad -b \le y < 0 \tag{5-6}$$

$$u_{x,2}(y) = \frac{\Delta p b^2}{2\rho L \mu_1}\left[-\left(\frac{y}{b}\right)^2 - \frac{y}{b}\left(\frac{\mu_1-\mu_2}{\mu_1+\mu_2}\right) + \frac{2\mu_1}{\mu_1+\mu_2}\right], \quad 0 \le y \le b \tag{5-7}$$

where *L* is the length of the horizontal wall and *b* is the distance between the interface and the wall boundaries. The comparison of the velocity profile between interFoam, DW-BVOF solvers and analytical solutions for three different viscosity ratios is present in Figure 5-22. The velocity scale is here chosen as $\bar{u}$, the average velocity of the channel. Both the two solvers show close agreement with the exact solutions even for a relative high viscosity ratio.

Table 5-1 Physical parameters for two-phase Poiseuille flow.

$\mu_1(Ns/m^2)$	$\mu_2(Ns/m^2)$	μ_1/μ_2
5	1	5:1
10	1	10:1
10	0.1	100:1

To quantitively investigate the effect of viscosity to the velocity field, the following relative error is applied:

$$E_u = \frac{\sum_y |u_x^n(y) - u_x^a(y)|}{\sum_y |u_x^a(y)|}, \tag{5-8}$$

where the subscripts *n* and *a* denote the numerical and analytical solutions. The results are listed in Table 5-2. It is found that a very small relative error can be derived by both solvers. The relative errors do not grow much with viscosity ratio and no spurious velocity is generated near the interface in the simulations of the original interFoam solver.

As shown in Figure 5-22 and Table 5-2, the differences between the two solvers are extremely slight. The designed boundary layer in DW-IBVOF solver does not harm the accuracy of the interFoam solver. One of the reasons is that the mesh size is relatively small and the velocities of only one layer of mesh above the interface are modified by the DW approach. A more important reason is that the densities of the two phases are equal. The two phases have the same weights when smoothing the velocity fields. The smoothed velocity field does not show as much differences as section 4.2 with large density ratios.

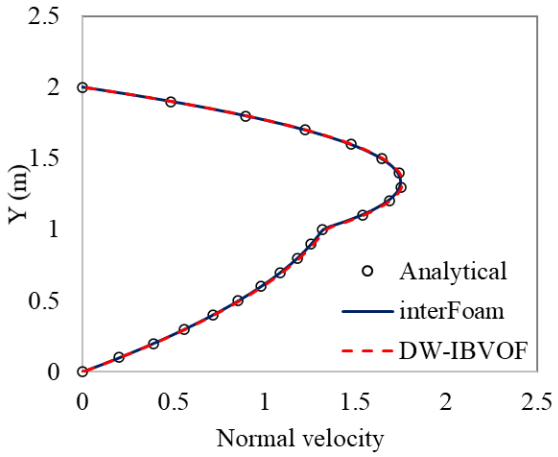

(a) Viscosity ratio 5

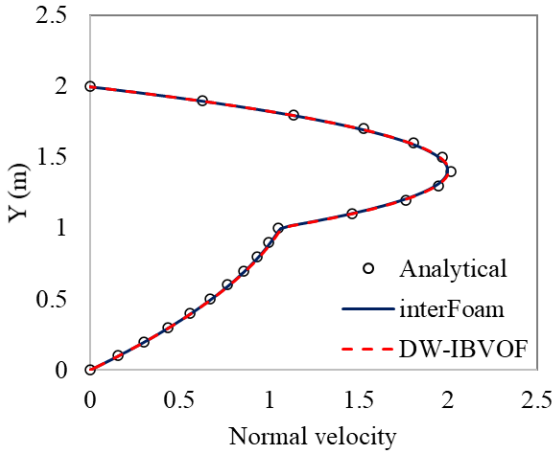

(b) Viscosity ratio 10

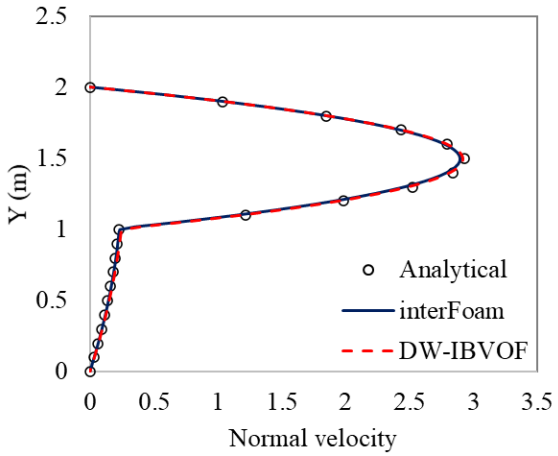

(c) Viscosity ratio 100

Figure 5-22 Comparison of the velocity profile between interFoam, DW-BVOF solvers and analytical solutions for three different viscosity ratios.

Table 5-2 Relative errors of the horizontal velocity in layered Poiseuille flow.

Viscosity ratio	interFoam	DW-IBVOF
5	7.9e-3	8.5e-3
10	5.9e-3	6.2e-3
100	9.2e-3	7.8e-3

5.6 Surface tension effect

Surface tension is another important parameter in the simulations of free surface flows. As mentioned in Chapter 2, the VOF methods are widely applied to problems with large interface movement and topological changes. Despite the popularity of the VOF methods, there are issues when applying them to surface-tension-dominated flows[64]. Parasitic currents are often observed around the interface in the numerical results of VOF simulations[59][100][101]. This problem arises from the instability of the surface tension algorithm to evaluate a constant interface curvature from the discontinuous volume fraction function field is one of the major issues in inertia-dominated flow simulations.

The values of the volume fraction that change over a thin region create errors in calculating the normal vectors and the curvature of the interface and eventually results in errors in evaluating the interfacial forces. In order to check the performance of the two solvers in simulation of surface-tension-dominated flows, a benchmark test, a circular droplet in static fluid, is used in this section.

The computation is conducted for a domain of [0 m, 1 m]×[0 m, 1 m] with a uniform grid. A droplet with diameter D=0.5 m is initially placed in the air with its centre at (0.5m, 0.5m). To keep focus on effect of surface tension to the velocity field, same density $\rho_1 = \rho_2 = 1\ kg/m^3$ and viscosity $\mu_1 = \mu_2 = 1\ kg/(m\ s)$ are set for the phases both inside and outside the droplet. Gravity is neglected in this case. The surface tension coefficient is $\sigma = 0.1\ N/m$. Periodic boundary conditions are imposed for the computational domain. Two sets of uniform mesh are considered, ranging from 60×60 to 120×120, while the maximum Courant number, Co, equals 0.1 and the maximum time step, 1e-4 s for limiting the growth if spurious velocities in both cases.

Figure 5-23 and Figure 5-24 show snapshots of the parasitic currents after the droplet has relaxed to its steady shape with the two solvers. The corresponding errors in velocity on different grid resolution are summarised in Table 5-3. Comparing the magnitude of the parasitic currents, the

currents are slightly reduced by the new solver. The refinement of mesh does not help to reduce the errors. It is reasonable in this case. The errors induced non-physical parasitic currents also exist in the fluid inside of the droplet due to the numerically computed curvature. The magnitude of velocity near the interface in the phase inside of the droplet is slightly smaller than the region outside of the droplet. That explains that maximum and average errors in velocity change little though the velocity field is smoothed.

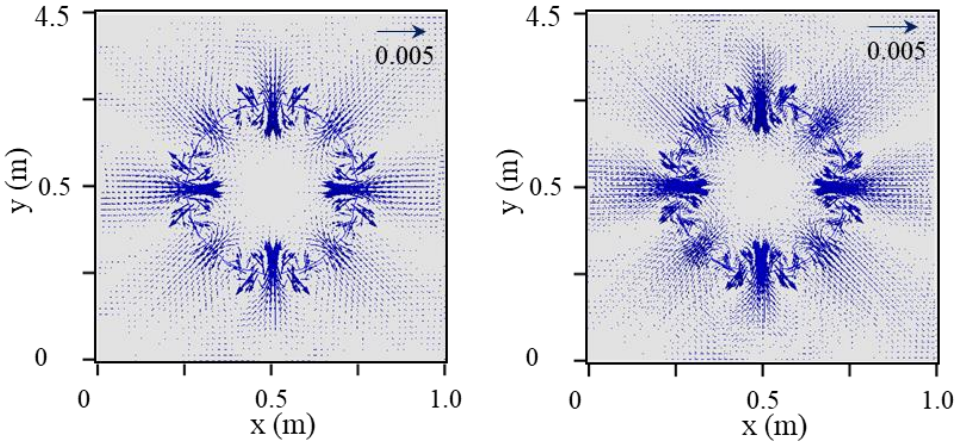

(a) $\Delta x = \Delta y = \frac{1}{60} m$ (b)$\Delta x = \Delta y = \frac{1}{120} m$

Figure 5-23 Snapshots of interface shape and the parasitic currents with the interFoam solver.

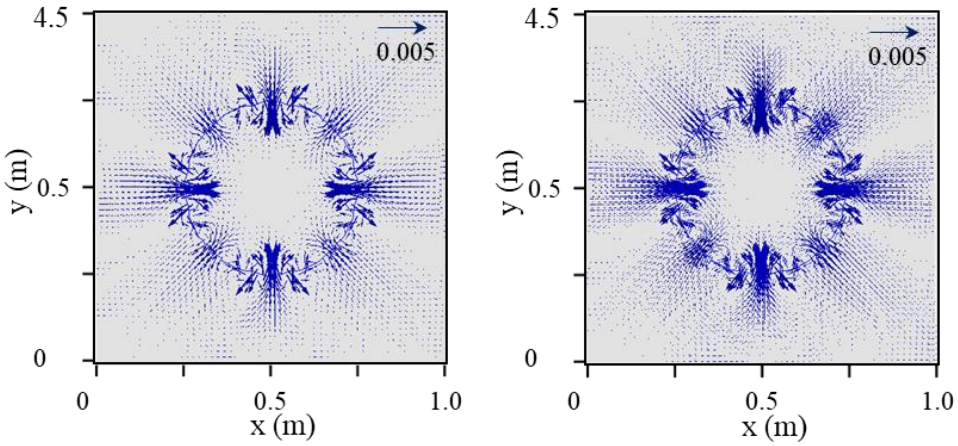

(a) $\Delta x = \Delta y = \frac{1}{60} m$ (b)$\Delta x = \Delta y = \frac{1}{120} m$

Figure 5-24 Snapshots of interface shape and the parasitic currents with the DW-IBVOF solver.

Unfortunately, the proposed DW-IBVOF solver fails to deal with the errors induced by the surface tension. These errors mainly be caused by the calculation of normal vectors and the curvature of the interface. Parasitic currents can be reduced by using a different, additional fields, such as a level set function[52], a height function[102] or a smoothed VOF function[64], that is used only to calculate curvature. An in-depth study of this parasitic currents, however, beyond the scope of the present discussion.

Table 5-3 Errors in velocity on different grid resolution for the static droplet.

Mesh size	interFoam		DW-IBVOF	
	Max $\|u\|$	Avg. $\|u\|$	Max $\|u\|$	Avg. $\|u\|$
1/60	5.1e-3	6.3e-6	4.5e-3	5.8e-6
1/120	4.9e-3	6.2e-6	4.3e-3	5.6e-6

5.7 Droplet splashing on thin liquid film

The dynamics of a droplet impact on a thin liquid file at short time are investigated in order to further validate the new two-phase flow solver. This problem is relatively real-life and is a common process in nature and industry, such as rain and ink-jet printing, where a robust and accurate flow solver is required. In this study, the experimental case with a droplet (diameter D= 4.2 mm) in [103] is simulated. The computation is conducted for a domain of [-7.5D, 7.5D] ×[0, 5D] with a uniform square grid. The droplet is initially placed in the air with its centre at (0, D) and a thin layer of liquid is filled with a height of h= 0.5D just below the droplet. The computational setup is shown in Fig. 19.

The droplet is given a constant downward velocity of $\mathbf{U}_0 = (\mathbf{0}, 5.099)$ m/s while the air and the liquid are initially at rest. Different from the test cases in section 4.1 and 4.2, viscosity of both phases and surface tension are considered. All the physical parameters of both phases are set the same as the experimental condition. The key dimensionless parameters for this problem are $Re = \frac{\rho_l U_0 D}{\mu_l} = 2010$, $We = \frac{\rho_l {U_0}^2 D}{\sigma} = 1168$, where ρ_l and μ_l are density and dynamic viscosity of the liquid phase and σ is the surface tension coefficient. The density and viscosity ratios of the two phases are $\frac{\rho_l}{\rho_g} = 1200$ and $\frac{\mu_l}{\mu_g} = 1486$. Three meshes are considered, ranging from 300×100, 600×200 to

900× 300, while the maximum Courant number, Co, equals 0.1 for limiting the growth if spurious velocities in all these cases.

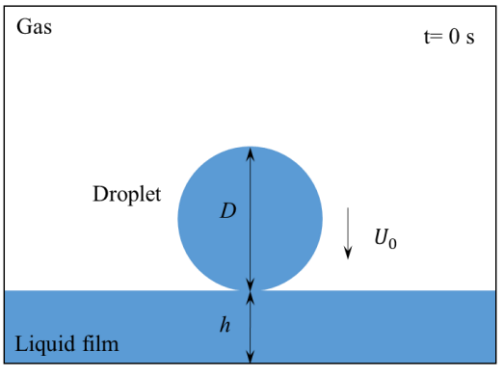

Figure 5-25 Model of a single droplet impact on a thin liquid film

The comparison of simulation results with experimental investigations in [103] at t= 0.3 ms, 1 ms and 3 ms is presented in Fig. 20. It is found that the numerical results from both solvers are in good agreement with the experimental observations. Three stages of droplet impact are captured with similar shapes and positions. A pair of liquid jet are generated immediately after impact from the neck region where the droplet contacts with the liquid film at t= 0.25 ms. Then the liquid jets move outward and transmit into a liquid crown at t= 1 ms. When the crown walls expand upwards, they become thinner with time and height. The height of crown wall increases at t= 3 ms. However, slight difference is observed between the two solvers at the shape of the thin crown wall and the angle between the crown wall and the liquid film. The evolution of the interface between liquid and gas and the velocity fields are enlarged and investigated.

Figure 5-27, Figure 5-28 and Figure 5-29show the velocity fields at the three stages. The fields are nearly symmetric. For visualization purpose, the figures are divided into two parts. The left half shows the coloured velocity magnitude, and the right half shows the velocity directions with arrows. The position of the interface (iso-surface with $\alpha = 0.5$) is shown with a purple line. Unfortunately, the velocity field is unavailable from the experiment since the technology limit, so the focus is on the difference between the two solvers and to investigate the effect of the designed layer.

As shown in Figure 5-27, thin liquid jets eject from the connected region between the droplet and liquid film surface with relative high velocities. According to theories in [104] and [105], this is caused by the large pressure gradient produced in the neck region. Similar jets and velocity increase are observed in both solvers, however, the velocity obtained from the interFoam is much higher than the IBVOF solver. The maximum value of velocity with the interFoam reaches 20.57 m/s near the tips of the jets while the maximum value in the IBVOF solution reaches 14.38 m/s. More specifically, the horizontal velocity components are higher while the vertical components are

similar. This leads to the different shape of the crown that transform form the jet sheet. What's more, the large velocity gradients generated across the interface finally results in a series of vortex especially in the air region as shown in Figure 5-28 (a).

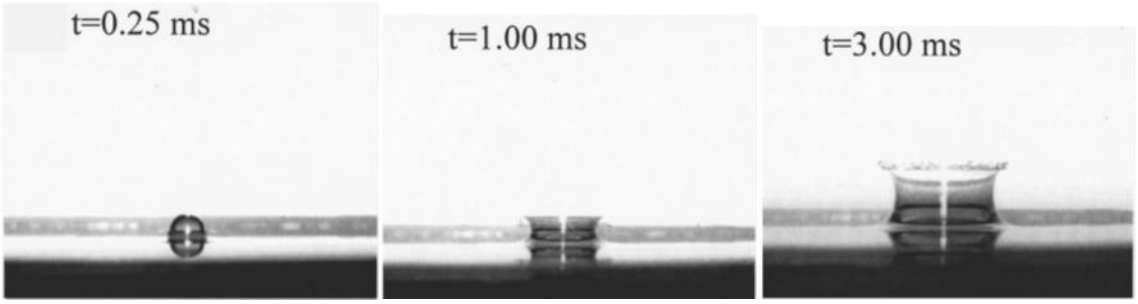

(a) Experimental images [103]

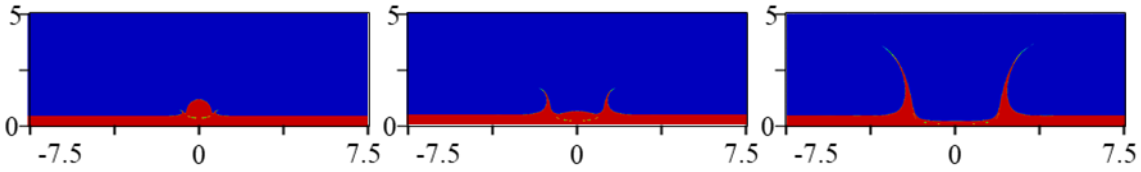

(b) interFoam solver

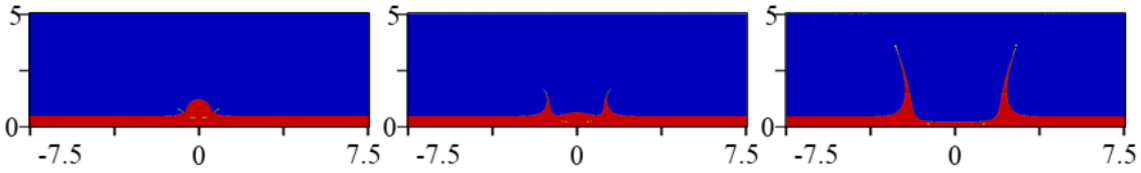

(c) IBVOF solver

Figure 5-26 Instantaneous profile of droplet splashing on a thin liquid film with the interFoam solver and the DW-IBVOF solver.

In the early stage (t= 0.25 ms) of droplet impact liquid film, it is clear to see that the liquid below the droplet moves downwards to the bottom of the domain because of the droplet impact. The velocity direction is than changed once the liquid reaches the bottom and radial flow is produced (t= 1 ms). The jets that initially generated by the droplet impact is pushed by the radial flow and expand upward into thin liquid sheets, which are called crown walls. Compared to the interFoam solutions, lower velocity magnitude and less vortexes are generated in the gas phase. The shape and position of the interface are similar to each other while the tips of the crown wall in the interFoam tends to advance to the horizontal direction, but almost vertical walls are observed with the IBVOF solver.

When the crown walls expend upwards, their thinness turns thinner and thinner with time and height since they meet the surrounding static gas and push it away. The velocities of the liquid keep decreasing by gravity at the same time. In the IBVOF solutions, the tips of crown wall turn blunt from t= 2.8 ms and break up into a droplet at t= 3ms (shown in Figure 5-29) which is also observed in the experimental image. However, the interFoam solver fails to capture the detached droplet. The thickness of the interface at the tips of the crown wall, the width of the region where the cell contains both liquid and gas, increases with time though the iso-surface with $\alpha = 0.5$ is getting shaper. It is therefore evident that the proposed IBVOF improves the accuracy of modelling of two-phase flows with high density ratio.

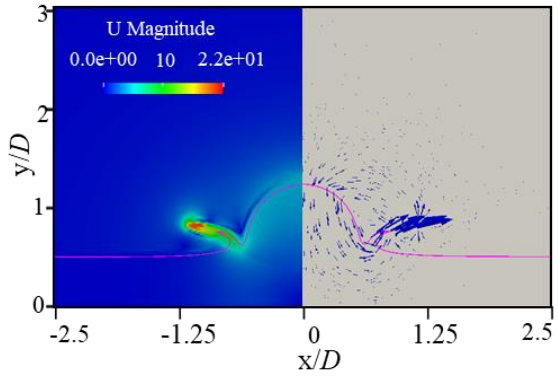

(a) InterFoam

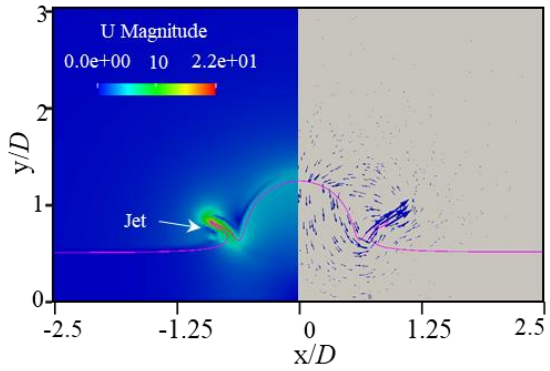

(b) IBVOF solver

Figure 5-27 Velocity field of droplet splashing with the interFoam solver and the DW-IBVOF solver at t= 0.3 ms.

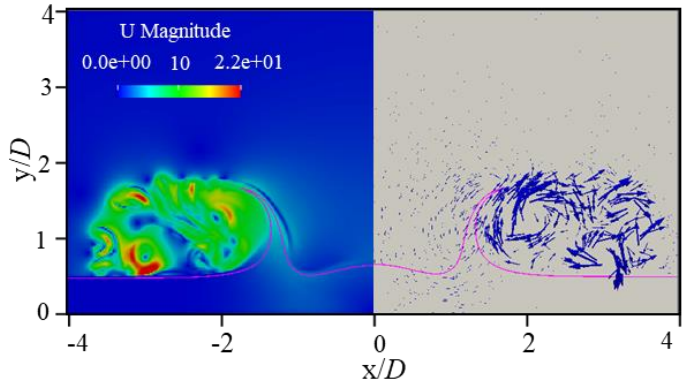

(a) InterFoam

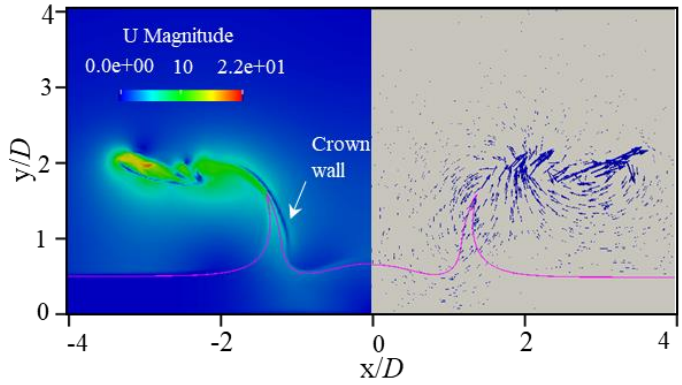

(b) IBVOF solver

Figure 5-28 Velocity field of droplet splashing with the interFoam solver and the DW-IBVOF solver at t= 1 ms.

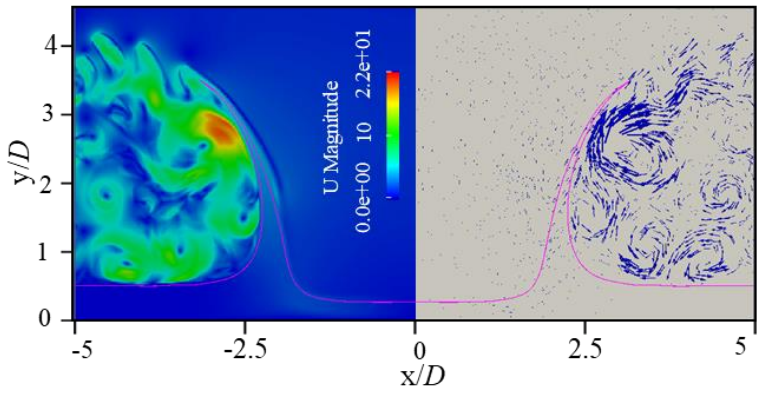

(a) InterFoam

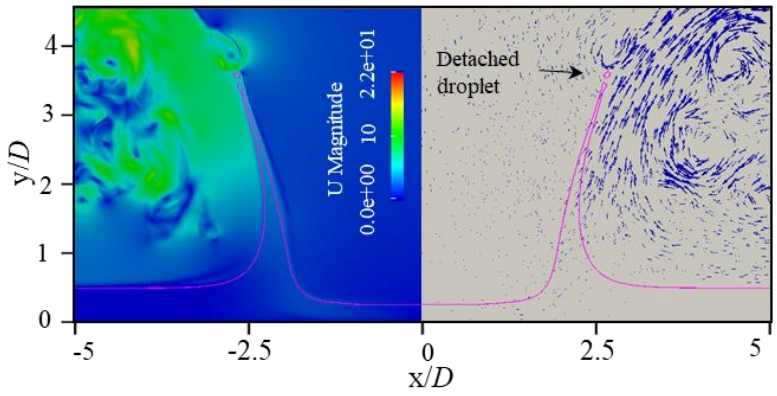

(b) IBVOF solver

Figure 5-29 Velocity field of droplet splashing with the interFoam solver and the DW-IBVOF solver at t= 3 ms.

The introduction of surface tension introduces more numerical errors to the case, which are not addressed in the present work. This is also the reason why the cases of steady stratified flow and convection of a high-density droplet, are designed to separate the two potential sources of problems and demonstrate the effect of a high-density ratio on the spurious velocity. Though compared to the first two cases, the last case, droplet splashing on thin liquid film, exhibits reduced differences between the two solver, the present IBVOF solver does improve the accuracy of modelling of two-phase flows with high density ratio, in particular the formation of droplets in the flow.

It is shown from the IBVOF method description that additional steps have to be performed (e.g., identification of interface, velocity extrapolation, IBM forcing) by comparison with the original interFoam solver. However, in the proposed method, the interface is identified directly from the original VOF function. The velocity extrapolation process and pressure update are only carried out very close to the interface.

5.8 Conclusion

The DW approach has been implemented to extend the application of the proposed IBVOF solver. Compare to the EV approach, more liquid and gas cells are used with the DW approach in the smoothing process and the denser has larger effect on the velocity in the designed free surface boundary due to the density weight. The DW-IBVOF solver is therefore more reasonable in terms of fluid physical property. The performance of the DW-IBVOF solver has been evaluated through the steady stratified flow and the 2D high-density droplet convection cases, where the spurious velocity generated near the interface has been well reduced.

What's more, it is easier of the DW-IBVOF solver to extend its applications to unstructured mesh cases and 3D simulations. No coordinate information is required in the smoothing process, which means irregular or unstructured mesh is allowed. The computed results of 3D high-density droplet simulation are compared with the original interFoam solver, and better performance is obtained in terms of shape preservation and sharpness.

The effect of fluid viscosity is investigated through the viscous two-phase Poiseuille flows. Excellent results are obtained by both the original interFoam solver and the proposed IBVOF solver. When the density of the two phases keeps the same, the viscosity ratios between the two phases do not generate the spurious velocity across the interface as the density ratios do.

Besides of the discontinuities in material properties, the inaccurate interface curvature is the other main source of spurious velocities. The IBVOF solver is also checked by the simulation of surface-tension-dominated flows, a benchmark test, a circular droplet in static fluid. Unfortunately, the proposed solver fails to deal with the parasitic currents raised form the instability of the surface tension algorithm.

The DW-IBVOF solver is finally applied to simulate a real-life problem of a droplet impact on a thin liquid file at short time and the computational results are compared with the original interFoam and published experimental data. The three stages of droplet impact observed in the experiment are well captured by the DW-IBVOF solver. The designed boundary layer smoothing of the velocity field helps to prevent the tearing of the interface due to the tangential velocity between the two phases across the interface. It is shown to improve the robustness and stability of two-phase flow simulations.

Chapter 6 Wave propagation and breaking up

6.1 Introduction

In two-phase flow simulations, wave propagation and break-up are very common and important phenomena that need to be considered in the design of ship and offshore structures. A thorough understanding of the physics of the nonlinear flow phenomena is necessary for the better insight into the two-phase flow problems and is widely investigated.

In this chapter, the performance of the proposed DW-IBVOF solver is further evaluated through two sets of numerical benchmark tests with solitary waves and Stokes waves. In both sets of benchmark tests, the fluids are first modelled as inviscid for wave propagation simulations. This assumption allows the comparison with the well-controlled potential theory. In the later cases of wave breaking, the influence of fluids viscosity and surface tension are considered, and the numerical results are compared with the published experimental data.

6.2 Solitary waves

Two benchmark tests, propagation and runup of a solitary wave [95], are firstly conducted to check the numerical stability and robustness of the new method for non-linear wave simulations. Viscosity and surface tension are neglected. This allows the direct comparison of the new solver and the original VOF solver in interface convection. The results of all the test cases are compared with the original VOF solver, analytical solutions, or one-phase flow solvers. Then, plunging wave breaking on a slope is simulated to demonstrate the capability of the new solver to capture strong air-water interactions in real world. The overall wave breaking process, wave surface profile and velocity field are investigated, and the results are in good agreement with published experimental data.

In this section, the new two-phase flow solver validated above is first tested against two benchmark problems defined by Pawel A[95]. In the first case, a solitary wave propagated in a numerical wave flume with a horizontal flat bottom. In the second one, a solitary wave runs up on a plane beach with a slope of $\theta = 10°$. In both benchmark cases, the fluids are set as inviscid and without surface tension. This allows the direct comparison of the two-phase flow solvers against the well-controlled potential theory without the influence of viscosity or other spurious effects. Then, a case of plunging breaking solitary waves on a slope is preformed to further validated the new solver in the application of free surface flow problems in the real world. Both viscosity and surface tension are considered in this case and the results are compared with experimental data.

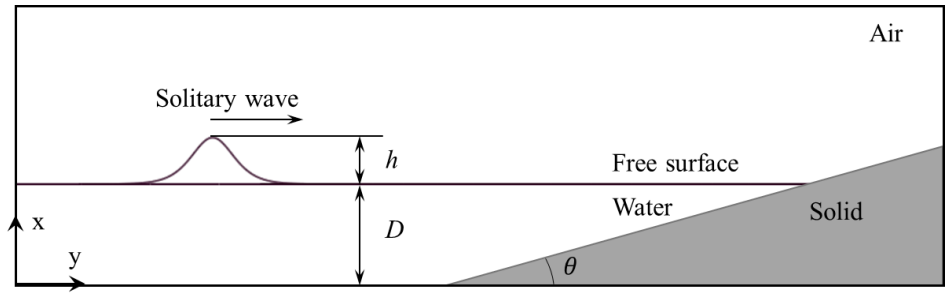

Figure 6-1 Numerical setup for the solitary wave cases.

The numerical setup for the three cases is similar as shown in Figure 6-1 and Table 6-1. The defining waves parameters are the water depth, *D*, wave height, *h*, and slope of beach, θ. For the first case in Section 6.2.1, the flume bottom is horizontal so the slope $\theta = 0°$. The origin of the coordinate system is defined at the bottom left of the corner at the inlet boundary, positive x-axis pointing downstream and y-axis pointing upward.

Table 6-1 Parameters for the solitary wave simulations

Cases	D	h/D	θ
S1.	1m	0.3	0°
S2.	1m	0.3	10°
S3.	0.205m	0.33	5.2°

6.2.1 Propagation of a solitary wave in a constant depth

The benchmark test is carried out in a two-dimensional numerical wave tank with L= 72.6 m and H=2.7 m. The still water level over the horizonal bottom is *D*= 1m. A solitary wave is initially placed with its crest at x= 15 m and propagates alongside the wave tanks for 9 s. In this test, both phases are set as inviscid, so a uniform mesh is used in the whole domain and slip boundary conditions are applied on the walls of the wave flume. Theoretically, the solitary wave is expected to remain the initial wave height and free surface shape when propagating in the flume under these conditions. The results of a one-phase flow solver in OpenFOAM, pimpleFoam, is used as a reference solution in this case.

The numerical setup for the pimpleFoam is similar to section 4.3, where the fixed circle is replaced by a wave-profiled bump and the initial velocity is set the same as the celerity of the solitary wave, *c*= 3.56 m/s. In the validated cases in Chapter 4 and in the reference [95], the grid convergence of

the two-phase flow solvers has been checked. The finest mesh size with $\Delta x = \Delta y = 0.017$ m is used to compare the new solver with the reference solution and other two-phase flow solvers. The time step is controlled by the Courant number condition, *Co*= 0.5 in this case.

Figure 6-2 shows the final wave profiles after 10 s of propagation with the interFoam solver and the new DW-IBVOF solver. The analytical results according to the solitary wave theory [106] are given in dots. Good agreements are obtained with both solvers. The wave height remains the same with the theory and almost no visible phase shift is observed. However, in terms of surface presentation, better performance is obtained with the DW-IBVOF solver on the left side of the wave crest where interFoam solver gives a wiggly surface.

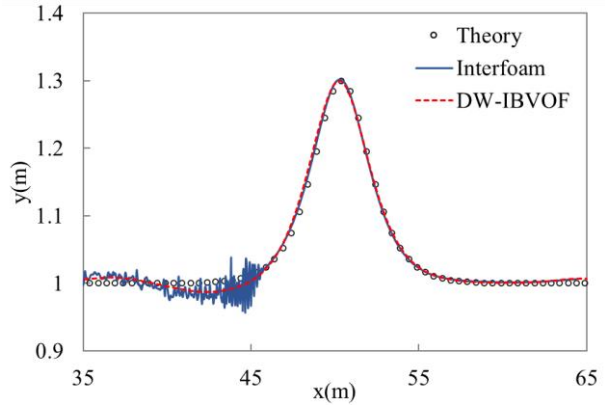

Figure 6-2 Wave profiles after 10s of the solitary wave propagation.

The velocity fields in this region x= [40m, 48m] with the two solvers are shown in Figure 6-3. The position of the free surface is shown with the iso-surface α=0.5 in a white line. As shown in Figure 6-3 (a), the velocity below the free surface is similar to theory solution [106] which is close to zero, while a large spurious velocity is observed in the air region with the interFoam solver.

The maximum value of relative velocity $\mathbf{U}_r = c - \mathbf{U}$ in this region getting from in the one-phase flow solver simulations is 0.34 m/s while the maximum value in the interFoam solution reaches 7.504 m/s. The spurious velocity comes from the imbalance between pressure gradient and density gradient in the momentum equation and accumulates with time. The effect of the numerical error on the air phase is much greater than on the water phase since the same stress is generated from the momentum equations.

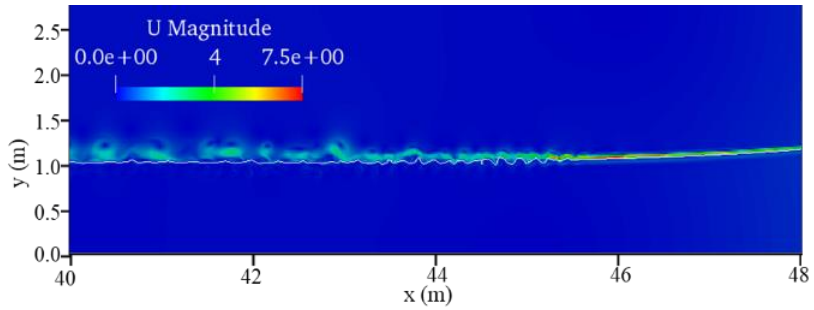

(a) interFoam

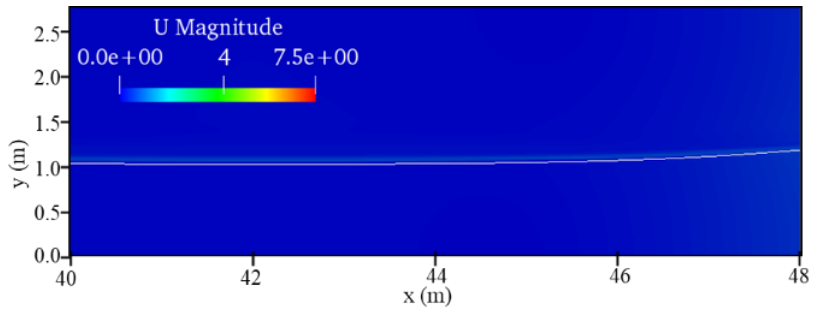

(b) DW-IBVOF solver

Figure 6-3 Velocity field during solitary wave propagation at t= 10 s. The white line represents the position free surface with the iso-surface $\alpha = 0.5$.

A set of non-viscous vortex are generated in the interFoam solution on the upper left region of the droplet since the air velocity adapts to the droplet movement to preserve continuity and momentum. The vortex is enlarged by the large velocity gradients in the air region as a result of the discontinuous velocity across the interface. The spurious velocity is then used in the convection of the volume fraction and eventually results in a wiggle surface.

Compared to the interFoam, the DW-IBVOF solver shows its ability in suppressing the spurious velocities. The maximum value of velocity in DW-IBVOF solver is 0.667 m/s. Though double to the one-phase flow solver value, it is in the same order of magnitude. The discontinuity in the velocity between the air and water across the free surface is smoothed by the built free surface boundary layer. The interface instabilities and unphysical tearing of the interface are suppressed. A smoother free surface is obtained.

To better understand the behaviour of the free surface, the horizontal velocity profiles along a vertical cross-section going up through the wave crest at t= 10s are investigated. In Figure 6-4, the reference result consists of two parts. For the air phase with y> 1.3 m, the reference velocity is the

relative velocity $\mathbf{U}_r$ getting from the one-phase flow solver, and for the water phase with y< 1.3 m, the reference equals to the solitary wave theory. The two parts are connected with a straight line.

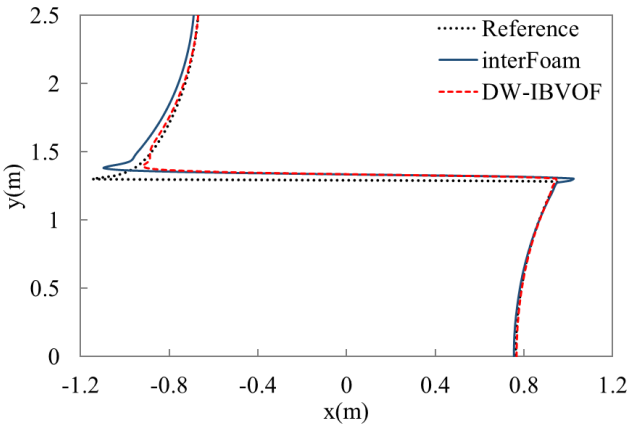

Figure 6-4 The horizontal velocity profiles of the two phases along a vertical cross-section going the solitary wave crest at t= 10 s.

It is evident that the velocity profiles of both the two two-phase flow solvers agree well with the reference solutions especially for the main bulk of the water phase. In both two-phase solvers, a narrow band is generated to transfer the velocity across the interface from water phase to air phase. This jump of the velocity mainly exists in air phase since the air phase is much lighter than the water phase. The large velocity gradient acts as the source of the no-viscous vortex on the left side of the wave crest and eventually effects the behaviour of water with time as shown in Figure 6-3. Smaller velocity gradient is observed in the results with the DW-IBVOF solver. The boundary layer designed by the density-weight smoothing method and immersed boundary method smooths the jump of the velocity field and reduces the velocity gradient in the lighter fluid near the interface.

Beside of the large velocity gradient in the air phase, an increase of velocity in water phase close to the interface is generated in the results of interFoam solver. The overshooting in the particle velocities in the top of the crest is a common feature in other two-phase flow solvers like Thetis as shown in Figure 6-5. Truchas shows a very close result as the reference solution but presents artificially high velocities at the front of the solitary wave [95]. In simulations with Gerris, a reduced gravity approach, with which gravity is applied in a bond around the interface. The approach helps to reduce the imbalance of dynamic pressure gradient and density gradient.

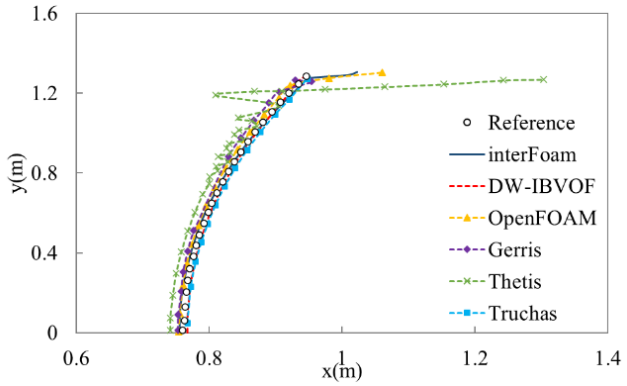

Figure 6-5 The horizontal velocity profiles of the water phase along a vertical cross-section going the solitary wave crest compared with the benchmark results at t= 10 s. The data of OpenFoam, Gerris, Thetis and Truchas are obtained from benchmark cases [95].

Among all these two-phase solvers, the velocity profiles obtained with DW-IBVOF solver follow the reference solution quite well, both in sense of the water phase and air phase. The particle kinematics in the wave crest is an important feature in wave propagation simulations [96]. The spurious velocity can have an important effect on the advection of the free surface in a long-time simulation and the proposed DW-IBVOF solver provides much better accuracy in the two-phase flow calculations.

6.2.2 Run-up of a solitary wave on a slope

The second benchmark case used in present work is the runup of a solitary wave on a plane slope. The numerical test is carries out in a two-dimensional numerical wave tank with L=45 m and H=2.7 m. The slope starts at x= 30m with an angel of $\theta = 10°$. The solitary wave (parameters given in Table 6-1) is initially placed with its crest at x= 15 m and propagates towards to the slope for 10s.

Both phases are set as inviscid and the surface tension is neglected to compare the results of the two-phase flow solvers with a fully non-linear boundary integral solver based on potential theory [107]. Slip boundary conditions are applied on the walls of the wave flume. According to the solitary wave and slope parameters, no breaking should occur in this benchmark test. Similar to case S1, the highest resolution in reference [95] is used in present work. The maximum Co number equals 0.5 in each case.

Figure 6-6 shows the snapshots of volume fraction α distribution with the two solvers during wave runup process at t= 5.4 s. A wiggly surface is clearly observed close to the wave crest in the results of interFoam. Similar to the wiggly surface in case S1, the considerably distorted interface is caused by the spurious velocity generated near the interface. Figure 6-7 presents the velocity field at t=

5.4s with the two solvers. Artificially high velocities are present in the air phase with a maximum value of 11.6 m/s. A strong increase of velocity is also observed in the water phase closed to the interface. These spurious velocities directly lead to the unphysical shear of the interface since the they are used in the convection of the volume fraction.

With a higher velocity than the main body of the wave, the water that closed to the interface moves in a spurious way and tends to spread to the air region from the tip of the swash tongue as shown in Figure 6-6. A mini plunging breaking wave is generated at around x= 35.5m on the slope with several separated droplets, which should not happen in this case. This problem is commonly present in solutions of Gerris and Thetis [95] and simply refining the mesh cannot remove the droplets during the simulation. It is therefore important to reduce the spurious velocity near the interface.

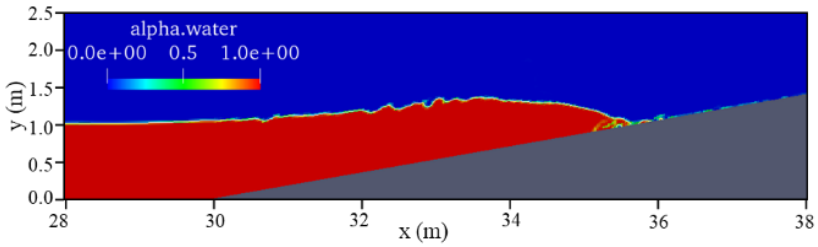

(a) InterFoam solver

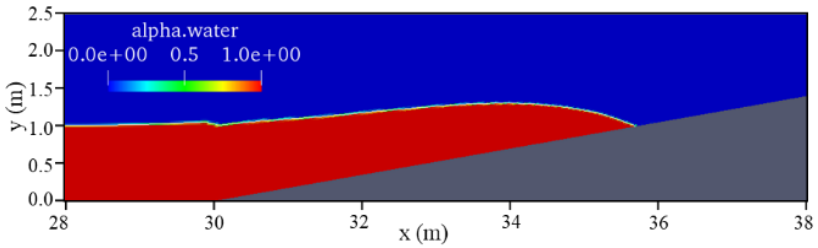

(b) DW-IBVOF solver

Figure 6-6 Volume fraction α distribution during the solitary wave runup at t= 5.4 s.

Compare to the interFoam solver, the DW-IBVOF solver is superior in prediction in both interface shape and velocity field as shown in Figure 6-6(b) and Figure 6-7(b). The velocity of the water phase beneath the interface is extended into the air phase above the interface due to the high-density ratio between water and air. The maximum value of the velocity with DW-IBVOF in the same region is only 7.7 m/s. A better predicted velocity field improves the accuracy of volume fraction convection and a smooth free surface is obtained without any separated droplets from the tip of the wave.

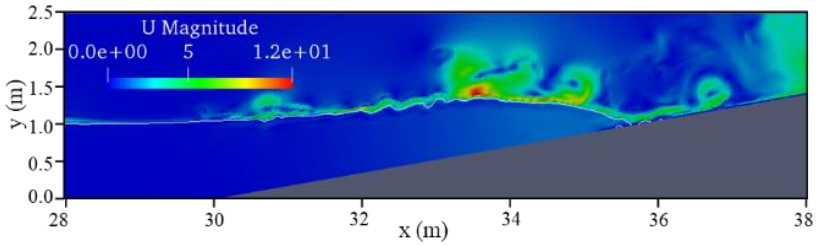

(a) InterFoam solver

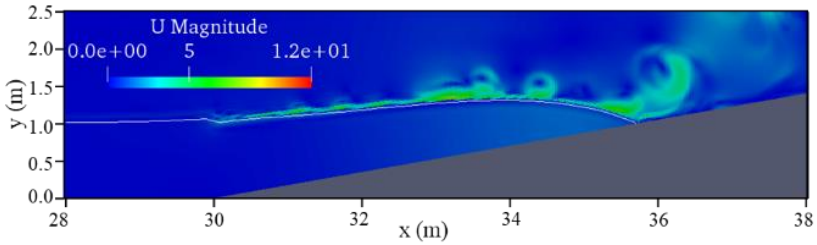

(b) DW-IBVOF solver

Figure 6-7 Velocity field during solitary wave runup at t=5.4 s. The white line represents the position free surface with the iso-surface $\alpha = 0.5$.

In the benchmark test [95], the evolution of the maximum elevation of the free surface with four two-phase flow solvers are collected and compared with potential solutions (shown in Figure 6-8). The separated drops are removed from the results and only the largest connected water region is taken into account. The results of the original interFoam (with and without the spurious droplets) and the DW-IBVOF solvers are added into the Figure 6-8.

It is surprising to see the large distance between the separated droplets and the main body of the wave which is almost equal to the height of the maximum runup elevation of the wave. The elevation of the main body with interFoam shares same trend with other solvers. Among all the solvers, Gerris and DW-IBVOF solvers give the closest results with the reference. No separated droplets are found in these two solvers, which could be the reason. Gerris seems to be the best solver from Figure 6-8, but some bubbles are reported that sticked to the slope during the wave runup and rundown process, which may eventually damage the flow simulations. The overall good performance of the DW-IBVOF proves that the present methods improve the accuracy of two-phase flow simulations.

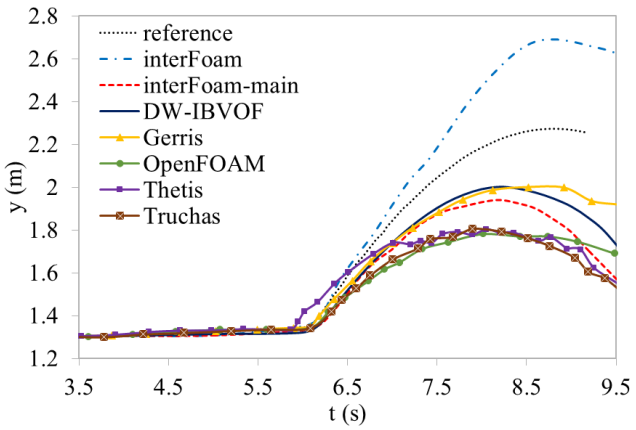

Figure 6-8 Evolution of the maximum elevation of free surface compared with the benchmark results during solitary wave runup.

It is interest to see that even for the main water body, the interFoam in present work is better than the OpenFoam used in the reference paper [95]. A main issue may the different treatment of the solid boundaries. An immersed solid boundary condition is applied on the beach in the benchmark test which the authors are unsuccessful in using it. A slip boundary condition is used instead. Another reason could be the mesh configuration. Even though the mesh used in present work is designed as the same as the benchmark test, the size and shape of the mesh could be slightly different, especially in the junction region of horizonal bottom and the slope, because of the irregular shape of the wave flume. A discussion of mesh configuration is given in [95], but is beyond the scope of the present work.

6.2.3 Plunging breaking solitary waves on a slope

To demonstrate the capability of the proposed solver in the application of free surface simulations in the real ocean engineering, numerical simulations for an experimental case are carried out in this section. Different to case S1 and S2, both viscosity and surface tension are taken into account and the numerical results are compared with the experimental data [108].

The numerical simulations are carried out in a three-dimensional (3D) numerical wave tank with length L=8 m, height H=0.6 m and width W= 0.3m. The numerical setup is similar to case S2 and shown in Figure 6-1. The slope with an angle of $\theta = 5.1°$ starts at x= 4m. The still wave depth is D= 0.205m. A solitary wave with amplitude h/D= 0.33 is initially placed at x= 1.815 m and propagates towards to the slope. The simulations end up after the runup process is completed and a plunging breaker is generated. All the physical parameters, densities, viscosities, and surface tension are set the same as the experiments. No-slip boundary condition is imposed on all the walls of the numerical wave tank.

A structured mesh is used to discretize the computation domain. The lower edge is aligned with the bottom of the domain and the surface of the slope while upper edge is horizonal. The cells at the top of the beach become smaller on the right end of the domain. The grids are uniform in the spanwise and streamwise direction, $\Delta x = \Delta z = 3\ mm$, but nonuniform in the vertical direction, i.e., $\Delta y_{max} = 3\ mm$ and $\Delta y_{min} = 0.2\ mm$. The meshes near the bottom of the wave tank and the surface of the slope are smaller to capture better the near-wall turbulent flow. The maximum Co number is set to be 0.5, the same as the numerical setup in c. A standard $k - \varepsilon$ turbulence model along with the Reynolds averages Navier-Stokes equations (RANS) is used to describe the turbulent flow in the two phases.

When the solitary wave travels close to the slope, the characteristics of the wave such as wave height and velocities, change due to the water depth. The wave crest becomes steep and generates a plunging breaker towards to the slope. Figure 6-9, Figure 6-10 and Figure 6-11present the computed free surface profiles compared with the experimental data in the pre-breaking zone; no breaking has occurred yet. The numerical solutions with two-phase flow solver Truchas in [108] are also given in the comparison as a reference. Overall, the numerical results from the three two-phase flow solvers, Truchas, the proposed DW-IBVOF and the original interFoam, fit well with the experimental data for the locations and wave profiles.

At t= 2.525 s, the wave starts shoaling and transforming. In terms of surface shape prediction, the interFoam solver gives the steepest wave crest on the wave front among the three solvers. The discrepancies between numerical results of interFoam solver and experimental data grow with time. At t= 2.64 s, the experimental wave front is almost vertical while in the results of interFoam, the plunging breaker have generated and tend to overturn.

The Truchas solver, on the contrary, shows a much gentler wave profile. At t= 2.525 s, the results of Truchas are in good agreement with the laboratory wave front. The differences occur during the wave runup process. According to Mo et al's work [108], the wave overturn predicted by Truchas is later than the experimental data and is around 85 mm further away from the inlet boundary, which is proved by Figure 6-11 where the Truchas still shows a relatively gradual wave profile with non-breaking characteristics. This may be caused by the resolution is not fine enough to capture the variation of velocity. The finest mesh near the bottom of the computational domain that Mo used is 4 mm is larger than the coarsest mesh in the present work.

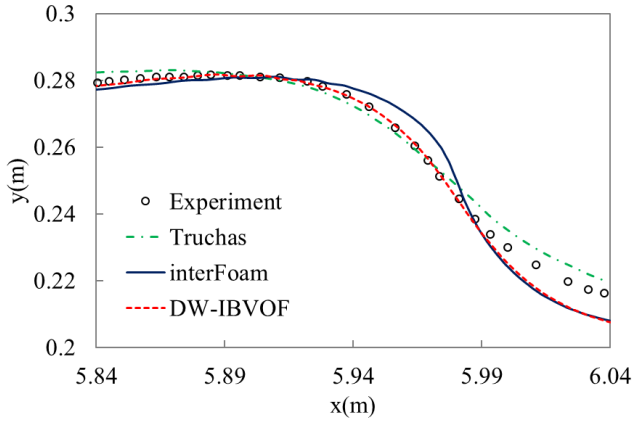

Figure 6-9 Comparison of experimental data and numerical solutions for free surface elevation for the plunging breaking solitary waves on a slope at t= 2.525 s.

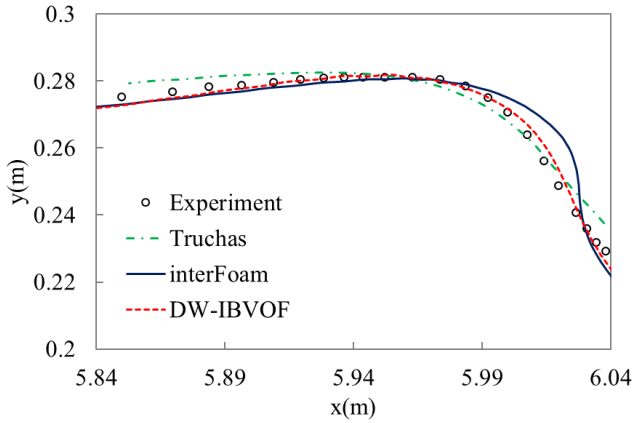

Figure 6-10 Comparison of experimental data and numerical solutions for free surface elevation for the plunging breaking solitary waves on a slope at t= 2.57 s.

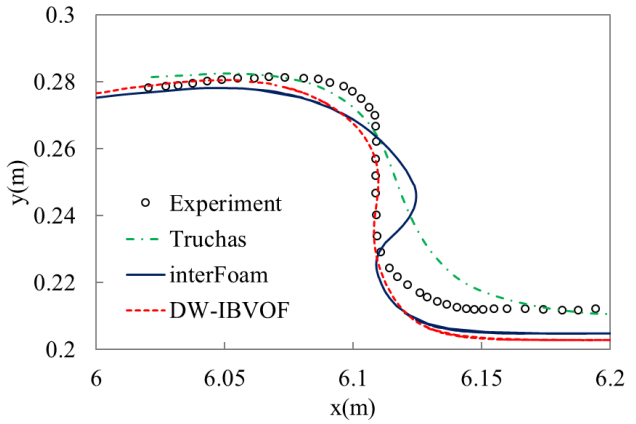

Figure 6-11 Comparison of experimental data and numerical solutions for free surface elevation for the plunging breaking solitary waves on a slope at t= 2.64 s.

Among the three solvers, the proposed DW-IBVOF solver shows the best agreement with the experimental observations. The discrepancies on the wave crest between numerical results of interFoam solver and experimental data are corrected by the modified velocity field. Similar to case S1 and case S2, artificial high velocities are observed in the air phase and a strong increase of velocity occurs in the water phase closed to the interface. To better understand the reasons behind the wave front shape, the velocity profiles of water phase is investigated in the next section.

It is interesting to observe that the positions of the free surface closed to the slope obtained from experiment and Truchas in reference [108] are slightly higher than still water level. However, in other authors [109][110][111] research and the present work, the water near the slope stays undisturbed and the height of water remains initial value until the wave reaches.

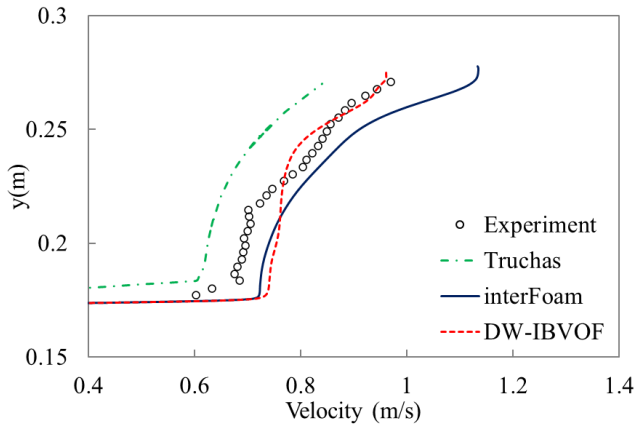

(a) Section x= 5.94 m

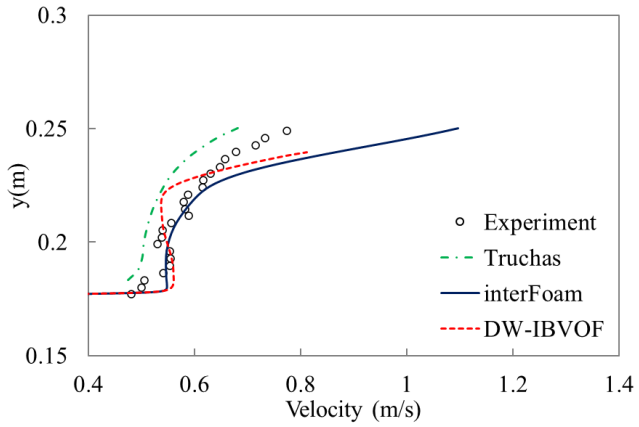

(b) Section x= 5.98m

Figure 6-12 Vertical profiles of horizontal velocity for the plunging breaking solitary waves on a slope at t= 2.525 s.

The horizontal velocity profiles of the water phase are investigated to understand the deformation of the wave front. According to the wave profiles, the vertical profiles of horizontal velocity at different sections at different times are shown in Figure 6-12, Figure 6-13 and Figure 6-14. It is obvious that the values of velocity obtained from the Trucha are 10% -15% lower than the experimental data and the other two solvers, even though the shape of velocity profiles compare well. These differences directly result in the late overturning of wave crest in the simulations with the Truchas.

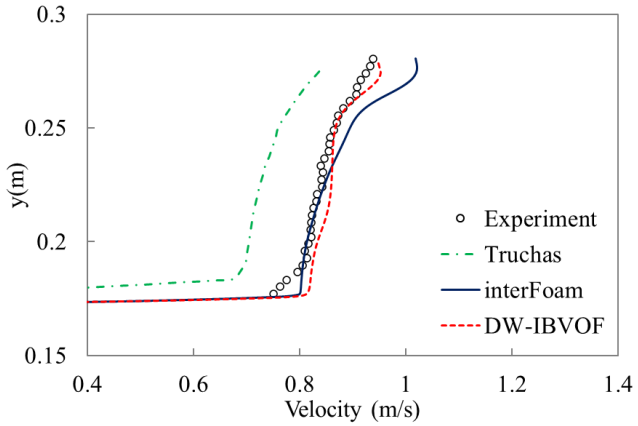

(a) Section x= 5.94 m

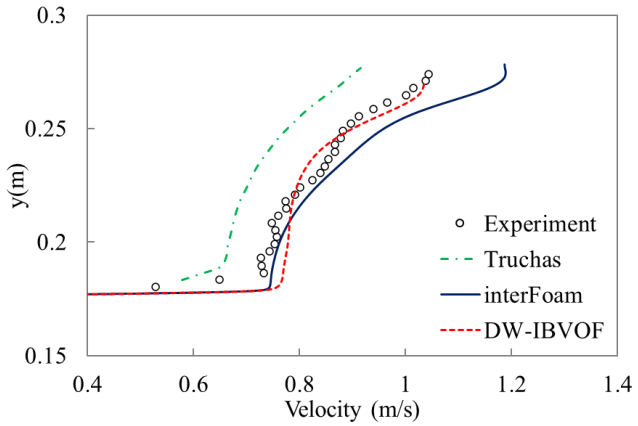

(b) Section x= 5.98m

Figure 6-13 Vertical profiles of horizontal velocity for the plunging breaking solitary waves on a slope at t= 2.57s

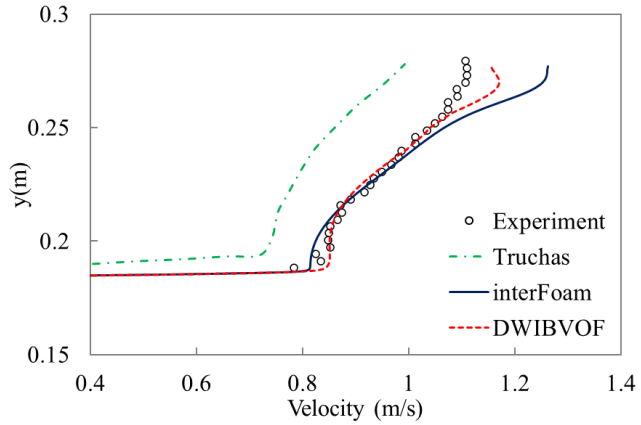

(a) Section x= 6.094 m

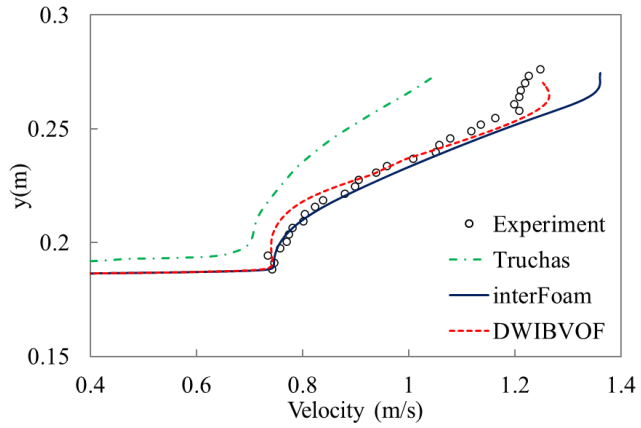

(b) Section x= 6.098m

Figure 6-14 Vertical profiles of horizontal velocity for the plunging breaking solitary waves on a slope at t= 2.64s

In general, the velocity profiles with the interFoam and the DW-IBVOF solvers in present work compare satisfactorily with the experimental observation, both in the magnitude and the shape. Similar to case S1 and S2, strong air flows are induced with a series of vortices in both air and water. As shown in the figures, the high velocity always presents in the results obtained with the interFoam closed to the free surface and gradually decreases alongside the vertical direction. The discrepancies between the numerical simulations and experimental date are larger at sections x= 5.98m and x= 6.098 m which are closed to the wave front, which is the source of the observed overturned plunging breaker.

To accurately predict the behaviours of free surface with strong air-water inactions, it is critical to develop a high-fidelity and robust solver that can handle the moving boundaries. The comparison between the DW-IBVOF results with the original interFoam further validate the proposed numerical method. The spurious velocities are eliminated especially on the tips of the wave front and the regions near the free surface, and the gradient of velocity are corrected.

6.3 Stokes waves

The stokes wave is a non-linear and periodic gravity wave that is widely used in the design of ships and marine structures. The stokes wave with a relatively small amplitude propagates with constant velocity in an inviscid fluid and it is therefore often used in the validation cases of numerical models. The behaviour of the stoke is found to change with the increase of its initial steepness ($\epsilon = ka$). According to Iafrati's research [112], the stokes wave keeps steady non-breaking propagation when $\epsilon < 0.33$ and breaking wave is generated with higher steepness, $0.33 \leq \epsilon < 0.37$ for spilling breaking wave and $\epsilon \geq 0.37$.

The non-breaking wave with $\epsilon = 0.2$ is first used to validate the new solver. Both viscosity and surface tension are neglected to compare the numerical results and theorical solutions. Then the plunging waves with $\epsilon = 0.55$ are investigated by increasing the wave amplitude. The viscosity and surface tension are included since in short scale, surface tension have effects on shape of wave profiles.

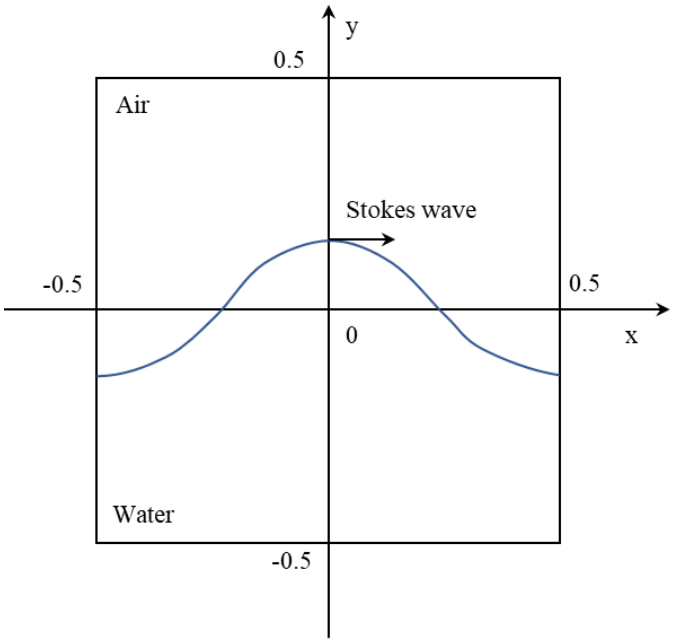

Figure 6-15 Initial interface profile of Stokes wave

The numerical setup for the stokes waves is shown in Figure 6-15. The computation is conducted for a domain of [-0.5, 0.5]×[-0.5, 0.5] with periodic boundary conditions at the two sides. The origin of the coordinate system is defined at the centre of the domain, positive x-axis pointing downstream and y-axis pointing upward. A periodic Stokes wave is initially placed in the middle of the computational domain. The initial surface profile is assigned as [113]:

$$\eta(x,0) = \frac{1}{2\pi}\left(\epsilon\cos(2\pi x) + \frac{1}{2}\epsilon^2\cos(4\pi x) + \frac{3}{8}\epsilon^2\cos(6\pi x)\right) \quad (6\text{-}1)$$

6.3.1 Validation case of non-breaking waves

The non-breaking wave case with $\epsilon = 0.2$ is first investigated. Three uniform square grids are applied in this case, which consecutively increased sizes from 256×256, 384×384 to 512×512. Adaptive time steps are used based on a maximum allowed Courant number, Co=0.2. Viscosity and surface tension are not included in this case, so that the results can be compared with the theory solutions. Both the two solvers, interFoam and DW-IBVOF solver are applied to check their ability in stokes wave propagation simulations.

Figure 6-16, Figure 6-17 and Figure 6-18 show the wave elevation with the two solvers. It is obvious that the shape of wave deforms from around t= 8 in the interFoam solutions with the coarsest mesh 256 × 256, while superior shape preservation is obtained with the DW-IBVOF solver. Similar deformation also happens on finer meshes within shorter time, around t= 1 and t= 0.5, respectively.

Figure 6-19 shows the distribution of volume fraction with the interFoam solver on mesh 512×512 at t = 0.5. Similar wiggly surface to section 4.2.3 is observed on the left side of the wave, which is caused by numerical errors origins from the high velocity and pressure gradients across the interface in this region. The errors accumulate and enlarge with time and eventually ruin the main body of the non-breaking wave.

It is not a surprise that the wiggly interface is more likely to generate with a finer mesh. The smaller the cell is, the less mass it contains and the more sensitive it is to the numerical errors. The velocity, pressure and density gradients are averaged or smoothed by larges cells, so the imbalance between pressure gradient and density gradient are weaken. Another reason is that the coarser mesh fails to capture the detailed deformation of interface at the early stage. The effect of the numerical errors starts when they are large enough to change the wave profile. Though the start point of the deformation in interFoam simulation with the coarser mesh is later, the disparity of the wave elevation to the DW-IBVOF solver results is larger.

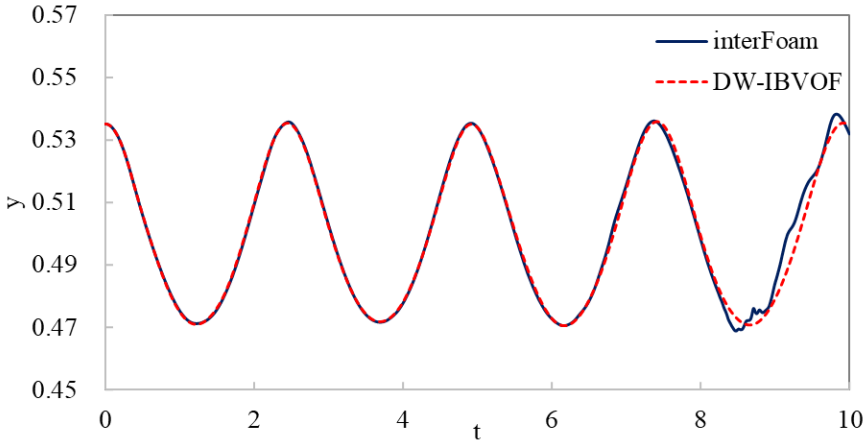

Figure 6-16 Wave elevation of Stokes wave propagation for $\epsilon = 0.2$ at x= 0 with mesh 256×256.

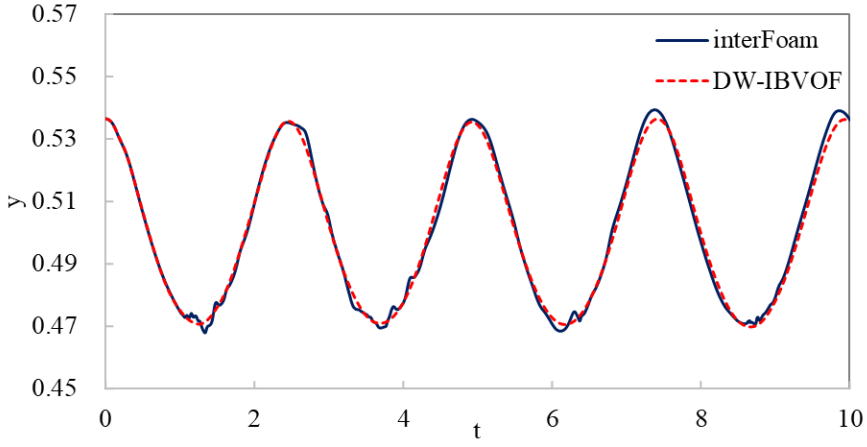

Figure 6-17 Wave elevation of Stokes wave propagation for $\epsilon = 0.2$ at x= 0 with mesh 384×384.

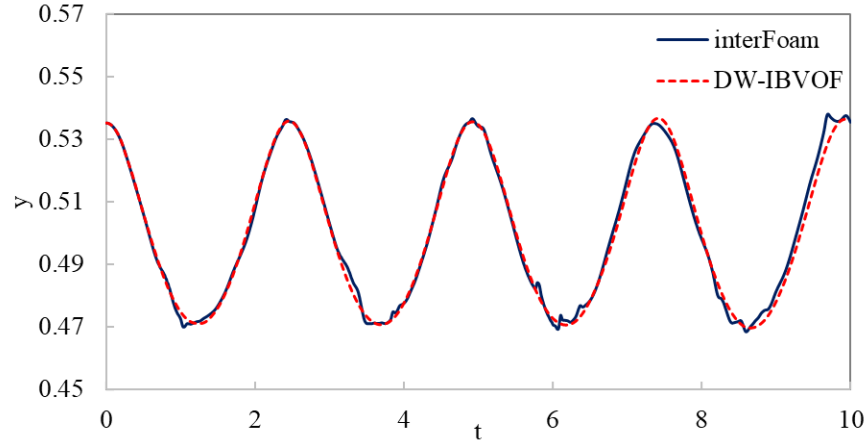

Figure 6-18 Wave elevation of Stokes wave propagation for $\epsilon = 0.2$ at x= 0 with mesh 512×512.

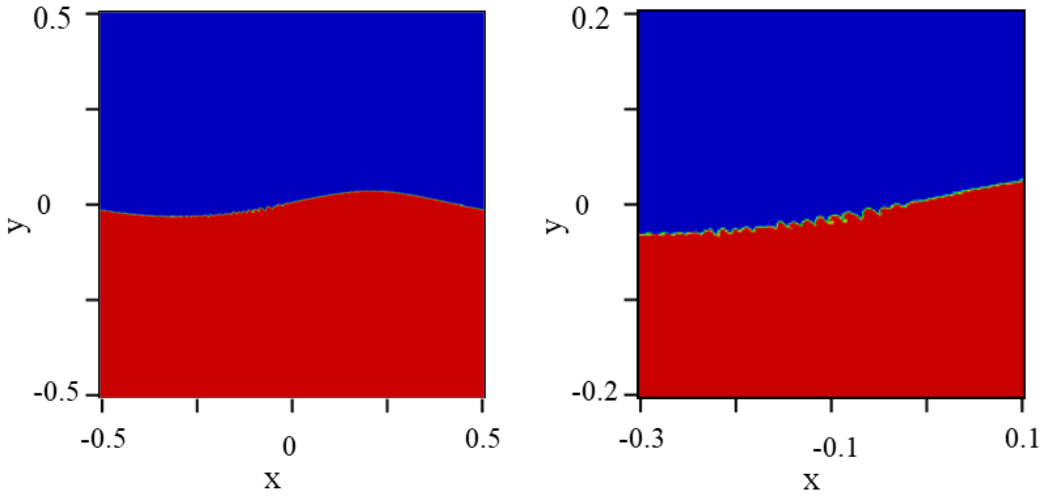

Figure 6-19 Distribution of volume fraction of Stokes wave propagation for $\epsilon = 0.2$ with the interFoam solver on mesh 512×512 at t = 0.5.

In terms of surface shape preservation, a much better performance is obtained with the DW-IBVOF solver on all three meshes. The wave profiles with the DW-IBVOF solver at t=20 are shown in Figure 6-20. The numerical results are in excellent agreement with the experiment. The maximum value of difference between the numerical results and theory is less than half of the mesh size, which is acceptable since the wave surface is presented by iso-surface $\alpha = 0.5$. Even though a reasonable results is obtained by the coarsest mesh for the non-breaking wave case, the finest mesh 512×512 is chosen for breaking wave cases in the next section since a finer grad is able to capture more details of the free surface, such as droplets or air bubbles.

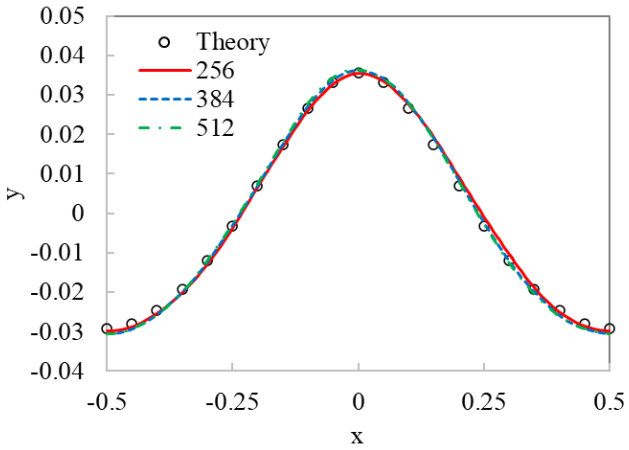

Figure 6-20 Wave profiles of Stokes wave propagation for $\epsilon = 0.2$ with the DW-IBVOF solver on different meshes at t= 20.

6.3.2 Plunging breaking wave case

The initial wave slope for this case is $\epsilon = 0.55$, the same as the parameters in simulation [113]. It is steeper than any irrotational and is an unsteady wave that tends to evolve to the plunging breaking waves. It is believed to the most powerful breaker in deep and shallow water [113] involving strong air-water interactions. In this case, the viscosity and surface tension are taken into account as the reference paper. Four dimensionless parameters are used as: $Re = \frac{\rho_w g^{\frac{1}{2}} \lambda^{\frac{3}{2}}}{\mu_w} = 10000$, the Bond number $B = \frac{\rho_w g \lambda^2}{\sigma} = 10000$, the density ratio $\bar{\rho} = \frac{\rho_w}{\rho_a} = 100$ and the viscosity $\bar{\mu} = \frac{\mu_w}{\mu_a} = 2.5$.

The plunging wave breaking process has been characterized by four major phases including steep wave formation, jet formation, splash-up and air entrainment. The major events are shown in Figure 6-25 with snapshots from both reference paper and DW-IBVOF solver. It is clear to see that the predicted wave profiles are in a good agreement with the reference.

At t= 0, the initial velocity of water is given by the velocity potential and the air is at rest. The wave is then driven by gravity and moves from left to right. The symmetry stoke wave becomes more and more asymmetric, especially in the crest region. At t= 0.56, the steep wave is generated with an approximately vertical front face of the crest. At t= 1.2, a jet of water is formed forward of the crest of the water and project downward by the influence of gravity. At t= 1.44, the jet is about to touching the smooth tough of the wave and entraps a large amount of air below the jet.

Once the jet tip touches the trough surface, splash-up initiates and develops at the location where the jet impacts. The process is followed by a second jet impinges onto the forward face. The height of the second jet is smaller than the first one and entraps a relatively small amount of air. At t= 1.76, a third jet is formed as the second jet touches the trough surface and the plunging breaking process repeats. The wave system loses both its potential and kinetic energy during a time series of wave breaking and splashing no longer occurs after the three jets.

To better understand the behaviour of the plunging breaking waves, the velocity fields of both water and air phases as well as the energy distribution are investigated at the time steps that correspond to the four major events. Figure 6-22-Figure 6-27 show the velocity field obtained with the DW-IBVOF solver at different time. Air and water are presented separately, for clarification of the two-phase flow. All the contour plots are presented in the same dimension vary from 0 to 1.

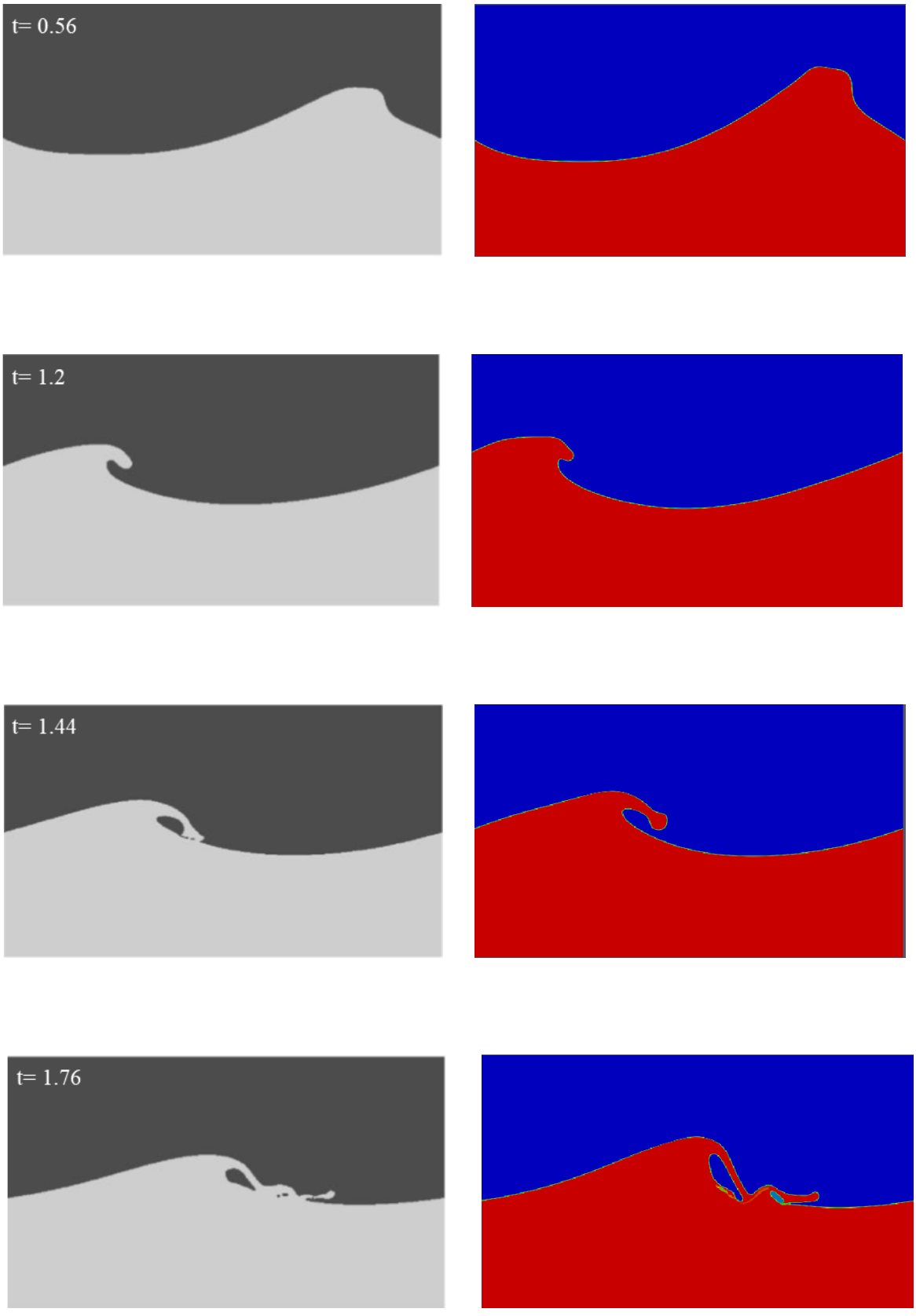

(a) Results from Chen et.al [113] (b) DW-IBVOF solver

Figure 6-21 Instantaneous free surface profiles of the plunging Stokes wave breaking process for $\epsilon = 0.55$.

The initial velocity is given symmetry with the maximum value 0.53 on the crest and the phase 0.46. One of wave breaking criterion is that the breaking occurs when the crest particle velocity exceeds the phase speed [114]. As shown in Figure 6-22, the maximum value of velocity on the wave crest 0.48, which is smaller than the initial velocity because of viscosity, is still larger than the phase velocity. The velocity of air phase on the front side is slightly larger than the water phase. A vortex is generated around the wave crest when the Stokes wave moves.

The wave crest keeps moving horizontally from left to right. Once the vertical front face of the crest exceeds 180° , the crest is accelerated and changes its direction with the effect of gravity. An overturning jet of water is generated and project downward to trough of wave. As shown in Figure 6-23 and Figure 6-24, the maximum velocity of water phase reaches 0.75 at t= 1.2 and 0.80 at t= 1.4. High particle accelerations occur on the water jets with the maximum value 3 times larger than gravity and approximately towards the centre of curvature of the overturning loop. The air phase keeps the similar behaviour as t= 0.56 that mentioned above. Higher velocities and accelerations are observed in the region near the jet of water, especially at t= 1.4. This is due to the air entrapped beneath the overturing water jet that develops high pressure between the tip of the jet and the trough of the wave.

A comparison of the present solver with a potential-flow theory with a boundary integral formation [113] is also conducted in this case. The wave profile and velocities along the interface at t= 1.4 are shown in Figure 6-25. The same initial conditions as the two-phase simulation are used in the potential flow solvers with and without viscosity and surface tension.

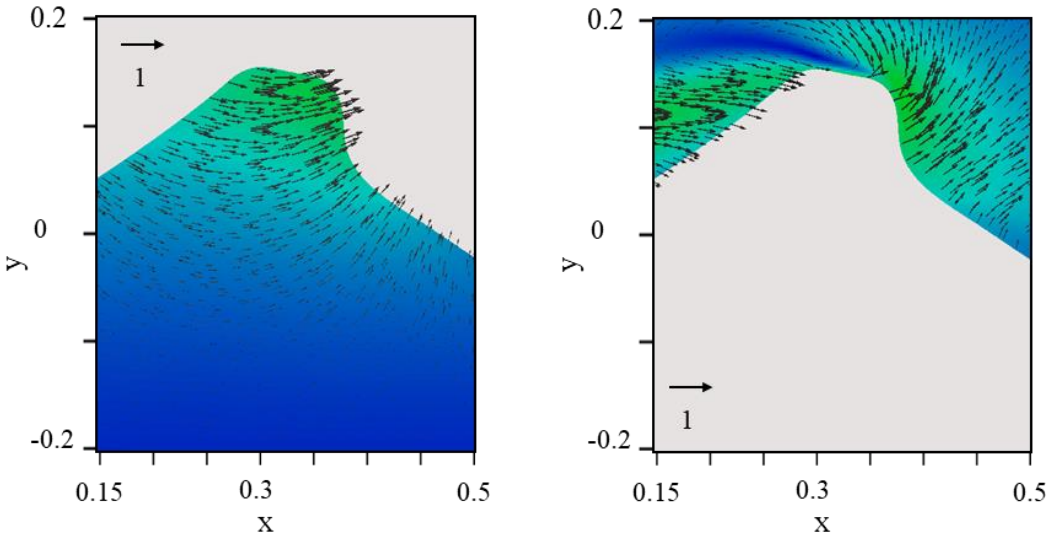

(a) Water phase (b) Air phase

Figure 6-22 Velocity fields of steep wave formation of Stokes waves for $\epsilon = 0.55$ at t= 0.56.

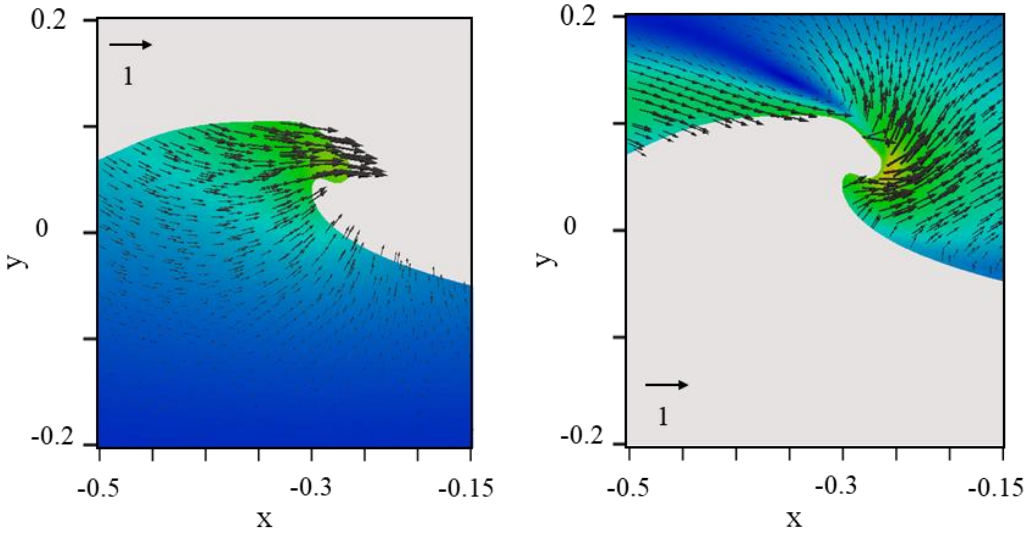

(a) Water phase (b) Air phase

Figure 6-23 Velocity fields of overturning motion of Stokes waves for $\epsilon = 0.55$ at t= 1.2.

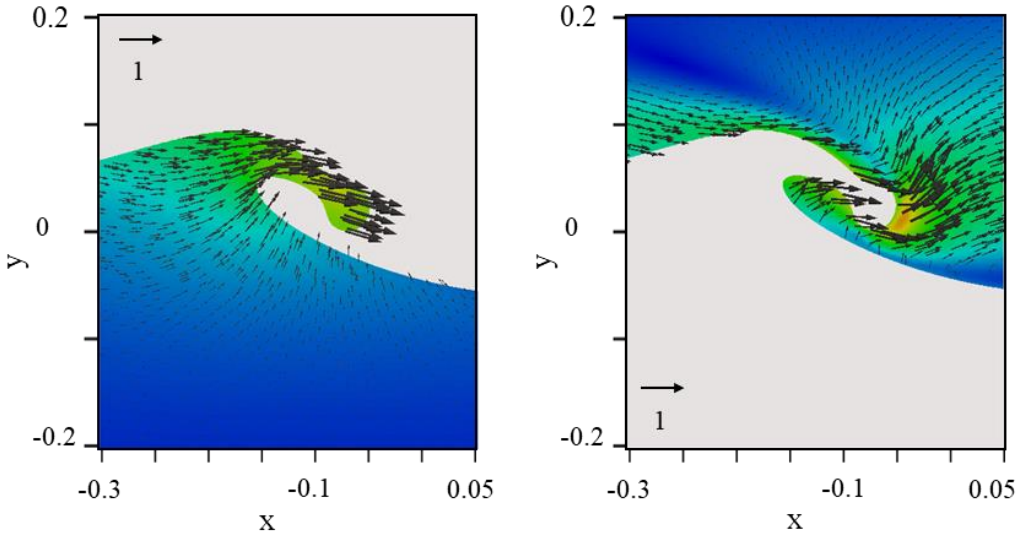

(a) Water phase (b) Air phase

Figure 6-24 Velocity fields of overturning motion of Stokes waves for $\epsilon = 0.55$ at t= 1.4.

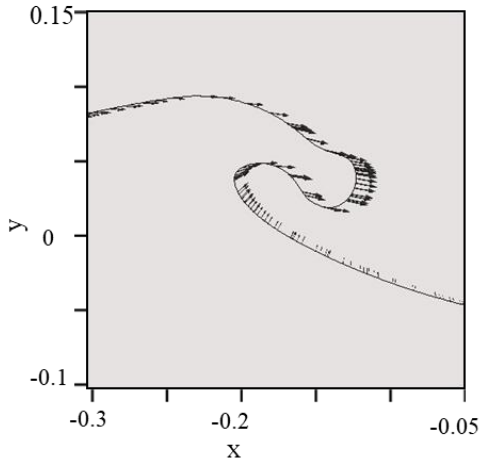

(a) DW-IBVOF solver

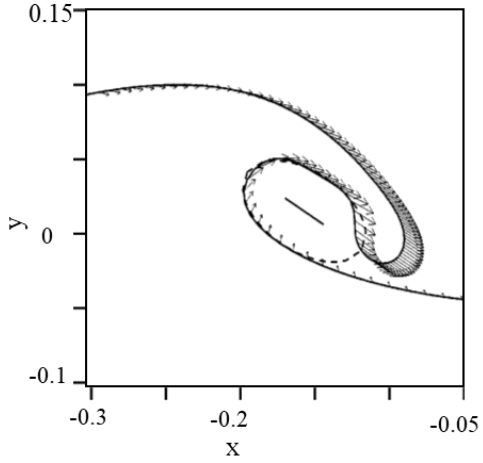

(b) Potential flow with surface tension and viscosity [113]

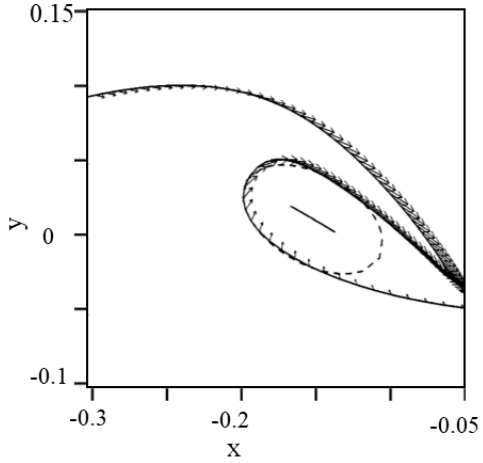

(c) Potential flow without surface tension and viscosity [113]

Figure 6-25 A comparison between the DW-IBVOF solver with potential-flow theory of Stokes waves at t=1.4.

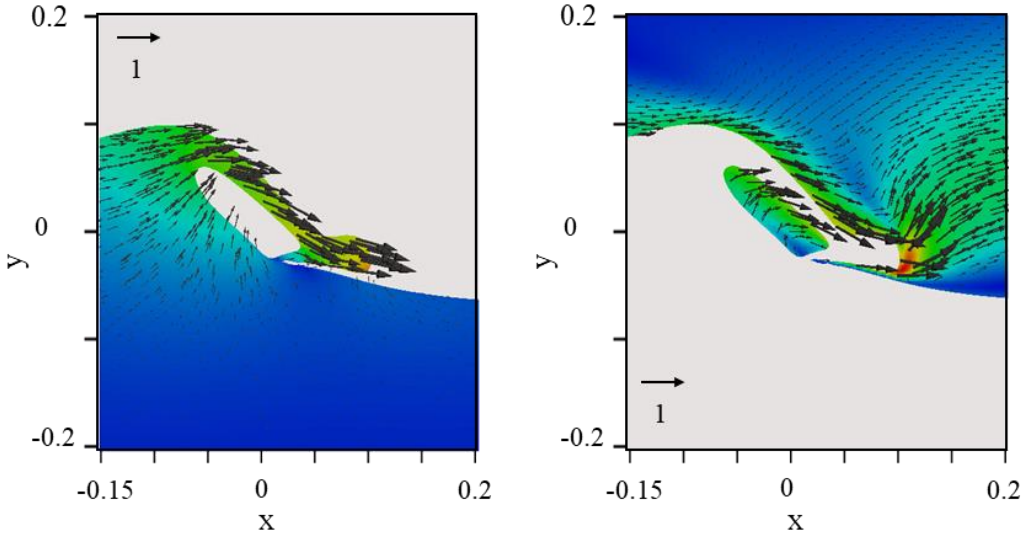

(a) Water phase (b) Air phase

Figure 6-26 Velocity fields of splash-up of Stokes waves for $\epsilon = 0.55$ at t= 1.56.

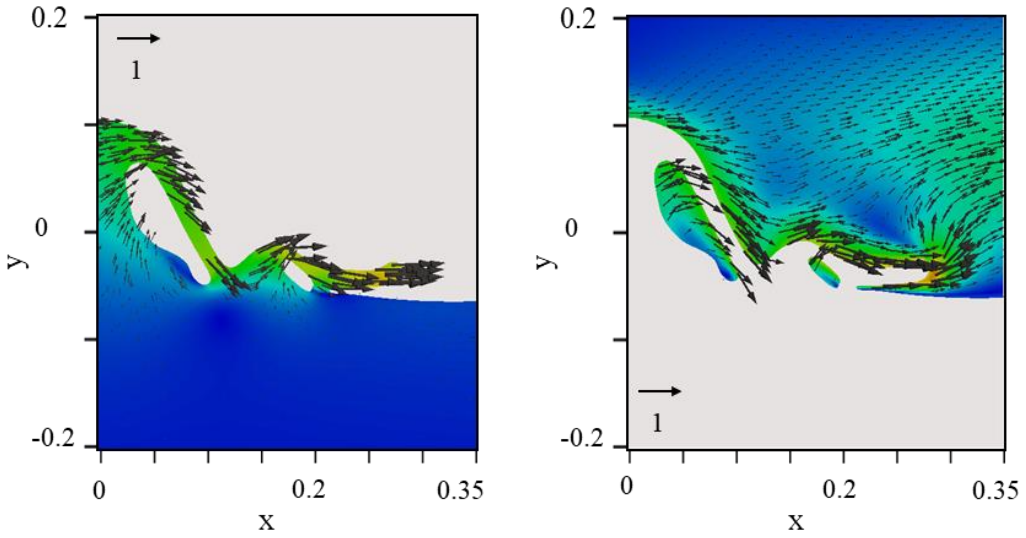

(a) Water phase (b) Air phase

Figure 6-27 Velocity fields of air entrainment of Stokes waves for $\epsilon = 0.55$ at t= 1.76.

The predicted wave profiles are in good agreement between the present solver and the potential-flow computation with similar wave height and position. The main discrepancy lies in the shape of water jet and size of the entrapped air. It is clear to see the effect of surface tension on the shape of the plunging jet from the comparison between Figure 6-25 (b) and (c). The thickness of tip turns thinner and thinner with time when the jet propagates without surface tension, while a rounded tip is obtained with surface tension. A similar rounded tip is obtained with the two-phases flow solver.

It is not a surprise that the sizes of water jet and the enclosed air are slightly different with two-phase flow solver and the potential-flow calculation. In the potential-flow simulation, frictional and inertial influences of the air around the jet are not included. This is also the reason why the velocity of water with two-phase flow solver is slightly smaller than the potential-flow theory.

At t= 1.56, the first plunge occurs when the overturning jet impinges onto the free surface of the trough. Once the jet tip touches the trough surface, an oblique splash-up initiates and develops at the location where the jet impacts. At this stage, the water in the splash-up comes from the overturning jet. As shown in Figure 6-26, the trough of wave remains undisturbed in terms of wave profile and velocity field. The undisturbed surface acting like a solid surface and the jet bounced of the surface. The velocity of the splash-up have similar velocity magnitude as the original water jet but have a different direction. Then, the jet penetrates the surface below and pushes up a portion of water by its forward motion and downward momentum.

The splash-up keeps moving forward and downward on the effect of gravity and the second splash-up is generated when it touches the surface of wave trough. Different from the first splash-up, the water of the second splash-up partly comes from the second jet and partly comes from the preciously undisturbed wave trough. As shown in Figure 6-27, the water in the region around (0.15, -0.05) has large upward velocity that used to be close to zero before the second plunge.

After the second splash-up, a third water is formed but the velocity and the height of the jet is much smaller than the first one and the second one. No more plunger is generated after that. Large amount of energy is lost during the whole process of the plunging breaking, the series of jet impacts, energy transform between wave kinetic energy and potential energy and energy dissipation by vorticities.

The case of the plunging breaking Stokes waves is used to further investigate the effect of designed boundary condition to the behaviour of the interface. The two other solvers mentioned in section 4.4, IBVOF10 and IBVOFW, are applied again. The mesh size of this case is relatively small, the

interface boundary of IBVOFW is further widened from 2 cell layers into 4 cells and the solver is renamed as IBVOFW4. The solver IBVOF10 keeps the same as before.

Figure 6-28 shows the distribution of volume fraction with the three solvers on mesh 512×512 at t = 0.16. The wiggly surface observed in the results of interFoam solver is seen in the same area in the IBVOF10 solver. The deformation is smaller, however, still there and eventually ruin the main body of the wave before it breaks up. This further proves the ability of the designed IBVOF solver to reduce the numerical errors across the interface.

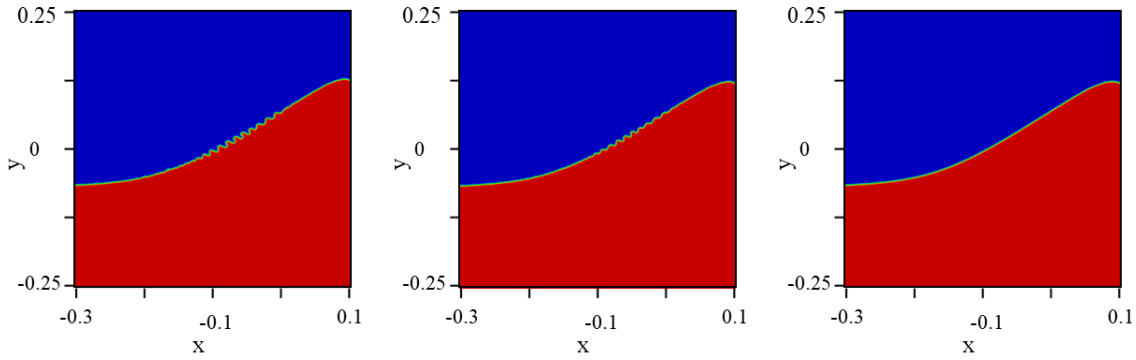

(a) interFoam (b) IBVOF10 (c) IBVOF

Figure 6-28 Distribution of volume fraction of Stokes wave propagation for $\epsilon = 0.55$ with three different solvers on mesh 512×512 at t = 0.16.

A comparison of the IBVOF solver and IBVOFW4 solver is conducted in this case. The wave profiles at five stages are shown in Figure 6-29. As shown in Figure 6-29(a) and (b), the profiles of the two solvers are very similar to each other. At the early stages, the waves are mainly driven by the water phase due to the larger fluid density, viscosity, and surface tension. The divergency between the two solvers begins at t=1.4, where the first water jet falls down and close to the free surface below. Strong interactions between air and water starts to generate and the differences in the air phase between the two solvers are as large to affect the behaviour of water.

Figure 6-31 and Figure 6-31 show the velocity profiles with IBVOF and IBVOFW4 solvers at t=1.4 and t= 1.76. The while lines are the position of the interface, the colour shows the magnitude of the velocity of air and water in x- direction and the arrows give the velocity magnitude and direction of air phase. In IBVOFW4 solver, the velocities of water phase have been extended into the air phase. As shown in Figure 6-31 (b) and Figure 6-31(b), the velocity magnitude of air phase is smaller than the IBVOF solver, especially in the areas that close to the interface. Compared the results of the two solvers, the IBVOFW averages the velocity in a thicker boundary layer and smooths out the effect of the air in this layer to the water phase.

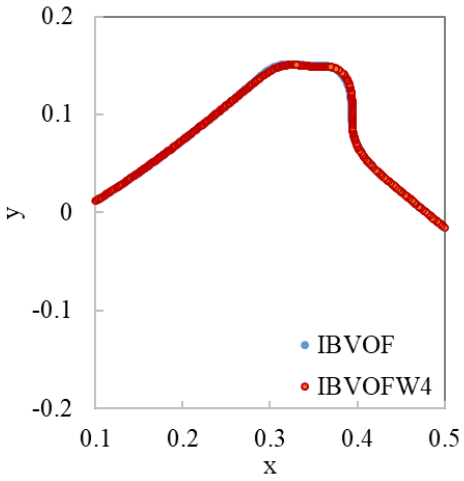

(a) t= 0.56

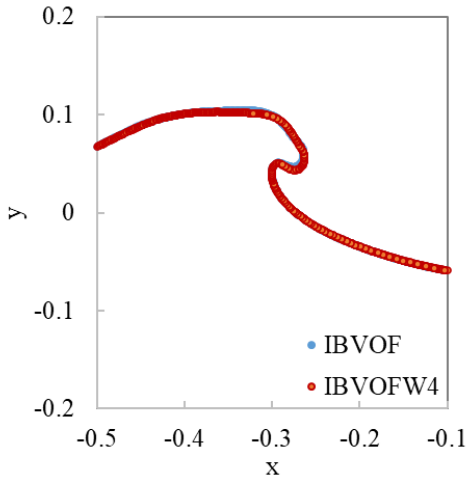

(b) t= 1.2

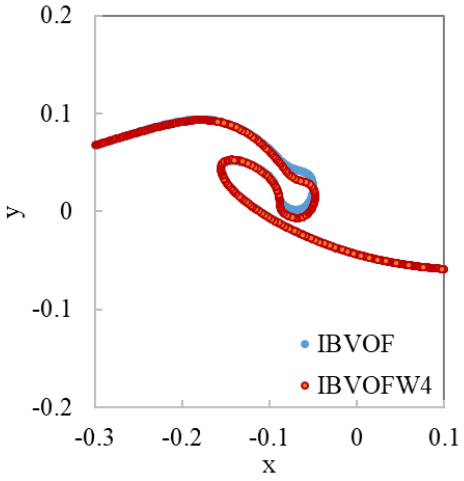

(c) t= 1.4

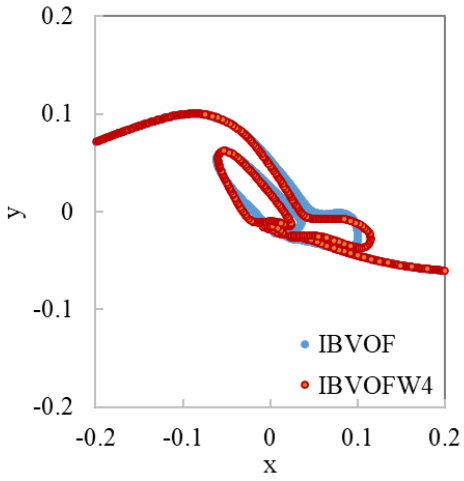

(d) t= 1.56

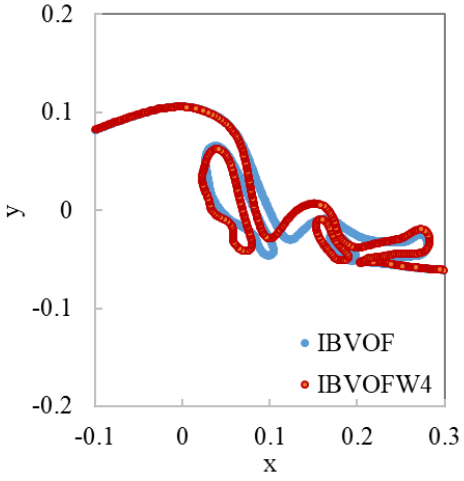

(e) t=1.76

Figure 6-29 A comparison of surface profile between the IBVOF solver and IBVOFW4 solver.

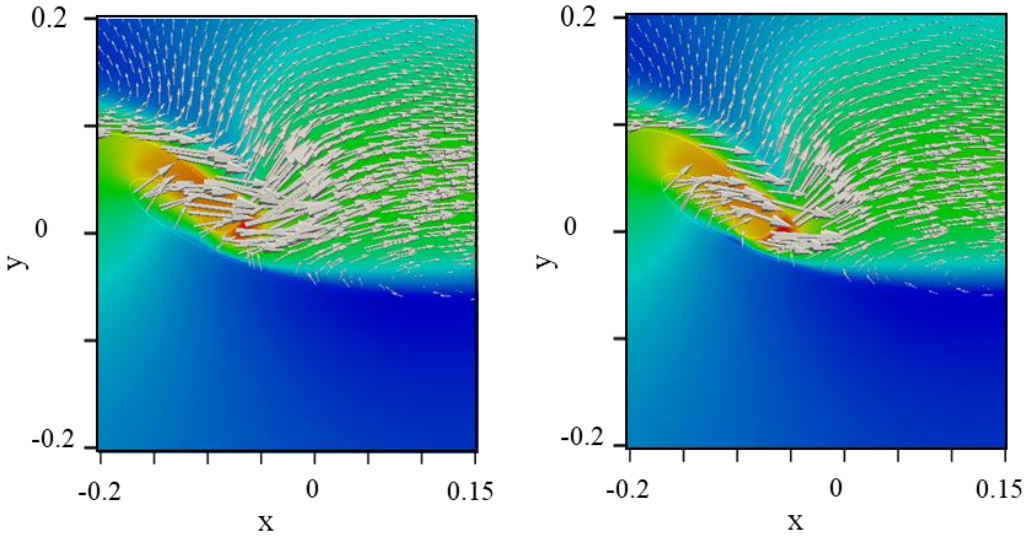

(a) IBVOF solver at t=1.4 (b) IBVOFW4 solver at t=1.4

Figure 6-30 Velocity fields of Stokes waves with IBVOF and IBVOFW4 solvers for $\epsilon = 0.55$ at t=1.4.

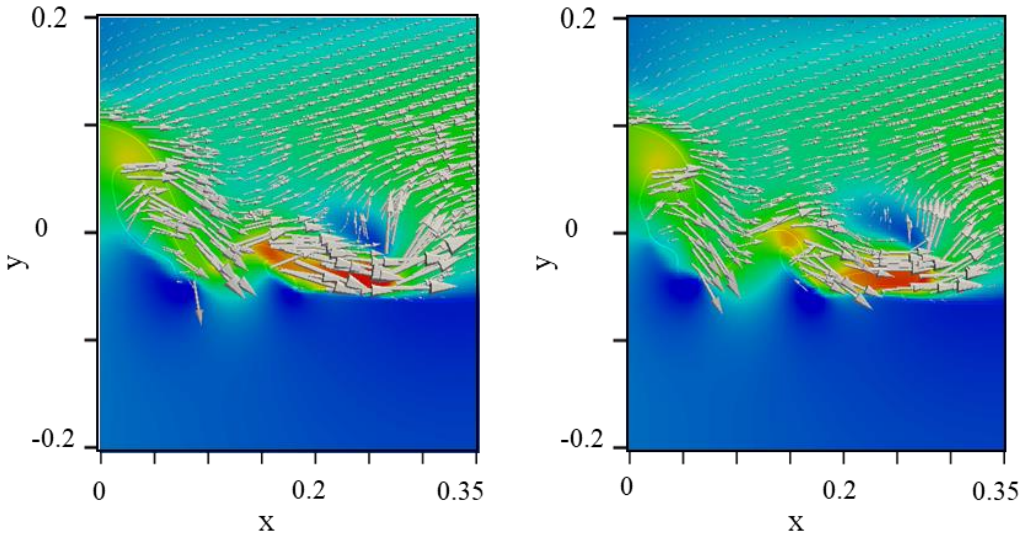

(a) IBVOF solver at t=1.76 (b) IBVOFW4 solver at t=1.76

Figure 6-31 Velocity fields of Stokes waves with IBVOF and IBVOFW4 solvers for $\epsilon = 0.55$ at t=1.76.

6.4 Conclusion

In this chapter, two sets of benchmark cases, solitary waves and stokes waves, are designed for the two-phase flow solver IBVOF solver, with focus on applications in ocean and coastal engineering. In the simulations of solitary waves, two two-dimensional no-viscous benchmark tests, the propagation and the run-up of a solitary wave, have been carried out. The free surface profiles and

velocity fields have been compared with theorical results or one-phase flow solver results, and better agreement has been obtained with the proposed DW-IBVOF solver. The investigation of the velocity field revealed that spurious currents appearing in the vicinity of the interface, resulting in a local increase of the velocity which might have influences the shape of the free surface. The proposed density-weight smoothing (DW) method and the designed boundary layer on the interface suppress the spurious velocities and improve the accuracy and stability of air-water flow simulations.

Then, the simulations of the new solver have been extended to three-dimensional cases. Viscosities of both phases and surface tension are added and RANS turbulent model is used. The case of plunging breaking solitary waves on a slope further validated the solver in the applications in the real world. The spurious velocity in the water phase near the interface finally results in the fake deformation of the interface.

In the second set of cases, the IBVOF solver is used to simulate the propagation of non-breaking Stokes waves and the plunging breaking waves induced by a steep Stokes wave. Similar conclusions can be draw from the propagation of the Stokes wave to the solitary wave. Wave breaking of a steep Stokes wave is also modelled and the results are very closed to the numerical results available in the literature, which further validate the reliable of the proposed IBVOF solver.

Chapter 7 Ship bow breaking waves

7.1 Introduction

Wave breaking is one of the most violent air-water interaction phenomena. A thorough understanding of the physics of this highly unsteady two-phase flow phenomena is important for investigating ship bow breaking waves. It is known that the waves produced closest to the bow of fine fast ships turn over after leaving the hull, create a jet which impacts the free surface and cause evident splashing, droplets, and bubble formation. In this chapter, the proposed two-phase flow solver, IBVOF solver, is used to resolve and investigate bow wave breaking waves.

An assessment of the capability of the IBVOF solver is first performed on a test case specifically conceived, plunging breaking waves generated by a sharp wedge-shaped bow. A numerical towing tank is constructed with a vertical wedge fixed in the middle of the tank and the incident flow set as uniform. The numerical results of the bow wave profile at different locations in the vicinity of the bow are compared to experiments to validate the two-phase flow solver. Then, the IBVOF solver is used to simulation the wave pattern generated by the KRISO Container Ship (KCS) in forward motion. The focuses are put on the hydrodynamic simulation of the whole process of plunging breaking waves and the velocity and vorticity field in the region of the bow and in the breaking waves. Further numerical analysis is performed for different inlet flow velocity to investigate the influence of Froude number on the shape of bow breaking waves.

7.2 Plunging breaking waves on a wedge-shaped bow

Plunging wave breaking is one of the most violent air-water interaction phenomena. A thorough understanding of the physics of this highly unsteady two-phase flow phenomena is important for investigating ship bow breaking waves. To separate the spilling breaking waves with plunging breaking waves and keep focus on the latter, a simplified case is required. A good example is the wedge flow represented by Waniewski et al.[19], Karion et al. [21] and Noblesse et al.[9] in which overturning plunging waves are generated by a sharp wedge-shaped bow. Valuable experimental data are provided like wave elevation and extent of wave breaking. Noblesse et al. [9] also proposed some simple analytical relations for ship bow waves based on his experiments data and potential flow theory. However, even with the simplified case, it is not still possible to achieve a complete description of the complicate phenomena by EFD and the analytical expressions[112].

In order to test the capacity of the presented DW-IBVOF solver, a simplified case is devised to simulate the plunging breaking waves. In this section, the whole process of plunging breaking waves generated by a sharp wedge-shaped bow is investigated with the focus on wave profiles, velocity and vorticity fields around the wedge. A numerical towing tank is constructed with a vertical wedge fixed in the middle of the tank and the incident flow set as uniform. The numerical results of the bow wave profile at different locations in the vicinity of the bow are compared to experiments [19] and the original solver interFoam to validate the proposed two-phase flow solver, IB-VOF solver. Further numerical analysis is performed for different inlet flow velocity to investigate the influence of Froude number on the shape of bow breaking waves based on the proposed solver.

The computational domain and boundaries are shown in Figure 7-1. Since the wedge model is fixed in the numerical wave tank, only half domain is used in the simulation with a symmetry boundary condition on the front side. Non-slip boundary condition is imposed at the wedge and non-slip boundary conditions are used at all the other boundaries. The simulations are conducted on a 3D computational domain of x= [-1, 3], y= [0, 2.5], and z= [-0.0745, 0.5]. The uniform water flow comes from the inlet boundary and comes out from the outlet boundary. The geometry model is built from the wedge shape following the experiment [19]. The side length of the wedge is L=0.75m, and the half wedge angle is θ=26°. For the validation case, the water depth is set as d=0.0745m according to the experiment. An initial uniform velocity is prescribed to the whole computational domain and the velocity imposed at the inlet boundary is fixed with U=2.5m/s. The corresponding Reynolds number, $Re = \rho U d/\mu$ =1.64e5, and the Froude number, $Fr = U/\sqrt{gd}$ =2.93.

The mesh of the blocks consists of conformal non-orthogonal structured elements throughout the whole computational domain. A more refined mesh is employed around the wedge and the plunging breaking wave area compared to the rest of the domain to capture better the near wall turbulent flow and the free surface behaviour. The non-equilibrium wall function is employed for the near wall treatment. The distance to the wall is defined with non-dimensional parameter y+ and the values of y+ around the wedge are in the range of 5-20.

The non-equilibrium wall function is employed for the near wall treatment. The estimation of the distance to the wall is based on the skin friction coefficient (C_f) as follows:

$$C_f = \frac{0.026}{Re^{1/7}}. \tag{7-1}$$

The distance to the wall is defined with the non-dimensional parameter y^+. The values of y^+ around the hydrofoil and the bottom in the present simulations are in the range 5-10.

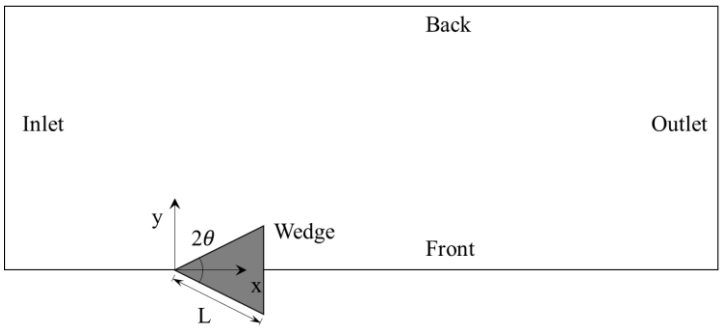

(a) Plan view

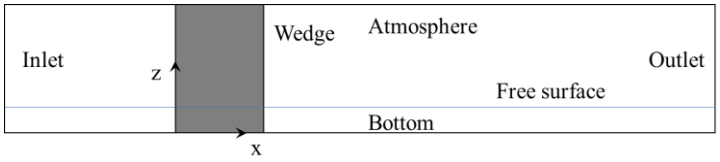

(b) Side view

Figure 7-1 Computational domain of plunging breaking waves generated by wedge-shaped bow with boundaries.

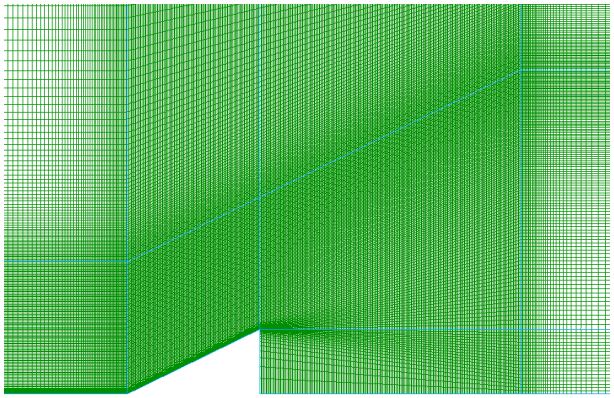

Figure 7-2 Computational mesh around the wedge-shaped bow.

To check the grid independency of the results, three grids are applied in present work with consecutive increased (by a factor $\sqrt{2}$) sizes from mesh A with 7,256,220 grids to mesh B with 5,130,800 grids and mesh C with 3,245,730 grids. The spacing of grids in the area of plunging breaking waves are 0.019m 0.011m and 0.0063m respectively. The maximum Courant number, Co, equals to 0.5 in all these three cases. The wave profiles (α=0.5) obtained by the DW-IBVOF solver at x=0.45m for the three grids are shown in Figure 7-3.

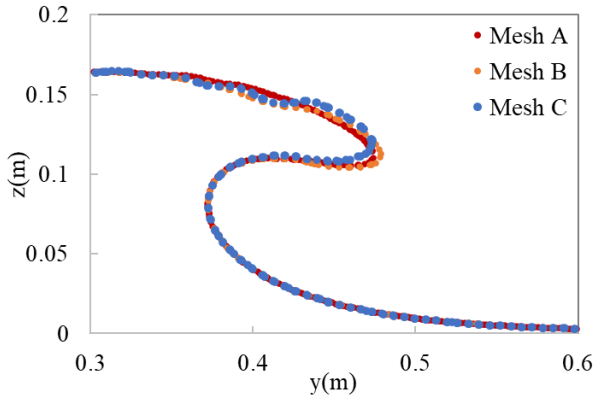

Figure 7-3 Wave profiles of wedge flow obtained by the DW-IBVOF solver with three different grids

The overall structures of the water jet on the three grids are very similar. There are some fluctuations on the backside of the jet on the coarsest grid mesh A. This is due to the lack of sufficient cells per wave height. The result with finer mesh B is much better compared to mesh A. The shape of water jet is much smoother. The jet tip is slightly sharper on the finest grid since a finer mesh can capture more detailed information of free surface with higher grid resolution. In order to capture more detailed wave evolution and the velocity field, the finest mesh is chosen here for better understand of the process of the plunging breaking waves.

7.2.1 Wave profiles compared with the experiment

The two-phase solver is first validated though the comparison with the experiment. Figure 7-4. shows the computed bow wave profile (α=0.5) compared with the EFD photo. As shown in the figure, the overall structure of the plunging breaking waves is well prescribed. A thin sheet of water is generated alongside the side of wedge. The sheet of water is projected sideward into a characteristic overturning motion. The first plunge occurs when the overturning sheet impinges on to the free surface of the water tank followed by splashes at the wake.

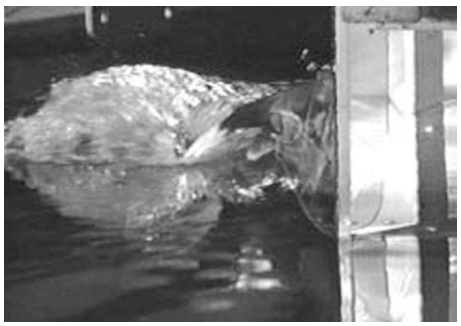

(a) EFD photo [19]

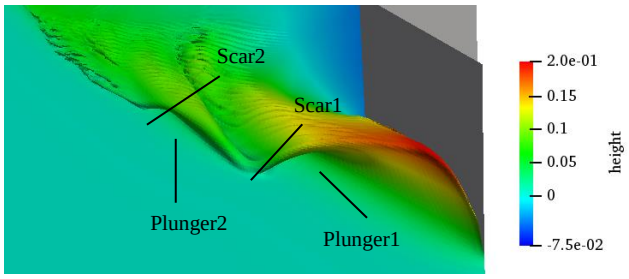

(b) CFD simulation

Figure 7-4 Wave profiles generated by a wedge-shaped bow.

The shape of the main body of water is more obvious with a second plunge in CFD simulations instead of messy white water in EFD. This is a result that might be related to visualization. The iso-surface α=0.5 is usually used to represent the position of free surface. When the droplets are smaller than the grid cells, they are not visible in iso-surface α=0.5. The white water that contains both air and water is represented with α=0.01-0.99. Further grid refinement is required to increase the resolution in the wake to effectively capture the droplets and bubble.

The bow wave profiles, the profiles of the maximum free surface height of the wave alongside x-direction compared with EFD data[19] are shown in Figure 7-5. The EFD 1 is the experimental results done with a wedge model in a towing tank and EFD 2 is the results with an angled plate in a water flume. As shown in the figure, the results in the water flume are slightly lower than in the towing tank. As explained by Waniewski et al. [19], this could be caused by the camera orientations. This indicates that there would be some errors with the observations and the further away from the wedge, the larger the errors would be.

Three profiles with different iso-surface (α=0.01, α=0.5 and α=0.99) from CFD simulation are shown in the figure. The overall trend of wave profiles is similar with the experiments, especially for the near wall area. The heights of wave are lower than the EFD data. The change of mesh seems not increase the height of wave but the iso-surface of α=0.01 is much closer to the EFD results. This may be due to there are breakups on the edge of the thin sheet of water.

Though the wave profile of the iso-surface α=0.01 is closer to the EFD results, the following parts of work is focus on the main body of water and the water phase with $0.5<\alpha \leq 1$ to investigate the velocity and vorticity fields below the free surface.

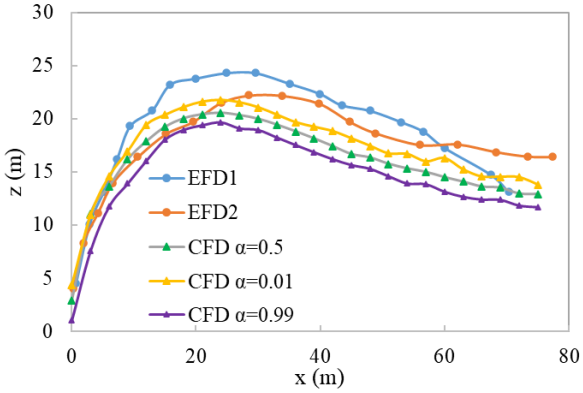

Figure 7-5 Maximum wave height alongside x-direction

7.2.2 Wave Breaking Process

Similar with plunging breaking waves generated by a submerged bump [115], the process of bow plunging breaking can be characterized by five major phases including highest wave formation, the first thin water sheet formation and overturning, the first splash-up, the second water jet and the second splash-up. The major processes of the plunging wave breaking are shown in Figure 7-6 with the velocity vector fields at various x-directions.

The bow wave breaking process is initiated by the pressure field generated by the wedge model. At section x=0.27m, the wave reaches its maximum height and start to overturn. Although the velocity magnitude decreases with the wave height due to the gravity, the y-direction and x-direction velocity components increase and extend towards the sideway. At section x=0.48m, the thin sheet of water is fully generated and projected toward the undisturbed free surface. This part of water is pushed by the side of wedge and accelerated by gravity. The y and z-direction velocity components keep increasing towards the tip of jet. The rest parts of the domain remain the initial conditions with a uniform velocity field.

At section around x=0.60m, the first plunge occurs when the overturning jet impingers onto the undisturbed free surface. With the overturning jet, a large amount of air below the jet is entrapped which forms a big air bubble. This could be one of the major sources of underwater noise and white-water wake [116]. Another source of air entrainment would be the impact of the water jet on the face of water. The resulting splash-up generates the second water jet at around section x=1.02m (see Figure 7-6(d)) and the second splash up at section around x=1.2m (see Figure 7-6(e)). The second plunger basically repeat the process of the first one with smaller wave height and less wave energy. The energy dissipation mechanism during the bow plunging wave breaking need further investigations.

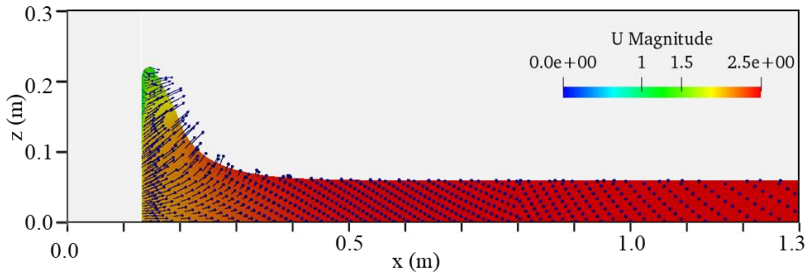

(a) Max height, x=0.27m.

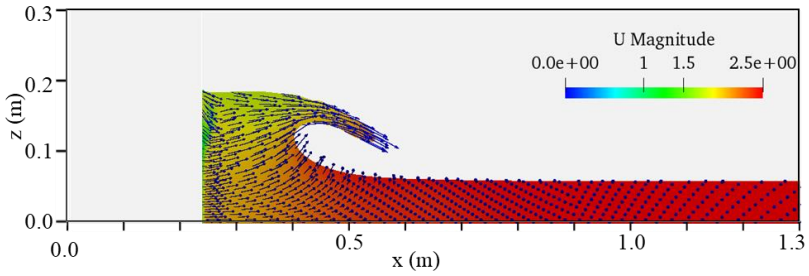

(b) First jet, x=0.48m.

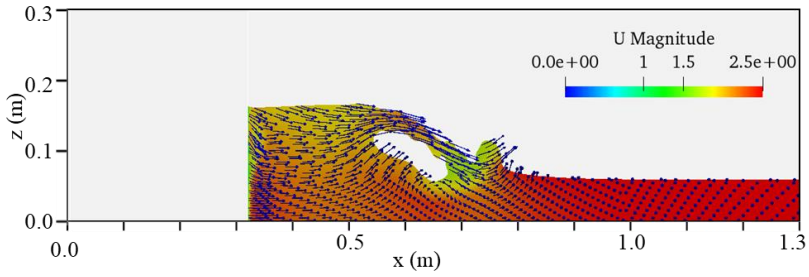

(c) First splash-up, x=0.65m.

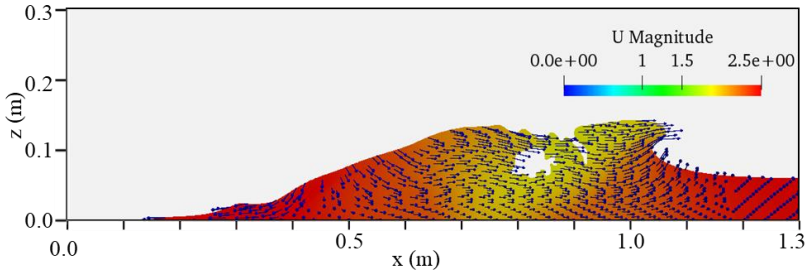

(d) Second jet, x=1.05m.

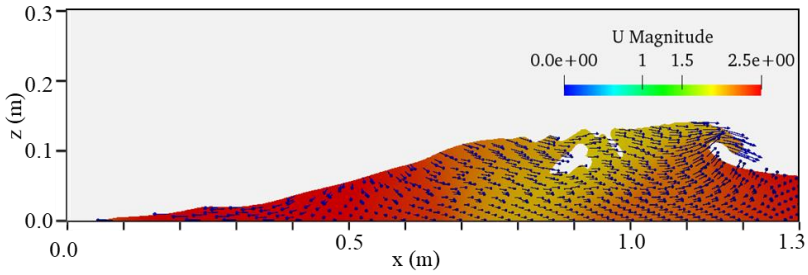

(e) Second splash-up, x=1.2m.

Figure 7-6 Wave profiles and velocity field alongside x-direction.

7.2.3 Vorticity Profiles during the wave breaking process

The investigation of the turbulent flow below the plunging breaking waves are in terms of the vorticity fields. The layouts of axial vorticity distributions at various transverse sections are presented in Figure 7-7. It is obvious that the vorticity is mainly concentrated near the wall of wedge and the free surface. The positive vorticity near wall is generated by the viscous boundary layer due to the non-slip boundary condition. This indicates that the turbulent flow is well described by the solver with the standard k-ω SST turbulence model. It is also clear that the bow wave breaking induces two pair of counter-rotating vortices corresponding to the two plunging breakers.

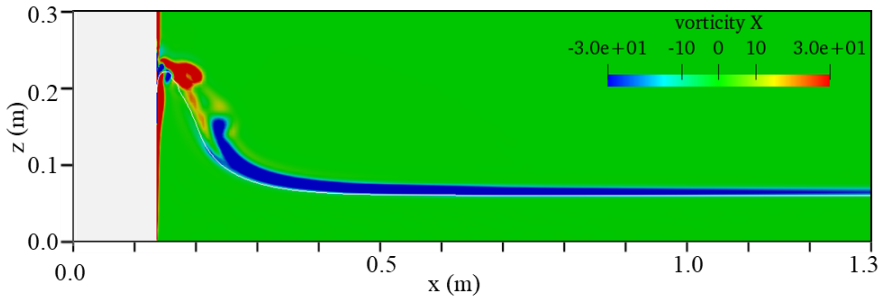

(a) Max height, x=0.27 m.

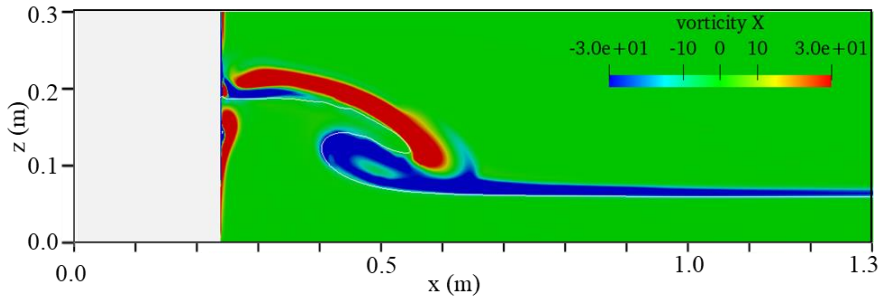

(b) First jet, x=0.48 m.

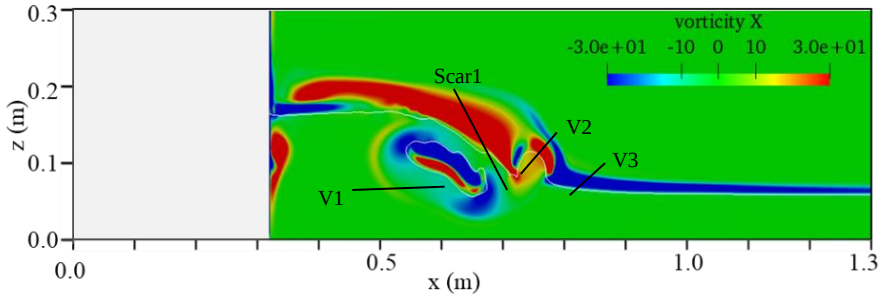

(c) First splash-up, x=0.65 m.

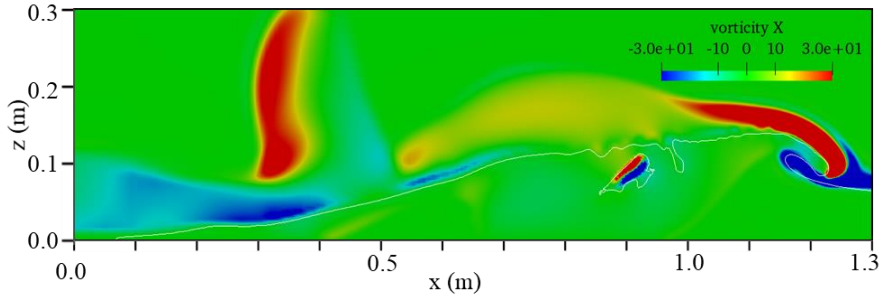

(d) Second jet, x=1.23 m.

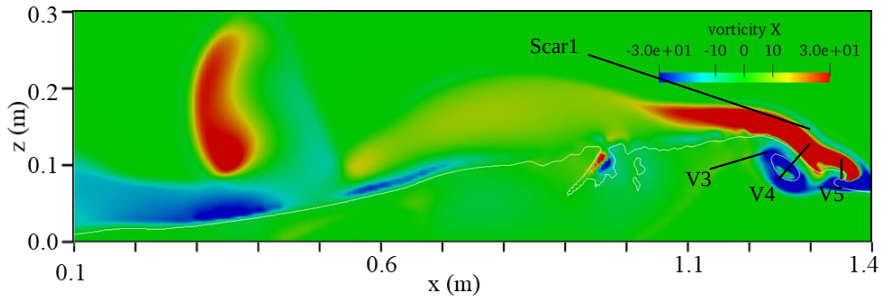

(e) Second splash-up, x=1.35 m.

Figure 7-7 Vorticity profiles alongside x-direction.

Despite the vorticities generated near the non-slip wall, the first region of negative axial vorticity V1 appears close to the throat of the plunger at around x=0.60m. The location of the vortex core was found near the free surface associated with the small radius of curvature of the overturning bow wave. A positive vorticity area is generated on the tip of the water jet. At the section x=0.6m, when the tip of the first jet impacts the undisturbed free surface, the free surface is deflected with an oblique splash up. The angle and velocity of the second plunger is not only determined by the interaction between the two parts of water which follows the momentum theorem but also affected by the pair of vortexes i.e. negative vortex V1 and positive vortex V2 at the deflection point. This vortex pair leads to the generation of the first scar (scar1) and has a rotating orientation pumps fluid upward forming a new water jet. This process repeat itself at the second plunger. The energy

of the second plunger is much small than the first one, but it is still clear visible at section x=1.2m that the vortexes V3, V4, V5 and the scar2.

7.2.4 The Effect of Fr Number

In this section, the influence of change in the inlet flow i.e., the Fr number on the hydrodynamic behaviors of bow wave breaking is investigated. The main characteristics of a ship bow wave, more specially, the plunging breaking waves, includes the height of the wave, the shape of the bow wave (bow wave profile), the distance between the stem and the bow wave crest, the position of scars and the angle of the bow wave. Some simple expressions of the relationship have been given in [9] based on the experiments and potential flow theory. In present work, a quantitative study is given based on the simulations of the two-phase flow solver and a detailed qualitative relationship will be investigated in the future work.

Increasing the incident flow velocity from U=2.5 m/s to U=3.0 m/s and U=3.5 m/s, the corresponding Fr number increases from 2.93 to 3.52 and 4.09. Figure 7-8 shows the plan views of the bow waves of three cases colored by the height of wave. It is obvious that the bow wave in higher ship speed will generated the increase of height of the first plunger. The highest wave crest reaches to 33.27 cm for Fr=3.52, which is 1.5 times of that for Fr=4.09.

Figure 7-9 shows the summary of bow wave profiles results from different Fr number. The maximum height of the wave crest shows the similar trend in the two smaller Fr number case. The height increases shapely with the first plunger generated by the side of wedge and decrease gently while the first plunger impacts into the undisturbed free surface in the region of 0<x<0.8m. For the highest velocity runs in the simulation, both the first and the second plunger are less obvious.

The first water jet is much thinner than the bow wave shown in Figure 7-4 and the water sheet breaks up into droplets before it reaches the undisturbed free surface. Figure 7-10 shows the wave profiles for Fr=4.09 visualized by α=0.5 and α=0.01. As mentioned above, the iso-surface α=0.5 (Figure 7-10(a)) shows the position of the main body of water, while the iso-surface α=0.01 (Figure 7-10 (b)) represent the distribution of cells containing droplets that are smaller than half size of the grid cell. The iso-surface α=0.01, however, doesn't represent the shape and the size of droplets. In present work, with the grid spacing 0.75mm near the wedge and 6.3mm in the plunging wave area, the smallest droplet can be effectively captured would be around 7mm which is still too large than the droplets observed in the experiments.

Despite the height of bow plunging waves, the Fr number have effect on the position of the scar and the angle of wake pattern. As shown in Figure 7-9, P is the start point of the first scar, D is the

vertical distance between the scar1 to the side of wedge, θ is the bow wave angle. It is clear that the position of P tends to be further away from the back edge of the wedge, the distance tends to be shorter, and the wave angle tend to be smaller with the increase of Fr number. This trend is due to the increase of inlet water which is similar to the narrow Kelvin ship waves (Noblesse et al., 2016). However, the simple analytical relations of large-scale wake angle are not applicable for the highly non-linear viscous flow. The effect of small-scale detailed plunging breaking, spray formation and air entrainment to the overall ship bow waves is required quantitatively investigation in the future work.

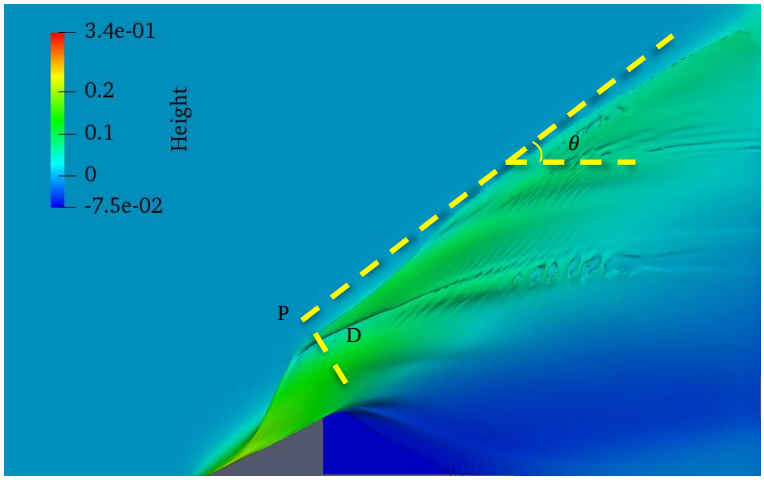

(a) U=2.5 m/s, Fr=2.93, α=0.5.

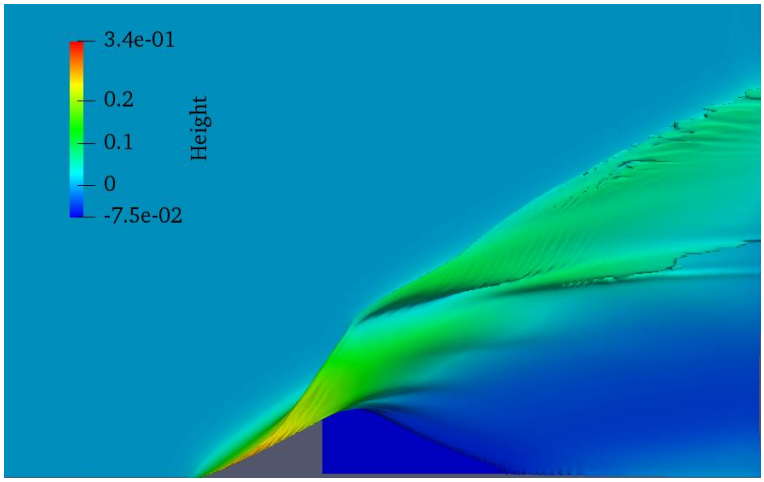

(b) U=3.0 m/s, Fr=3.52, α=0.5.

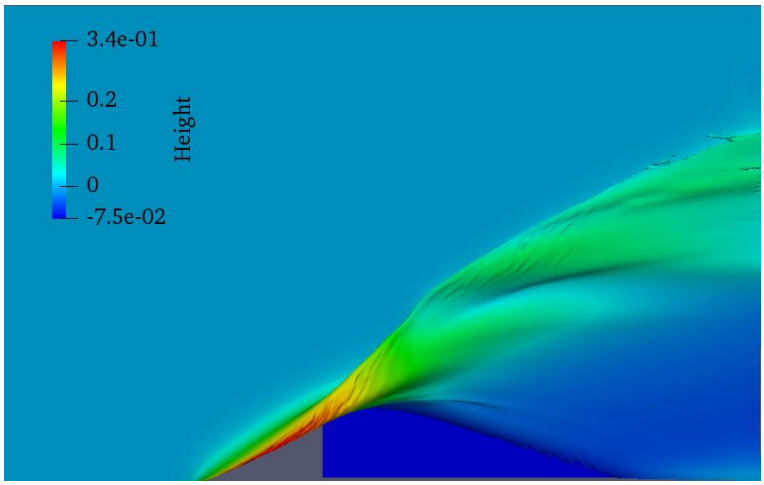

(c) U=3.5 m/s, Fr=4.09, α=0.5.

Figure 7-8 Plan views of the waves generated by the wedge-shaped bow at different speeds.

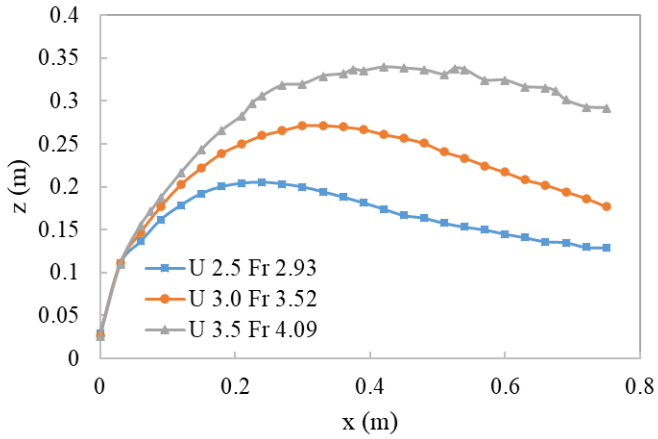

Figure 7-9 Wave profiles generated by a wedge-shaped bow with different Fr number.

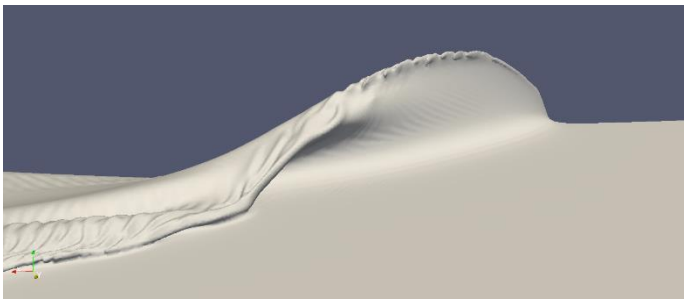

(a) U=3.5 m/s, Fr=4.09, α=0.5

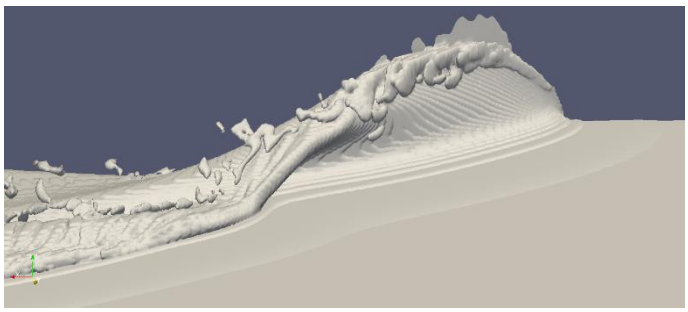

(b) U=3.5 m/s, Fr=4.09, α=0.01

Figure 7-10 Free surface distributions on the wave crest for the wedge-shaped bow case

The major processes of the plunging wave breaking are well predicted including the highest wave formation, the first thin water sheet formation and overturning, the first splash-up, the second water jet and the second splash-up. The bow wave breaking process is initiated by the pressure field generated by the wedge model and mainly dominated by gravity and inertial force. A large amount of air entrapment and droplets are generated near and after the plunger which are significant sources of underwater noise and while water wake. In the process of plunging wave breaking, the angle and velocity of the second plunger is not only determined by the interaction between the two parts of water which follows the momentum theorem but also affected by the pair of vortexes.

7.3 KCS bow breaking waves

The KRISO Container Ship (KCS) modelled with length of L= 6.0702m is used for the present numerical simulations. The KCS ship model is conceived to provide data for CFD validation for a modern container ship with bulb bow and stern. A numerical towing tank is constructed with a fixed KCS in the middle of the tank.

7.3.1 Numerical set-up for KCS bow breaking waves

The main objective of this work is to simulation the bow breaking waves around the KCS ship in forward motion. The KCS hull without rudder is selected in present simulation to keep focus on the bow area. The geometry model is shown in Figure 7-11 and the principal dimensions are listed in Table 7-1. A validation study is first conducted with a lower speed ($Fr = U/\sqrt{gL}$ =0.26) to check the prediction accuracy of the current two-phase flow solver DW-IBVOF solver with experiment data. Then, simulations are performed over a range of higher speeds to investigate the local behaviours of bow breaking waves and scale effects.

The computational domain and boundaries for KCS flow are shown in Figure 7-12. Since the KCS model is fixed in the numerical wave tank, only half of the computational domain is used in the simulation with a symmetry boundary condition on the front side to save computational costs. Non-slip boundary condition is imposed at the KCS hull and slip conditions are put on the tank bottom and roof.

Figure 7-11 Geometry of KCS hull model

Table 7-1 Principal dimensions of KCS (full scale and model scale)

Main particulars		Full scale	Model scale
Length between perpendiculars	L_{pp} (m)	230	6.0702
Maximum beam of waterline	B_{WL} (m)	32.2	0.8498
Draft	T(m)	10.8	0.2850
Displacement volume	Δ (m^3)	52030	0.9565
Wetted surface area (with rudder)	S_0 (m^2)	9645	6.7182

The simulations are conducted on a 3D computational domain of x= [-L, 4L], y= [0, 1.5L], and z= [-1.5L, 0.75L] where L is one ship model length. The uniform water flow comes from the inlet boundary and comes out from the outlet boundary. An initial uniform velocity is prescribed to the whole computational domain for both water and air phases, and the velocity imposed at the inlet boundary is fixed.

The $k-\omega$ Shear Stress Transport (SST)model is used to achieve good modelling of both near-field turbulence used to achieve good modelling of both near-field turbulence (inside boundary layer) and far-field turbulence (wake and ambient turbulence.) A small, fixed value corresponding to 3% of the fixed inlet velocity is set on the inbound turbulence intensity to model the presence of some initial turbulence in the tank. This is in line with commonly used values of 1-5% for towing tank and wind tunnel simulations. Furthermore, a value of the specific dissipation rate ω is given as the inlet boundary condition.

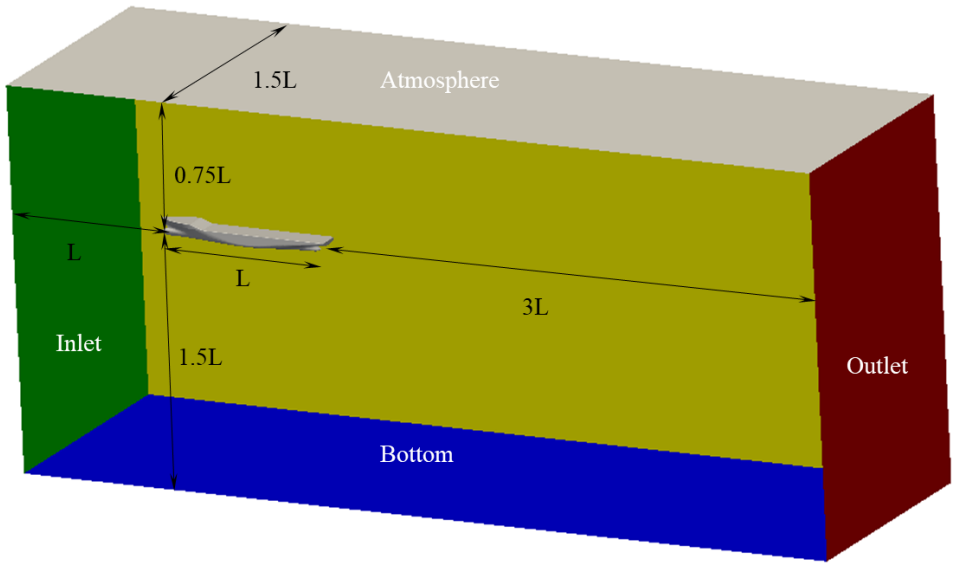

Figure 7-12 Computational domain of KCS flow with boundaries.

7.3.2 Mesh generation and convergence study

There are several factors need to be considered when generate mesh for the numerical water tank. First of all, the mesh sizes in the free surface region are supposed to be small enough to capture the evolution of waves generated around the ship. Secondly, mesh density should increase in the region around the ship hull to capture the boundary layer. Thirdly, a mesh refinement zone is required in the bow region to capture the bow breaking waves. What's more, it is important to minimis total number of cells to speed up calculation time.

The unstructured mesh is generated based on an original structured background mesh with 77×23×76 in x, y, z direction within the computational domain. 6 refinement zones are added to refine the meshes in three different zones the free surface region, the near-hull region and the bow region. The arrangement of the refinement zones is shown in Figure 7-13. Based on the original structured mesh, cells are selected and split in horizontal and vertical direction in these zones. The extent of the refinement zone is reduced after each refinement level step for smooth transitions

between areas of different mesh densities. In the final refinement step, the finest mesh zone exists near the hull and free surface. Base on that, several layers are added closed to the ship hull to capture the boundary layer.

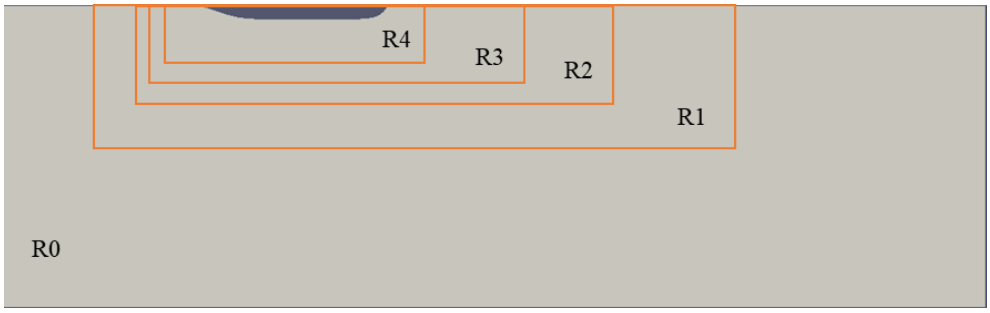

(a) Global view of refinement zones

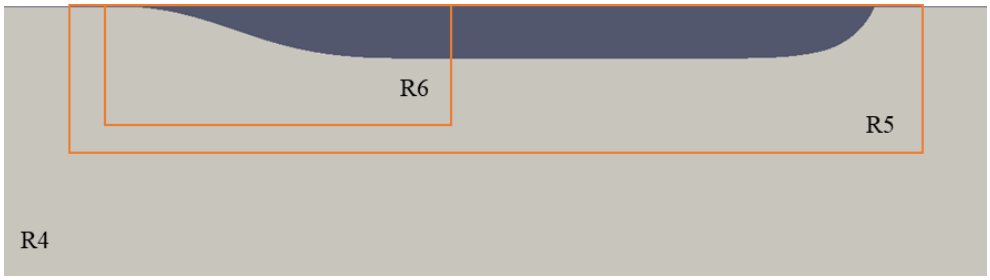

(b) Local view of refinement zones

Figure 7-13 Mesh generation and refinement zones for KCS bow breaking waves

Discretisation error is the main source of computational errors[117] which arise from numerical schemes, mesh style and number used to discretize the equations, etc. The uncertainty relating to the mesh resolution is therefore required to be discussed. In this part, mesh-size and time-step convergence study is carried out to verify the efficiency and accuracy of the numerical water tank and the proposed DW-IBVOF solver.

To check the grid independency of the results, three grids are applied in present work with consecutive increased (by a factor $\sqrt{2}$) sizes from mesh A with 4,354,625 grids to mesh B with 5,833,872 grids and mesh C with 4,478,533 grids. The spacing of grids in the area of plunging breaking waves are 0.01m 0.008 m and 0.006m respectively. The maximum Courant number, Co, equals to 0.5 in all these three cases.

For validation purposes, a case study with a lower speed U= 2.017 m/s ($Fr = U/\sqrt{gd}$ =0.26) is first conducted. The lower speed case is selected in this part for the reason that the detailed experimental data including wave pattern is only available of this case[118].

Figure 7-14, Figure 7-15 and Figure 7-16 show the comparison of the free surface profiles at different longitudinal section (y/L= 0.0741, 0.1509 and 0.4224) with the three mesh sizes and experimental data. Figure 7-17 shows the results of wave profiles on the hull surface. The wave height (z) is normalized by the ship length. For the free surface profiles, the numerical results obtained from the three grids are very similar and in a good agreement with the experiment data both for the near field and far field from the ship hull.

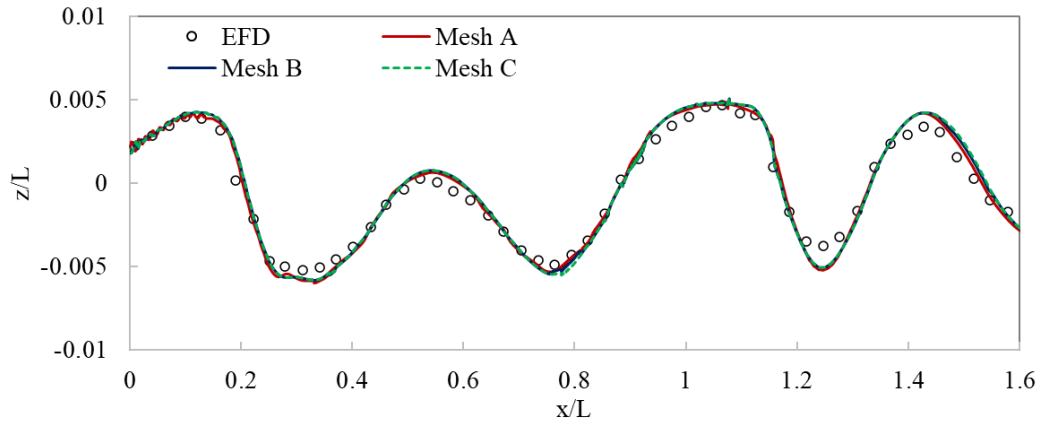

Figure 7-14 Free surface profile at y/L= 0.0741 for Fr= 0.26 on different mesh sizes compared with experimental data[118]

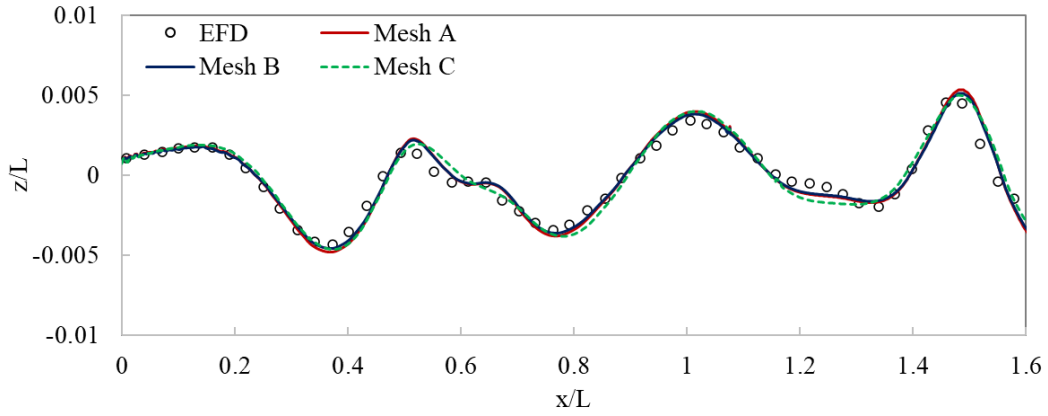

Figure 7-15 Free surface profile at y/L= 0.1509 for Fr= 0.26 on different mesh sizes compared with experimental data[118]

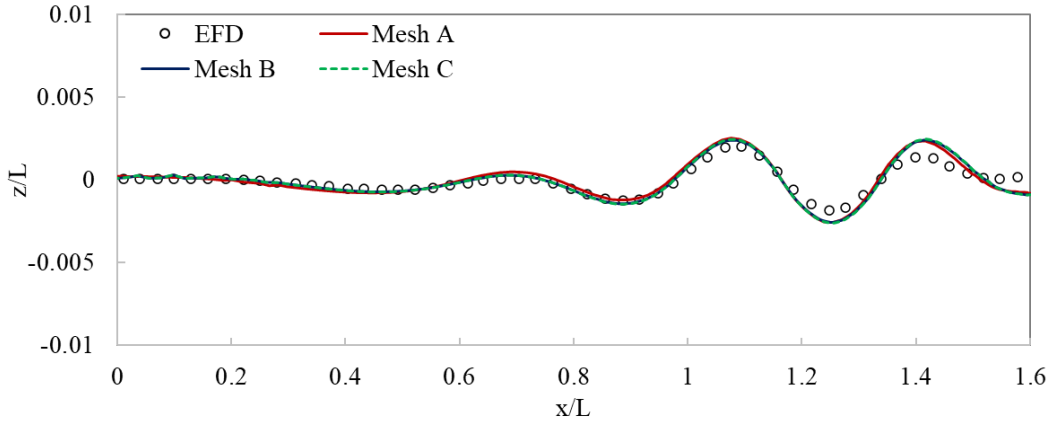

Figure 7-16 Free surface profile at y/L= 0.4224 for Fr= 0.26 on different mesh sizes compared with experimental data[118]

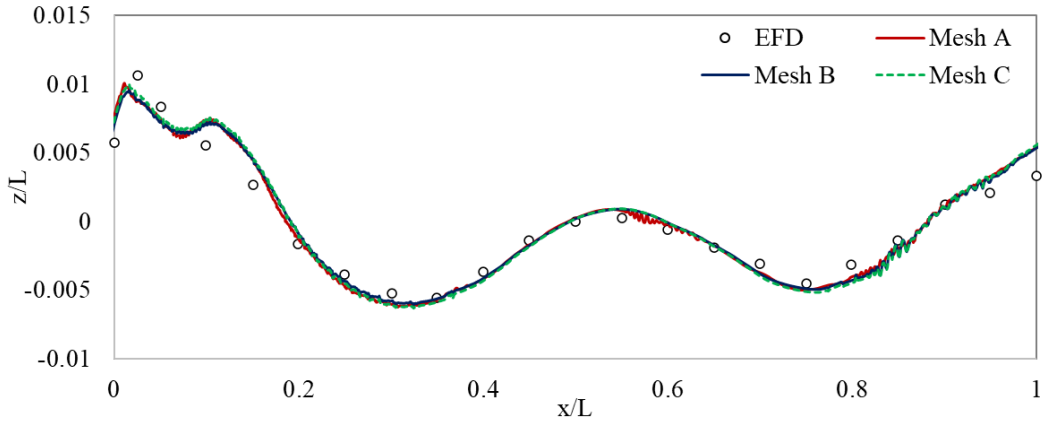

Figure 7-17 Wave profile on ship hull surface for Fr= 0.26 on different mesh sizes compared with experimental data[118]

In this work, the analysis of convergence study is performed for the height of the wave crest generated by the ship at section y/L = 0.0741. The convergence condition is assessed through the convergence ratio (R) which is given by[117]:

$$R = \frac{\varepsilon_{12}}{\varepsilon_{23}} \tag{7-2}$$

where ε_{12} is the change in the numerical solution between Mesh A and Mesh B and ε_{23} is the change between the Mesh B and Mesh C. According to definition from Stern et al[119], the numerical model is monotonically converging when the convergence ratio R is 0<R<1. The details of convergence parameters are illustrated in Table 7-2.

Table 7-2 Convergence statics for height of wave crest at Fr= 0.26

Parameters	First crest	Second crest	Third crest
Mesh A	4.15e-3	7.27e-4	4.76e-3
Mesh B	4.13e-3	7.12e-4	4.74e-3
Mesh C	4.12e-3	6.94e-4	4.71e-3
ε_{BA}	1.34e-5	1.52e-5	1.65e-5
ε_{CB}	1.56e-5	1.84e-5	2.78e-5
R	0.861	0.830	0.592

The wave elevation generated around the ship hull is sensitive to the grid change. According to Table 7-2, the change of the wave crest hight decreases slightly through refinement from a coarse grid to the fine mesh. This suggests that the convergence has already achieved by Mesh C. All the three mesh in the free surface region is fine enough to be able to capture the propagation of surface waves for the validation case with Fr= 0.26. The calculated wave profile on ship hull surface in Figure 7-17 changes slightly with the gird sizes, which reals that the effect of the grids are small for the present range of grid size. The mesh near the hull is fine enough to resolve the development of the boundary layer. However, in order to provide fine mesh to capture more details for higher Fr cases, the Mesh A is selected for the highest resolution though more calculation is required. The overall cell count for Mesh A is within appropriate limits for free surface computations for ships.

7.3.3 Free surface wave field

In section 7.3.2, the lower speed case Fr= 0.26 is selected to validate the accuracy of the DW-IBVOF solver compared with experimental data and analysis the mesh convergence. It is obvious that the predicted free surface elevation agrees very well with the experimental measurements both for the near and far fields. The accurate prediction for the validation cases lays a good foundation for the high-speed ship simulations.

At Fr= 0.28, the free surface profiles show a relatively smooth topology without large-scale plunging breaking, though weak and very small-scale bow wave curling, and spilling breaking is observed near the ship bow and shoulder in a closer examination. The bow waves become steeper and higher when the ship speed increases. At Fr= 0.35, a strong plunging breaking bow wave is observed in the simulation with significant air entrainment. In order to investigate the free surface features of breaking waves, the case of Fr= 0.35 is chosen in the following sections.

Figure 7-18 shows the comparisons of CFD simulations of wave fields by the two two-phase flow solvers. The predicted bow wave, first trough, and shoulder wave structures are in very good agreement between the two solvers. The effects of the breaking bow plunger can clearly be seen on the wave pattern. The wave pattern is slightly different from a classical Kelvin pattern. Figure 7-18 (b) provides a close-up perspective view of the predicted breaking bow wave around the ship model. The DW-IBVOF solver solution shows two scars that separate the bow waves into three waves. The two scars are the position where the plungers hit and rebound on the undisturbed free surface.

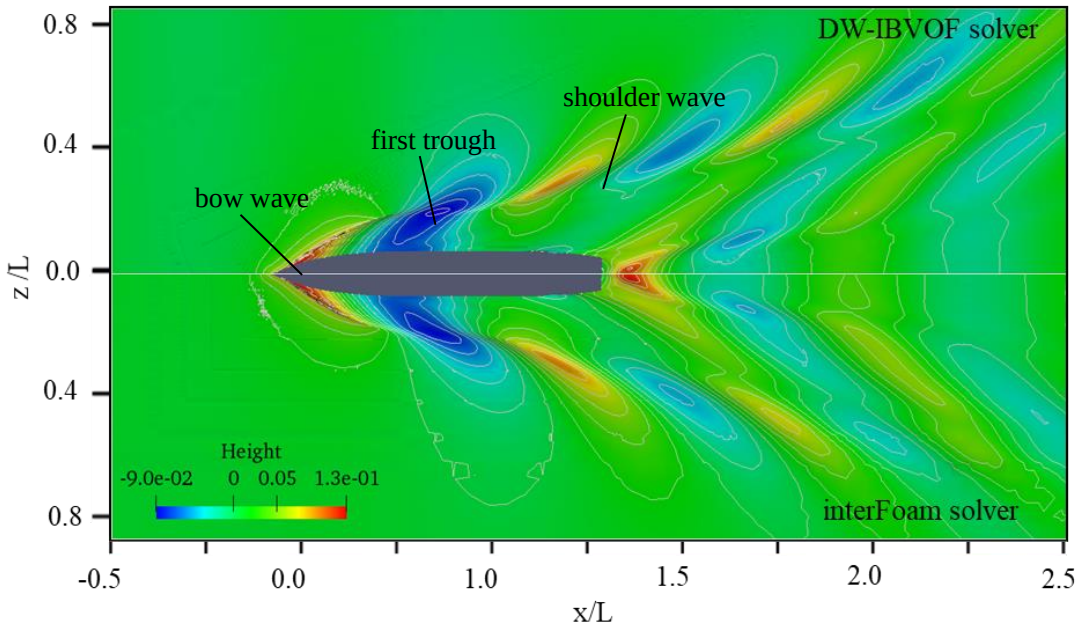

(a) Global wave contours

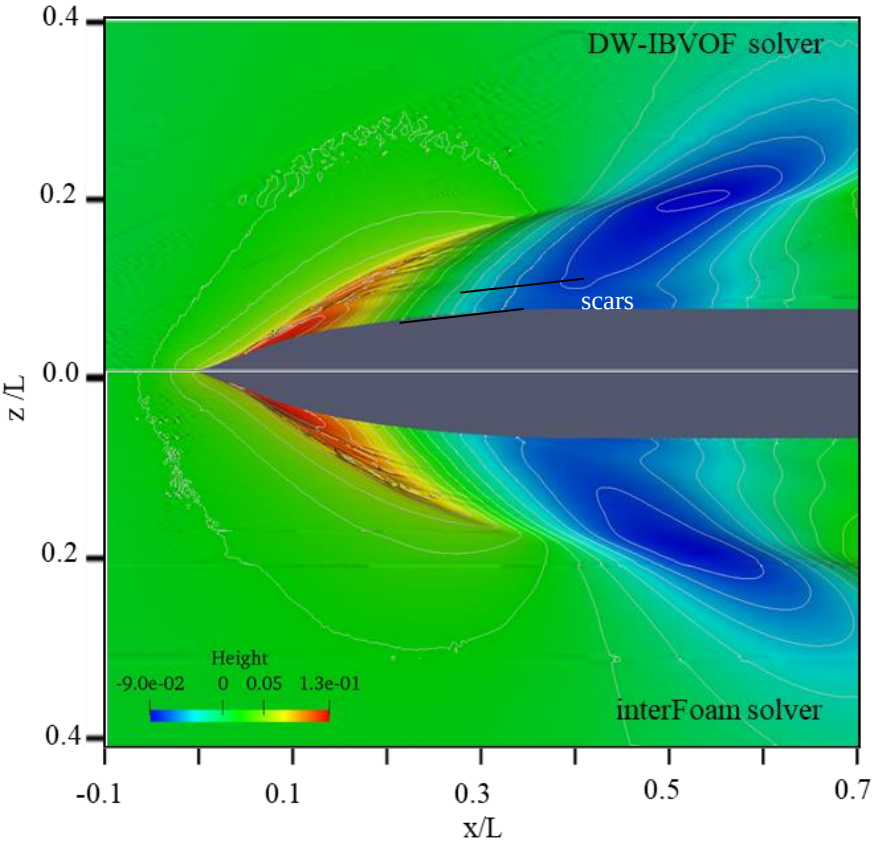

(b) Bow wave profiles

Figure 7-18 Comparison of CFD solutions of the DW-IBVOF solver and the interFoam solver for KCS wave contours, Fr= 0.35

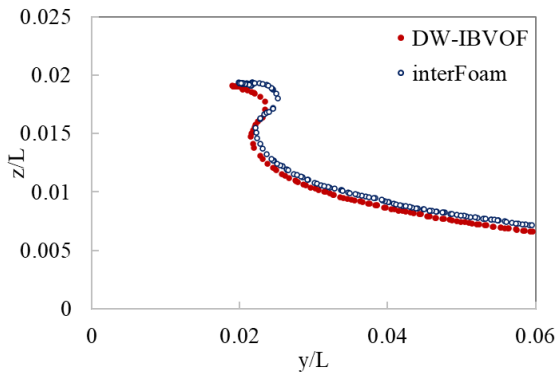

(a) Free surface profile at x/L= 0.05

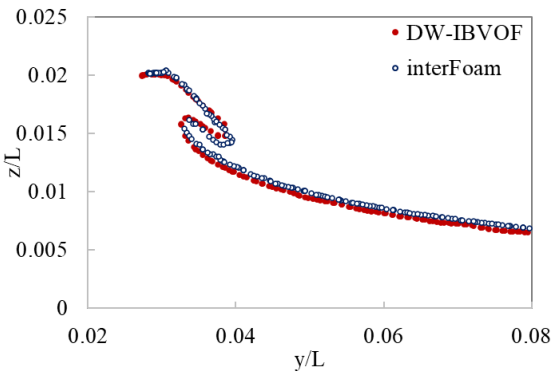

(b) Free surface profile at x/L= 0.07

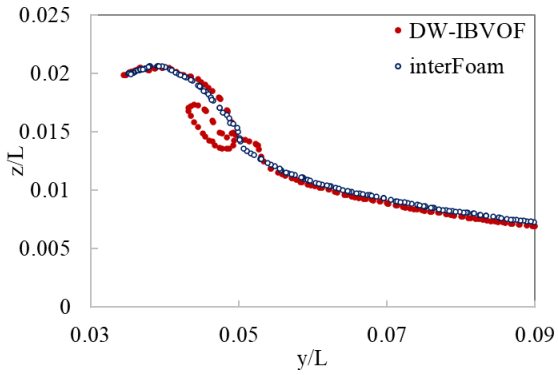

(c) Free surface profile at x/L= 0.09

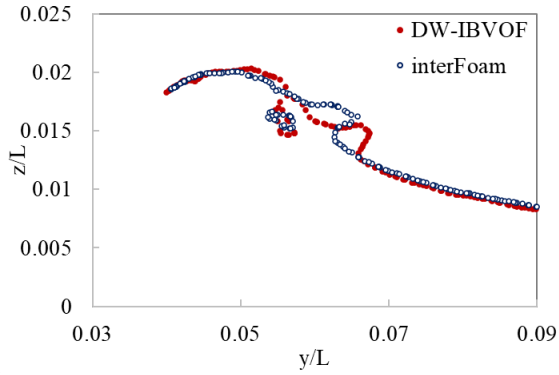

(d) Free surface profile at x/L= 0.11

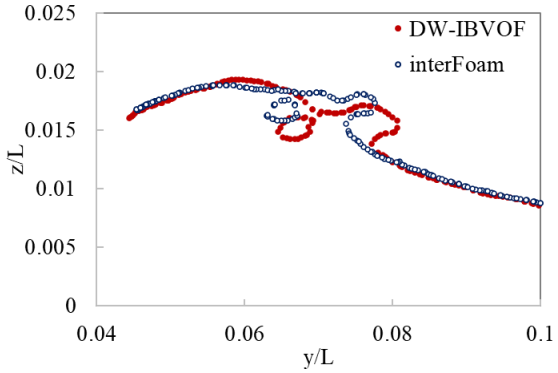

(e) Free surface profile at x/L= 0.13

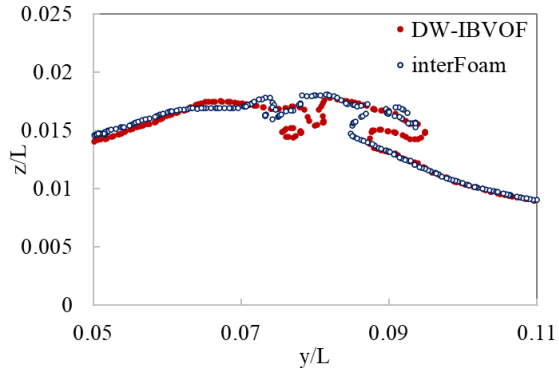

(f) Free surface profile at x/L= 0.15

Figure 7-19 Comparison of CFD solutions of the DW-IBVOF solver and the interFoam solver for KCS transverse waves cuts, Fr= 0.35

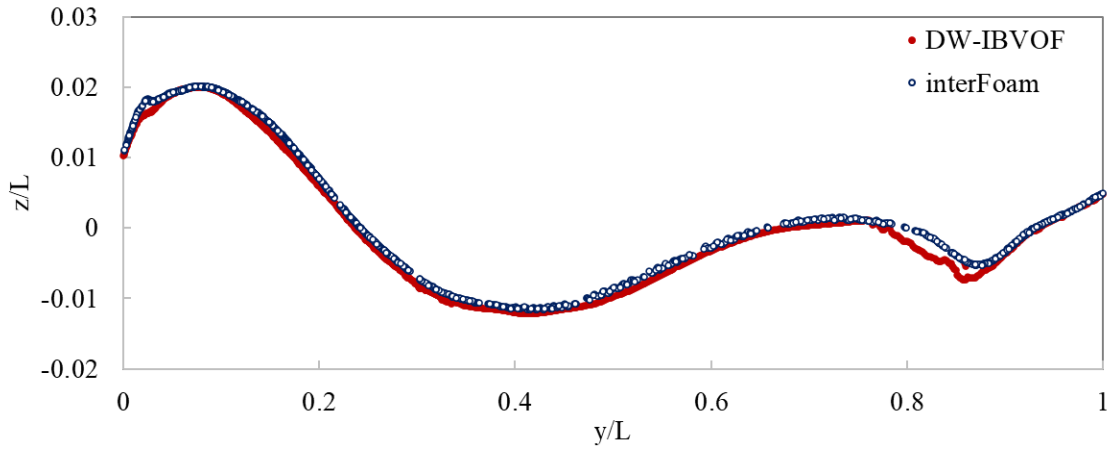

Figure 7-20 Wave profile on ship hull surface for Fr= 0.35 with the DW-IBVOF solver and the interFoam solver

Compare to the IBVOF solver, it seems that the interFoam solver results are more violent and unsteady. The plungers tend to break-up before they hit the undisturbed free surface. However, the amplitude of waves obtained from the interFoam is slightly smaller than the IBVOF solver. The wave height range of the IBVOF solver is from -0.094m to 0.125m while in interFoam solution, the range is from -0.086m to 0.123m. The IBVOF solver prediction shows a slightly more steep and sharp shoulder wave than the interFoam.

A more quantitative comparison of the wave field is provided in Figure 7-19 and Figure 7-20. The transverse wave cuts (iso-surface $\alpha = 0.5$) from x/L= 0.05 to 0.15 and the wave profile at the hull surface are directly compared to illustrate the bow wave elevation and the difference by the two solvers. As shown in Figure 7-19, the breaking wave phenomena, plunger formation, reconnection and rebound, are well captured by both solvers, while the IBVOF solver shows larger wave amplitude for each section.

At section x/L= 0.05 and 0.15, the results of two solver are in good agreement. The differences occur when the plunger hits the undisturbed free surface. At section x/L= 0.09, with the overturning plunger, a large amount of air below the plunger is entrapped which forms a big air bubble. In the solutions of the IBVOF solver, the interface between the air bubble and the plunger are clearly observed while the interFoam solver fails to capture. This doesn't mean that no air entrainment happens in the interFoam solutions. Figure 7-21 shows the snapshots of volume fraction α distribution with the two solvers at section x/L= 0.09. The white line is the position of the interface between air and water represented by iso-surface $\alpha = 0.5$. In the interFoam solution, less air is entrapped by the plunger and the cells below the plunger contain both water and air with values of water volume fraction around 0.7. The iso-surface $\alpha = 0.5$ fails to represent the air bubble at this section.

Compared to the interFoam solver, the IBVOF solver shows a smoother and sharper interface. At the later section x/L= 0.11 and 0.13, although the interFoam and IBVOF bubbles are located at almost the same place, the size of the air bubble in IBVOF solver is slightly larger than the interFoam. At section x/L= 0.15, the free surface breaks up in the interFoam solution while a second plunger is generated in the IBVOF solutions after the first plunger reconnection and rebound from the undisturbed free surface. Based on the above evidence, the proposed IBVOF solver is more appropriate for the simulation of KCS bow breaking waves and is adopted for the following analysis.

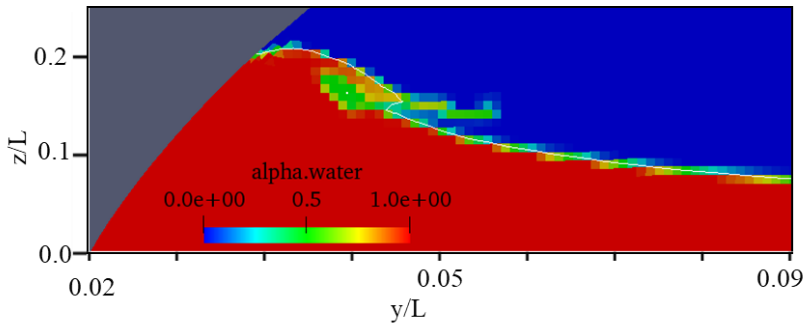

(a) InterFoam solver

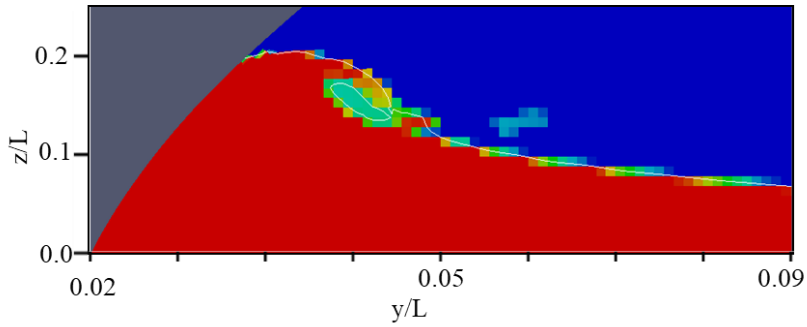

(b) DW-IBVOF solver

Figure 7-21 Volume fraction α distribution for KCS transverse waves cut x/L= 0.09, Fr= 0.35

7.3.4 KCS bow wave breaking pattern

The strength of the initial plunging jet which develops at the crest of the overturning bow wave is crucial in determining the severity of subsequent splashing and submerged vertical structures[120]. In order to give better descriptions of the breaking waves, the initial stages of bow wave breaking for the case Fr= 0.35 is analysed.

Figure 7-22 shows the cross-flow velocity magnitude ($U_{cross} = \sqrt{U_y^2 + U_z^2}$) with the velocity vector fields at six cross-sectional planes (x/L= 0.05, 0.07, 0.11, 0.15, 0.20 and 0.25) through the breaking bow waves. The axial vorticity and turbulent kinetic energy are shown in Figure 7-23 and Figure

7-24. The major process of the plunging wave breaking by the KCS hull is similar to the wedge-shaped bow in section 7.2. The water around the hull is pushed away and runs to the side and up alongside the ship hull.

At section x/L= 0.05, a steep bow wave forms and starts to overturn due to the turning of the flow at the leading edge of the bow. Although the velocity magnitude is decelerated due to gravity, the crossflow velocity magnitude increases and extend towards to the sideway. The higher transverse velocity at the top of the steep bow wave forms a pair of vortexes. In the high curvature region of the overturning wave, the negative axial vorticity is generated in the process that the initial plunger is falling. Also shown is the lager value of positive vorticity and turbulent kinetic energy k contained within the sheet of turbulent boundary layer.

At section x/L= 0.07, the first plunger has already formed due to the large transvers velocity at the crest and is falling towards the free surface below. The crossflow velocity keeps increasing towards the tip of the shin sheet of water. The large differences in the cross-plane velocity components in the plunger tip and the free surface below is one of the main reasons that the plunging breaking waves are formed. Apart from the turbulent boundary layer near the ship hull, very small turbulent kinetic energy k is observed in the plunger and the free surface (see Figure 7-24 (b)). The plunger that consist of the detached thin sheets of water is mostly steady until it hit the main free surface and undergo turbulent breaking up and diffusion.

At the third section x/L=0.11, the first plunge occurs when the overturning wave impinges onto the free surface below. With the overturning jet, a large amount of air is entrapped which forms a big air bubble below the overturning wave. Once the first plunger touches the free surface, splash-up initiates and develops at the location where it impacts. As shown in Figure 7-22(c), an oblique splash-up is generated and a second plunger tends to form.

Compared to section x/L= 0.07, the maximum value of cross flow velocity at the section x/L=0.11 decreases due to the impact. The large jump in velocity components across the reconnection part of the tip and the free surface generates a counter-rotating vortex pair at the newly formed second plunger. This vortex pair has an rotational orientation and is responsible for the formation of the second plunger[121] visible at section x/L= 0.15.

As shown in Figure 7-24(c) and (d), large turbulent energy is observed as soon as the first plunger reconnects with the free surface. The plunger impact ends the mostly steady state of the overturning water sheet. The interactions of the first plunger and the free surface create a turbulent kinetic energy source and the vortex pair intensifies the turbulent flow by accelerating the cross flow in a short distance across the reconnection region.

The last two sections x/L= 0.2 and x/L= 0.25 show the wave pattern after the bow plunging breaking waves. As shown in Figure 7-22 (e) and (f), the differences in the cross-plane velocity components in the region closed to the free surface and the water far below is much less than section (b) and (c). Though weaker axial vorticity is observed in Figure 7-23 (e) and (f), the relatively high kinetic turbulent energy remains in Figure 7-24 (e) and (f). A large amount of energy is dissipated in the region of the plunging breaking waves, and a third plunger fails to generate.

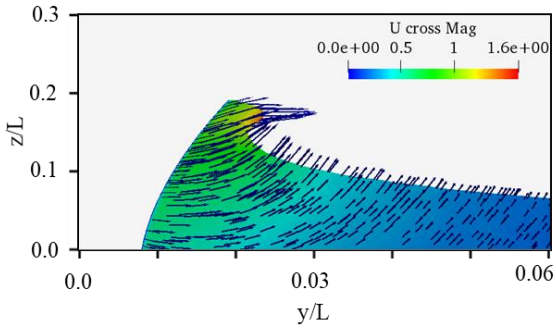

(a) Section x/L= 0.05

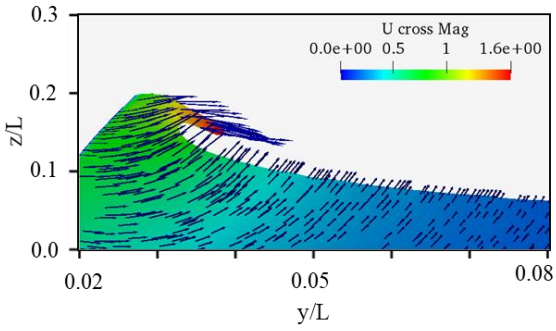

(b) Section x/L= 0.07

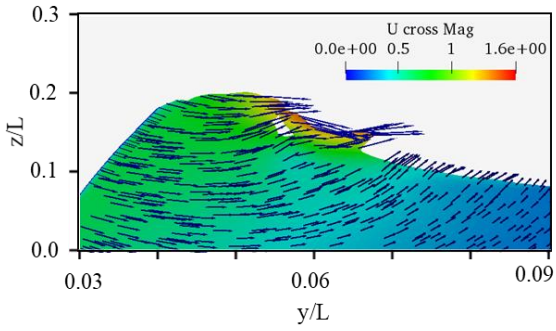

(c) Section x/L= 0.11

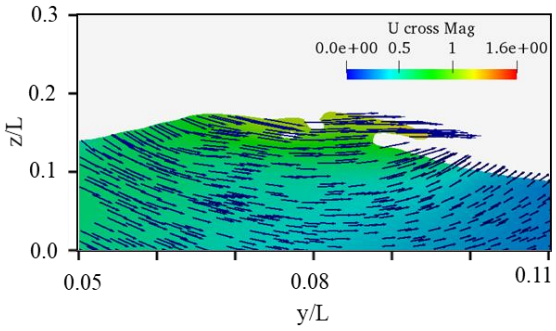

(d) Section x/L= 0.15

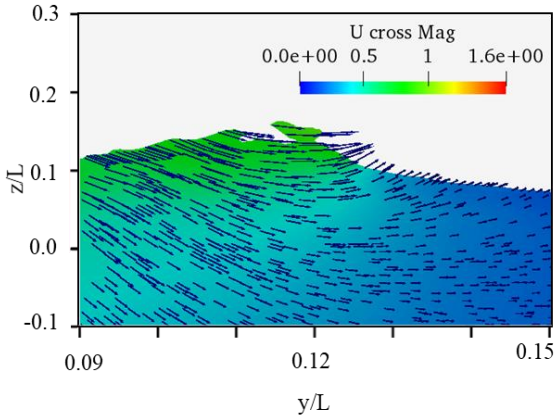

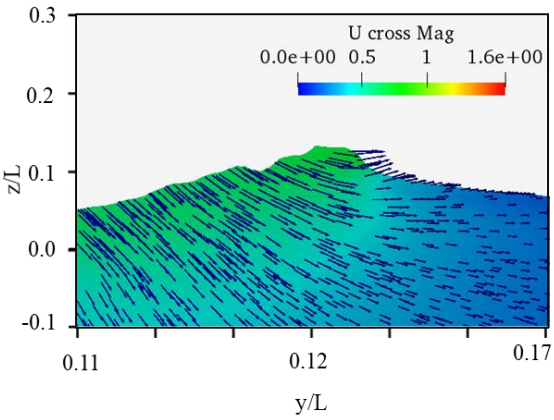

(e) Section x/L= 0.20 (f) Section x/L= 0.25

Figure 7-22 Initial bow wave development at six cross-sectional planes, cross flow velocity magnitude.

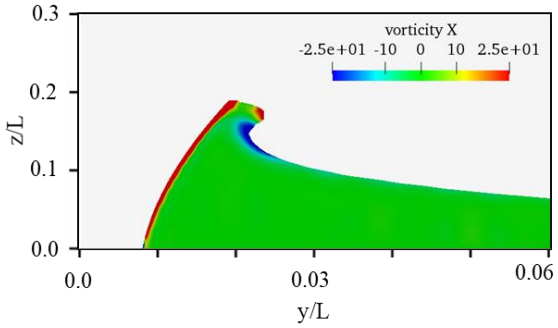

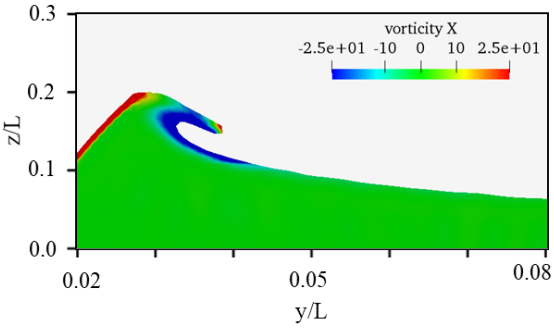

(a) Section x/L= 0.05 (b) Section x/L= 0.07

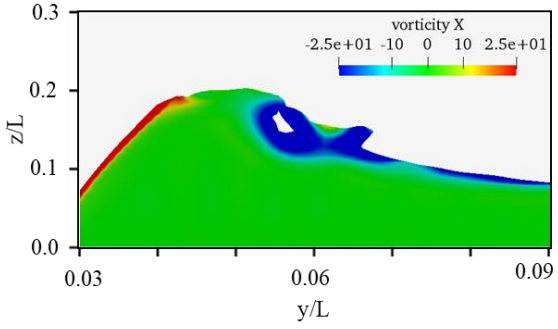

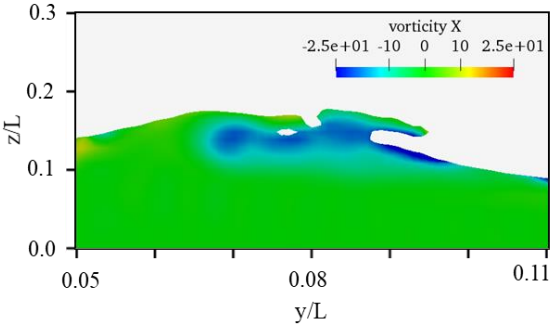

(c) Section x/L= 0.11 (d) Section x/L= 0.15

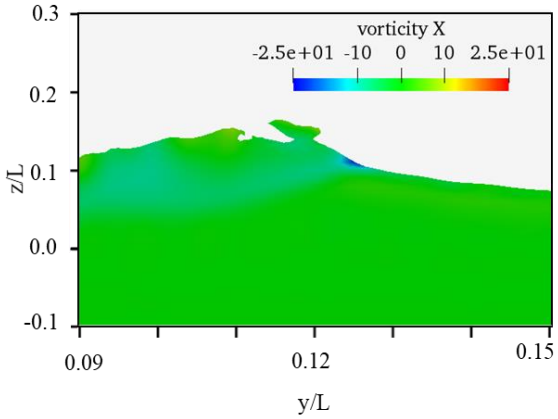

(e) Section x/L= 0.20

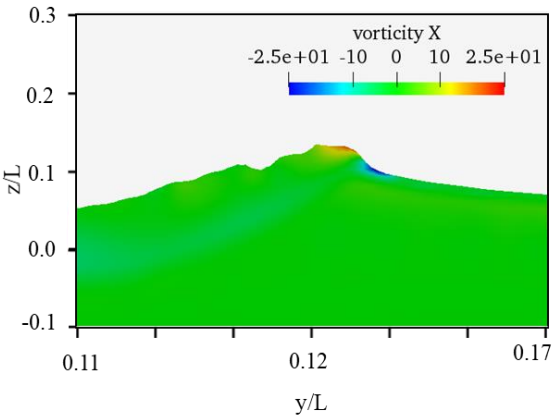

(f) Section x/L= 0.25

Figure 7-23 Initial bow wave development at six cross-sectional planes, axial vorticity distribution.

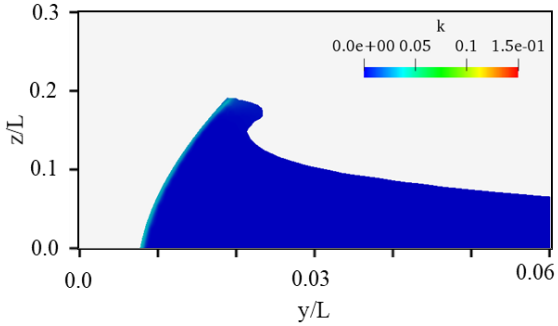

(a) Section x/L= 0.05

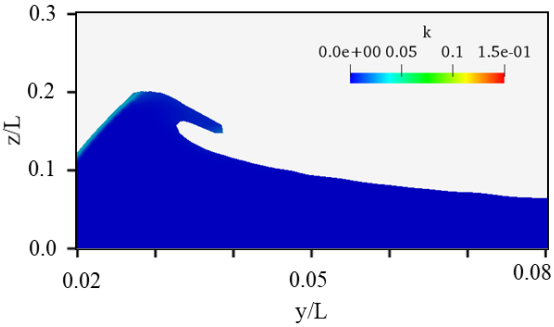

(b) Section x/L= 0.07

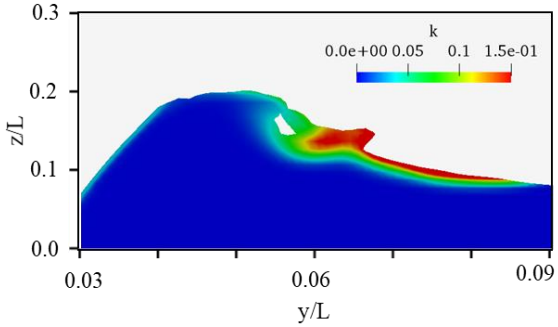

(c) Section x/L= 0.11

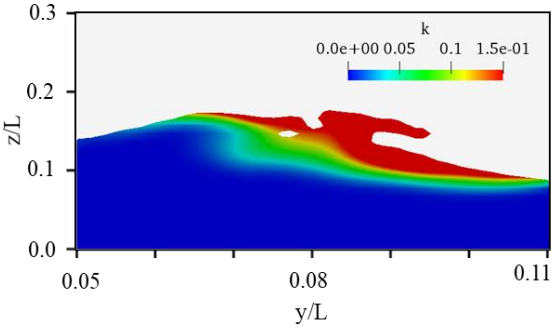

(d) Section x/L= 0.15

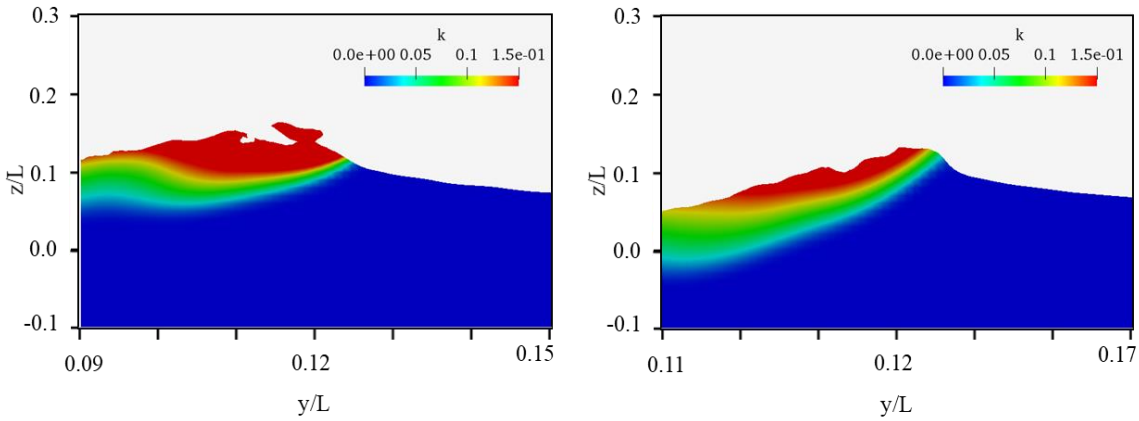

(e) Section x/L= 0.20 (f) Section x/L= 0.25

Figure 7-24 Initial bow wave development at six cross-sectional planes, turbulent kinetic energy.

7.3.5 Froude number effects on bow plunging breaking waves

In this section, the effect of the Froude number on the KCS bow breaking waves is analysed using the IBVOF solver. The strength of the initial plunging jet which develops at the crest of the overturning bow wave mainly depends on the velocity of the head currents. Figure 7-25 shows the wave profiles of the plunging jet for four Froude numbers between 0.35 and 0.40, gradually modifying and extending along the Froude number increases.

The major process of the plunging wave breaking is very similar for the different Fr numbers. A steep bow wave forms and starts to overturn due to the turning of the flow at the leading edge of the bow. It is obvious that the bow wave in higher ship speed will generated the increase of height of the first plunger. At an aft position increasing with Fr number, a lateral wave initiates and moves away from the hull forming a jet.

The jet size, jet velocity and impingement angle are key parameters for modelling air entrainment by plunging jets[19]. The location of the first plunge point is shown in Figure 7-26. Figure 7-27 shows the geometric parameters of the plunge jet, jet length and impingement angle. As expected, the size of the first jet increases almost linearly with Fr while the angles of jet tip inclination at impact keep similar at approximately 43° below the horizontal.

Though the global structure of plunging wave jet is well described, the present simulation fails to capture the detailed air entrainment when the jet impinges the free surface and the droplets

splashing outward after the impingement. The mesh size is too large for these small-scale phenomena. Finer mesh is still required in the future simulation.

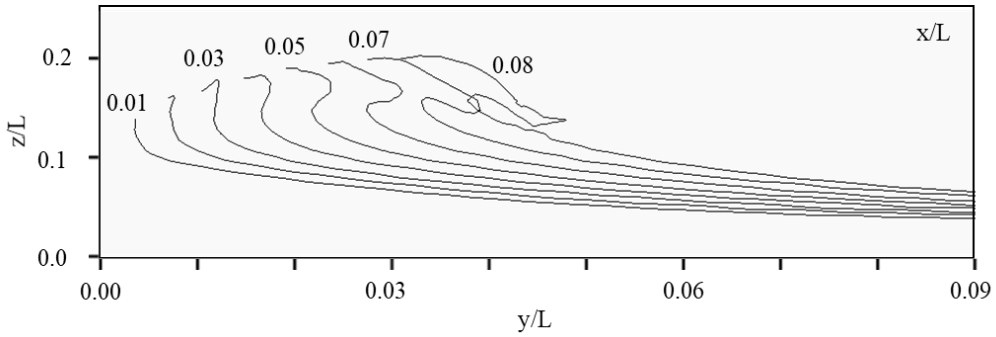

(a) Froude number Fr= 0.35

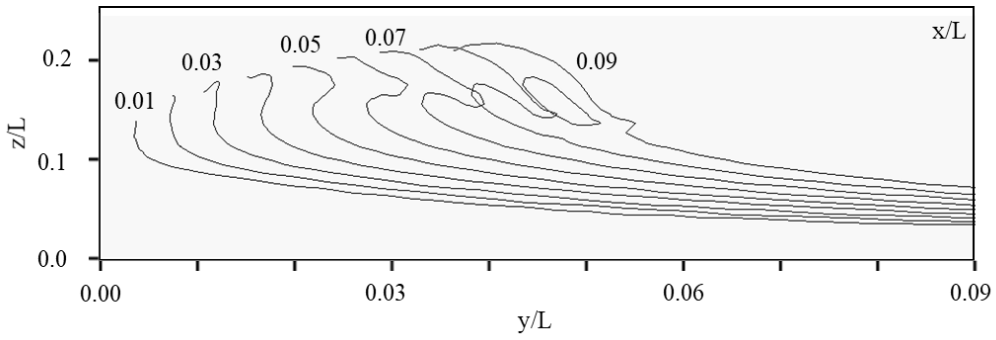

(b) Froude number Fr= 0.36 0.54

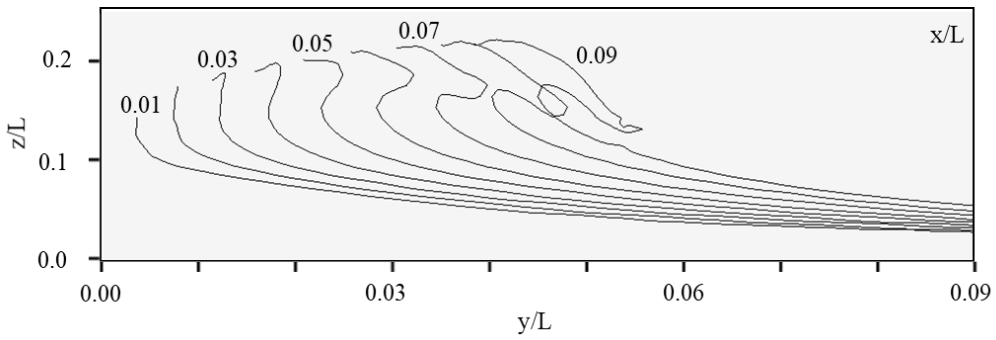

(c) Froude number Fr= 0.38 0.54

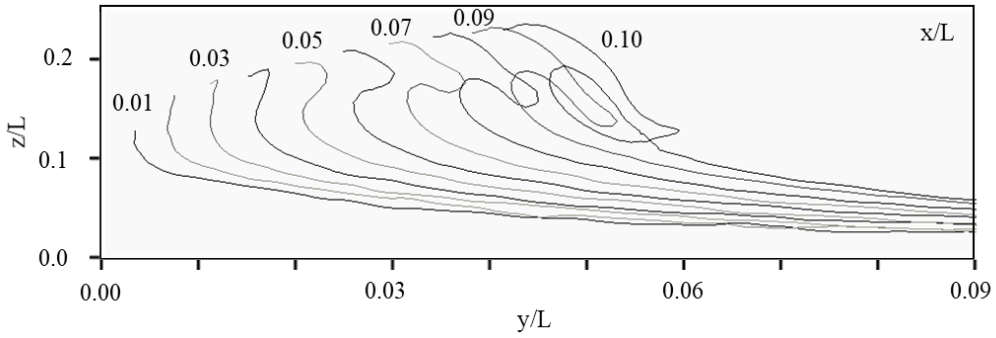

(d) Froude number Fr= 0.40 0.6

Figure 7-25 Slices of the wave profiles alongside x-direction with four Froude numbers

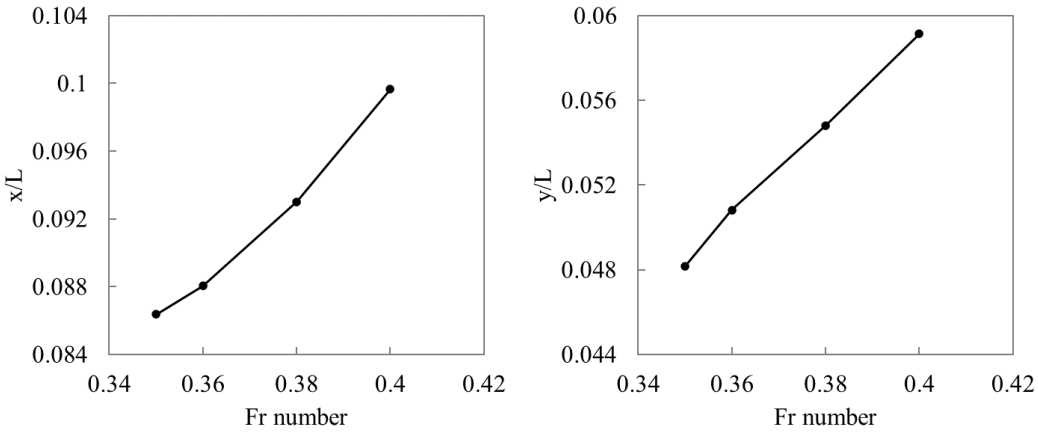

(a) Longitudinal location (b) Transverse location

Figure 7-26 Location of the plunge point.

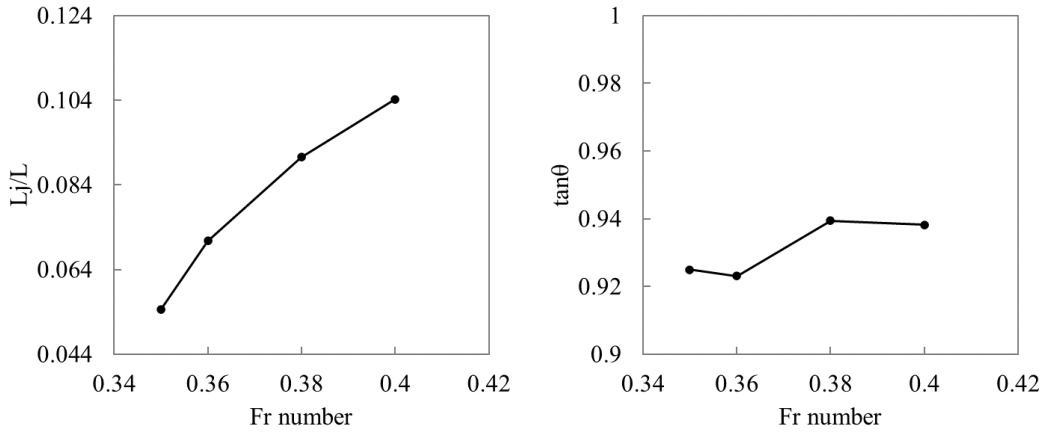

(a) Jet length (b) Angle of impact

Figure 7-27 Geometric parameters of the plunge jet.

7.4 Conclusion

In this Chapter, the numerical analysis is focused on breaking bow waves. The proposed IBVOF solver is applied for the simulation of the plunging breaking waves generated by a fix sharp wedge-shaped wedge and a fixed KCS hull in uniform flows. The major processes of the plunging wave breaking are well predicted including the highest wave formation, the first thin water sheet formation and overturning, the first splash-up, the second water jet and the second splash-up.

The bow wave breaking process is initiated by the pressure field generated by the ship model and mainly dominated by gravity and inertial force. An energetic plunging jet is generated and impact onto the underlying free surface, entrapping air and creating circulation and vorticity. A large amount of air entrapment and droplets are generated near and after the plunger which are significant sources of underwater noise and while water wake. In the process of plunging wave breaking, the angle and velocity of the second plunger is not only determined by the interaction between the two parts of water which follows the momentum theorem but also affected by the pair of vortexes.

Chapter 8 Concluding remarks

8.1 Conclusions

The study of breaking bow waves has significant benefits due to its influence in many aspects. The consequences caused by breaking bow waves include, but are not limited to, the increase of resistance, increased detectability and damage to port facilities. Analytic studies are not suitable for this problem because of over-simplified model. Present experimental studies are costly and not robust. Accurate and appliable numerical simulations are required for developing mathematical models to understand the features of bow waves and better predict their behaviours.

It is a challenge to resolve the flow of the two phases and the evolution of the interface between them. Various free surface flow solution methods are available, but all have their own limitation. This thesis builds an air-water boundary layer model to overcome the discontinuity over the two-phase interface and presents a combined volume of fluid and immersed boundary method for simulations of ship bow breaking waves. It is shown to improve the robustness and stability of two-phase flow simulations.

Bow wave breaking has been a difficult phenomenon to model theoretically for both spilling and plunging breaking waves because the bow wave changes continuously through the interaction of air and water with significant differences in properties. Experimental measurements are the most reliable methods, but they are costly and not robust. As alternatives to experimental measurements, CFD simulations have become a powerful tool to predict detailed wave breaking process and velocity profile in both water and air phases. The trend of CFD research is to improve hydrodynamic tools with accurate prescription and prediction of air-water interface behaviour.

The review also carried out a summary of the air-water interface modelling. Various air-water interface tracking/capturing methods have been compared and discussed. Among them, two-phase flow solvers are more suitable for breaking wave simulations while improvements are required to resolve the free-surface boundary layer with large density jump between air and water. The free surface boundary layer is not resolved in all implicit interface capturing methods with large density jumps between air and water and unphysical flow tends to be generated at the interface due to the numerical inadequacies. A physics-based viscous air-water boundary layer model is required to be developed and applied to VOF methods to deal with the discontinuity in the fluid properties over the two-phase interface and to offer a better resolution of the free-surface.

The sources of spurious velocities near the interface are identified based on governing equations. The source of the problem in the original solver is believed to lie in the interpolation of the momentum flux and the imbalance of the dynamic pressure gradient and density gradient because of the density jump across the interface. Conventional linear momentum flux interpolation practices can lead to significant errors, which cause 'fake' momentum and numerical instability when the density ratio increases and ultimately results in spurious velocities and spurious shear near the interface.

A two-phase flow solver, IBVOF solver has been developed to simulate multiphase flows with high density ratios. The numerical method is presented in detail with the emphasis on the treatment of the interface boundary. An extrapolated velocity (EV) approach is developed to extend the velocity from the denser phase to the lighter phase, and an immersed boundary method is used to build a thin boundary layer above the interface. Such treatment reduces the spurious velocity caused by the momentum interpolation errors across the interface and improve the accuracy and stability of high-density ratio two-phase flow simulations.

Two sets of test cases have been designed to confirm the source of the spurious velocity observed in the normal VOF solver and to validate the proposed IBVOF method: steady stratified flow and convection of a high-density droplet. The results of the two solvers are compared with analytical solutions, single phase flow solver results. The spurious errors in momentum cannot be eliminated with mesh or time refinement and finally distort the interface.

The IBVOF solver presented in this thesis provides a solution to this problem. The designed boundary layer smoothing of the velocity field helps to prevent the tearing of the interface due to the tangential velocity between the two phases across the interface. It is shown to improve the robustness and stability of two-phase flow simulations, and higher accuracy can be obtained on a relatively coarse grid compared to the original solver.

Another velocity extrapolated method, the DW approach, has been implemented to extend the application of the proposed IBVOF solver from 2D uniform mesh to unstructured mesh cases and 3D simulations. Compare to the EV approach, more liquid and gas cells are used with the DW approach in the smoothing process and the denser has larger effect on the velocity in the designed free surface boundary due to the density weight. The DW-IBVOF solver is therefore more reasonable in terms of fluid physical property.

The effects of fluid viscosity and surface tension are investigated through two benchmark tests, the viscous two-phase Poiseuille flows and a circular droplet in static fluid. When the density of the two phases keeps the same, excellent results are obtained by both the original interFoam and the

proposed IBVOF solver. The viscosity ratios between the two phases do not generate the spurious velocity across the interface as the density ratios do. As for the surface tension, unfortunately, the proposed solver fails to deal with the parasitic currents raised form the instability of the surface tension algorithm.

The DW-IBVOF solver is applied to simulate a real-life problem of a droplet impact on a thin liquid file at short time and the computational results are compared with the original interFoam and published experimental data. The surface tension and fluid viscosity are considered. The three stages of droplet impact observed in the experiment are well captured by the DW-IBVOF solver. The designed boundary layer smoothing of the velocity field helps to prevent the tearing of the interface due to the tangential velocity between the two phases across the interface.

The two-phase flow solver IBVOF solver is then further validated with two sets of benchmark cases, the propagation and breaking-up of solitary waves and stokes waves with focus on applications in ocean and coastal engineering. The investigation of the velocity field revealed that spurious currents appearing in the vicinity of the interface, resulting in a local increase of the velocity which might have influences the shape of the free surface. The proposed density-weight smoothing (DW) method and the designed boundary layer on the interface suppress the spurious velocities and improve the accuracy and stability of air-water flow simulations.

Finally, the numerical analysis is focused on breaking bow waves. The proposed IBVOF solver is applied for the simulation of the plunging breaking waves generated by a fixed sharp wedge-shaped wedge and a fixed KCS hull in uniform flows. The major processes of the plunging wave breaking are well predicted. The bow wave breaking process is initiated by the pressure field generated by the ship model and mainly dominated by gravity and inertial force. The initial plunger is created due to the formation and subsequent thickening of the bow wave sheet. The reconnection of the first plunger is associated with large cross flow differences between the plunger tip and free surface below, generation of large turbulent kinetic energy and the formation of a free surface scar. The angle and velocity of the second plunger is affected by the axial vorticity with a rotational orientation.

This research was supported by the University of Southampton, the China Scholarship Council (No. 201706950085) and National Science Foundation of China (Grant No. 51720105011).

8.2 Suggestions for future work

There are still many interesting questions on all fronts of this research. Suggestions for future studies that can build from or improve on this work are listed below.

The IBVOF method proposed in this thesis has reduced the spurious velocity caused by the momentum interpolation errors across the interface and improve the accuracy and stability of high-density ratio two-phase flow simulation. However, the solver fails to deal with the spurious current origins from surface tension force term caused by inaccurate interface curvature in VOF methods. Several strategies have been employed to mitigate the errors caused by the surface tension force [70][76][78]. Combining one of the strategies with the proposed IBVOF method could further improve the accuracy of the two-phase flow solver.

The IBVOF method proposed in this thesis is designed for VOF method based on the OpenFoam platform. The free surface boundary layer is not resolved in all implicit interface capturing methods with large density jumps between air and water. The air-water boundary layer model is therefore also applicable for other two-phase solvers where there is no slip between the two fluids and could be extended to simulations with Level set methods or Coupled Level Set and Velocity of Fluid (CLSVOF) methods.

The simulations in this thesis have been run with fine meshes to ensure accurate representation of the flow. The investigation of KCS bow breaking waves has not been fully completed. Though the main process of the bow breaking waves has been described, the air bubbles or water droplets are unable to captured when the scale is smaller than the grid spacing. The droplets and bubbles in breaking waves are estimated by volume fractions with some limitations due to the numerical model adopted in the simulations. To well demonstrate the detailed information of droplets, much finer mesh is required for further investigation. What's more, the effect of small-scale detailed plunging breaking, spray formation and air entrainment to the overall ship bow waves is required quantitatively investigation in the future work.

The unsteady RANS model tends to predict a breaking bow wave which is more coherent, steady, and smooth than that from experiment. Resolution of extremely small-scale unsteady free surfaces will probably require increased spatial and temporal resolution or large eddy or detached eddy simulation modelling. There are no available experimental flow data to validate the present computations results. It is worth conducing towing tank experiments for better understanding of the KCS bow breaking waves.

This thesis has presented a new two-phase flow solver for simulations of ship bow breaking waves. In general ship flow simulations, on the other hand, single-phase flow solvers are commonly used especially in the industry since they are believed to be more effective and efficient. The investigation of bow breaking waves by experiments and two-phase flow solvers helps to build a physical based model for dynamic free surface boundary conditions for one-phase flow solvers and improve the accuracy and robustness of the one-phase flow solvers.

List of References

[1] F. Stern, J. Yang, Z. Wang, H. Sadat-Hosseini, M. Mousaviraad, Computational ship hydrodynamics: Nowadays and way forward, in: Int. Shipbuild. Prog., 2013. https://doi.org/10.3233/ISP-130090.

[2] A. Olivieri, F. Pistani, R. Wilson, E.F. Campana, F. Stern, Scars and vortices induced by ship bow and shoulder wave breaking, J. Fluids Eng. Asme. 129 (2007) 1445–1459. https://doi.org/10.1115/1.2786490.

[3] J. Wackers, B. Koren, H.C. Raven, A. van der Ploeg, A.R. Starke, G.B. Deng, P. Queutey, M. Visonneau, T. Hino, K. Ohashi, Free-Surface Viscous Flow Solution Methods for Ship Hydrodynamics, Arch. Comput. Methods Eng. 18 (2011) 1–41. https://doi.org/10.1007/s11831-011-9059-4.

[4] Z. Wang, J. Yang, F. Stern, An improved particle correction procedure for the particle level set method, J. Comput. Phys. 228 (2009) 5819–5837. https://doi.org/10.1016/j.jcp.2009.04.045.

[5] T.C. Fu, T. Ratcliffe, T.T. O'Shea, K.A. Brucker, R.S. Graham, D.C. Wyatt, A Comparison of Experimental Measurements and Computational Predictions of a Deep-V Planing Hull, (2014) 12–17.

[6] F. Xiao, M. Dianat, J.J. McGuirk, A robust interface method for drop formation and breakup simulation at high density ratio using an extrapolated liquid velocity, Comput. Fluids. (2016). https://doi.org/10.1016/j.compfluid.2016.06.021.

[7] F. Noblesse, G. Delhommeau, H. Liu, D.C. Wan, C. Yang, Ship bow waves, J. Hydrodyn. 25 (2013) 491–501. https://doi.org/10.1016/S1001-6058(11)60388-1.

[8] E. Korkakaki, Process optimization for polyhydroxyalkanoate (PHA) production from waste via microbial enrichment cultures, 2017. https://doi.org/10.4233/uuid.

[9] F. Noblesse, G. Delhommeau, M. Guilbaud, D. Hendrix, C. Yang, Simple analytical relations for ship bow waves, J. Fluid Mech. 600 (2008) 105–132. https://doi.org/10.1017/S0022112008000220.

[10] M. Kandasamy, T. Xing, F. Stern, Unsteady free surface wave-induced separation: Vortical structures and instabilities, J. Fluids Struct. 25 (2009) 343–363. https://doi.org/10.1016/j.jfluidstructs.2008.05.002.

[11] S.H. Rhee, F. Stern, RANS Model for Spilling Breaking Waves, J. Fluids Eng. 124 (2002) 424. https://doi.org/10.1115/1.1467078.

[12] Q. Jin, D. Hudson, P. Temarel, Numerical simulation of plunging breaking waves on a ship bow by a two-phase flow solver, in: Proc. Int. Offshore Polar Eng. Conf., 2020.

[13] H. MIYATA, H. ORIHARA, Y. SATO, Nonlinear ship waves and computational fluid dynamics, Proc. Japan Acad. Ser. B. 90 (2014) 278–300. https://doi.org/10.2183/pjab.90.278.

[14] T. Inui, Non-Linear Properties of Wave Making Ships Resistance of Wide-Beam, (n.d.).

[15] B. Coefficient, F. Stern, MEAN-FLOW MEASUREMENTS IN THE BOUNDARY I ° 01000Coo a, (2016).

[16] J.H. Duncan, The breaking and non-breaking wave resistance of a two-dimensional hydrofoil, J. Fluid Mech. 126 (1983) 507–520. https://doi.org/10.1017/S0022112083000294.

[17] R.R. DONG, J. KATZ, T.T. HUANG, On the structure of bow waves on a ship model, J. Fluid Mech. 346 (1997) S0022112097005946. https://doi.org/10.1017/S0022112097005946.

[18] G.I. Roth, D.T. Mascenik, J. Katz, Measurements of the flow structure and turbulence within a ship bow wave, Phys. Fluids. 11 (1999) 3512–3523. https://doi.org/10.1063/1.870209.

[19] T. a Waniewski, C.E. Brennen, F. Raichlen, Bow wave dynamics, J. Sh. Res. 46 (2002) 1–15.

[20] A. Olivieri, F. Pistani, A. Di Mascio, Breaking wave at the bow of a fast displacement ship model, J. Mar. Sci. Technol. 8 (2003) 68–75. https://doi.org/10.1007/s00773-003-0155-5.

[21] A. Karion, T.C. Fu, J.R. Rice, D.C. Walker, D.A. Furey, Naval Surface Warfare Center by, (2004).

[22] E. Maxeiner, Physics of Breaking Bow Waves: A Parametric Investigation using a 2D+ T Wave Maker, (2009).

[23] H. Orihara, H. Miyata, Evaluation of added resistance in regular incident waves by computational fluid dynamics motion simulation using an overlapping grid system, J. Mar. Sci. Technol. 8 (2003) 47–60. https://doi.org/10.1007/s00773-003-0163-5.

[24] G.B. Deng, E. Guilmineau, P. Queutey, M. Visonneau, Ship Flow Simulations with the ISIS CFD Code Laboratoire de Mécanique des Fluides , UMR CNRS 6598, (2005).

[25] M. Wood, J. Izquierdo, RANSE with free surface computations around fixed DTMB 5415 model and other Baliño ' s fishing vessels, Proc. 9th Int. Conf. (2007) 5–8.

[26] G. Weymouth, K. Hendrickson, D.K.P. Yue, T. O'Shea, D.G. Dommermuth, P. Adams, M. Valenciano, Modeling breaking ship waves for design and analysis of naval vessels, Dep. Def. - Proc. HPCMP Users Gr. Conf. 2007; High Perform. Comput. Mod. Progr. A Bridg. to Futur. Defense, DoD HPCMP UGC. (2007) 440–445. https://doi.org/10.1109/HPCMP-UGC.2007.48.

[27] P.M. Carrica, R. V. Wilson, F. Stern, Unsteady RANS simulation of the ship forward speed diffraction problem, Comput. Fluids. 35 (2006) 545–570. https://doi.org/10.1016/j.compfluid.2005.08.001.

[28] A. Colagrossi, M. Landrini, Numerical simulation of interfacial flows by smoothed particle hydrodynamics, J. Comput. Phys. 191 (2003) 448–475. https://doi.org/10.1016/S0021-9991(03)00324-3.

[29] S. Marrone, A. Colagrossi, M. Antuono, C. Lugni, M.P. Tulin, A 2D+t SPH model to study the breaking wave pattern generated by fast ships, J. Fluids Struct. 27 (2011) 1199–1215. https://doi.org/10.1016/j.jfluidstructs.2011.08.003.

[30] Z. Wang, J. Yang, F. Stern, Numerical simulations of wave breakings around a wedge-shaped bow, Small. (2010).

[31] Z. Wang, J. Yang, B. Koo, F. Stern, A coupled level set and volume-of-fluid method for sharp interface simulation of plunging breaking waves, Int. J. Multiph. Flow. (2009). https://doi.org/10.1016/j.ijmultiphaseflow.2008.11.004.

[32] J. Yang, F. Stern, Sharp interface immersed-boundary/level-set method for wave-body interactions, J. Comput. Phys. (2009). https://doi.org/10.1016/j.jcp.2009.05.047.

[33] Z. Wang, J. Suh, J. Yang, F. Stern, Sharp Interface LES of Breaking Waves by an Interface Piercing Body in Orthogonal Curvilinear Coordinates, Methods. (2012) 1–10. https://doi.org/10.2514/6.2012-1111.

[34] G. Tryggvason, B. Bunner, A. Esmaeeli, D. Juric, N. Al-Rawahi, W. Tauber, J. Han, S. Nas, Y.J. Jan, A Front-Tracking Method for the Computations of Multiphase Flow, J. Comput. Phys. 169 (2001) 708–759. https://doi.org/10.1006/jcph.2001.6726.

[35] Y. Tahara, F. Stern, A large-domain approach for calculating ship boundary layers and wakes and wave fields for nonzero froude number, J. Comput. Phys. 127 (1996) 398–411. https://doi.org/10.1006/jcph.1996.0183.

[36] P.M. Carrica, R. V. Wilson, R.W. Noack, F. Stern, Ship motions using single-phase level set with dynamic overset grids, Comput. Fluids. 36 (2007) 1415–1433. https://doi.org/10.1016/j.compfluid.2007.01.007.

[37] A. Di Mascio, R. Broglia, R. Muscari, On the application of the single-phase level set method to naval hydrodynamic flows, Comput. Fluids. 36 (2007) 868–886. https://doi.org/10.1016/j.compfluid.2006.08.001.

[38] M. Hoestra, Numerical simulation of ship stern flows with a space-marching Navier Stokes method, 1999.

[39] P. Ferrant, L. Gentaz, C. Monroy, R. Luquet, G. Ducrozet, B. Alessandrini, E. Jacquin, a Drouet, Recent Advances Towards the Viscous Flow Simulation of Ships Manoeuvering in Waves, Ocean Eng. (2007) 2005–2008.

[40] S.H. Rhee, B.P. Makarov, H. Krishinan, V. Ivanov, Assessment of the volume of fluid method for free-surface wave flow, J. Mar. Sci. Technol. 10 (2005) 173–180. https://doi.org/10.1007/s00773-005-0205-2.

[41] F.H. Harlow, J.E. Welch, Numerical calculation of time-dependent viscous incompressible flow of fluid with free surface, Phys. Fluids. 8 (1965) 2182–2189. https://doi.org/10.1063/1.1761178.

[42] S.O. Unverdi, G. Tryggvason, A front-tracking method for viscous, incompressible, multi-fluid flows, J. Comput. Phys. 100 (1992) 25–37. https://doi.org/10.1016/0021-9991(92)90307-K.

[43] N. Foster, R. Fedkiw, Practical animation of liquids, (2005) 23–30. https://doi.org/10.1145/383259.383261.

[44] R. Bakhtyar, D.A. Barry, A. Yeganeh-Bakhtiary, A. Ghaheri, Q. Zhao, S. Armfield, K. Tanimoto, Numerical simulation of breaking waves by a multi-scale turbulence model, Coast. Eng. 51 (2009) 250–263. https://doi.org/10.1016/j.coastaleng.2003.12.002.

[45] S. Shao, C. Ji, SPH computation of plunging waves using a 2-D sub-particle scale (SPS) turbulence model, Int. J. Numer. Methods Fluids. 51 (2006) 913–936. https://doi.org/10.1002/fld.1165.

[46] A. Fluent, Ansys Fluent Theory Guide, ANSYS Inc., USA. (2013).

[47] I. ANSYS, ANSYS® Academic Research, ANSYS CFX-Solver Model. Guid. (2013).

[48] Siemens, STAR-CCM+ CFD Software, (2021). https://mdx.plm.automation.siemens.com/star-ccm-plus.

[49] OpenFOAM, Open∇FOAM - The Open Source CFD Toolbox - User Guide, OpenFOAM Found. (2014). https://doi.org/10.1023/A.

[50] S. Osher, J.A. Sethian, Fronts propagating with curvature-dependent speed: Algorithms based on Hamilton-Jacobi formulations, J. Comput. Phys. (1988). https://doi.org/10.1016/0021-9991(88)90002-2.

[51] D. Enright, R. Fedkiw, J. Ferziger, I. Mitchell, A hybrid particle level set method for improved interface capturing, 2002. https://doi.org/10.1006/jcph.2002.7166.

[52] M. Sussman, E.G. Puckett, A Coupled Level Set and Volume-of-Fluid Method for Computing 3D and Axisymmetric Incompressible Two-Phase Flows, J. Comput. Phys. (2000). https://doi.org/10.1006/jcph.2000.6537.

[53] E. Olsson, G. Kreiss, A conservative level set method for two phase flow, J. Comput. Phys. 210 (2005) 225–246. https://doi.org/10.1016/j.jcp.2005.04.007.

[54] C. Hu, M. Kashiwagi, A CIP-based method for numerical simulations of violent free-surface flows, J. Mar. Sci. Technol. 9 (2004) 143–157. https://doi.org/10.1007/s00773-004-0180-z.

[55] C.W. Shu, S. Osher, Efficient implementation of essentially non-oscillatory shock-capturing schemes, J. Comput. Phys. 77 (1988) 439–471. https://doi.org/10.1016/0021-9991(88)90177-5.

[56] X.D. Liu, Weighted essentially non-oscillatory schemes, J. Comput. Phys. 115 (1994) 200–212. https://doi.org/10.1006/jcph.1994.1187.

[57] C.W. Hirt, B.D. Nichols, Volume of fluid (VOF) method for the dynamics of free boundaries, J. Comput. Phys. (1981). https://doi.org/10.1016/0021-9991(81)90145-5.

[58] J. Roenby, B.E. Larsen, H. Bredmose, H. Jasak, A new volume-of-fluid method in openfoam, in: 7th Int. Conf. Comput. Methods Mar. Eng. Mar. 2017, 2017.

[59] S.S. Deshpande, L. Anumolu, M.F. Trujillo, Evaluating the performance of the two-phase flow solver interFoam, Comput. Sci. Discov. (2012). https://doi.org/10.1088/1749-4699/5/1/014016.

[60] H.T. Ahn, M. Shashkov, Adaptive moment-of-fluid method, J. Comput. Phys. 228 (2009) 2792–2821. https://doi.org/10.1016/j.jcp.2008.12.031.

[61] M. Jemison, E. Loch, M. Sussman, M. Shashkov, M. Arienti, M. Ohta, Y. Wang, A coupled level set-moment of fluid method for incompressible two-phase flows, J. Sci. Comput. 54 (2013) 454–491. https://doi.org/10.1007/s10915-012-9614-7.

[62] E. Aulisa, S. Manservisi, R. Scardovelli, A surface marker algorithm coupled to an area-preserving marker redistribution method for three-dimensional interface tracking, J. Comput. Phys. 197 (2004) 555–584. https://doi.org/10.1016/j.jcp.2003.12.009.

[63] Z. Wang, J. Yang, F. Stern, A new volume-of-fluid method with a constructed distance function on general structured grids, J. Comput. Phys. 231 (2012) 3703–3722. https://doi.org/10.1016/j.jcp.2012.01.022.

[64] D.A. Hoang, V. van Steijn, L.M. Portela, M.T. Kreutzer, C.R. Kleijn, Benchmark numerical simulations of segmented two-phase flows in microchannels using the Volume of Fluid method, Comput. Fluids. (2013). https://doi.org/10.1016/j.compfluid.2013.06.024.

[65] S.J. Cummins, M.M. Francois, D.B. Kothe, Estimating curvature from volume fractions, Comput. Struct. 83 (2005) 425–434. https://doi.org/10.1016/j.compstruc.2004.08.017.

[66] Y. Renardy, M. Renardy, PROST: A parabolic reconstruction of surface tension for the volume-of-fluid method, J. Comput. Phys. 183 (2002) 400–421. https://doi.org/10.1006/jcph.2002.7190.

[67] S. Popinet, An accurate adaptive solver for surface-tension-driven interfacial flows, J. Comput. Phys. 228 (2009) 5838–5866. https://doi.org/10.1016/j.jcp.2009.04.042.

[68] A. Iafrati, A. Di Mascio, E.F. Campana, A level set technique applied to unsteady free surface flows, Int. J. Numer. Methods Fluids. 35 (2001) 281–297. https://doi.org/10.1002/1097-0363(20010215)35:3<281::AID-FLD91>3.0.CO;2-V.

[69] D.L. Chopp, Computing minimal surfaces via level set curvature flow, J. Comput. Phys. 106 (1993) 77–91. https://doi.org/10.1006/jcph.1993.1092.

[70] M.M. Francois, S.J. Cummins, E.D. Dendy, D.B. Kothe, J.M. Sicilian, M.W. Williams, A balanced-force algorithm for continuous and sharp interfacial surface tension models within a volume tracking framework, J. Comput. Phys. 213 (2006) 141–173. https://doi.org/10.1016/j.jcp.2005.08.004.

[71] M. Meier, G. Yadigaroglu, B.L. Smith, A novel technique for including surface tension in PLIC-VOF methods, Eur. J. Mech. B/Fluids. 21 (2002) 61–73. https://doi.org/10.1016/S0997-7546(01)01161-X.

[72] S. Popinet, S. Zaleski, A front-tracking algorithm for accurate representation of surface tension A front tracking algorithm for the accurate representation of surface tension, (2017).

[73] E. Shirani, N. Ashgriz, J. Mostaghimi, Interface pressure calculation based on conservation of momentum for front capturing methods, J. Comput. Phys. 203 (2005) 154–175. https://doi.org/10.1016/j.jcp.2004.08.017.

[74] T. Ménard, S. Tanguy, A. Berlemont, Coupling level set/VOF/ghost fluid methods: Validation and application to 3D simulation of the primary break-up of a liquid jet, Int. J. Multiph. Flow. 33 (2007) 510–524. https://doi.org/10.1016/j.ijmultiphaseflow.2006.11.001.

[75] S. Tanguy, T. Ménard, A. Berlemont, A Level Set Method for vaporizing two-phase flows, J. Comput. Phys. (2007). https://doi.org/10.1016/j.jcp.2006.07.003.

[76] C. Galusinski, P. Vigneaux, On stability condition for bifluid flows with surface tension: Application to microfluidics, J. Comput. Phys. 227 (2008) 6140–6164. https://doi.org/10.1016/j.jcp.2008.02.023.

[77] S. Hysing, A new implicit surface tension implementation for interfacial flows, Int. J. Numer. Methods Fluids. 51 (2006) 659–672. https://doi.org/10.1002/fld.1147.

[78] Z. Guo, B.S. Haynes, D.F. Fletcher, Simulation of microchannel flows using a 3D height function formulation for surface tension modelling, Int. Commun. Heat Mass Transf. (2017). https://doi.org/10.1016/j.icheatmasstransfer.2017.09.017.

[79] M. Rudman, A volume-tracking method for incompressible multifluid flows with large density variations, Int. J. Numer. Methods Fluids. (1998). https://doi.org/10.1002/(SICI)1097-0363(19980815)28:2<357::AID-FLD750>3.0.CO;2-D.

[80] M. Raessi, A level set based method for calculating flux densities in two-phase flows, Cent. Turbul. Res. Annu. Res. Briefs 2008. (2008) 467–478.

[81] O. Desjardins, V. Moureau, Methods for multiphase flows with high density ratio, Cent. Turbul. Res. Proc. Summer Progr. (2010).

[82] F. Gibou, L. Chen, D. Nguyen, S. Banerjee, A level set based sharp interface method for the multiphase incompressible Navier-Stokes equations with phase change, J. Comput. Phys. (2007). https://doi.org/10.1016/j.jcp.2006.07.035.

[83] V. Vukčević, H. Jasak, I. Gatin, Implementation of the Ghost Fluid Method for free surface flows in polyhedral Finite Volume framework, Comput. Fluids. (2017). https://doi.org/10.1016/j.compfluid.2017.05.003.

[84] M. Alidoost, A.R. Pishevar, On Importance of the Surface Charge Transport Equation in Numerical Simulation of Drop Deformation in a Direct Current Field, J. Fluids Eng. Trans. ASME. (2018). https://doi.org/10.1115/1.4040301.

[85] M.S. Lee, V. Aute, A. Riaz, R. Radermacher, A Review on Direct Two-Phase , Phase Change Flow Simulation Methods and their Applications, in: Int. Refrig. Air Cond. Conf., 2012.

[86] T.C. Fu, T.T. O'Shea, C.Q. Judge, D. Dommermuth, K. Brucker, D.C. Wyatt, A detailed assessment of numerical flow analysis (NFA) to predict the hydrodynamics of a deep-V planing hull, Int. Shipbuild. Prog. 60 (2013) 143–169. https://doi.org/10.3233/ISP-130087.

[87] W.F. Pfeffer, The Divergence Theorem, Trans. Am. Math. Soc. (1986). https://doi.org/10.2307/2000057.

[88] C.M. Klaij, M. Hoekstra, G. Vaz, Design, analysis and verification of a volume-of-fluid model with interface-capturing scheme, Comput. Fluids. (2018). https://doi.org/10.1016/j.compfluid.2018.05.016.

[89] A. Albadawi, D.B. Donoghue, A.J. Robinson, D.B. Murray, Y.M.C. Delauré, Influence of surface tension implementation in Volume of Fluid and coupled Volume of Fluid with Level Set methods for bubble growth and detachment, Int. J. Multiph. Flow. (2013). https://doi.org/10.1016/j.ijmultiphaseflow.2013.01.005.

[90] J. Xin, F. Shi, Q. Jin, C. Lin, A radial basis function based ghost cell method with improved mass conservation for complex moving boundary flows, Comput. Fluids. (2018). https://doi.org/10.1016/j.compfluid.2018.09.004.

[91] M. Sussman, K.M. Smith, M.Y. Hussaini, M. Ohta, R. Zhi-Wei, A sharp interface method for incompressible two-phase flows, J. Comput. Phys. (2007). https://doi.org/10.1016/j.jcp.2006.06.020.

[92] Q. Jin, D. Hudson, P. Temarel, W.G. Price, Performance of a Two-Phase Flow Solver for the Simulation of Breaking Waves, in: Proc. ASME 2019 38th Int. Conf. Ocean. Offshore Arct. Eng., American Society of Mechanical Engineers, 2019: pp. 1–7. https://doi.org/10.1115/OMAE2019-96326.

[93] M. Bussmann, D.B. Kothe, J.M. Sicilian, Modeling high density ratio incompressible interfacial flows, in: Am. Soc. Mech. Eng. Fluids Eng. Div. FED, 2002. https://doi.org/10.1115/FEDSM2002-31125.

[94] V. Le Chenadec, H. Pitsch, A monotonicity preserving conservative sharp interface flow solver for high density ratio two-phase flows, J. Comput. Phys. (2013). https://doi.org/10.1016/j.jcp.2013.04.027.

[95] P.A. Wroniszewski, J.C.G. Verschaeve, G.K. Pedersen, Benchmarking of Navier-Stokes codes for free surface simulations by means of a solitary wave, Coast. Eng. (2014). https://doi.org/10.1016/j.coastaleng.2014.04.012.

[96] J. Roenby, H. Bredmose, H. Jasak, A computational method for sharp interface advection, R. Soc. Open Sci. (2016). https://doi.org/10.1098/rsos.160405.

[97] T.C. Fu, T.T. O'Shea, C.Q. Judge, D. Dommermuth, K. Brucker, D.C. Wyatt, A detailed assessment of numerical flow analysis (NFA) to predict the hydrodynamics of a deep-V planing hull, in: Int. Shipbuild. Prog., 2013: pp. 143–169. https://doi.org/10.3233/ISP-130087.

[98] B. Lafaurie, C. Nardone, R. Scardovelli, S. Zaleski, G. Zanetti, Modelling merging and fragmentation in multiphase flows with SURFER, J. Comput. Phys. (1994). https://doi.org/10.1006/jcph.1994.1123.

[99] H. Liang, J. Xu, J. Chen, H. Wang, Z. Chai, B. Shi, Phase-field-based lattice Boltzmann modeling of large-density-ratio two-phase flows, Phys. Rev. E. (2018). https://doi.org/10.1103/PhysRevE.97.033309.

[100] M. Magnini, B. Pulvirenti, J.R. Thome, Characterization of the velocity fields generated by flow initialization in the CFD simulation of multiphase flows, Appl. Math. Model. (2016). https://doi.org/10.1016/j.apm.2016.02.023.

[101] M.H. Moghimi, N.J. Quinlan, A model for surface tension in the meshless finite volume particle method without spurious velocity, Comput. Fluids. (2019). https://doi.org/10.1016/j.compfluid.2018.11.019.

[102] S.J. Cummins, M.M. Francois, D.B. Kothe, Estimating curvature from volume fractions, Comput. Struct. (2005). https://doi.org/10.1016/j.compstruc.2004.08.017.

[103] A.B. Wang, C.C. Chen, Splashing impact of a single drop onto very thin liquid films, Phys. Fluids. (2000). https://doi.org/10.1063/1.1287511.

[104] R.L. Vander Wal, G.M. Berger, S.D. Mozes, Droplets splashing upon films of the same fluid of various depths, Exp. Fluids. (2006). https://doi.org/10.1007/s00348-005-0044-2.

[105] Y. Guo, L. Wei, G. Liang, S. Shen, Simulation of droplet impact on liquid film with CLSVOF, Int. Commun. Heat Mass Transf. (2014). https://doi.org/10.1016/j.icheatmasstransfer.2014.02.006.

[106] J. Fenton, A ninth-order solution for the solitary wave, J. Fluid Mech. (1972). https://doi.org/10.1017/S002211207200014X.

[107] G.K. Pedersen, E. Lindstrøm, A.F. Bertelsen, A. Jensen, D. Laskovski, G. Sælevik, Runup and boundary layers on sloping beaches, Phys. Fluids. (2013). https://doi.org/10.1063/1.4773327.

[108] W. Mo, A. Jensen, P.L.F. Liu, Plunging solitary wave and its interaction with a slender cylinder on a sloping beach, Ocean Eng. (2013). https://doi.org/10.1016/j.oceaneng.2013.09.011.

[109] P. Lin, K.A. Chang, P.L.F. Liu, Runup and rundown of solitary waves on sloping beaches, J. Waterw. Port, Coast. Ocean Eng. (1999). https://doi.org/10.1061/(ASCE)0733-950X(1999)125:5(247).

[110] B.M. Sumer, M.B. Sen, I. Karagali, B. Ceren, J. Fredsøe, M. Sottile, L. Zilioli, D.R. Fuhrman, Flow and sediment transport induced by a plunging solitary wave, J. Geophys. Res. Ocean. (2011). https://doi.org/10.1029/2010JC006435.

[111] C. Lin, P.H. Yeh, M.J. Kao, M.H. Yu, S.C. Hsieh, S.C. Chang, T.R. Wu, C.P. Tsai, Velocity fields in near-bottom and boundary layer flows in prebreaking zone of a solitary wave propagating over a 1:10 slope, J. Waterw. Port, Coast. Ocean Eng. (2015). https://doi.org/10.1061/(ASCE)WW.1943-5460.0000269.

[112] A. Iafrati, Numerical study of the effects of the breaking intensity on wave breaking flows, J. Fluid Mech. (2009). https://doi.org/10.1017/S0022112008005302.

[113] G. Chen, C. Kharif, S. Zaleski, J. Li, Two-dimensional Navier-Stokes simulation of breaking waves, Phys. Fluids. (1999). https://doi.org/10.1063/1.869907.

[114] Z. Tian, M. Perlin, W. Choi, Evaluation of a deep-water wave breaking criterion, Phys. Fluids. (2008). https://doi.org/10.1063/1.2939396.

[115] D. Kang, S. Ghosh, G. Reins, B. Koo, Z. Wang, F. Stern, Impulsive plunging wave breaking downstream of a bump in a shallow water flume-Part I: Experimental observations, J. Fluids Struct. 32 (2012) 104–120. https://doi.org/10.1016/j.jfluidstructs.2011.10.010.

[116] G. Rojas, M.R. Loewen, Void fraction measurements beneath plunging and spilling breaking waves, J. Geophys. Res. Ocean. (2010). https://doi.org/10.1029/2009JC005614.

[117] M. Mohseni, P.T. Esperanca, S.H. Sphaier, Numerical study of wave run-up on a fixed and vertical surface-piercing cylinder subjected to regular, non-breaking waves using OpenFOAM, Appl. Ocean Res. 79 (2018) 228–252. https://doi.org/10.1016/j.apor.2018.08.003.

[118] J. Wang, Z. Ren, D. Wan, Study of a Container Ship with Breaking Waves at High Froude Number Using URANS and DDES Methods, J. Sh. Res. (2020). https://doi.org/10.5957/josr.09180081.

[119] F. Stern, R. V. Wilson, H.W. Coleman, E.G. Paterson, Comprehensive approach to verification and validation of CFD simulations—Part 1: Methodology and procedures, J. Fluids Eng. Trans. ASME. (2001). https://doi.org/10.1115/1.1412235.

[120] M. Landrini, A. Colagrossi, M. Greco, M.P. Tulin, The fluid mechanics of splashing bow waves on ships: A hybrid BEMSPH analysis, Ocean Eng. (2012). https://doi.org/10.1016/j.oceaneng.2012.06.027.

[121] R. V. Wilson, P.M. Carrica, F. Stern, Simulation of ship breaking bow waves and induced vortices and scars, Int. J. Numer. Methods Fluids. (2007). https://doi.org/10.1002/fld.1406.

Appendix A Turbulence and energy dissipation mechanisms in steady spilling breaking waves induced by a shallowly submerged hydrofoil

Appendix B Simulation of plunging breaking waves induced by a submerged bump